

# **SHOCK WAVE FOCUSING**

## **Technical Report**

PREPARED FOR:

US Department of the Interior

Minerals Management Service

<b>1</b>	<b>Introduction.....</b>	<b>3</b>
1.1	Overview.....	3
1.2	Explosive cutting techniques for offshore decommissioning .....	4
1.2.1	Small offshore platforms.....	4
1.2.2	The UMIST and REVERSE Engineering contribution.....	7
1.3	The present work.....	7
<b>2</b>	<b>Background on Related Topics .....</b>	<b>9</b>
2.1	Dynamic fracturing .....	9
2.1.1	Introduction .....	9
2.1.2	Spalling .....	9
2.1.3	Failure models.....	9
2.1.4	Adiabatic Shear .....	14
2.1.5	Fields of maximum shear trajectories.....	18
2.2	Metallurgical changes under dynamic loading.....	18
2.3	Fracturing Charges .....	20
2.3.1	Introduction .....	20
2.3.2	Demolition Charges .....	21
2.3.3	Diamond Charges and Fracturing Belts.....	24
2.3.4	Waveguide Charges.....	27
	Figures Section 2.....	33
<b>3</b>	<b>Numerical analysis of SWF Technique .....</b>	<b>47</b>
3.1	Introduction .....	47
3.2	<i>SWF Technique</i> .....	49
3.2.1	Introduction .....	49
3.2.2	Initial Considerations.....	50
3.2.3	Modelling of SWF and waveguide charges using AUTODYN-2D..	53
3.3	Discussion of numerical results .....	58
3.3.1	SWF cutting mechanism .....	58
<b>4</b>	<b>Experimental Programme .....</b>	<b>86</b>
4.1	Introduction .....	86
4.2	Charge Design .....	86
4.2.1	Waveguide Geometry Design.....	87
4.3	Experimental Design .....	88
4.3.1	Introduction .....	88
4.3.2	Charge Manufacture .....	88
4.3.3	Experimental Set-up.....	95
4.3.4	Test Sites.....	96
4.4	Instrumentation .....	97
4.5	Target Material.....	97
4.6	Experimental Results .....	99
4.6.1	Tests on Plates.....	109
4.6.2	Testing on Curved Plate and Tubulars .....	123
4.7	Metallographies and Hardness Profiles of Selected Samples. ....	131
4.7.1	Metallographic Examination .....	131
4.7.2	Hardness profiles .....	132
4.8	Discussion and conclusions of SWF Technique experimental results ..	133
4.8.1	Overview.....	133
4.8.2	Discussion of SWF experimental results .....	134
	Figures Section 4.....	141

<b>5</b>	<b>Comparison between numerical and experimental results .....</b>	<b>196</b>
5.1	Comparison between numerical and experimental results.....	196
5.1.1	Curved Waveguides (Types 1,2 and 3) .....	196
5.1.2	Segmental Waveguides (Types 4, 5,6 & 8).....	197
5.2	Discussion of experimental and numerical results and proposed cutting mechanism for SWF technique .....	199
<b>6</b>	<b>General Discussion and Conclusions .....</b>	<b>199</b>
6.1	Discussion .....	199
6.1.1	Proven Capabilities.....	199
6.1.2	Reliability .....	201
6.1.3	Relative Environmental Impact .....	202
6.2	General Conclusions.....	203
	<b>Bibliographic References .....</b>	<b>204</b>

## 1 Introduction

Initially this project was conceived to be funded by the AMOCO Corporation, the EPSRC in the UK and the Mineral Management Services. AMOCO Corporation and EPSRC declined to fund the project at a late stage. Phillips Petroleum Norway replaced AMOCO in the initial stages of the project. The project was then carried out at slower speed with Reverse Engineering Limited and its subsidiary NEC funding the remaining work. To enable the project to be complete testing, theoretical analyses and numerical modelling were carried out over a period of 3 years. The findings of this project were included as part of the Doctor in Philosophy Thesis submitted by Alex De Joode to UMIST. The extensive analytical and numerical work presented in this report allowed for the first time the identification of design boundaries for the SWF cutting tool, and the description of the SWF cutting process, essential in the engineering of SWF for practical applications.

### 1.1 Overview

This report describes the work carried out for the development the **Shock Wave Focusing (SWF)** explosive cutting technique. Experimental, analytical and numerical investigations were performed leading to the identification of design parameters, cutting mechanism and a “Cutting Window” where the reliability of the SWF Technique is comparable to established explosive cutting techniques like Shaped Charges.

Explosive cutting charges have been used in the decommissioning of small offshore structures in the GoM for many years. These structures are scattered in an ecologically sensitive environment and despite their small size and weight, the effect of explosive cutting operations on the environment resulted in regulations to limit the maximum explosive weight. In fact, the requirement for decommissioning itself is originated by environmental concerns, and the associated international regulations.

The present work gives continuity to a part of a more comprehensive pool of technologies and studies carried out by UMIST and Reverse Engineering Limited to support the effort of oil companies and governments to reduce the environmental impact of the decommissioning operations of offshore structures.



## **1.2 Explosive cutting techniques for offshore decommissioning**

### **1.2.1 Small offshore platforms**

Normally small platforms are fixed to the seabed by steel piles driven inside the legs. Therefore, in most cases, what must be cut is not the platform leg but the internal piles (20 feet below the mud line) which are also made from structural steel. Other important factors to be considered are the necessity of extracting the pile after the cutting using a crane and the maximum explosive load permitted. Depending on the cutting method employed, the produced cut profile, or any bulging of the tubular could interfere with the extraction of the piles from the inside of the platform legs. The enlarged diameter and jagged edges of the pile can create serious difficulties for the crane vessel pulling the internal piles, resulting in increased time of the overall operation and consequent cost implications.

The following explosive cutting techniques are used in the decommissioning of small offshore structures:

- Bulk Charges
- Collision Charges
- Hollow Shaped Charges

#### **1.2.1.1 Bulk charges**

A bulk charge can be described as a drum filled with explosive. The drum is placed inside the tubular to be cut and then at the position of the cut. After the explosive drum is detonated, the steel tubular fracture and collapses due to the massive amount of energy liberated. The cut profile is the poorest of the three methods and can produce substantial enlargement of the pile diameters and jagged edges.

Despite its common use, this method is considered to be a very inefficient way to use explosives as it increases unnecessarily the environmental impact of the cutting operation. Bulk charges are used mainly due to their simplicity and their low cost. In most cases, they are used for the cutting of piles under the mud line. The excessive amount of explosives used is becoming less and less acceptable world wide, and alternative methods like collision charges and hollow shaped charges are expected to substitute the bulk charges eventually.

The performance of bulk charges can be improved by initiating the charge at both ends. This procedure results in collision of the detonation fronts at the centre of charge, generating a substantial increase in the pressure output. Bulk charges initiated in such fashion are also known as collision charges. A more sophisticated type of collision charge is discussed in the following subsection.

#### **1.2.1.2 Collision charges**

A collision charge consists of a torus shaped explosive material initiated at several points of its circumference. The explosive ring is placed inside the tubular and the multiple number of initiation points produces a similar number of regions where the detonation fronts collide. Due to the positive interaction between the colliding pressure pulses, the pressure in these collision regions is higher than in the remaining regions. A number of cracks are initiated on the tubular at the collision regions and propagate due to the action of the gas expansion of the detonation products. Despite the fact that less explosive than in bulk charges is used, the collision charges still require a large amount of explosive to propagate the cracks successfully. The damage produced in mild steel tubular can extend to a distance of 20 metres, due to the propagation of the cracks along the length of the tubular.

The cut profile produced by bulk or collision charges can interfere with the removal of the internal piles and the amount of explosive used is often not suitable for operations above the mud line. In these circumstances, the hollow shaped charges and the fracturing charges can be deployed. Nevertheless, the higher cost of these charges must be taken into consideration. Hollow shaped charges and fracturing charges are considered to be the only alternative for the large structures and are therefore discussed in the following section.

#### **1.2.1.3 Fracturing charges**

Fracturing charges produce a cut by inducing the metal to fracture under the action of reflected tensile waves. To some extent, fracturing charges use the same principle of collision charges as the crack is generated inside the material by the interference of tensile stress waves. In the case of fracturing charges, the crack is continuously generated inside the metal through the entire length of the cut, in contrast

to the collision charges where the initial cracks are propagated due to the expansion of the detonation products. Some crack propagation may occur through the thickness of the plate, as the charge design is able to concentrate the tensile reflected stress waves in specific regions of the central plane perpendicular to the surface [4]. The main types of fracturing charges are:

- Demolition Charges
- Diamond Charges
- Fracturing Belts
- Flat wave guides
- Shock Wave Focusing Charges

A Demolition Charge consists of a block of explosive substance placed in direct contact with the metal to be cut. The dimensions and shape of the blocks can be determined using empirical relationships developed for military applications [5]. The technique is often used for military purposes but it has not usually been used for underwater commercial applications. Despite the numerous experiments carried out to develop the empirical formulas, very little was published as far as the relationship between the explosive shape and the cutting achieved is concerned.

The potential for further reduction of the explosive load using this type of charge is low as extensive trial programmes have been carried out for the definition of empirical formulas. Despite its suitability for military applications, the method is considered to be the least effective among the fracturing charges.

Diamond charges consists of a sheet of plastic explosive cut into a tetragonal shape and initiated at two opposite vertices. The cut is produced by the interference of reflected tensile stress waves at the centre line between the initiation points. Diamond charges are particularly useful for cutting flat or round bars.

Fracturing belts were engineered to cut in similar fashion of diamond charges. The colliding detonation fronts are synchronised along one line. The synchronisation is achieved by using an inert substance to change the path of the detonation front. By changing the path, it is possible to increase or decrease the distance covered by the detonation front and also to split the detonation front into multiple fronts [7].

Flat waveguides and the Shock Wave Focusing charges are fracturing charges and consist of a linear shaped inert material placed in between two strips of explosive detonated at one end simultaneously. The inert material acts as a “lens”, converging the stress waves generated by the detonation of the two strips of explosive. The use of the word “lens” is a commercial simplification as the cutting phenomena proved to be more complex than the light theory. Flat Wave guides and Shock Wave Focusing are considered to have the best potential to produce a cutting charge with the lowest amount of explosive of all explosive cutting charges.

### **1.2.2 The UMIST and REVERSE Engineering contribution**

UMIST has been one of the leading institutions in the development of explosive cutting tools for the last 20 years. In the 1990's, the development of such tools has been focused on the specific needs of the offshore decommissioning. Several Thesis in this field have been carried out in UMIST and research projects in conjunction with Reverse Engineering [2],[4],[9] to [17].

### **1.3 The present work**

The present report describe the investigation into the SWF cutting process, make contributions to the understanding of the SWF cutting phenomenology, capability and reliability. The work supported by the MMS gives continuity to the experimental programme carried out as a part of the EXCUT project, which was funded by the Commission of the European Communities (CEC) under the THERMIE programme, and the work carried out by Al-Hassani and Burley [4][18][19].

Section 2 gives some background information regarding the fracturing of metals and reviews the relevant aspects of fracturing charges.

Section 3 describes numerical analysis of selected experiments. The participation of the interference of incident shock waves is identified as an important part of the cutting mechanism. This is proposed in addition to the interference between reflected tensile stress, which are also observed.

Section 4 describes the experimental work, which addresses trials with plates, curved plates and full tubulars of up to 1 metre diameter. Metallographic and hardness examinations of selected samples are also presented. The results suggest that the distribution of the explosive on the waveguide surface is an important parameter in the

charge design. The experimental results were analysed in conjunction with the work of Al-Hassani and Burley [4][19] taking into account the explosive distribution and waveguide geometry. This analyses allowed the identification of a “Cutting Window”, inside which the charge reliability is greatly improved.

Section 5 compares experimental and numerical results of the SWF technique, and proposes a cutting mechanism to explain the complex fracture patterns observed in Section 4. The boundaries of the “Cutting Window” are discussed in conjunction with the proposed cutting mechanism.

Section 6 presents a general discussion and conclusions.

## 2 Background on Related Topics

### 2.1 Dynamic fracturing

#### 2.1.1 Introduction

The dynamic fracturing of metals due to an explosive load or high velocity impact often leads to the phenomena such as adiabatic shear, spalling, twinning and brittle fractures in general. The fracture of a particular specimen may contain one or more fracture mechanisms as well as plastic deformation. Some of the relevant aspects of each type of failure mechanism are discussed in this section. Due to its military origins this literature is often focused on other metals than steel, and one has to be careful when extrapolating the behaviour of one type of material to another.

#### 2.1.2 Spalling

Spalling or scabbing is a failure due to the interference of incident and reflected stress waves from a free surface as shown in **Figures Section 2**

Figure 2.1 [27]. The failure generally occurs in a plane parallel to the free surface, but the fracturing patterns and fracturing mechanisms produced by an explosive load are ultimately a function of the interference of waves within a body. The stress and shock waves will be affected by several parameters discussed in the preceding sections. Generally the dynamic fracture can be considered as having four basic stages [29]:

- Rapid nucleation of microfractures at a large number of locations in the material.
- Growth of the fracture nuclei in rather symmetric manner.
- Coalescence of adjacent microfractures.
- Spallation or fragmentation by formation of one or more continuous fracture surfaces through the material.

#### 2.1.3 Failure models

Several models are proposed for the failure of metals under impact conditions and a review can be found in ADJ [30]. The models can be divided into two groups, the first group assumes an abrupt failure criterion, i.e. failure occurs when a critical value is reached. The

second group is based on the nucleation and growth of microcracks / microvoids (under tension) and micro-shear bands (under compression) [30].

### 2.1.3.1 Abrupt failure models

Abrupt failure models assume the instantaneous failure of the material when stress or strain reach a critical value. In two and three dimensional code calculations of high energy impact, stress is often approximated by pressure, and in this case failure is assumed when a critical pressure is reached[ADJ2].

The use of a strain criterion has to take into account the effects of stress triaxiality on the critical strain. This is achieved via the introduction of a non dimensional parameter to take into account the decrease of critical strain for higher values of triaxiality [ADJ3][30].

All the three criteria mentioned above equally assume the instantaneous failure of the metal when the respective critical value is reached, but experimental evidence had shown that the long duration pulses fracture metals at lower stresses. Turler and Butcher [31] introduced a criterion where a threshold tensile stress corresponds to the initiation of the failure process. The failure process is integrated in time according to the equation below. The material fails when the value of the integral is above a critical value  $K_c$ [ADJ4]

$$\int_0^{t_f} (\sigma - \sigma_0)^{\lambda} dt \geq K_c \quad (2.27)$$

where  $t_f$  is the total time for the completion of the failure process,  $\sigma_0$  is a threshold where failure starts.

In some cases the instantaneous fracture models can adequately describe the failure when the load applied is in the form of a square pulse like in a plate impact test. For loading conditions that are not similar to the plane impact test, the “time independent models” tend to super-estimate the actual spall stress [30].

Johnson and Cook [ADJ5][32] introduced further sophistication by taking into account the loading history and the cumulative damage concept. Despite these considerations, the model developed is classified as an instantaneous failure model because it abruptly makes the

material fail when the cumulative critical value is reached. The damage concept proposed by Johnson and Cook is defined as a summation of the equivalent plastic strains that occur during tensile loading. The concept of damage has different definitions and can be considered a scalar (directionless) despite the fact that it can introduce anisotropy into an isotropic material. The most common definition considers it as the void volume per unit of volume aggregate material.

### **2.1.3.2 Nucleation and growth models**

The reality of dynamic fracturing process includes stages of crack nucleation, and growth before the failure of metallic specimen. The evolution of the models in terms of sophistication reflects the complexity of material behaviour included in the model [33].

#### **2.1.3.2.1 Microstatistical Fracture Mechanics approach to spallation**

A “Microstatistical Fracture Mechanics” (MFSM) approach has been proposed based on the concepts of Griffith and Irwin on “Linear Elastic Fracture Mechanics” (LEFM) and the “Elastic Plastic Fracture Mechanics”(EPFM) [34]. In LEFM and EPFM the reduction of the material strength due to the presence of a macroscopic crack is considered. The LEFM and EPFM are very successful theories, and widely applied in the fields of fatigue, fatigue of welded joints and failure analyses [35],[36][37]. To treat the nucleation and propagation of microcracks with the LEFM and EPFM is an impractical task because it would involve individual treatment of each microcrack. The approach used in MFSM is to treat some key measures of average microscopic void behaviour as internal state variables in the constitutive relations of the material.

#### **2.1.3.2.2 Nucleation**

MFSM defines the nucleation of cracks at microscopic level with sizes comparable with the “graininess” which define the continuum of the material. For polycrystalline metals voids of one micrometer will constitute nucleation. Void nucleation is often initiated at a sub-microscopic size when the triaxial tensile stress exceeds the surface tension. However, the



stress state at such small sizes is very difficult to evaluate [ADJ6][34]. For this reason the nucleation of fractures is considered to occur at microscopic heterogeneity. Table 2.2 lists some common sites for nucleation and the nucleation mechanisms [34][ADJ7].

**Table 2.2 – Experimentally observed microscopic fracture nucleation processes**

<b>Nucleation site</b>	<b>Nucleation mechanism</b>	<b>Governing continuum load parameters</b>
Pre-existing flaws (voids or cracks)	Growth of flaw	Tensile stress and plastic strain
Inclusions and second phase particles	Cracking of inclusion, debonding at interface or fracture of matrix material near the inclusion	Tensile stress and plastic strain
Grain boundaries	Vacancy clustering, grain boundary sliding, or mechanical separation	Tensile stress and plastic strain
Subgrain structure	Dislocation pileup	Shear strain

Specific microstructural models of void nucleation at grain boundaries, inclusions, or other microscopic heterogeneity can be classified in two groups: (a) tensile stress/temperature-driven and (b) deformation (plastic strain) - driven. Stress/temperature-driven nucleation models are based on the effect of stress on the free energy functions for the diffusion of vacancies to form and grow a microscopic void. All models in this category have in common a requirement for a stress threshold for the onset of the nucleation and considered the void nucleated if the void is within a stress field sufficient to overcome the surface tension. The models also consider a coefficient which is related to the total number of potential nucleation sites and diffusion coefficient for the nucleation process (which varies with the nucleation site)[34].

An interesting example of the detrimental effect of inclusions is described by Shockey and Erlich [38]. They used cylindrical targets machined from a 100 mm thick steel plate, see Figure 2.2, and explosively loaded from the inside. They found significant evidence that the

metallurgical texture, i.e. the elongation and alignment of inclusions induced by metal working, left in medium carbon hot rolled plates, causes anisotropy in tensile properties and in shear banding behaviour. They found as well a dramatic increase of shear band activity with hardness in AISI 4340 steel but were not able to correlate this activity and shear band nucleation with microstructural features.

Deformation-driven nucleation models are based on local shear stress effects on grain boundary sliding, local flow around inclusion, and on dislocations pileups. The models proposed include two critical strain approaches. One requires that when de-bonding between particle and matrix occur, the work done must be at least equal to the energy required to create the new internal surface. The second criterion requires that a critical strain must be exceeded. Some models suggest that this critical strain is directly proportional to the heterogeneity size and to concentration [39].

#### 2.1.3.2.3 Incubation times for nucleation of microvoids

The strain based nucleation models include an incubation time controlled by the mobility of the dislocations. Stress temperature-driven models handle the incubation time implicitly by the thermal activation theory. In both cases Kalthoff and Shockey [40] reviewed models from several authors that an additional time is required for the stress to make a flaw unstable. The models say that the load must have a minimum finite time to interact and be fully applied on the heterogeneity or microcrack considered.

#### 2.1.3.3 Growth of microcracks (after nucleation)

According to Curran et al. [34] the dynamic fracture process involves ductile and brittle mechanisms. Different processes will occur depending on the strain rate, temperature, state of stress and strain. The growth of microscopic failure can be classified for polycrystalline solids in two groups: ductile void growth or brittle crack growth.

The models for ductile growth can include growth by diffusion (at moderate stress and high temperatures) and growth by microscopic plastic flow. Curran et al [34] suggests that for high stresses plastic flow may become an important mechanism and at high rate fractures,

plastic flow is the probable growing mechanism. The effect of combined plastic flow and nucleation processes was also suggested [41].

For very brittle materials like glass the velocity of brittle crack growth is limited to the Rayleigh wave speed in the material [34]. For structural materials at high tensile stresses Seaman et al [42] suggests that smaller velocities are imposed by the plastic flow at the tip of the crack.

#### 2.1.4 Adiabatic Shear

Adiabatic shear is a phenomenon known since 1944 [43], but it is only since the 1970's that it has received a greater attention. As the name suggests the adiabatic shear phenomena is a mechanism of plastic flow where the heat generated by an increment of plastic flow significantly softens the material promoting its propagation [44].

Ninety five per cent of the work done through plastic flow is converted to heat. If the work is done so quickly that the heat flow can be neglected (adiabatic conditions) the resultant thermal softening effect can appear as a reduction in the rate of work hardening. In conditions where the work done through shear deformation is high, the rate of thermal softening can exceed the rate of work hardening, and the metal will soften [45]. Woodward [45] proposes a condition for instability, assuming that all work is transformed in heat, given by:

$$\left| \frac{\sigma}{\sigma C_p} \cdot \frac{d\sigma}{dT} \right| \geq \left| \frac{d\sigma}{d\varepsilon} \right| \quad (2.28_{[ADJ8]})$$

where  $C_p$  is the specific heat and  $T$  is temperature. By using the above relation above it is possible to assess the susceptibility of several metals to adiabatic shearing. **Figure 2.3** shows ranking of metals in terms of strength-to-weight ratio and theoretical susceptibility (based on eq. 2.28) to adiabatic shear.

Stelly and Dorneval [46] reviewed nine different instability criteria and concluded that all models agree that the susceptibility of metals to adiabatic shearing is promoted by the following: low strain hardening and strain rate hardening, large thermal softening and low

thermal diffusivity. They also concluded that thermal conductivity and strain hardening primarily control the susceptibility to adiabatic shearing.

Based on experimental evidence provided by Walker and Shaw [47] and Olson et al. [48] suggest the existence of a “pressure dependent shear instability” criteria for mild steels. Walker and Shaw [47] carried out plane-strain linear shear experiments in cold worked mild steel under isothermal conditions. A constant uniaxial compressive load was superimposed normal to the shear plane. They observed higher values of effective shear stress for the instability to occur ( $\gamma_i$ ) for higher values of applied normal compressive pressures. Olson et al [48] also extended their analyses for high-strain-rates and observed the increase on the value of  $\gamma_i$  with pressure up to critical value of pressure beyond which  $\gamma_i$  assumes a constant value associated with thermal softening alone.

Mescall [49] analysed the relative roles of strain-hardening and thermal softening, and pointed out, when considering thermal softening, that a linear dependence of flow stress on temperature is not a good approximation for the range of temperatures considered (from room temperature to melting). Materials that have been processed to higher strengths are more sensitive to increases of temperature than those of intermediate and lower strengths.

Swegle and Grady [50] calculated the thermal trapping in adiabatic shear bands in aluminium alloys. They emphasise the role of the shock stress level effect on the shock rise times and its consequence on the thermal balance. The assumption that the heat conduction occurs in time scales longer than the shock risetimes, had to take into account that this might not be the case for low shock stresses, where the shock risetime might be long when compared with the thermal diffusion time. They calculated the bulk and shear band temperatures profiles through the plastic shock front for 5 and 10 GPa. Their results show that at 5 GPa the shock rise time is long enough for the band to stay in thermal equilibrium with the bulk of the material. For 10 GPa the situation is reversed and due to the additional irreversible work and the smaller shock rise time, the resultant effect was a substantial amount of thermal trapping which persisted after the passage of the shock wave. **Figure 2.4** shows the comparison of

calculated bulk and shear band temperatures profiles through the plastic shock front for 5 and 10 GPa shocks in aluminium.

Shockey [44] studied the materials aspects of adiabatic shearing and concluded that microstructural features appear to have much less effect on shear bands than on the nucleation of voids or cracks<sub>[ADJ9]</sub>. He pointed out that despite the major role that shear bands play on failures under high rate compressive loads, shear bands are significantly less well understood than the tensile failure modes, cracks and voids

Rogers et al. [51] studied adiabatic shear in steels induced by impact of flat-nosed projectiles at velocities of 100 to 250 feet per second. The targets were discs 1/4 to 5/16 inch thick cut from stock bars. They analysed the adiabatic shear regions of several steels and concluded the following: in most ferric steels adiabatic shearing will occur if the rate and magnitude of the deformation are sufficient. The formed adiabatic bands are normally preceded by deformed bands. AISI 1040 quenched and tempered produced adiabatic shear bands of constant hardness independent of the initial hardness and velocity of impact. The hardness of the adiabatic shear band remain constant along the length of the band, indicating minimum effects after austenization. The micro-hardness profiles of the deformed shear bands suggested that the gradients of work hardening resulting from strain concentration in bands are overwhelmed by temperature gradients during adiabatic deformation, including the formation of Heat Affected Zones in some cases.

Rogers et al [51] also concluded that, in plain carbon steels, the hardness within an adiabatic shear band was considerably higher than that obtained with conventional austenization and quenching for the same steels, and the hardness was linearly related with the carbon content. They explain the extreme hardness of the adiabatic shear bands by considering the combined effects of extreme fine grain within the shear band and the supersaturated solid solution of carbon during quenching. **Figure 2.5** shows the hardness values within adiabatic shear bands of different steels. The values are plotted against carbon content (in weight) where the linearity of the relation can be observed. The measurements

were made with a Tukon hardness tester with a small 25g Knoop indenter due to the small width of the shear band.

A study was carried out at higher strain rates by Moss [52] using an explosive driven punch, achieving an average strain rate within the adiabatic shear bands of  $9 \times 10^5 \text{ sec}^{-1}$ , and values as high as  $9.4 \times 10^7 \text{ sec}^{-1}$  near the surface of perforated samples. The targets consisted of Ni-Cr steel (C = 0.22, Mn = 0.26, Si = 0.19, Ni = 3.15, Cr = 1.06, Mo = 0.15/0.30, + Cu, V, Al, P and S) with clear planes of heterogeneity parallel to the rolling plane. The heterogeneities were used as references, and they observed strains near the surface of 57,200 % while the average strain was 532 %.

Moss [52] pointed out also that adiabatic shear band models assuming 100% conversion of plastic work into heat with no thermal softening or conduction would lead to temperatures above melting point and, according to him, it would over-estimate the temperature rise. Moss suggested solid state transformations to explain the abrupt change of the strain gradient in the adiabatic shear bands investigated. He concluded that thermal softening at the strain rate investigated was not appreciable for strains up to 570 %. The observations made have to consider the type of steel used and the range of impact velocities studied.

Meyer et al [53] studying a similar steel (0.35 C, 3.3 Ni, 1.3 Cr, 0.5 Mo) and a titanium alloy compared the respective behaviours when tested in shear conditions. A Split-Hopkinson bar was modified to include a die as depicted in **Figure 2.6**, the impact velocities varied from 2.7 to 7.1 m/s and the results compared with quasi-static conditions. They found that the adiabatic shear in the titanium alloy was onset exactly at the maximum value of true shear stress-strain curve. For the low alloy steel, however, no shearing was found up to values of 50% of deformation. They concluded that the onset of adiabatic shear is dependent more on the behaviour of the materials than on the existence of a critical maximum value.

### 2.1.5 Fields of maximum shear trajectories.

If the distribution of principal stress within a body is known, it is possible to calculate the position associated with maximum values of shear. In mild steel samples submitted to cold work, it is possible to observe the appearance of macroscopic lines associated with the onset of plastic deformation at the regions of maximum shear. These lines form what is known as Lüders patters, famous for appearing at  $45^\circ$  in mild steel tensile specimens [55]. **Figure 2.7** shows an example of Lüders patters in mild steel [56].

Fields of maximum shear can also appear in explosively loaded specimens as Lüders patterns or fractures [ADJ10][27]. The maximum shear trajectories for the cases of a circular hole under internal pressure and a flat surface under contact pressure are depicted bellow in **Figure 2.8** [27].

It is often observed fractures following trajectories associated with maximum shear, an interesting example is described in [27] where an Aluminium alloy cylinder is explosively loaded from the outside. **Figure 2.9** shows resultant fractures of an Aluminium hollow cylinder with a  $\frac{3}{4}$ " internal diameter, 1 inch wall thickness loaded by  $\frac{1}{8}$  thick high explosive.

Another relevant example is the appearance, in ballistic targets, of a triangular "Dead Zone" under the region impacted by projectiles. Woodward et al [ADJ11][45] describe the results of Aluminium targets impacted at increasing velocities by flat fronted projectiles. **Figure 2.10** shows sections of those targets.

## 2.2 Metallurgical changes under dynamic loading

Some considerations were already made in the context of spalling and specially within the adiabatic shear band. The large strains experienced within and in the vicinities of an adiabatic shear band [27][52] are invariably accompanied by severe grain distortion, generally in the nature of an elongation of the grain in the same direction of the material flow [27].

The effects of the shock loading in steels and other metals consists however of a more complex range of phenomena including the generation of defects and phase transformations, where both hydrostatic and deviatoric components of the stress are important. A list of

phenomena and the relative whole of the hydrostatic and deviatoric stresses is presented in [ADJ12][28] and summarised in **Table 2.3** below:

**Table 2.3 Effects of deviatoric and hydrostatic stress on metallurgical phenomena**

Phenomena	Hydrostatic	Deviatoric
Dislocations	Affect the stacking-fault energy	Control the generation and motion
Point defects	Affect the diffusion rate	Generation controlled by shear stresses
Phase transformation (diffusionless)	Induces a number of phase transformations	Induces Martensitic transformations
Dispersed particles	Affect the whole of the dispersed particles as a source of dislocations	
Twining	Might have an indirect effect	Activated by shear stresses
Recovery and melting point	Generally increases the melting point.	

Dislocations are generated in metals by shock loading being the pressure the most important shock parameter. Meyers and Murr [28] proposed a model for the generation of dislocations which suggest:

- Dislocations are homogeneously nucleated at (or close to) the shock front by the deviatoric stresses set up by the state of uniaxial strain, the generation of these dislocations relieves the deviatoric stresses.
- These dislocations move short distances at subsonic speeds
- New dislocations interfaces are generated as the shock wave propagates through the material.



The influence of shock pulse duration is controversial, but is clear that the dislocations would have more time to reorganise in cell structures [28].

Twining is a highly favoured deformation mode under shock loading and even some metals that do not twin at ambient temperature under conventional loading can twin under shock. The existence of a pressure threshold for shock induced twining to occur was verified for Nickel and Copper and a pulse duration threshold was identified for Hadfield steel. The influence of the existing substructures was found to be able to inhibit the twining in pre-deformed iron with a significant density of dislocations [28].

The shock-induced transformations are present in several metals where pressure, shear stresses and temperature are controlling the phase transformation mechanisms. For iron the pressure has a significant effect on the transformation from the  $\alpha$  phase (BCC) to either  $\epsilon$  phase (HCP) or  $\gamma$  phase (FCC) depending on the temperature. In both cases the density of the transformed phase are higher than the  $\alpha$  phase, and the transformation thermodynamics are favoured by high pressures [28]. **Figure 2.11** shows the temperature - pressure transformation diagram for Iron for compressive loads

## 2.3 Fracturing Charges

### 2.3.1 Introduction

This section describes selected USA and UK research work on fracturing charges where relevant experimental data are available. This Section also provides the background for some of the concepts incorporated in the SWF designs discussed in Section 4. This brief review will concentrate on the design parameters and particular results of experimental works that were carried out using RDX and PETN based explosives. The fracturing charges to be discussed are:

- Demolition Charges
- Diamond Charges and Fracturing Belts
- Waveguide Charges

Some of the experimental development work of the above fracturing charges was re-analysed and a summary is presented in this Section and in Section 6. For completion, more detailed data from some of the experimental results are presented in their original format in Appendix 1. Numerical analyses of some of the demolition and waveguide charges discussed in this Section are presented in Section 5.

### 2.3.2 Demolition Charges

The term “demolition charges” when used for metal cutting consists of blocks of explosive in contact with the metal surface to be cut. This type of charge is used mainly for military purposes, being applied in cutting I-beams, built-up girders, steel plates, columns, angles, bars and other similar steel sections [22]. The relative dimensions of the explosive charge are calculated as a function of the thickness of the target plate or cross sectional area of the member [5] and can take into account underwater environment.

In the case of structural members like girders, generally 2 charges are used staggered on both sides of the member in order to produce an extremely powerful shear effect. **Figure 2.12** shows a typical set up for I-beams [23]. In the case depicted in **Figure 2.12** the following formulae were suggested for the calculation of the explosive loads [23]:

$$P = \frac{3}{8} A \quad , \text{ in air} \quad (3.1)$$

$$P = \frac{3}{4} A \quad , \text{ under water} \quad (3.2)$$

where P is the weight of TNT in pounds and A is the area of the cross section of member to be cut in square inches. Similar formulae is also suggested for cutting of chains:

$$P = A \quad , \text{ in air} \quad (3.3)$$

$$P = 2A \quad , \text{ underwater} \quad (3.4)$$

It can be observed from these empirical formulae that charges for underwater cutting require twice the explosive load of charges for cutting in air. No justification for this increase is given, but one can assume that the water on the back face will reduce the intensity of the reflected tensile waves responsible for spall formation. The effect of water on the side of explosive charge is believed to be beneficial as it increases the initial explosive density and provides confinement conditions for the detonation.

### 1965 US Army Report on Demolition Charges [5]

A description of unclassified material from the USA Army experimental work to optimise the formula to calculate such charges for plates [5] is presented in this section as a way to describe the effects the detonation of different dimensions of explosive in contact with mild steel plates and other members. This experimental work covers a period of 3 years where demolition charge designs were re-evaluated and developed through experimental testing on plates among several hundred tests on other structural elements. **Figure 2.13** shows the schematic representation of a demolition charge assembled on a steel plate.

The work from the US Army report of 1965 [5] was based on a previous report of 1957 from the Stanford Research Institute (SRI-1955/57). The SRI tests showed that rectangular C4 blocks of explosive chargers cut the same maximum thickness as square blocks, in that case the rectangular blocks had half the explosive load than the square blocks. The SRI work recommended the following relative dimensions for the cutting charges of plates:

$$t = 1/2T + 1/8 \quad (3.5)$$

$$W = 4t \quad (3.6)$$

where “T” is the target thickness in inches, “t” the explosive thickness and “W” the charge width.

The report suggested that the cutting mechanism comprehends the formation of a spall with approximately the width of the charge (but usually wider) and also reported the presence of a internal vertical crack, starting above the spall and propagating up to the opposite surface where the charge was placed. The vertical crack being responsible for the completion of the cut was regarded as the desired effect that charge optimisation should encourage. All tests on plates were carried out according to procedures, with the plate in contact with flat ground, and ensuring that the charge was in good contact with the plate (as their experience have shown the detrimental effect of air gaps between the charge and the target).

According to the SRI report a optimum relation must exist between the area of explosive in contact with the target and its thickness in order to transmit the greatest shock. For thinner charges the target was considered excessive (the detrimental effect of attenuation was suggested). It was also thought that the effect of the dimension of the reaction zone within

the explosive as for very thin charges may start to affect the propagation of the detonation (the reaction zone for RDX based explosive is about 2 mm [ADJ13][23]). For thick charges with narrow area of contact between the explosive and the charge, the effect of lateral loss of energy within the target was considered as a limiting factor.

For one inch plates of mild steels, the SRI conducted a series of tests where C4 charges of two inches wide were used with variable thickness from 1/8 to 1.5 inches. The 1/8" charge just dented the target, the thickness of explosive was then increased and partially vertical cracks appeared and for 1/2" thick charge achieved a successful cut. For thicker charges the depression on the surface were accentuated, and for charges 1-1/2 times wider than the thickness (3 inches) no additional destructive effect was noticed.

Dennis [5] extended the work from the SRI by conducting nearly two hundred tests on plates. On the first series of tests he analysed the performance of four types of explosives: C4, RDX paste (76% RDX), Aluminised RDX paste (18% Al) and Deta Sheet EL506A (85 % PETN). The aluminised paste explosive had the worst results and was not used in further analyses. The results were analysed in terms of the volume of the plastic deformation (indentation) left on the surface of 1 and 1/2 inch thick specimens. The preliminary results had already suggested that an optimum combination of charge width and thickness to produce the maximum indentation of the plate should be between 2:1 to 4:1.

In a second series of tests the total explosive load was kept constant but the widths and thickness of the charges varied. It was found that the widths of the charges had a significant effect on the size of the depressions. The results confirmed the proportions for charge thickness and width.

In two additional series of experiments the influence of the position of the initiation was evaluated using 12 inch long charges. No significant effect was found.

The work was completed with two series of "cutting charges", where for the first series of cutting charges the target was laid on flat ground and for the second the plates were supported to separate the back face from the ground. Over ninety eight experiments the target thickness varied from 1/4 to 3 inch. The target materials were mild steel and for the 3 inch plate was described just as "alloy steel".

The charges dimensions varied in width and thickness using equations 3.5 and 3.6 as guide for the first 49 tests. A new relation was proposed for the remaining 49 experiments as follow:

$$t = 1/2 T \quad (3.7)$$

$$W = 3 t \quad (3.8)$$

As it can be observed the proposed formula reduces the SRI charge width from approximately 2 times the target thickness to 1.5 times, but no significant alteration is made for the charge thickness.

Dennis [5] observed from the results of the first 49 tests (laid on flat ground) that the insufficient charge width resulted in failure (defined as not being able to cut the target). No comment is made on the effect of charge thickness and when the table of results is analysed one sees that all experiments were carried out with  $t \geq 1/2 T$ .

On the remaining 49 tests only Deta sheet (PETN based) and C4 (RDX based) were used, the results showed that 6 incomplete cuts and 43 complete cuts were achieved. From the 6 incomplete cuts 5 had the uncut areas restricted to a region under initiation. The failures were attributed to the lack of explosive thickness under the initiation. The sixth uncut target was a 3 inch alloy steel target. A thickness of 1/8 inch remained uncut. The thickness and the explosive load (Deta sheet) was considered of non optimum dimensions despite  $t = 1/2 T$  and  $W = 1.5 T$ . It is worth noting that the PETN based the Deta sheet explosive achieved comparable results to the RDX based explosives and superior to the RDX aluminised paste used.

### 2.3.3 Diamond Charges and Fracturing Belts

#### 2.3.3.1 Diamond charges

Diamond charges consist of a sheet of explosive in a polygonal shape from which it received this name. The charge is initiated simultaneously at the two vertices of the polygon as shown in **Figure 2.14** resulting in a fracture underneath the centre line between the initiation points. The proposed mechanism for the cutting phenomenology is depicted in **Figure 2.14** [6]. The sequence shows in Fig. 1 that the two sides of the polygon connected to a single detonation point using equal lengths of detonation cord to ensure that the detonation fronts from side 1 and 2 meet at the centre line of the polygon. Fig. 2 shows a two dimensional representation of the detonation front and induced wave fronts from sides 1 and 2 (FS1 and FS2) propagating with velocities  $V_{sf1}$  and  $V_{sf2}$  and associated particle velocities  $V_{s1}$  and  $V_{s2}$ . Fig. 3 shows the emergence of two reflected wavefronts (Fr1 and Fr2) propagating with velocities  $V_{fr1}$  and  $V_{fr2}$ . Fig. 4, shows the interference between the FS1

and FS2 at the of the target surface evolution the continuing propagation and reflection of the wavefronts FS1 and FS2 (FS1 is renamed Frs2 and FS2 is renamed Frs1 after passing through the S line). The particle velocity  $V_{rs}$  behind Frs1 and Frs2 is downwards towards the back-face. Figs 5 and 6 show the evolution of the sequence until Frs1 and Frs2 reach the back-face. Fig. 6 shows the initial development of a crack with particle velocities  $V_{f1}$  and  $V_{f2}$  at the crack tip. Fig. 7 shows the evolution of the sequence and the crack opening.

The diamond charges were initially developed in the Poulter Laboratories of Stanford Research Institute (SRI) for cutting of round bars only [6] and further developed to square bars by Dennis [5]. Denis described the fractures as tensile fractures which were believed to be induced by elastic waves that exceeded the yield strength of the material [5]. He observed that alloy steel bars required more explosive than mild steels and that the charges should surround completely the bars.

Davis [7] pointed out the inadequacy of using diamond charges for cutting plates due to the excessive explosive load and the necessity of initiation of several diamond charges to cut a length of plate. Based on the principle of diamond charges Hotforge developed and patented what was called a “Ladder” charge and can be considered as a fracturing belt, therefore is discussed in the following section.

#### 2.3.3.2 Fracturing Belts

A fracturing belt consists of a chain of demolition or diamond charges connected by a detonation path and inert obstacles. Plastic high explosive is generally used and the inert materials are rubber or Lead to allow flexibility to the belt. **Figure 2.15 to Figure 2.19** show examples of different fracturing belts. The initiation of the charge is arranged in such way to provide a synchronised collision of two detonation fronts at the centre line of the belt as showed in **Figure 2.16** [7]:

The geometry of the inert barriers was further improved with the introduction of “plane wave generators”, aiming to form a plane wave front within the explosive and to reduce the explosive load. **Figure 2.18** shows the schematic representation of a Fracturing Belt with added Plane-Wave Generators developed by Davis [7]:

Davis [7] studied the influence of the relative dimensions of the plane-wave generator and the central explosive load between the 2 plane-wave generators showed in **Figure 2.19**. The results showed different crack patterns, including cuts consisting of a spall plus vertical crack (similar to those obtained by Denis [5] demolition charges) and cuts without the presence of spall. Davis [7] showed that the width of the spall was similar to the central

explosive load  $W$  showed in **Figure 2.19**. When  $W$  was 0, i.e. the charges consisted of just 2 plane wave generator facing each other, a vertical cut was achieved without spall. The tests were carried out on one inch thick cold rolled and normalised mild steel, the test plates were supported avoiding contact of the back face with the ground.

The initial design methodology of Davis [7] was aimed to achieve a vertical plane (the cut plane) where reflected tensile stress waves converge creating a fracture. The diagram depicted in **Figure 2.20** by Davis [7] shows schematic representation of stress waves under the explosive charge described in **Figure 2.19**, and describes a similar situation as the diamond charge depicted in **Figure 2.14**. **Figure 2.20** shows a tentative calculation of the dimension  $(W + 2W_p)$  based on the angle  $\theta$  defined by the Velocity of Detonation of the explosive and the Sound Speed of the metal used. For an RDX/Steel combination  $\theta$  and  $(W+2W_p)$  can be calculated approximately as [7]:

$$\theta = \sin^{-1}\left(\frac{C_s}{C_D}\right) \cong \sin^{-1}\left(\frac{5000}{8000}\right) \cong 38.7^\circ \quad (3.9)$$

$$(W + 2W_p) = 4h \tan \theta = 3.2h \quad (3.10)$$

In a similar manner Davis [7] also analysed the minimum value of  $(W+2W_p)$  necessary for the tensile reflected stress wave to first meet. This situation is presented in **Figure 2.21**. According to this criteria the reflected tensile stress waves start to interact for values of  $(W+2W_p)$  greater than  $1.6h$ . Taking this assumption as correct, the explosive charge total width should be greater than 1.6 times the target thickness and smaller than 3.2.

Experimental results of Davis [7] however, showed that best results were achieved when  $W = 0$ , making the total charge width  $(W + 2W_p)$  of about  $1.7h$ . Additional width only contributed to the formation of a spall under the vertical crack. This seems incompatible with his initial design methodology as  $1.7h$  will only provide a tiny region for the reflected stress waves to interfere.

The (target thickness)/(charge width) ratio of 1.7 from Davis seems remarkably similar to 1.5 value proposed by Dennis [5] for demolition charges. Davis [7] however used an explosive thickness in his plane-wave generator charges about half of that recommended by Dennis [5] for demolition charges.

### 2.3.4 Waveguide Charges

The waveguide charges consist of two strips of high explosive placed on a central support made of different materials like steel, rubber or rubber saturated with metal powder. Several shapes of waveguides were tested like prismatic or semi-circular, **Figure 2.22** shows an example of a prismatic waveguide, also called flat waveguide charge placed on a target plate [19].

Both waveguide charges and fracture belts described in the previous section rely on the interference between two reflected tensile stress waves. In the case of fracturing belts, the angle between the reflected wave fronts is dependent on the explosive VOD, the velocity of wave propagation in the target metal and the angle between the two synchronised detonation fronts. In the case of waveguide charges, the two detonation fronts are parallel, but an initial angle is introduced between the two incident compressive wave fronts.

The design methodology aims to introduce an angle between the target and the incident stress/shock waves, resulting this way in oblique reflected waves capable of producing a fracture perpendicular to the thickness.

In some respects, the waveguide charge could be viewed as the inverse case of corner fractures in plates, where the interference of oblique reflected stress waves is well known [26][57]. In corner fractures the obliquity between the reflected waves is reached by the added effects of an oblique incident wave against (in general) two angled and symmetric free surfaces. **Figure 2.23** show the schematic representation of a typical corner fracture [26] in a plate containing a circular hole fitted with high explosive detonated at the centre. The incident circular shockwave is reflected from the four free surfaces as four tensile wavefronts which interact causing fractures to emanate from the corners.

In the case of the flat waveguide as described in **Figure 2.22** the initial obliquity of the incident waves produced oblique reflected stress wave fronts. Two types of geometries were tested; flat and curved waveguides.

#### 2.3.4.1 Flat Waveguides

Davis [7] investigated the Flat waveguide charge geometry by producing cracks in Perspex (plasticised polymethyl-methacrylate) models as in **Figure 2.24**. The initial trials showed that the cracks were initiated at surface irregularities and cracking of the specimens was suppressed when the back surface was polished. To achieve consistency in his results, the back surface was polished and a scribe mark was placed to induce crack initiation under



the centre line. High speed photography was used, which showed that the central fracture appear to be initiated at or near the free surface and no spall was developed.

Experimental and theoretical results of Davis [7] showed that the height of the crack and maximum stresses at the crack plane were relatively insensitive to the range of angles tested, between 15° to 45°. **Figure 2.25** shows Davis attempt to estimate the crack height:  $h_t$ , as function of the preset angle:  $\theta$ ,  $\alpha'$  the angle of propagation of the wave front for a charge initiated at the bottom of the wedge and  $\alpha$  the angle of incidence/reflection at the back surface.

The parameter  $h_t$  can be calculated as [7]:

$$h_t = \left( \frac{l}{2} - h \tan(\theta + \alpha') \right) \tan(\theta + \alpha') \quad (3.11)$$

The theoretical predictions of Davis [7] overestimated the maximum crack length despite taking into consideration the decay due to cylindrical expansion of the wave front. It is also important to notice that the polished samples failed to crack. Experimental results showed quite large scatter of results but in general smaller preset angles gave larger crack heights.

#### 2.3.4.2 Steel Waveguides

Burley and Al-Hassani [19] tested in conjunction with Hotforge Ltd, flat steel waveguides (See **Figure 2.22**) on 25.4 mm thick plates made of mild steel. The inclination of the wave guide angles varied from 25° to 40° and the waveguide width varied from 50 to 108 mm. The explosive used was an RDX based plastic explosive (Royal Ordnance - SX2). The tests also varied the acoustic coupling of the waveguides by including rust between the waveguide and the target. The results showed that the contact between the waveguide and the target was very important.

The results of Burley and Al-Hassani [19] are summarised in **Table 3.1**, The central area without explosive was not considered to be a variable as such, but its importance will become more clear as the results from rubber waveguides and Section 4 are discussed in Section 6. By analysing the results it was possible to group them into successful and unsuccessful ones as shown into **Table 3.1**:

**Table 3.1 The results with flat steel waveguides [19]**

Variable	Successful	Unsuccessful
Charge Width (mm)	55 to 83	50 to 108
Charge width/target thickness	2.2 to 3.3	2.0 to 4.3
Waveguide Angle Range	25° to 30°	30° to 40°
Central area without explosive (mm)	0 to 22*	19 to 20

\* Increasing the area without explosive reduced the spallation of the cut target.

The waveguide angle described in the table above can be considered equal to the compressive stress incident angle. This assumption takes into consideration the difference between the situations described in **Figure 2.22** and **Figure 2.24**. In **Figure 2.22** the initiation of the explosive strips is away from the cross section considered and for this cross section the explosive can be assumed as being totally detonated instantaneously. In the case of the Perspex trials described in **Figure 2.24** and **Figure 2.25** the initiation on the plane considered as the crack plane is only 12 mm deep. Being this way the propagation of the compressive incident stress wave for flat steel waveguides can be considered as normal to Waveguide/Explosive interface, as described in **Figure 2.26**.

#### 2.3.4.3 Flat Rubber Waveguides

The necessity to produce a waveguide that could be easily fitted to the target led to the development of a flexible waveguide made from a mixture of Iron powder and Polyurethane rubber. Flat flexible waveguides tested by Al-Hassani and Burley [19] had angles ranging from 11° to 30° and width varying from 50 to 107 mm. Two series of test were carried out, the first using SX2 (RDX based) and the second using Nobel's 1509 (PETN based). The tests using SX2 with a charge width of about 100 mm failed to cut despite fracturing the target. One charge with a 11° wedge angle and 107 mm width developed a large spall. The tests using 1509 cut the target with an angle/width combination of 20°/75mm and 30°/50mm. A combination of 10°/106 mm partially cut the target developing an attached spall. The results are summarised as follow:

**Table 3.2 The test results with flat rubber waveguides [4][19]**

Variable	Successful	Unsuccessful
----------	------------	--------------

Charge Width (mm)	50 to 95	60 to 172
Charge width/target thickness	2.0 to 4.3	2.5 to 6.8
Average Angle Range	20° to 40°	10° to 30°
Central area without explosive (mm)	0 to 20*	17 to 51

\* A waveguide with the combination of angle/width of 10/106 was also tested with no central area without explosive (waveguide completely covered with explosive). The result showed a partial cut with an attached spall.

#### 2.3.4.4 Curved Waveguides

Al-Hassani and Burley [4][19] developed the concept of curved waveguides by using the flat waveguide principles in conjunction with the stress wave focusing the work of Al-Hassani and Silva Gomes [58]. The method consists of a curved waveguide covered with a explosive layer as depicted in **Figure 2.27**.

Silva Gomes and Al-Hassani [25][58] investigated the focusing of stress waves by studying the formation of cracks in Perspex axisymmetric solids subjected to surface explosive loading. The experimental results showed excellent agreement with predictions based on the ray theory commonly applied in optics and acoustics. High speed photography was used to confirm predicted times for formation of cracks due to reflected S-waves, P-waves and also Rayleigh surface waves. The explosive load was generated by small commercial detonators and the Perspex solids investigated included spheres, paraboloids, hyperboloids and ellipsoids. **Figure 2.28** shows an example of internal fractures obtained when a Perspex ellipsoid of revolution is explosively loaded in one focus. **Figure 2.29** shows a schematic representation of the propagation of incident and reflected wave fronts for the same ellipsoid showing the focusing effect of the reflecting surface geometry.

Al-Hassani and Burley [4][19] studied the possibility of reducing the amount of explosive used by the flat waveguides by focusing the reflected stress waves into a small region, optimising the energy consumption during the crack nucleation and propagation processes. As the bigger amount of energy is required to initiate a crack than to propagate it, this concept was to promote a more effective use of energy than nucleate a crack over the whole thickness.

In [19] two series of tests using “Segmental Waveguides” were carried out using 1 inch EN3A (cold rolled) and 50D steel plates. A schematic representation of the waveguides

is shown in **Figure 2.30**. The fracture patterns for the EN3A (cold rolled) plates showed the presence of river lines pointing back to a point 6 mm away from the reflecting surface. This observation correlated well with the predicted crack initiation region. Despite the success with the EN3A plates all the tests with 50 D plates failed to produce cracks of any description even when the explosive load was tripled. The design parameters shown in the **Figure 2.30** are: radius (r), offset (b), separation between centres (a).

Al-Hassani and Burley [4] carried out further tests on 1 inch plates made from 070M20 steel using flexible cylindrical and segmental waveguides. By re-examining the charges geometry it can be observed that the charge width (including the explosive) varied from 55 to 70 mm and that the range of inclination experienced by the explosive on the curved surface of the waveguide varied from 20° to 40°. By analysing the results it is possible to group them into successful and unsuccessful as shown in **Table 3.3**.

**Table 3.3 Results with Curved and Segmental Rubber Waveguides on one inch target plates [19]**

Variable	Successful	Unsuccessful
Charge Width (mm)	55 to 73	62 to 70
Charge width/target thickness	2.2 to 2.8	2.5 to 3.27
Average Angle Range**	20° to 24°	24° to 32°
Central area without explosive (mm)	10 to 27*	23 to 35

\* The value for the central area without explosive drop to 16 mm when successful results with cold rolled EN3A steels are excluded.

\*\* The average angle range reflects the angular variation on the waveguide curved surface in contact with the explosive.

Al-Hassani and Burley [4] had also carried out 4 tests on 65 mm thick plates made from BS 4360 43A steel. Flexible cylindrical waveguides were used with a 104 mm radius, a small variation on the offset and centres separation were introduced in two tests. Al-Hassani and Burley analysed the results in conjunction with the 1 inch thick plates and produced the graphs shown in **Figure 2.31** and **Figure 2.32**. The graphs show a plot of two dimensionless parameters: Waveguide width / Target thickness, and Offset / Target thickness.

By re-examining the charges geometry used in the 65 mm plates it can be observed that the charge width (including the explosive) varied from 145 to 160 mm and that the range of inclination experienced by the explosive on the curved surface of the waveguide varied from 30° to 32°. By analysing the partially successful and unsuccessful results the following information can be extracted:

**Table 3.4: Results with Curved Waveguides (Rubber) on 65 mm target plates [19]**

Variable	Partially Successful	Unsuccessful
Charge Width (mm)	145	145 to 160
Charge width/target thickness	2.2	2.2 to 2.5
Average Angle Range	32°	30° to 32°
Central area without explosive (mm)	30	52 to 70

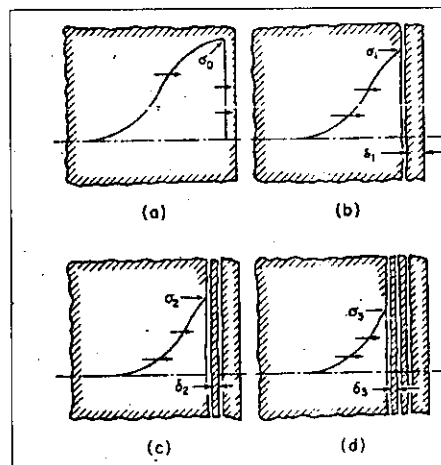


**Figure 2.1:** Formation of multiple spall [29]

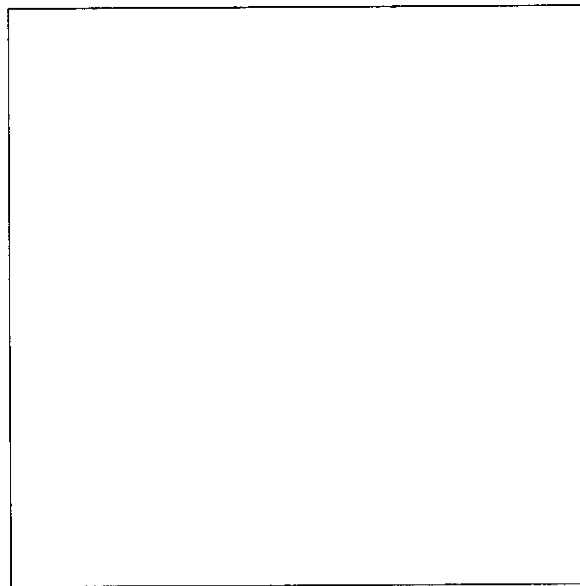


**Figure 2.2:** Effect of micro-structural anisotropy on the dynamic fracturing of cylinders machined from one steel plate [40].



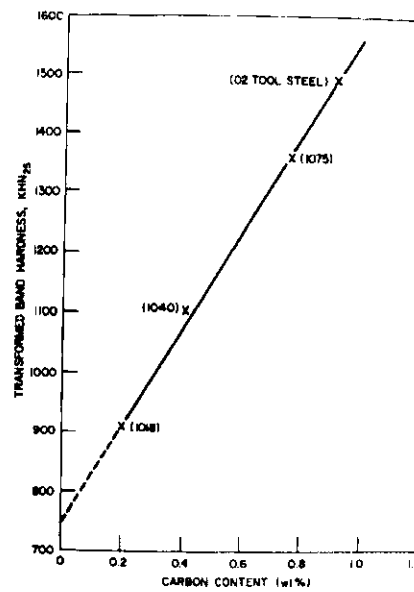


**Figure 2.5:** The effect of carbon content in the hardness of adiabatic shear bands in steels [53][ADJ3].

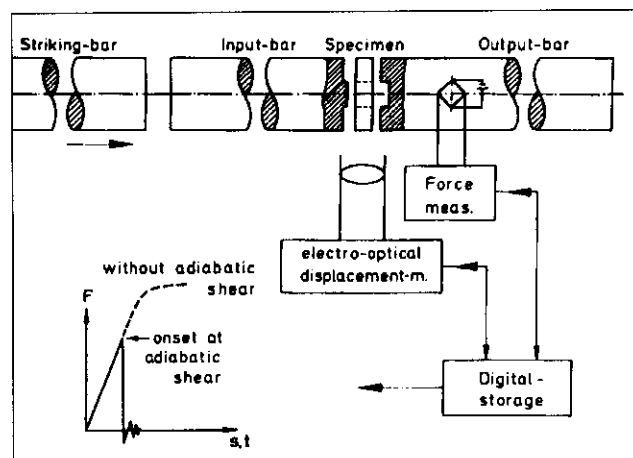


**Figure 2.6:** Split-Hopkinson bar set up for generating shear loading [55][ADJ4].



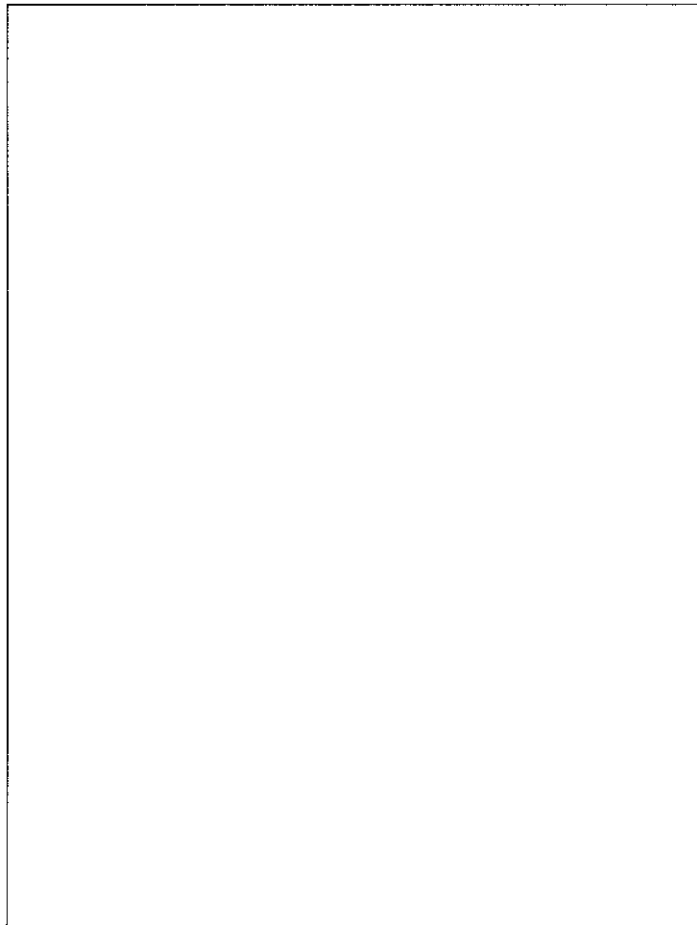


**Figure 2.7:** Lüders patterns in mild steel tensile specimen [58].

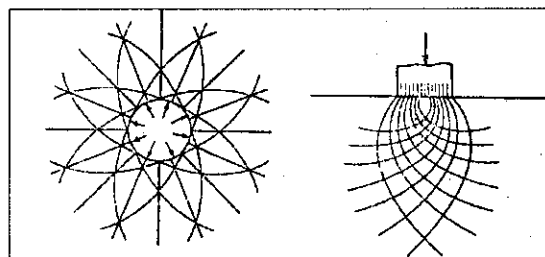


**Figure 2.8:** Fields of maximum shear for : (Left) Internal hole under internal pressure, (Right) Flat surface under contact pressure [29].

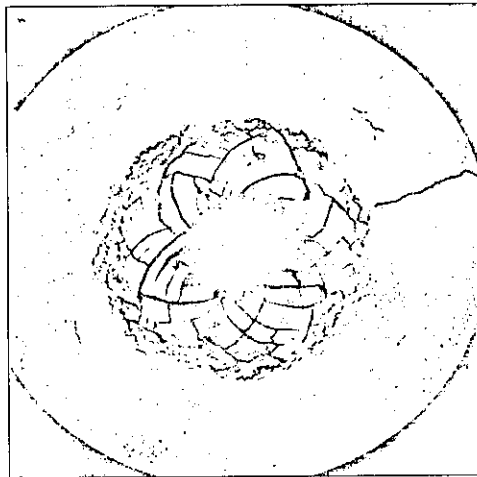


**Figure 2.9:** Cross section of a 24S-T Aluminium alloy hollow cylinder  $\frac{3}{4}$ " diameter, 1 inch thick loaded by  $\frac{1}{8}$  thick high explosive [29].

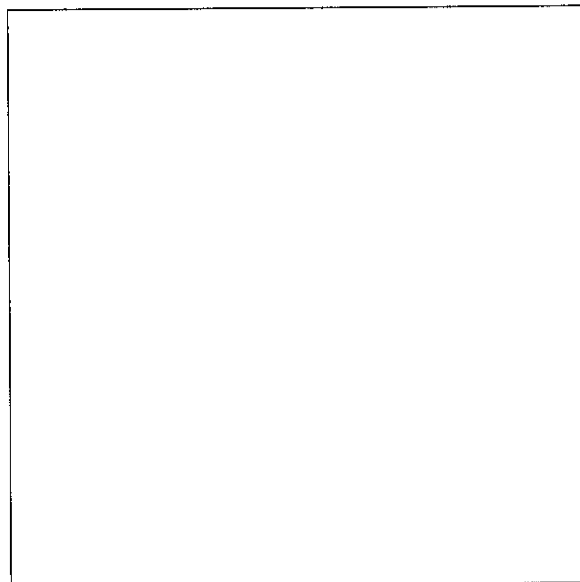


**Figure 2.10:** Section of Aluminium targets impacted by flat fronted projectiles at increasing velocities [47].

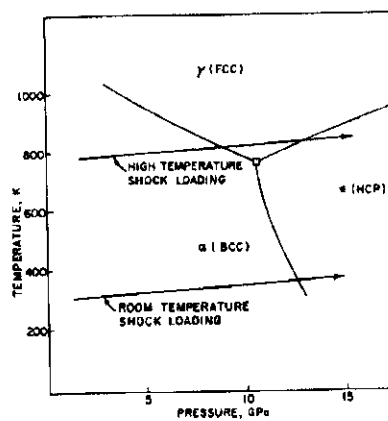


**Figure 2.11:** Temperature - Pressure diagram for Iron [30][ADJ5].

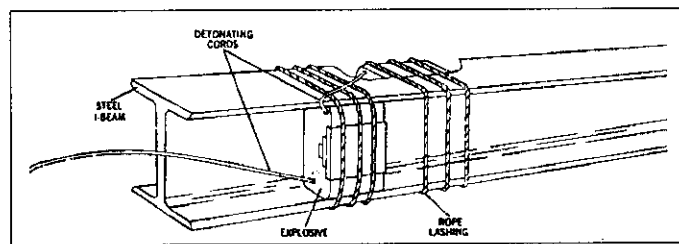


**Figure 2.12:** shows a typical set up for I-beams [25].

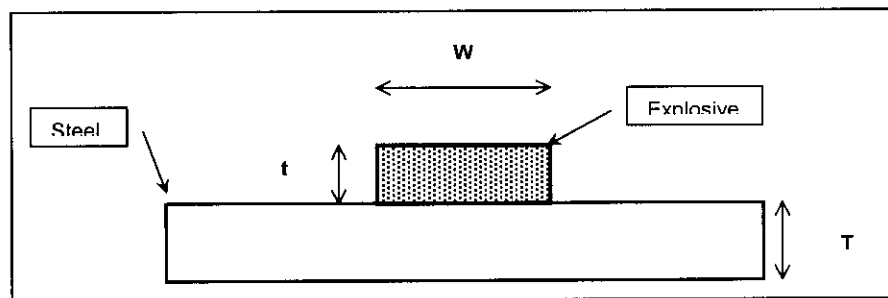


**Figure 2.13:** Schematic representation of a demolition charge placed on a steel plate.

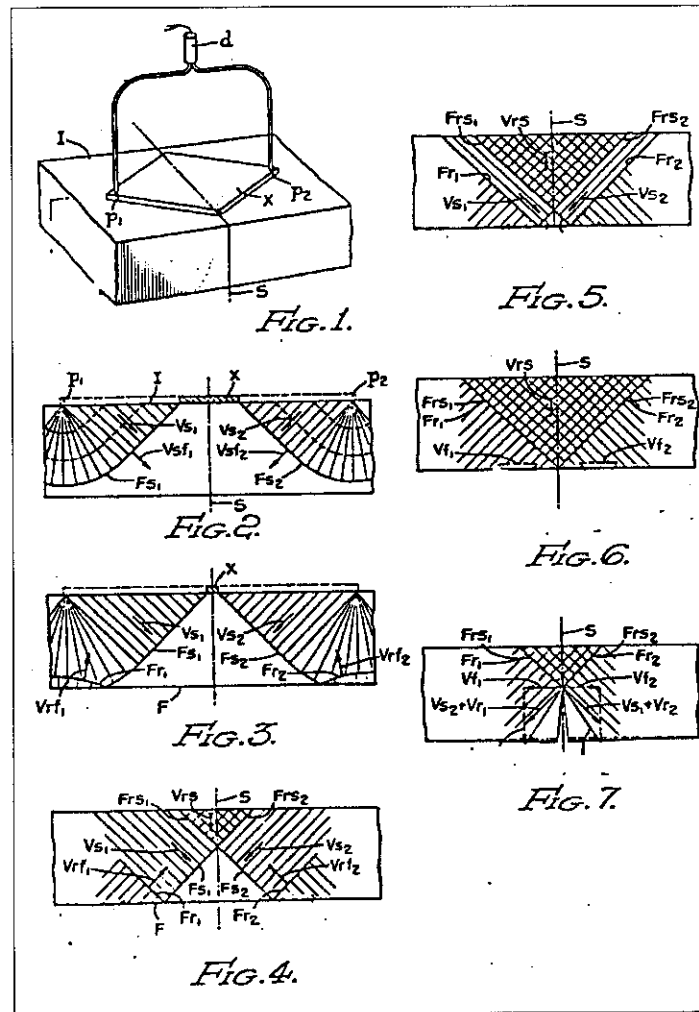


**Figure 2.14:** (Fig.1) Schematic representation of a diamond charge applied on a plate and (Fig.2 to Fig.7) the proposed pattern of reflected stress waves, initiating the crack from the back-face upwards. [8].

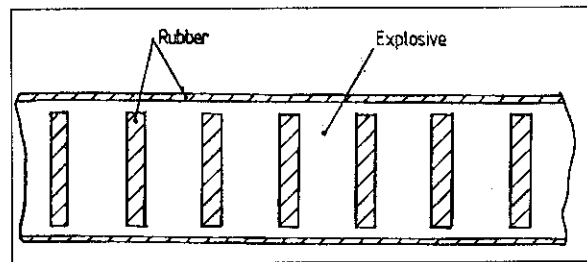


**Figure 2.15:** Fracture belt type "Ladder tape" [9].

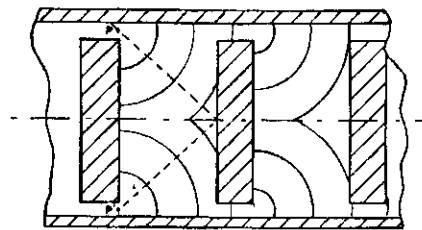


**Figure 2.16:** Schematic representation of the propagation of the detonation front in the ladder charge depicted in **Figure 2.15**: Fracture belt type "Ladder tape" [9].**Figure 2.15** [9].

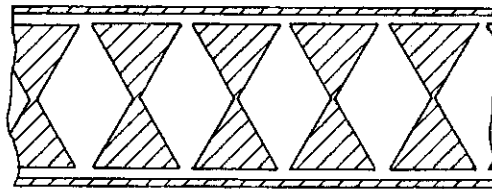


**Figure 2.17:** Fracture belt connecting several diamond charges [9].

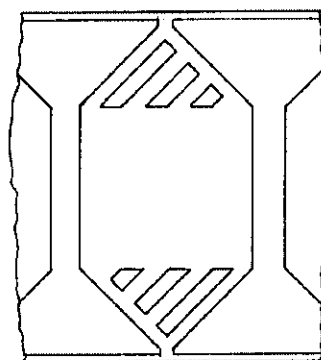


**Figure 2.18:** Fracture Belt with added Plane-Wave Generator[9].

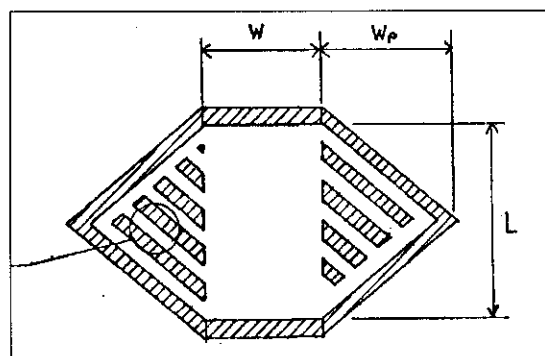


**Figure 2.19:** Fracture Belt with added Plane-Wave Generator relative dimensions [9].

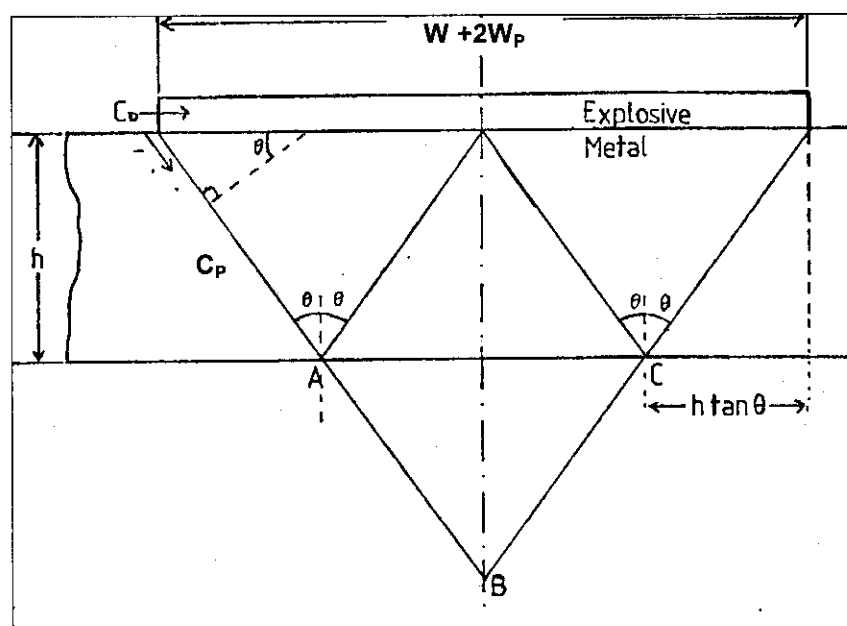


**Figure 2.20:** Geometrical analysis of plate cutting [9].  $C_D$ : Velocity of Detonation,  $C_p$ : Metal sound speed,  $\theta$ : Angle of incidence,  $h$ : Plate thickness.

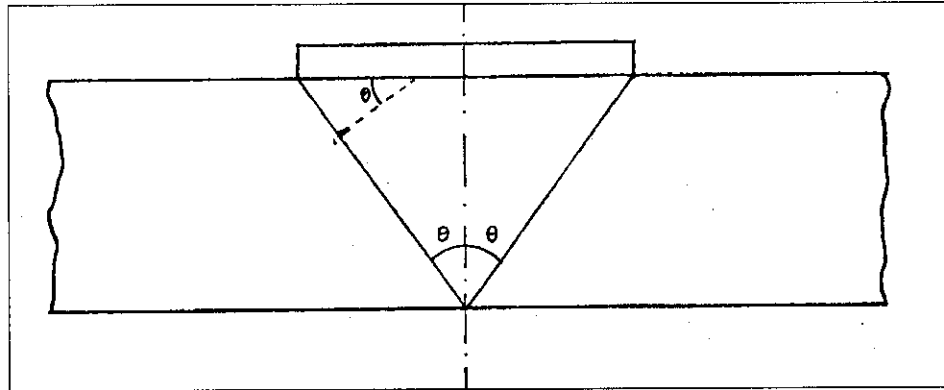


**Figure 2.21:** Geometrical analysis of plate cutting [9]. Minimum charge width for reflected stress waves to first interact.

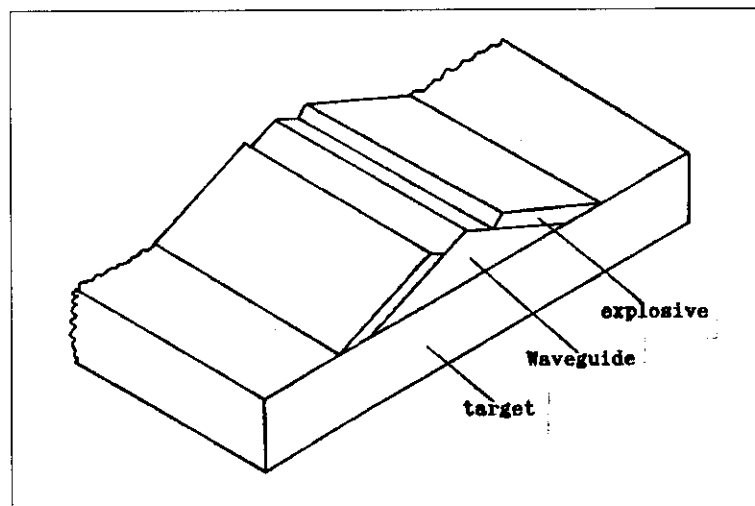


**Figure 2.22:** Flat waveguide [21].

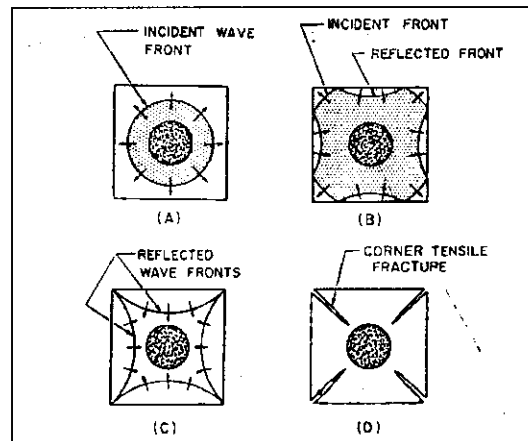


**Figure 2.23:** Development of corner fractures [28].

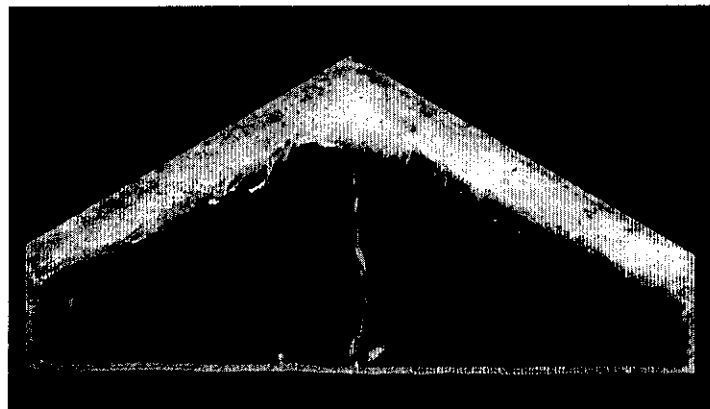


**Figure 2.24:** Perspex models experiments carried out by Davis [9].

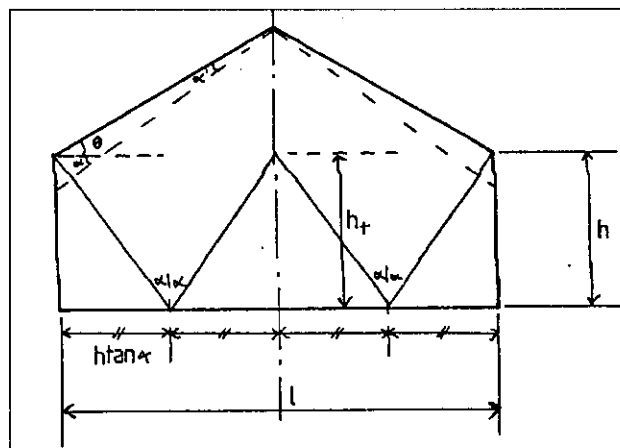


**Figure 2.25:** Geometry of maximum reflected height of plane stress wave[9][ADJ6].



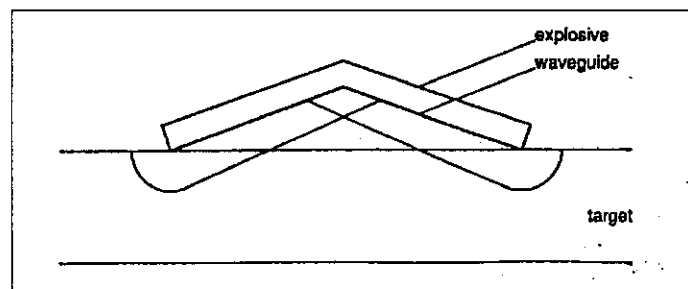


**Figure 2.26:** Propagation of the incident compressive stress wave front on flat steel waveguides [21].

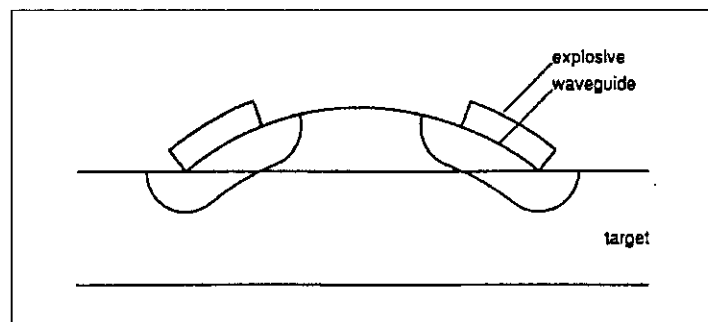


**Figure 2.27:** Cylindrical waveguide [6].

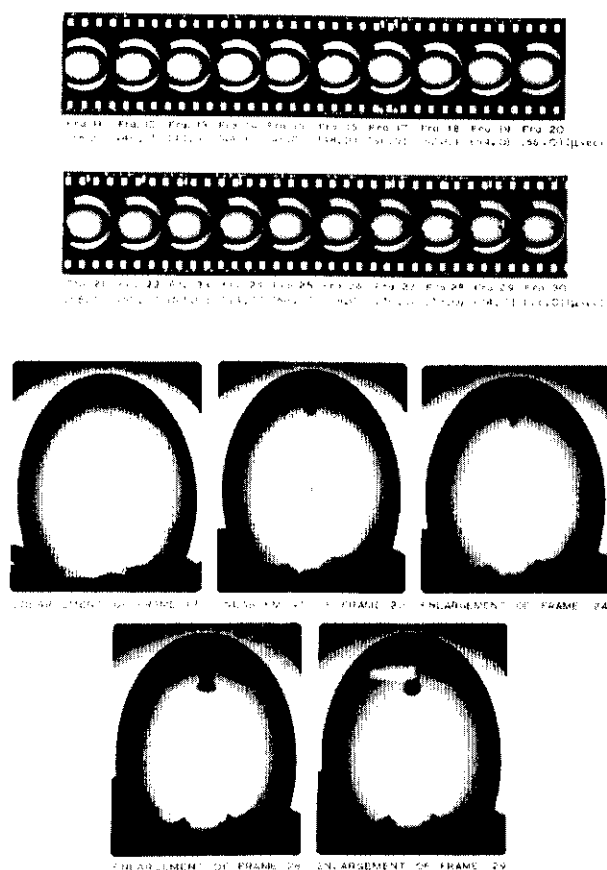


**Figure 2.28:** High speed photography of Perspex ellipsoid explosively loaded, showing crack development due to focusing of reflected stress waves.

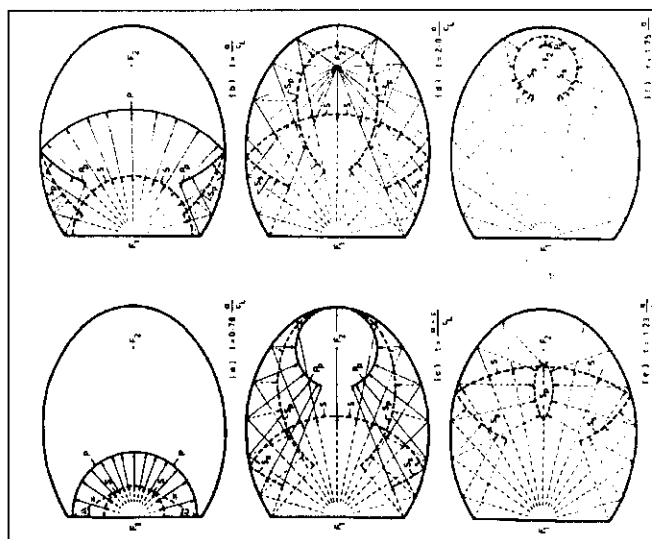


**Figure 2.29:** Schematic representation of incident and reflected stress waves in an axisymmetric ellipsoid.

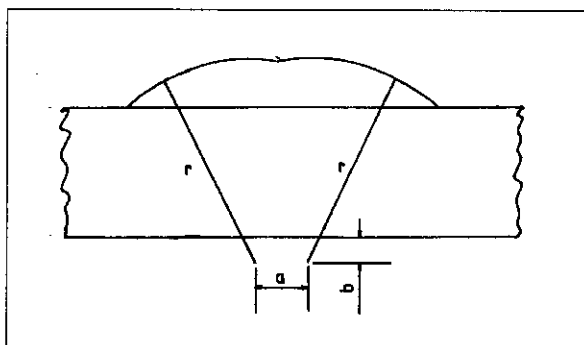


Figure 2.30: Segmental Waveguide [21].

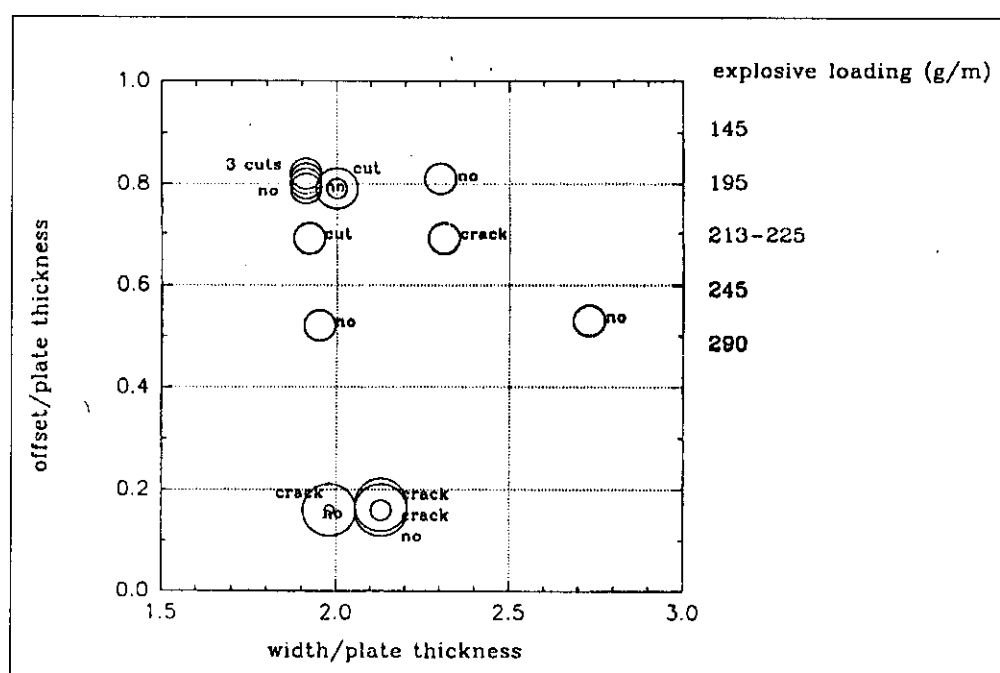
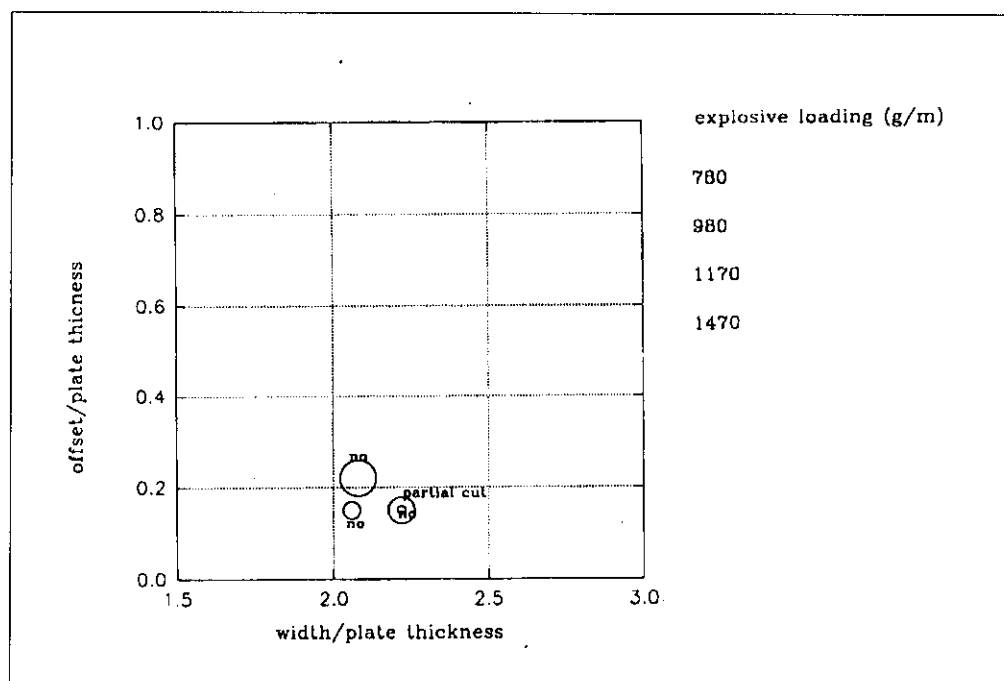


Figure 2.31: Dimensionless parameters for one inch target plates.[6]



**Figure 2.32:** Dimensionless parameters for 65 mm thick plates [6].

### 3 Numerical analysis of SWF Technique

#### 3.1 Introduction

The experimental observation of explosive cutting charges is notoriously difficult and is often limited to small transparent specimens and a few grams of high explosive. For the sizes of specimens and explosive weights tested in the present work the observation of the cutting process was considered impractical. In this context, the numerical analyses provide the means for the understanding of the cutting mechanisms and visualisation of the cutting process. The numerical analyses of the SWF and CSC tests were performed using AUTODYN™ 2D.

##### **The code**

AUTODYN™ is a finite difference code with Euler, Lagrange processors (solvers) which can be coupled allowing simultaneously use of Euler and Lagrange meshes on the same problem [60].

The Lagrange mesh defines the solid geometry, moves and distorts with material modelled and therefore is ideal to model solids like targets subjected to explosive load. In the Lagrange processor co-ordinates, velocities, forces, and masses are defined at the corner nodes; stress, strain, pressure, energies, and densities are cell centred. These features are particularly important when treating material history dependent properties as the material history is contained in the original cell. Free surfaces and material interfaces are located at cell boundaries [60].

In contrast the Euler processor mesh is fixed in space and allows the flow of material through the mesh. It is therefore more suited to handling fluids and gas behaviour, or in the specific case the explosive material as it expands to several times its original volume. An Euler – Lagrange interaction is possible by defining a surface of interaction on the Lagrange subgrid.

Materials are defined in the model using four types of information: i) Equation of state, which defines pressure as a function of density and internal energy; ii) Strength model which defines the yield surface; iii) Failure model, which defines when the material no longer has strength; iv) Erosion model which defines when one material is transformed from a solid to a free mass node. AUTODYN™ provide a series of options for the above categories as follows [60]:

### 3.1.1.1 Equations of state

- Linear: A bulk modulus and reference density are defined,
- Polynomial: A polynomial function describing the relation between pressure and density
- Ideal gas: Ideal gas constant is defined
- Shock: Mie-Gruneisen equation of state
- JWL: Jones-Wilkins-Lee equation of state used for explosives
- Tillotson: High-pressure equation of state
- Puff: Modified Mie-Gruneisen equation of state
- Porous: Used for porous materials
- P-Alpha: Used for porous materials
- Orthotropic: Used for orthotropic materials
- Two phase: Used in cases like pressurised vessels containing two phases
- Lee-Tarver: EOS that allows for dynamic ignition and growth of the detonation

### 3.1.1.2 Strength models

- None: No yield surface, no shear modulus. Material is fluid like
- Elastic: No yield surface. A constant shear modulus is defined
- Von-Mises: A constant yield surface and shear modulus are defined
- Johnson Cook, Zerilli-Armstrong, Steinberg-Guinan, Piecewise Linear, Johnson-Holmquist: Strain hardening model. Strain rate and temperature dependent.

### 3.1.1.3 Failure Models

- None: The material never fails
- Hydro: A hydrostatic tensile stress is defined, if this negative pressure is reached failure will occur
- Bulk strain: Failure occurs when the effective plastic strain exceeds the ultimate bulk strain limit
- Principal stress: Failure occurs if the maximum principal stress or shear stress exceeds a defined value.
- Principal strain: Analogous to Principal stress based on strain values
- Principal strain/Principal stress: Values of strain and stress are considered
- Material stress: Used when material fail along predefined planes, like laminate composites
- Material strain: Analogous to material stress based upon strain.
- Material stress/Material strain: Both material stress and material strength values are considered

- Cumulative damage: Use to describe macroscopic inelastic behaviour of brittle materials

#### 3.1.1.4 Erosion Models

Element is transformed into a free mass (with or without retained inertia) when a specified strain limit is reached.

### 3.2 SWF Technique

#### 3.2.1 Introduction

The numerical models of SWF charges presented in this Section were done after the experimental phase was completed and aimed to assist in the understanding of the cutting phenomenology discussed in Section 5.

The experimental analysis of explosively induced cracks has been successfully achieved using small transparent polymeric solids [7][25][57] but the explosive load in those cases was limited to detonators with a few grams of high explosive. In the case of the experiments described in Section 4, the analysis of the geometries using small scale Perspex samples was considered inadequate as the nature of the waves, target thickness and duration of the pressure pulse would affect the geometry of propagation and interference of the pressure pulses. The inability to observe the intermediate stages of an event is very common in explosive engineering where very often observation methods and facilities are not able to cope with large-scale experiments. In this context the numerical analysis provide a unique source of information to assist in the understanding of cutting process and engineering of real size explosive tools.

A comprehensive survey of computer codes for explosive and impact application can be found in [61] and include two and three dimensional finite difference and finite element codes specially developed for this kind of application. Among those AUTODYN™ is highly praised, and it is a finite difference code specifically designed for non-linear dynamics, being the most significant features the following:

- Being a finite difference code it allows the simultaneous use of Lagrange and Euler processors
- It is available in Personal Computer platform
- Impressive pre and post-processing capabilities
- Impressive experimental verification track record

Taking this reference into account, AUTODYN™ was chosen as the numerical code to be used in this work due to its previous experience in UMIST [9] and Reverse Engineering. Finite difference numerical techniques are well established and discussion of its application to explosive and hyper-velocity problems can be found in [62],[63]

The main limitation of the numerical analyses of explosive loading problems is, according to Zukas [61], the correct representation of failure. Zukas also pointed out that micro-mechanically based models applicable to multiaxial transient loading situations are generally not available and that those that exist require an excessive degree of material characterisation. Curiously Zukas [61] explains that the failure models tend to be simple for the following reasons:

- a. "Since material failure will be incorrectly modelled, it should be done as simply and cheaply as possible"
- b. "The material characterisation required, and therefore cost, is kept to a minimum".
- c. "In many cases, the simple models produce results that are in substantial agreement with experimental data...."

The correct description of the failure was in fact the main constraint faced during the present work. Despite being essential in the understanding of the propagation and interference of pressure pulses, the numerical prediction of the complex crack patterns described in the previous Section was limited by the following factors:

- Use of a 2 dimensional code did not allow to take into consideration the accurate direction of detonation, which affected the values of initial maximum pressure.
- Experimental results showed consistently fracture patterns including multiple failure modes.
- Lack of availability of experimental constants required by the failure models.
- Lack of accurate waveguide material Hugoniot data.

The numerical analysis of the waveguides was therefore limited to the evaluation of the effect of waveguide geometry in the propagation and interference of the pressure pulses without allowing the material to fail.

### **3.2.2 Initial Considerations**

#### **3.2.2.1 2D x 3D**

As described in Section 2, one of the most important characteristics of waveguide charges is its ability to create interference between pressure pulses created by two parallel and



synchronised detonation fronts. Being this way, by definition the detonation front is perpendicular to the waveguide surface and a grazing angle between the detonation front and pressure pulse propagating in the waveguide will occur. Also the initial pressure at the explosive/waveguide interface is considerably reduced when compared with a detonation front parallel to the waveguide surface [23][64]. The difference between the maximum pressure values obtained in both cases will decrease as the pressure pulse travels inside the material as shown in **Figures Section 3**

Figure 3.1 [64].

The values shown in **Figures Section 3**

Figure 3.1 are calculated taking into account the decay of pressure due to rarefaction waves and are function of explosive thickness. The pressure near the surface will decay as function of the explosive thickness and direction of detonation. This effect will be more noticeable for larger explosive thickness and therefore 2-D models that consider detonation fronts parallel to the waveguide surface are likely to overestimate the incident pressure pulse. This had to be taken into account when the explosive thickness is comparable to the waveguide thickness.

Unfortunately the use of 3D version of AUTODYN™ would require excessive CPU time and was considered not practical during the preparation of this work. This limitation is expected to be overcome by the availability of significantly faster computers in the near future.

### 3.2.2.2 Waveguide Material Property

Due to cost considerations, the waveguide material Hugoniot was not experimentally determined. In absence of the specific experimental data, the Hugoniot properties of a polymeric material included in the AUTODYN™ material library was modified to take into account the higher initial density. **Figure 3.2** shows shock velocities as function of pressure for some polymeric and metallic materials, the graph was constructed with data from reference [65].

It can be observed from **Figure 3.2** that Neoprene, Polyurethane and Polyrubber behave similarly when compared with metals like Iron, Copper and austenitic stainless steel 304 (18Ni 8Cr). Polyrubber was chosen due to its low initial sound speed velocity 850 m/s

which is comparable with approximately 1000 m/s measured values for the standard composite Iron/Polyurethane used.

### 3.2.2.3 Failure Models

The metallographic examination of the cut samples described in Section 4 shows two distinct failure modes, one responsible for the spalling and another responsible for the fracture at the top in shear.

The spall formation was characterised by the nucleation and growth of microcracks. The Microstatistical Fracture Mechanics (MFSM) proposed by Curran et al [34] is in principle suitable to describe one part of the fracture pattern obtained. The use of MFSM and subsequent Nucleation and Growth models (NAG) rely on the inclusion of average microstatistical values in the constitutive models which are unavailable for many materials. Some of the models proposed include from thirteen to twenty one material parameters [66], which demonstrate the complexity associated with the phenomenon described. This complexity includes the necessity to consider, for instance, incubation times for crack nucleation and the consequent effect of the pressure pulse duration [40]. It should be noted that microvoid/microcrack based models are valid only in tension and that micro-shear band models would be necessary to describe failure in shear or compression loads [ADJ20][30].

Macroscopic models have been proposed assuming a Damage concept to address the gap between more conventional dynamic failure models and NAG models. The concept of Damage assumes that failure will occur when the development of cracking builds up to a critical value of damage as a function of stress, hydrostatic stress, strain, strain rate, temperature and time [ADJ21][45]. Despite requiring less parameters, it is still an empirical approach which depends upon empirical material constants. An alternative macroscopic concept, Simple Unified Spallation (SUS) failure model, was proposed in reference [66] defining a critical tensile pressure and critical gross porosity for failure. The SUS model takes into consideration the reduction of the effective shear modulus and yield strength as a function of the growing values of porosity. Preliminary attempts to use the SUS model on waveguide Type 6 is described in reference [66], further tentative work has been done since to expand this analysis to other geometries but unfortunately the complexity of the cutting process could not be accurately described. Possibly due the lack of accurate waveguide material properties and to the inaccuracy of the two dimensional representation when compared with the three dimensional nature of the problem.

To assess the different geometries and the cutting phenomena the material was not allowed to fail. By using isopressure and shear stress plots in time, it was possible to correlate charge geometry variation with the overall experimental result.

### **3.2.3 Modelling of SWF and waveguide charges using AUTODYN-2D.**

#### **3.2.3.1 Propagation of stress pulses, excluding failure model**

The waveguide geometries modelled in this Section include Waveguide Type 1 using steel and polymeric waveguide, Types 2,3,4,5,6 and 8 using polymeric waveguides and three flat steel waveguides tested in [19].

Waveguides and explosive were modelled using Euler processor and the targets using Lagrange processor, allowing for interaction between the Lagrange and Euler subgrids.

##### **3.2.3.1.1 Flat Waveguides**

Prior to the analysis of curved waveguides tested in Section 4, a preliminary assessment was performed to describe a set of three flat steel waveguides tested in [19]. The tests were performed with 25.4 mm thick, EN3A cold rolled steel targets and are described in “Steel waveguides Series 1, Table 2” in [19]. **Figure 3.3 to Figure 3.5** aim to compare two successful geometries with an unsuccessful one as the cold rolled steel is not expected to be able to put great resistance to shock loading, and the uncertainties regarding waveguide material properties is eliminated due to use of a steel waveguide.

**Figure 3.3**, represents an isopressure sequence in time, showing the variation in resultant pressure profiles due to the propagation shockwaves and interference with reflected pressure pulse. The colours shown do not represent the same values of pressure throughout the sequence but aim to visualise the differences in pressure at each stage. The sequence shows the interference of incident shockwaves on the centre line of the between the two sides of the waveguide starting within the waveguide and the continuing down to the back-face of the target. It also shows the interference of reflected stress waves through the same centre line. Closer examination of the particle velocities shows, as expected that the resultant is perpendicular to the back surface. Experimental result was described as “cut with spall”.

**Figure 3.4** when compared with **Figure 3.3** shows lower values of pressure for the region of interference between the incident shockwaves, and notably the same values for the interference of reflected stress waves, this time at the vertical centre line. Experimental result was described as “cut with no spall”.

**Figure 3.5** shows a sequence for a waveguide with CS approximately 60% of the waveguide width. It can be observed that the trajectory of the two reflected stress pulses is such that they hardly interfere with each other. The experimental result was described as “Two 15 mm deep fractures developed on the underside, about 100 mm apart”.

#### 3.2.3.1.2 Curved Waveguides

Waveguide Type 1 was tested using both polymeric and steel waveguides on 65 mm thick 43 A steel targets. The numerical evaluation of Test 4 isopressure sequence is shown in **Figure 3.6**. The sequence show a pattern of interference between incident shockwaves followed by three separated regions of interference between reflected stress waves showed in detail in **Figure 3.7** and **Figure 3.8**. The tensile reflected waves interference patterns are in agreement with the spall planes obtained in the experimental results. The central space on the waveguide without explosive (CS) did not allow to clearly observe the focusing nature of the waveguide geometry, this is shown in **Figure 3.9** where a sequence of isopressures for waveguide Type 1 using CS=0. The convergent nature as the disturbance propagates can be seen on the sequence of **Figure 3.9** and in detail in **Figure 3.10**. The convergence of the reflected tensile stress is affected by interference with the incident pressure pulse, and it is only possible to observe properly the reflected stress pulse when it is already diverging as shown in **Figure 3.11**.

The modelling of a polymeric waveguide Type 1 is shown in **Figure 3.12** to **Figure 3.14**. In can be observed in the sequence shown in **Figure 3.12** that the isopressure profile associated with the propagation of shock front changes direction as it crosses the waveguide/target interface. The new direction of propagation is also associated with a change in direction of particle velocities at the shock front and associated induced stresses a trend that is in agreement with the experimental results shown in Test 8 where a vertical crack was obtained.

Waveguide Type 2 analyses are shown in **Figure 3.15** to **Figure 3.17**. The sequence shown in **Figure 3.15** describes a very similar pattern to **Figure 3.12**. The tensile values for the Waveguide Type 2 are marginally higher than waveguide Type 1, which could explain the different results. Based on the analysis and the experimental results it is believed that the failure of Waveguide Type 1 was marginal as Waveguide Type 2, achieved cut in three occasions and Waveguide Type 1 obtained a vertical crack cutting 2/3 of the target thickness.

Waveguide Type 3 is shown in **Figure 3.18 to Figure 3.19**. It can be observed that Waveguide Type 3 is flatter than Waveguides 1 and 2 resulting in a greater interference between incident and reflected pressure pulses as shown in **Figure 3.19**. In the case of Waveguide Type 3 the interference between reflected tensile pulses is greatly affected by the incoming shockwave and hardly interfere on their own at the centre line.

#### 3.2.3.1.3 Segmental Waveguides

Waveguide Type 4 successfully cut 43A and 50D targets and being a segmental waveguide with negative separation implies that the incident shockwaves will interfere within the waveguide. This interference between the incident shockwaves proved to be quite substantial for the explosive thickness used as shown in **Figure 3.21 and Figure 3.22** with an estimated value of 72 GPa as shown in **Figure 3.22**. Taking into consideration the experimental results even if this value is overestimate, it gives a comparative idea of the stress concentration achieved at this point. **Figure 3.23** shows the associated shear stress profile at the point in time where the interference region is in the target. It can be observed the central V shaped region on the target at the centre of line of the waveguide, which is in agreement with the experimental results.

Waveguide Type 5 isopressure profiles are shown in **Figure 3.24 to Figure 3.26**. It can be observed that the higher inclination of the waveguide gave rise to two regions of high pressure on the waveguide/target interface as shown in **Figure 3.24** at 7.2 and 13  $\mu$ s. The higher inclination of the waveguide also reduced pressure values of the transmitted shockwaves as expected. This resulted in lower pressures at regions of interference between the transmitted shockwaves. More importantly however is the fact that the transmitted pressure pulses pass through each other before reaching the back face resulting in a tensile tail behind the compressive pulse. The compressive pulses (shockwaves) go on to be reflected in a divergent fashion and hardly interfere with each other after being reflected.

Waveguide Type 6 isopressure sequence shows a similar pattern to the one obtained for Waveguide Type 4 as shown in **Figure 3.27**, however waveguide type 6 uses substantially less explosive than waveguide Type 4. **Figure 3.28** shows the interference of transmitted shockwaves at the target, just under the waveguide centreline where the pressure value reached 40 GPa. **Figure 3.29** shows a – 8GPa pressure value at the region of interference between the reflected tensile stress pulses. **Figure 3.30 to Figure 3.32** show shear stress profiles. It can be observed “V” shaped regions of maximum shear stress being formed as the regions of interference between the transmitted shock waves are formed through the target

thickness underneath the waveguide centreline. These results are in agreement with the shear failures obtained in the experimental testing.

### 3.2.3.2 Numerical Models including material failure

#### 3.2.3.2.1 BS 4360 - 50 D Hugoniot and dynamic spall strength

The dynamic properties of 50D steel were evaluated in [71]. Some of the results are presented here with permission of the contractor. Description of the experimental methods can be found in [71], the values are:

Equation of state:	$U_s = 4510 + 0.74U_p$
Hugoniot Elastic Limit:	$HEL_{50D} = 1.8 \text{ GPa} \pm 0.1 \text{ GPa}$
Spall Strength:	$S_s = 3.3 \text{ GPa} \pm 0.3 \text{ GPa}$ (for shock pressures up to 11GPa)
Bulk modulus:	$K = 160 \text{ GPa}$
Shear modulus:	$G = 84.4 \text{ GPa}$
Youngs' Modulus:	$E = 197 \text{ GPa}$

The specimens were not tested for dynamic shear strength. **Figure 3.33** shows the variation of spall strength with shock pressure for 50D steel [71]. The test results showed that the spall strength value remain constant, about 3.3 GPa for shock pressures up to about 11GPa reaching 7.5GPa for shock pressures of 17.5GPa [71]. For shock pressures smaller than 5.46 GPa the spall plane was identified only as a line of voids.

#### 3.2.3.2.2 Equation of state

The polynomial equation of state determined in [71],  $U_s = 4510 + 0.74U_p$  was used in the analyses.

#### 3.2.3.2.3 Failure Model

Principal stress failure model was used allowing the material to fail if either the maximum principal stress or shear stress exceeds a defined value. The spall strength value of 3.3 GPa was used as the tensile failure stress value.

The shear strength was initially approximated by 1.65GPa, (half of the spall strength value), without success. The shear strength value was gradually reduced down to 330 MPa, when the results for Waveguide type 6 started showing failure due to shear at the top of the specimen.

#### 3.2.3.2.4 Strength Model

The Johnson-Cook strength model was used. The Johnson-Cook model is an empirical constitutive equation where the strain rate and temperature effects are taken into consideration [72][73]. The model describe the Von Mises flow stress,  $\sigma$  as :

$$\sigma = (A + B\varepsilon^n) \left(1 + C \ln \dot{\varepsilon}^*\right) (1 - T^{*m}) \quad (5.3)$$

Where  $\varepsilon$  is the equivalent plastic strain,  $\dot{\varepsilon}^*$  is the dimensionless plastic strain rate defined as  $\dot{\varepsilon}^* = \dot{\varepsilon} / \dot{\varepsilon}_0$  for  $\dot{\varepsilon}_0 = 1.0 \text{ s}^{-1}$ ,  $T^*$  is the homologous Temperature defined as:

$$T^* = \frac{T - T_{room}}{T_{melting} - T_{room}} \quad (5.4)$$

Where  $T$  is the absolute temperature. Values for the five constants ( $A$ ,  $B$ ,  $n$ ,  $C$ ,  $m$ ) on (5.3) can be found for some materials in [30] and in AUTODYN material library.

#### 3.2.3.2.5 Numerical results

Two distinct experimental results were select to be modelled in order to assess capability of the simulation to distinguish between results containing spall only and results containing spall plus vertical and shear cracks. Therefore Waveguide type 2 with 9 mm of explosive (TEST 10) showing only spall and Waveguide type 6 with 18 mm of explosive (TEST 19 and 22) showing spall plus vertical and shear cracks were chosen.

A 0.5 mm Lagrangian mesh was used to describe the target and a 0.5 mm Euler mesh was used to describe the waveguide and explosives. The Euler mesh was removed once the

compressive stress waves were fully transmitted from the waveguide to the target. This procedure dramatically reduced the computational time.

The numerical results showed that the analysis is capable of capturing these very different charge performances, however this was only achieved when values of maximum shear strength were reduced from 1.65 GPa to 330MPa.

The following notation is used to categorise the direction and mode of failure (with exception of **Figure 3.36** where colours represent different materials):

- Dark Blue: Hydro, failure occurs when a negative hydrostatic pressure value is reached
- Green: Elastic, Material not fail and is not experiencing plastic deformation
- Light blue: Plastic, Material is experiencing plastic deformation
- Red: Bulk, Bulk failure
- Pink: Failed 11, Fail due to maximum tensile stress in the 11 direction (Vertical)
- Yellow: Failed 22, Fail due to maximum tensile stress in the 22 direction (Horizontal)
- Grey: Failed 33, Fail due to maximum tensile stress in the 33 direction (Perpendicular to the plane considered)
- Orange: Failed 12, Fail due to maximum shear stress

**Figure 3.34** shows waveguide Type 2 geometry covered with 9 mm of C4 (RDX based explosive). The dark blue colour denotes that the “Hydro” failure model was applied on the explosive and waveguide. **Figure 3.35** shows the results using tensile strength 3.3GPa and Maximum Shear Strength equals to 330 MPa for better comparison with **Figure 3.41**. The numerical results show the presence of spall and no vertical cracks or failure due to shear.

**Figure 3.36 to Figure 3.41** show the simulations using waveguide Type 6 geometry and 18 mm of C4. **Figure 3.36** shows material location. **Figure 3.37** shows the simulation using the value of maximum shear strength as 1.65 GPa, where only the appearance of a spall plane can be observed. The sequence depicted in **Figure 3.38 to Figure 3.40** show the initial failure at the top of the specimen due to shear, followed by the appearance of spall plane, and on a third and final stage the failure across the thickness due shear.

### 3.3 Discussion of numerical results

#### 3.3.1 SWF cutting mechanism

Based on the numerical results it is possible to propose a cutting mechanism with the participation of the interference of compressive shock waves at the top surface of the target.



The experimental results show consistently the failure of the target at the top surface of the target due to adiabatic shear, which is in agreement with the numerical results. At the strain rates considered, the formation of a region of concentrated high pressure at the top surface of the target generate the conditions and shear stresses necessary for the target material to fail due to adiabatic shear.

The numerical results for waveguide Types 4 and 6 showed the presence of highly concentrated pressures at top surface of the target on the centre line of the waveguide when compared with other waveguide geometries and explosive loads.

As shown in **Figure 3.36 to Figure 3.41** it is possible to stipulate a value of maximum shear strength where the numerical simulation of the cutting mechanism will include a failed region at the top due to shear and at the bottom due to spalling. This cutting mechanism is in agreement with experimental results but suggests in addition to the experimental evidence that the cutting process starts at the top on a first stage, followed by a second stage where the material fail at the back surface, and that the final stage is inside the target.

### **3.3.1.1 SWF charge parameters relative influence**

The results of the numerical analyses have to take into account the considerations discussed in section 3.3. It was possible to evaluate the relative influence of some of the SWF charge parameters like: the waveguide material, waveguide geometry and explosive distribution.

#### **3.3.1.1.1 Waveguide Material**

Steel and polymeric waveguide materials were modelled using waveguide type 1. By comparing the sequence showed in **Figure 3.6** for a steel waveguide with the sequence showed in **Figure 3.12** for a polymeric waveguide it is possible to observe the effect of waveguide material on direction of the transmitted stress wave and associated shape of the wavefront. This effect is more noticeable at the interface between the waveguide and the target. At the interface between the steel waveguide and the steel target it can be observed that the stress pulse pass undisturbed and that the wavefront remain concave after passing the interface. In the case shown in **Figure 3.12** the initial concave wavefront profile becomes convex after passing the interface.

#### **3.3.1.1.2 Waveguide Geometry**

The numerical study, with a few exceptions, were confined to the to the waveguide geometry and explosive actually tested and therefore the discussion here presented is limited to the geometries analysed.

Three main types of waveguide geometries were analysed: Flat, Curved and “Segmental”.

It is possible to compare the sequences of stress wave propagation of two different flat waveguides geometries showed in **Figure 3.4** and **Figure 3.5**, which used similar explosive loads. The waveguide shown in **Figure 3.4** is able to generate a region of interference between compressive shock waves within the target (but not within the waveguide), followed by the interference of the reflected tensile stress waves. By decreasing the waveguide angle and increasing its width it is possible to observe that the compressive shock waves do not interfere at all and that the reflected tensile stress waves hardly interfere. This suggests that both the waveguide width (for a particular target thickness) and the angle of the waveguide are important parameters of the waveguide charge design as they are able to inhibit the formation of regions of interference between the stress pulses.

Only three curved geometries were analysed and it is not possible based on the analyses to establish their main design parameters. In the case of the polymeric curved waveguides, as described in the previous section, after passing the interface between waveguide and target, the concave and convergent wavefront profile within the waveguide is replaced by a convex and convergent wavefront profile. These convex profiles are more similar to the ones generated by flat steel waveguides than the concave wavefront profiles generated by steel waveguides. Waveguide Type 3 simulation described in the sequence shown in **Figure 3.18** suggests that flatter waveguides result in a bigger region of destructive interference between incident compressive and reflected tensile waves.

The segmental waveguides analysed (Types 4,5,6) used twice the explosive thickness of curved waveguides and a direct comparison is therefore not possible. The effect of the interference of compressive shock waves within the waveguide is quite clear in the sequences showed in **Figure 3.21**, **Figure 3.24** and **Figure 3.27**. This effect is also noticed in **Figure 3.3** for flat waveguides and is responsible for the appearance of high pressures concentrated on the centre of the waveguide at the interface between waveguide and the target. The explosive distribution on top of the waveguide is able to affect the appearance of this area of concentrated compressive shockwaves as it is discussed in the next section.

Waveguide Type 5 simulation showed in the sequence of **Figure 3.24** and in detail in **Figure 3.25** and **Figure 3.26** showed that in the Type 5 geometry a great percentage of the energy incident compressive shock waves pass each other before of being reflected. This suggests the existence of an upper boundary for the inclination of the waveguide above which the charge efficiency is reduced.

#### **3.3.1.1.3 Explosive Distribution**

As it will be shown in Section 4, the way the explosive is placed on the surface proved to be an important parameter in the charge design. The participation of the interference of compressive shockwaves on the centre of the waveguide at the interface between waveguide and target seems able to fracture the metal in shear at the top surface as it will be shown in Section 4. This effect is in agreement with the simulations presented as discussed bellow.

It can be noticed that, for the same waveguide geometry, the numerical results show the influence of the distribution of explosive on top of the waveguide has on the region of interference between the incident shockwaves. For the same conditions of waveguide geometry, waveguide material, and explosive, this influence can be summarised as follows:

Concentrating the explosive at the edges of the waveguide results in the gradual movement downward of the position where the compressive shock waves first interfere. If both sides of the waveguide are covered with explosive, the compressive shock waves will start to interfere at the top of the waveguide. If the space between the explosive is strips is bigger than a certain amount the compressive shock waves will only start to interfere after being transmitted to the target. For certain waveguide geometries/target thickness combination is possible to reach as stage where the compressive shock waves are reflected before interfere. Therefore to achieve the intended shear fracture at the top surface of the target, it is necessary that the shock waves start to interfere within the waveguide.

For the same explosive thickness and waveguide geometry, the peak pressure of the incident shock waves will reduce its values as they travel in the waveguide, pass the waveguide/target interface and travel through the target. Therefore the later the shockwaves interfere in the target the lower will be the resulted peak pressure. Being this way, it is also more efficient to make compressive shock waves start to interfere within the waveguide.

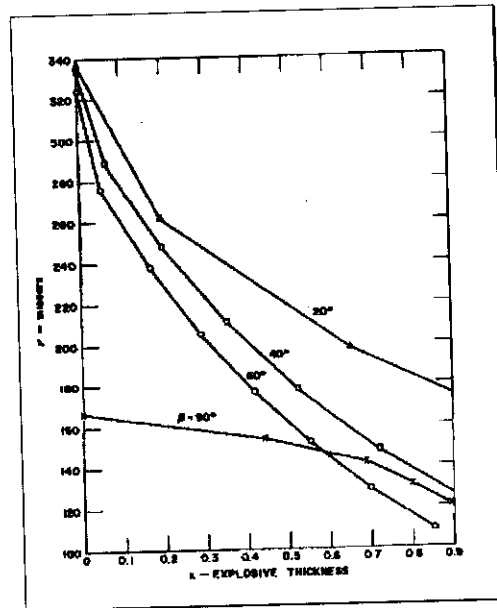


**Figure 3.1:** Pressure as function of distance from the explosive/metal interface measured in terms of explosive thickness for various angles between the interface and detonation front.  $\beta = 90^\circ$  describes a detonation front travelling perpendicularly to the surface. (Metal = Aluminium, Explosive = Composition B)[5.9].

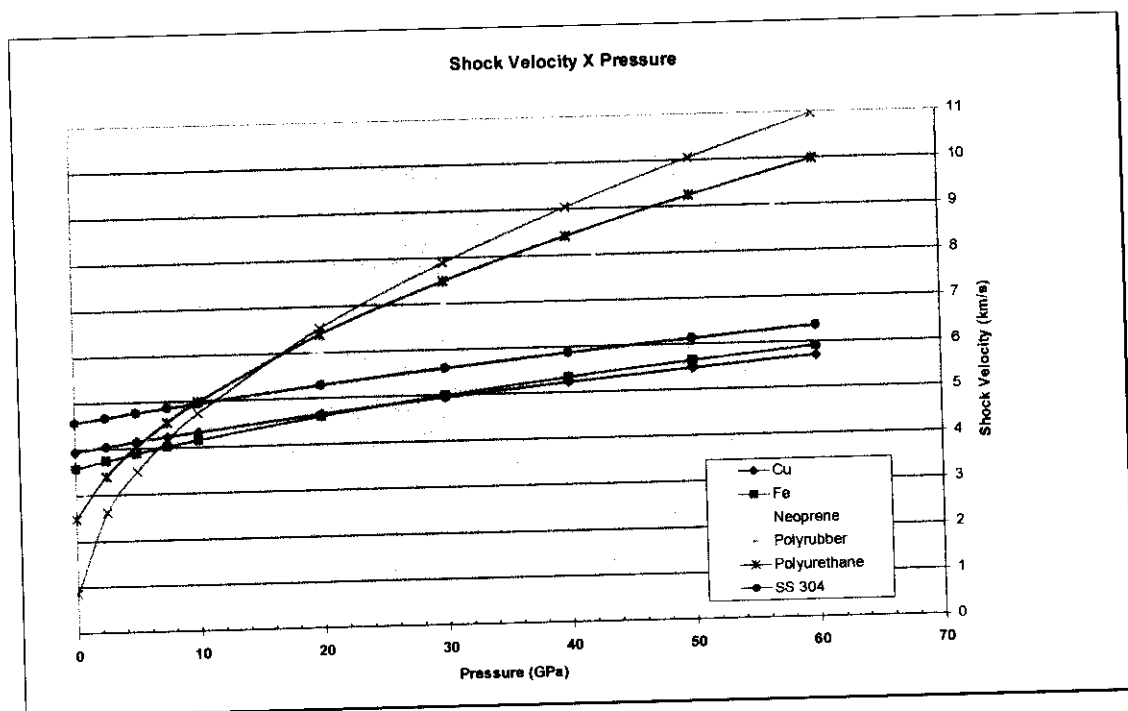


**Figure 3.2:** Shock Velocity x Pressure for selected metallic and polymeric materials, made with data from [5.11].

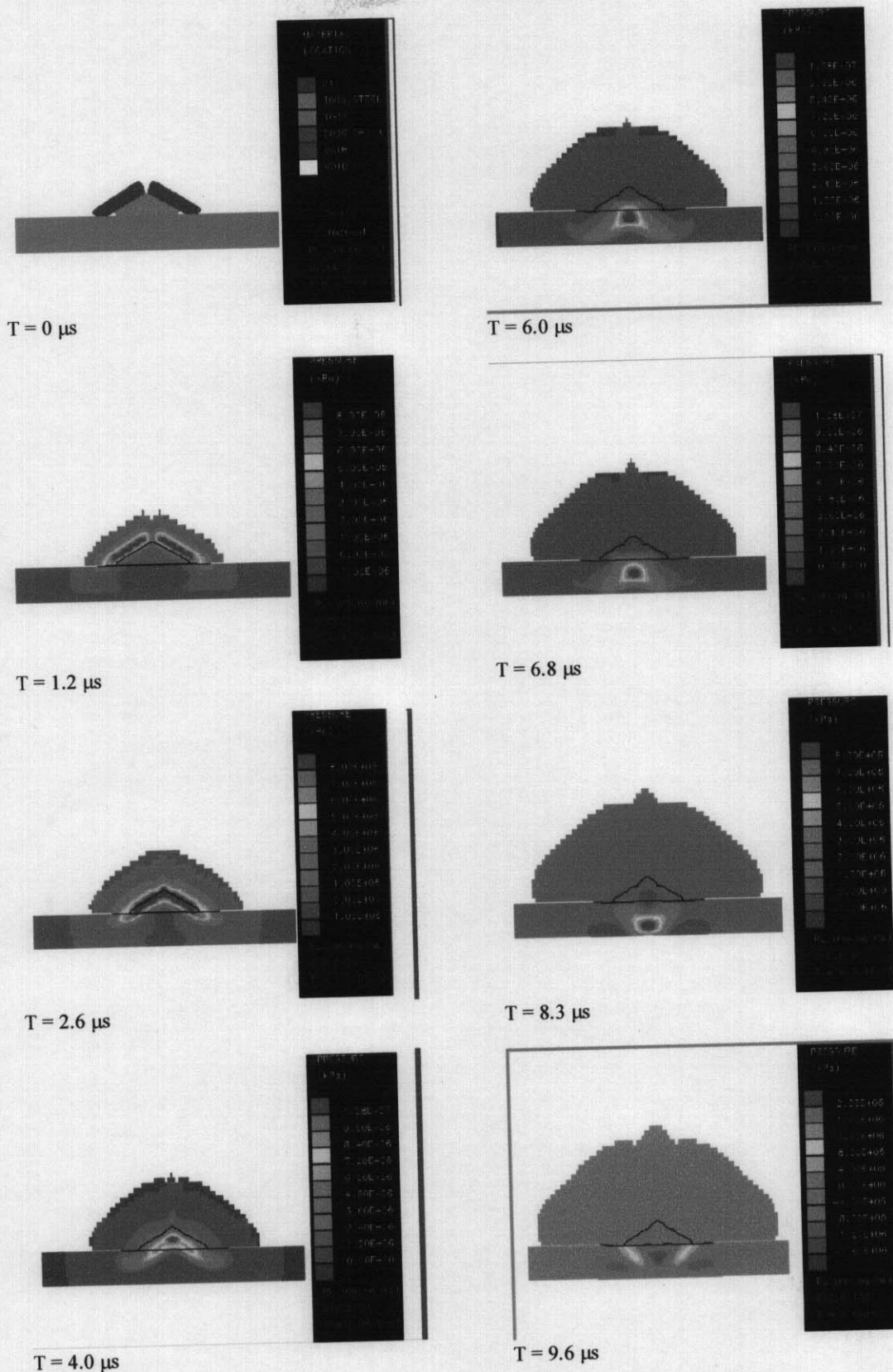


**Figure 3.3:** Sequence showing the development and interference for flat steel waveguide  $\alpha = 29.2^\circ$ , Waveguide width = 58 mm, CS = 0%.

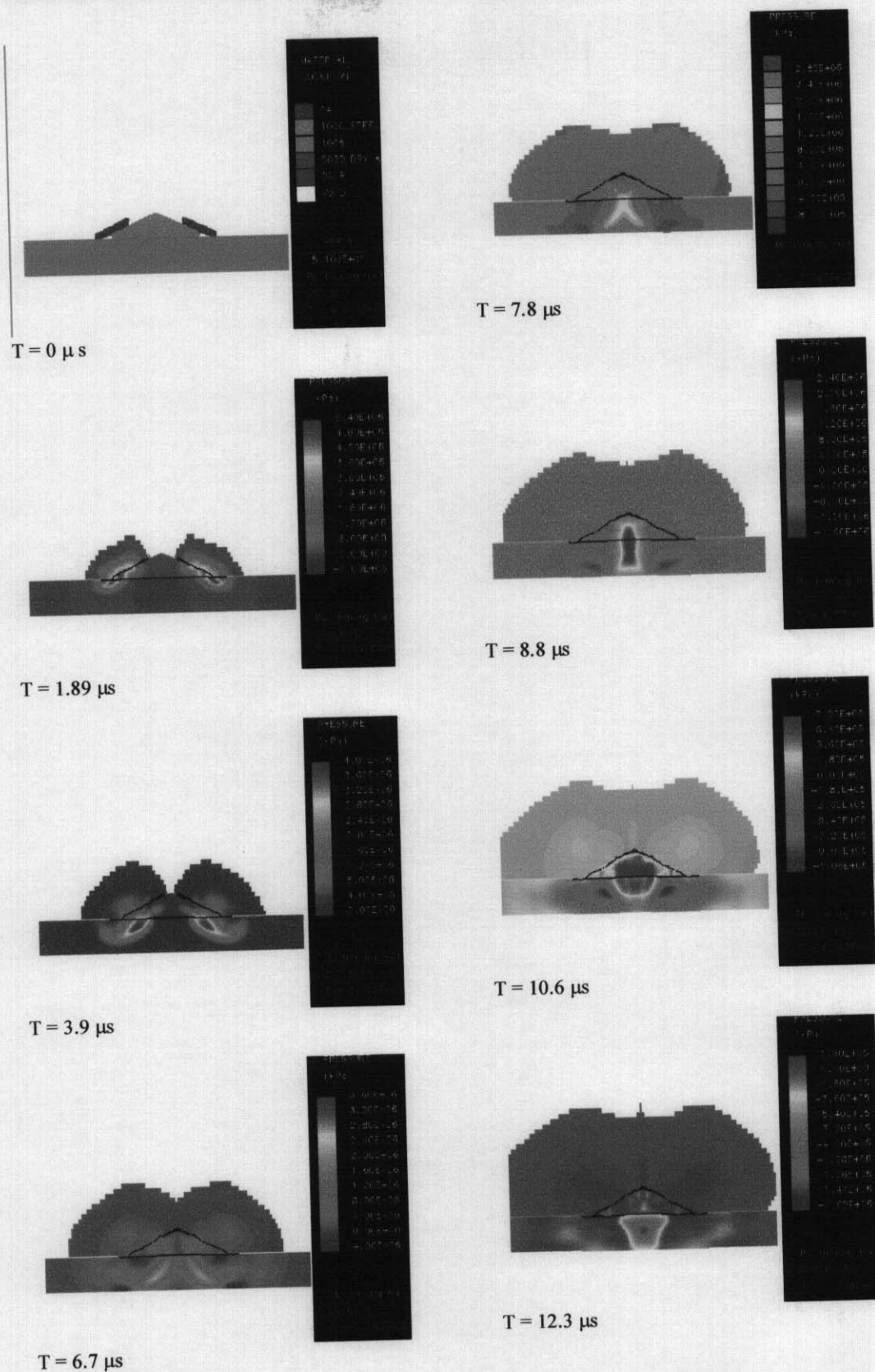


**Figure 3.4:** Sequence showing the development and interference of shockwaves for steel waveguide  $\alpha = 24.5^\circ$ , Waveguide width = 83 mm, CS = 47%.



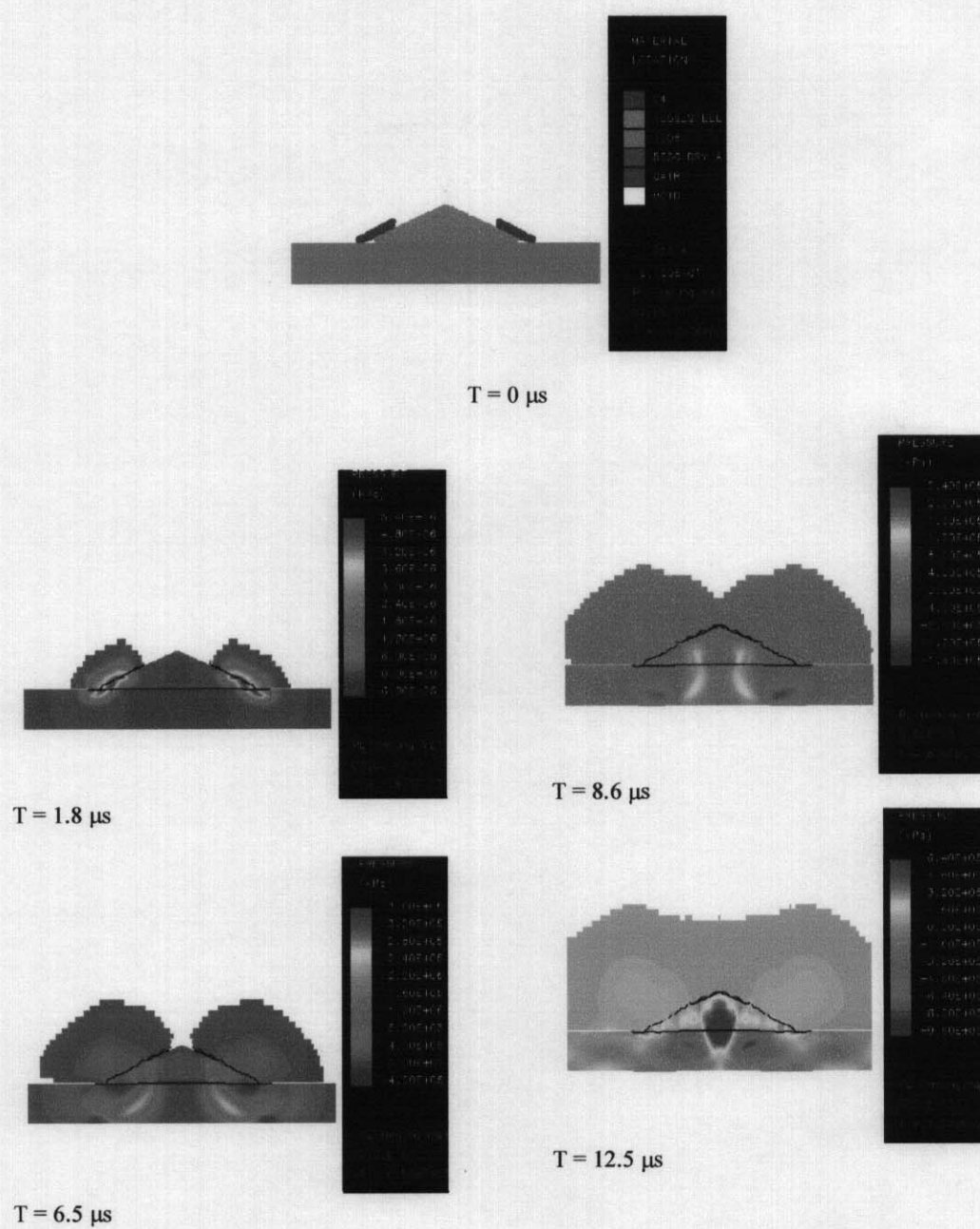


**Figure 3.5:** Sequence showing the development and interference of shockwaves for a steel waveguide  $\alpha = 24.8$ , waveguide width 108 mm, CS = 60%.

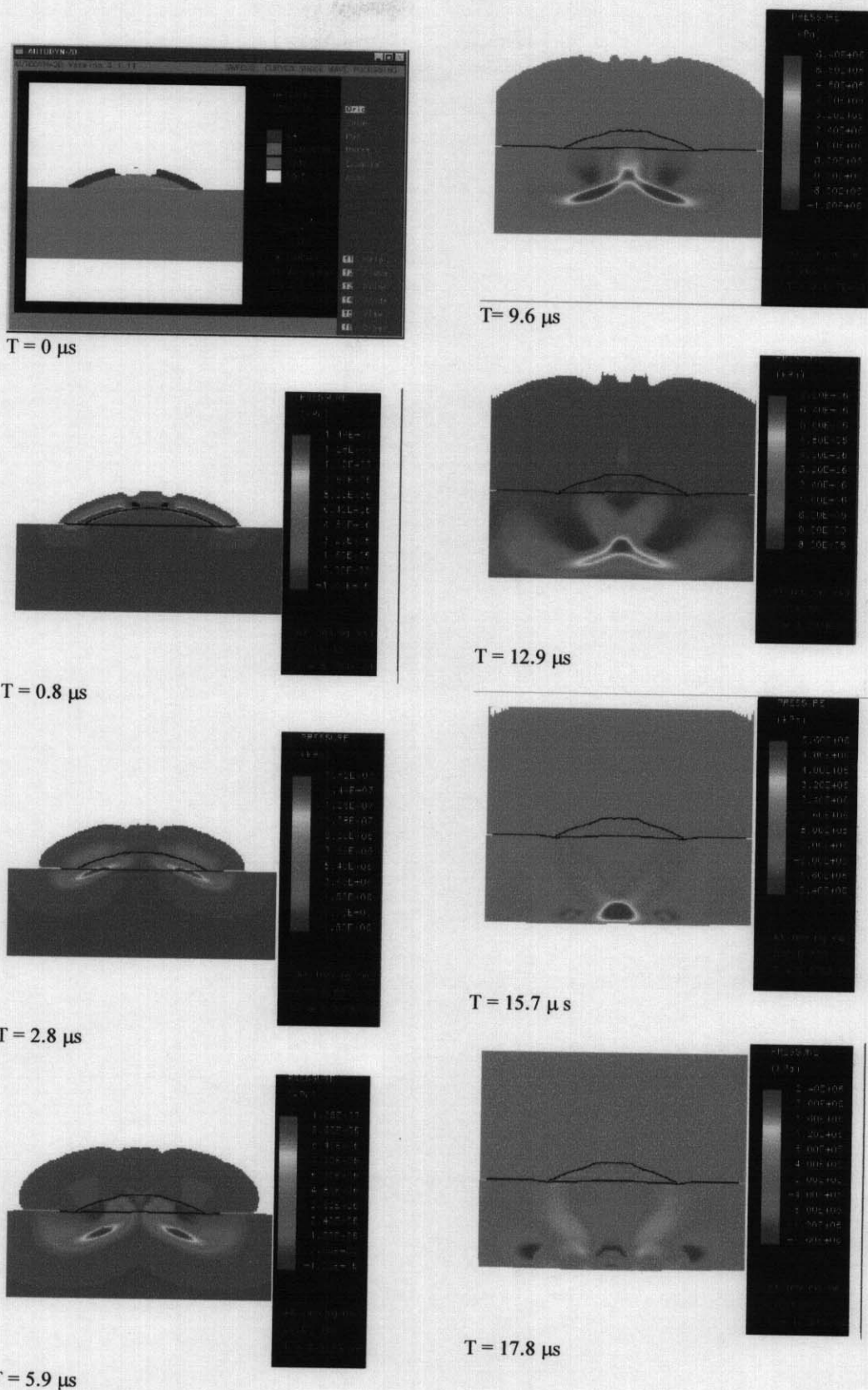


**Figure 3.6:** Sequence showing the development and interference of shockwaves for a steel waveguide Type 1 with CS = 40 mm.



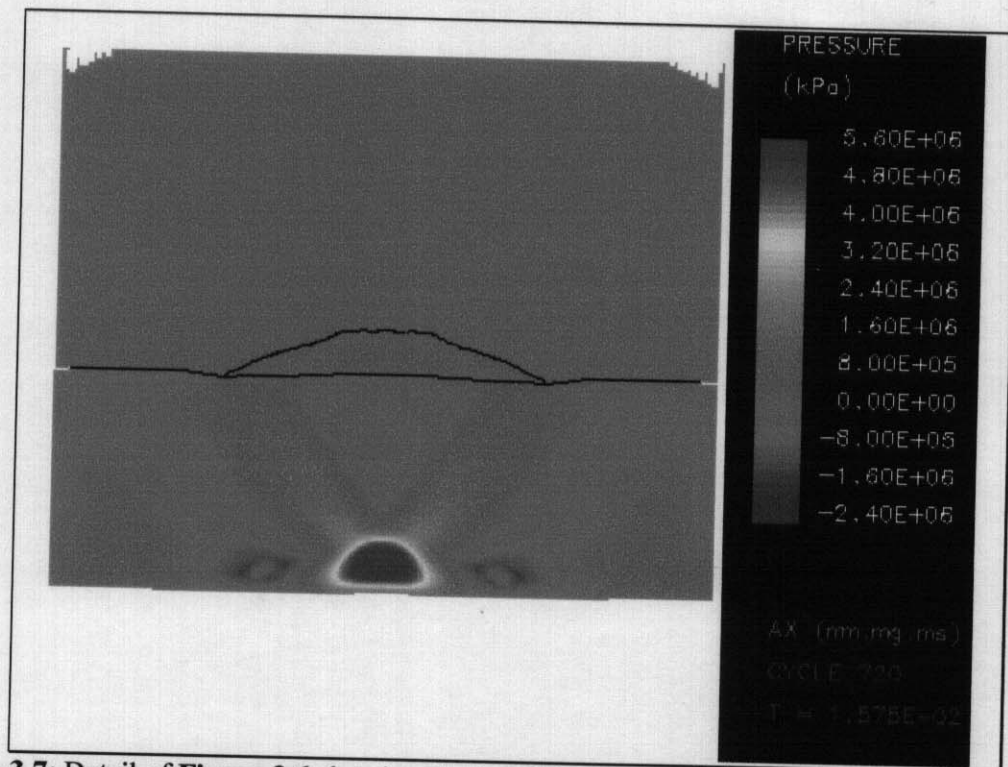


**Figure 3.7:** Detail of **Figure 3.6** showing the development of two separate regions subjected to tensile stress pulse ( $T = 15.7 \mu s$ ). Steel waveguide Type 1 with CS = 40 mm.

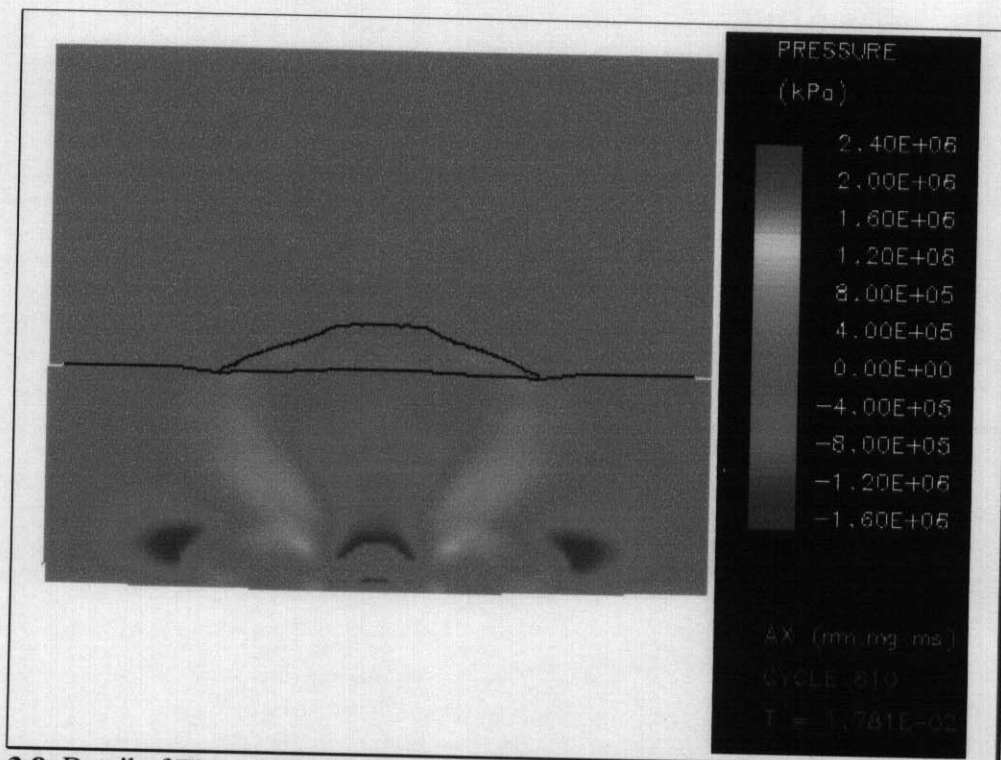


**Figure 3.8:** Detail of **Figure 3.6** showing the development of three separate regions subjected to tensile stress pulse ( $T = 17.8 \mu s$ ). Steel waveguide Type 1 with CS = 40 mm.

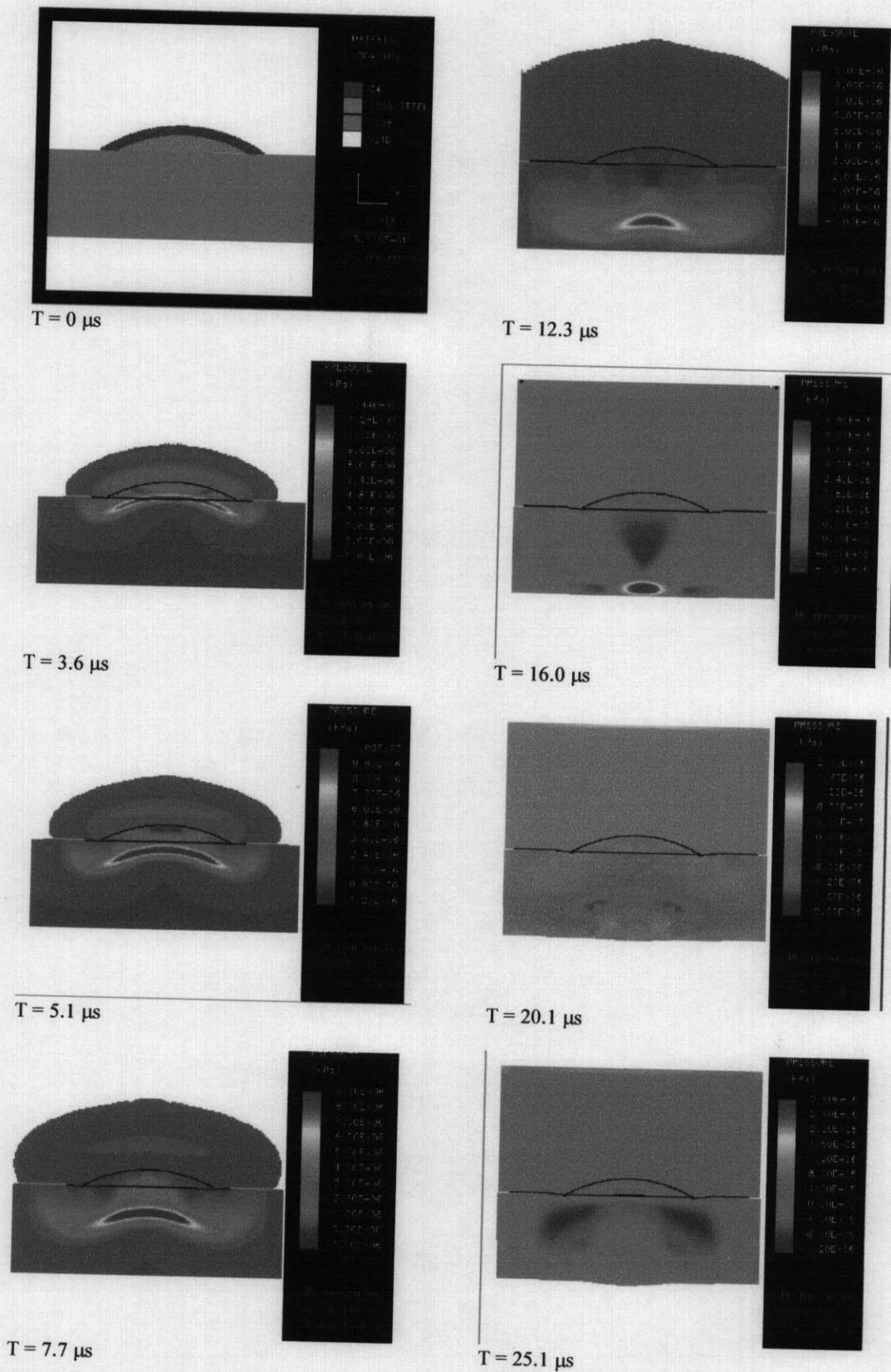


**Figure 3.9:** Sequence showing the development and interference of shockwaves for a steel waveguide Type 1 with  $CS = 0$ .



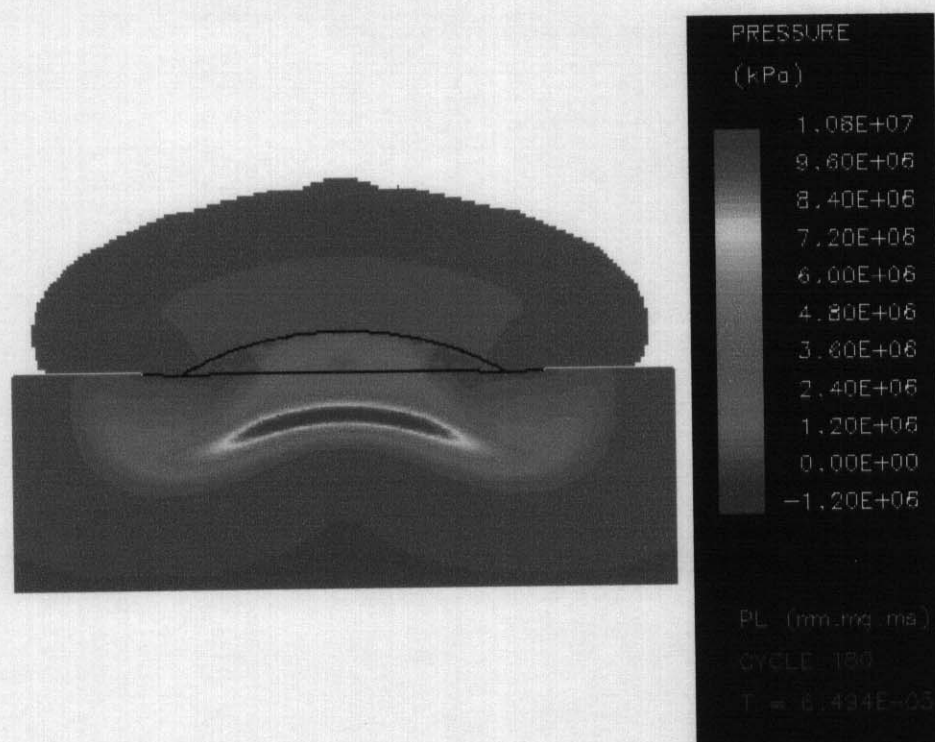


**Figure 3.10:** Detail from **Figure 3.9** showing the convergent nature of the shock front originated by a steel waveguide with CS = 0. ( $T = 6.5 \mu\text{s}$ )

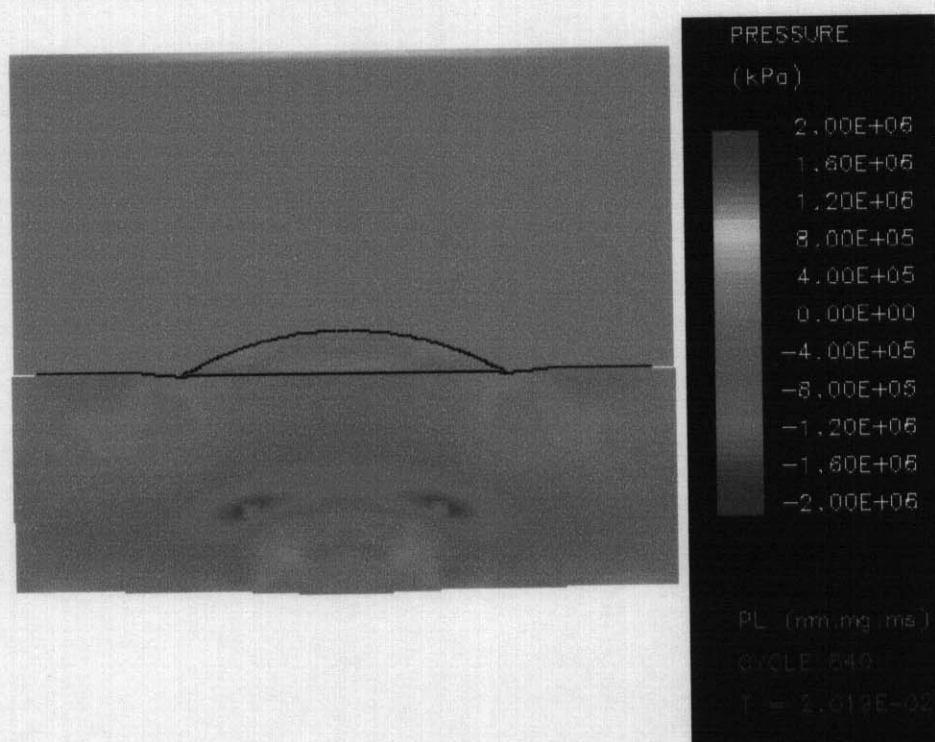
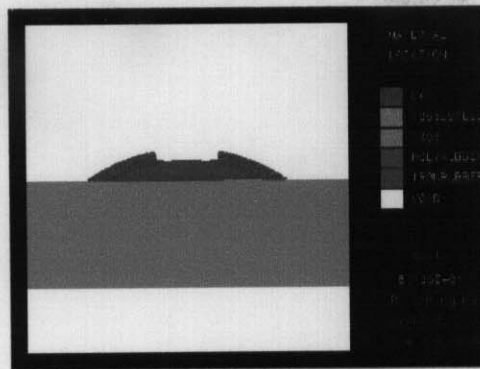
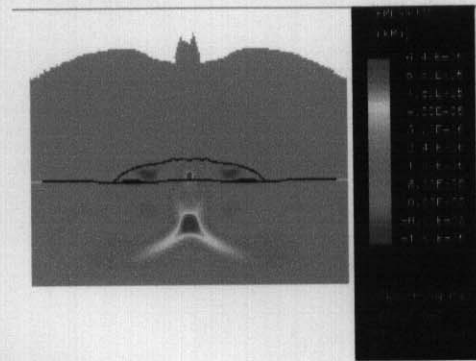


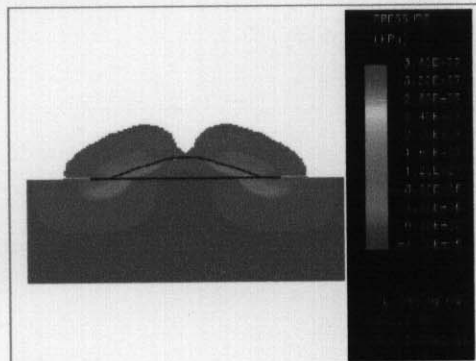
**Figure 3.11:** Detail from **Figure 3.9** showing the divergent nature of the reflected tensile stress pulse originated by a steel waveguide with CS = 0. ( $T = 20.1 \mu\text{s}$ )



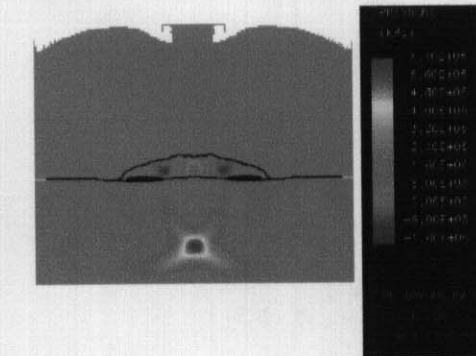
$T = 0 \mu s$



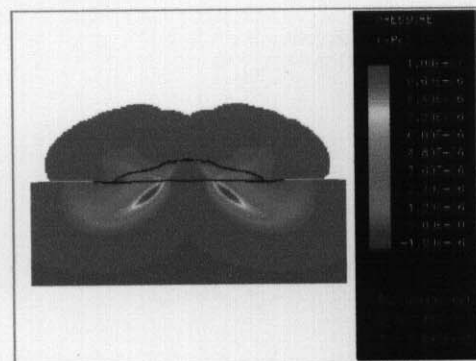
$T = 12.0 \mu s$



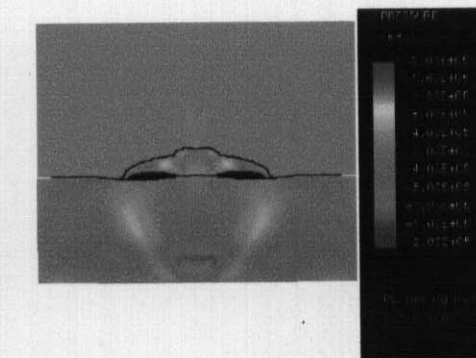
$T = 2.7 \mu s$



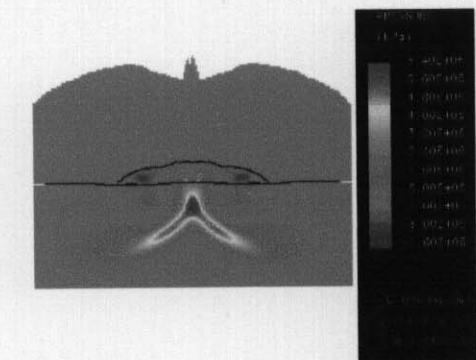
$T = 14.3 \mu s$



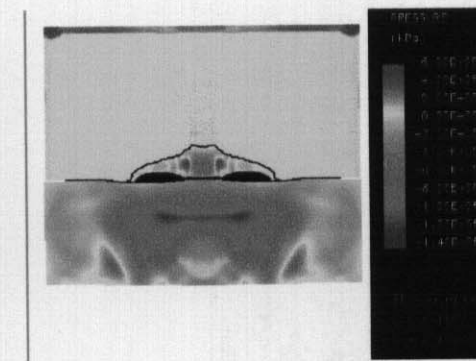
$T = 5.8 \mu s$



$T = 19.2 \mu s$



$T = 10.4 \mu s$



$T = 24.2 \mu s$

**Figure 3.12:** Sequence showing the development and interference of shock waves for a polymeric waveguide Type 1 using  $CS = 39 \text{ mm}$ .

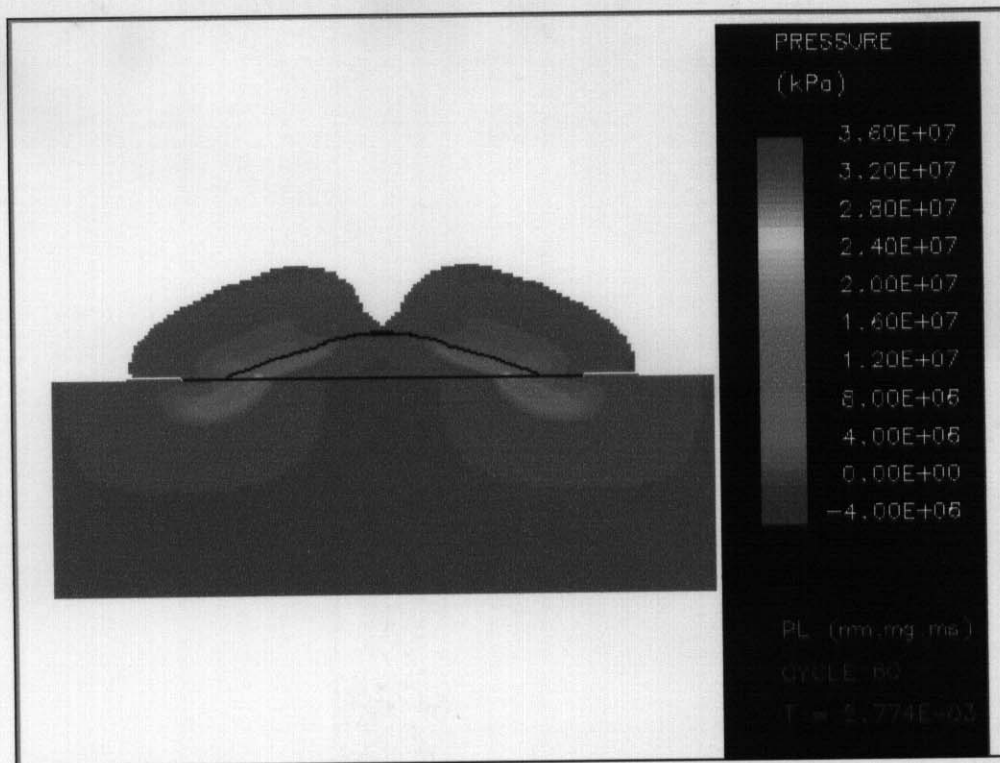


**Figure 3.13:** Detail from the sequence shown in **Figure 3.12** for  $T = 2.7\mu\text{s}$

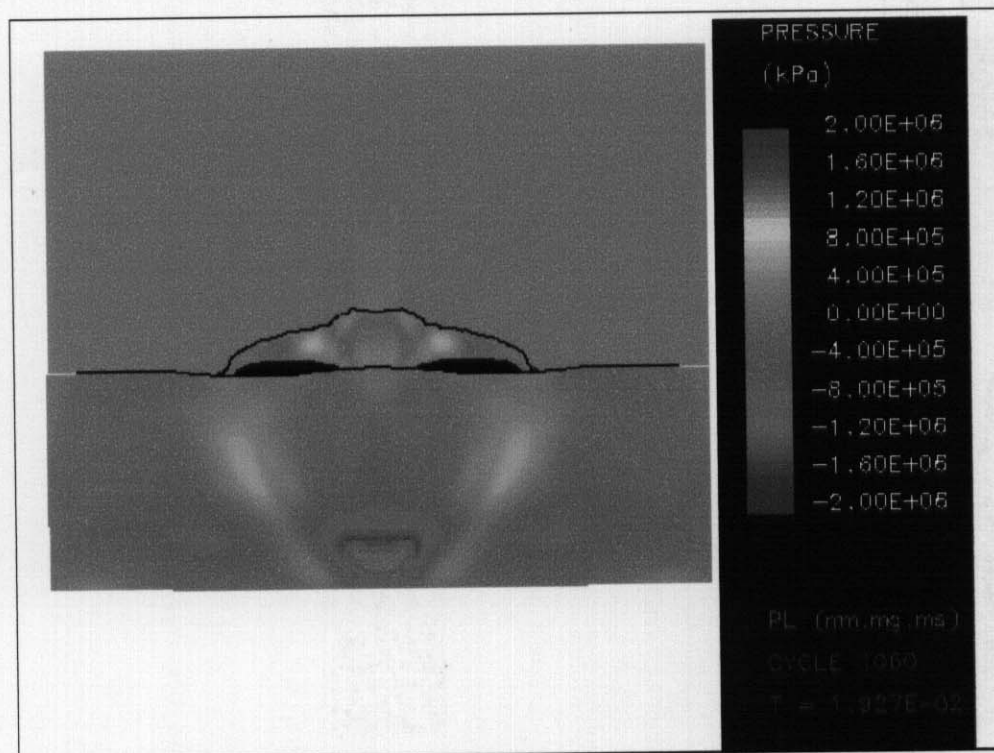


**Figure 3.14:** Detail from the sequence shown in **Figure 3.12** for  $T = 19.2\mu\text{s}$



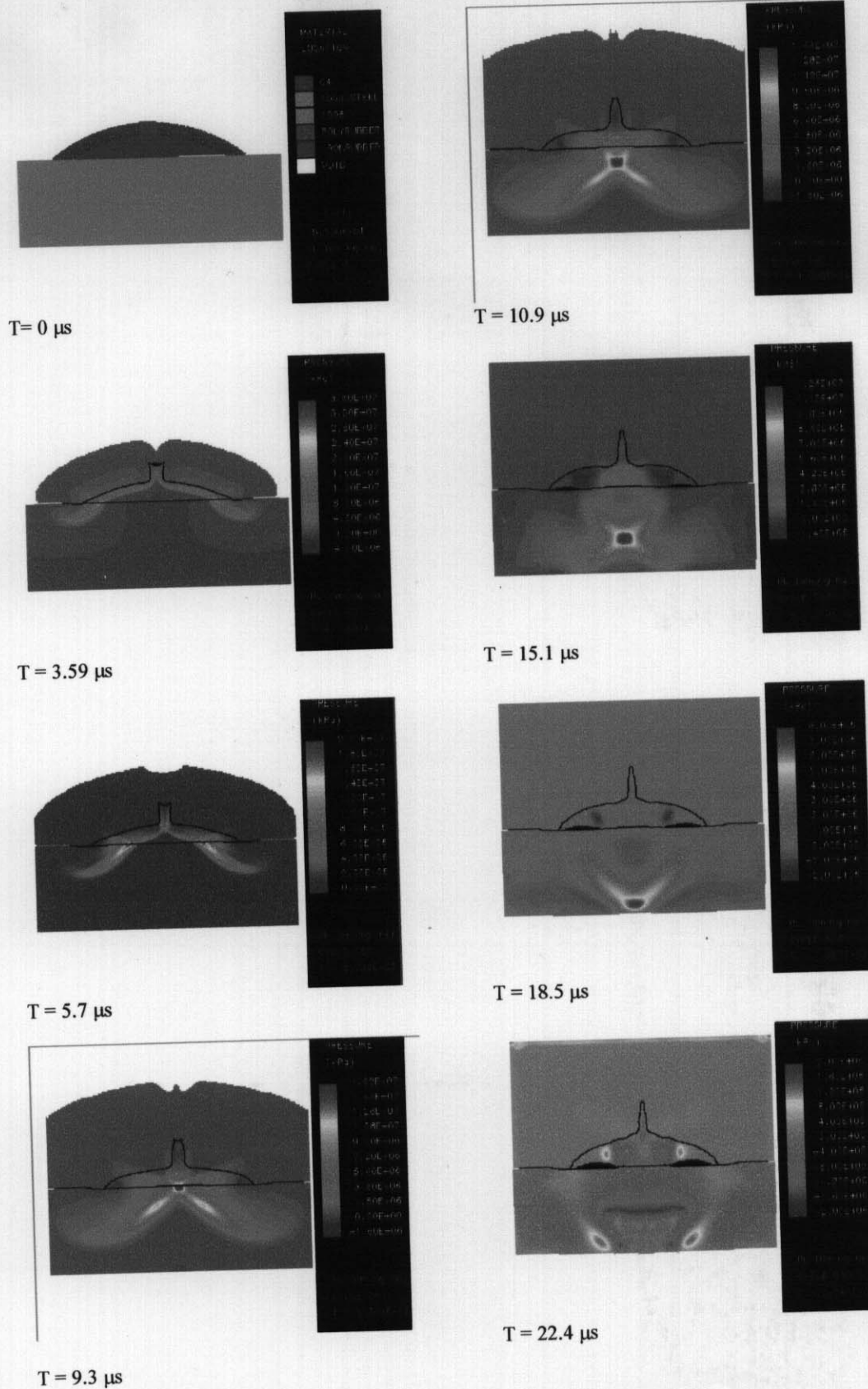


**Figure 3.15:** Sequence showing the development and interference of shockwaves using a polymeric waveguide Type 2 using CS = 10 % of waveguide width.

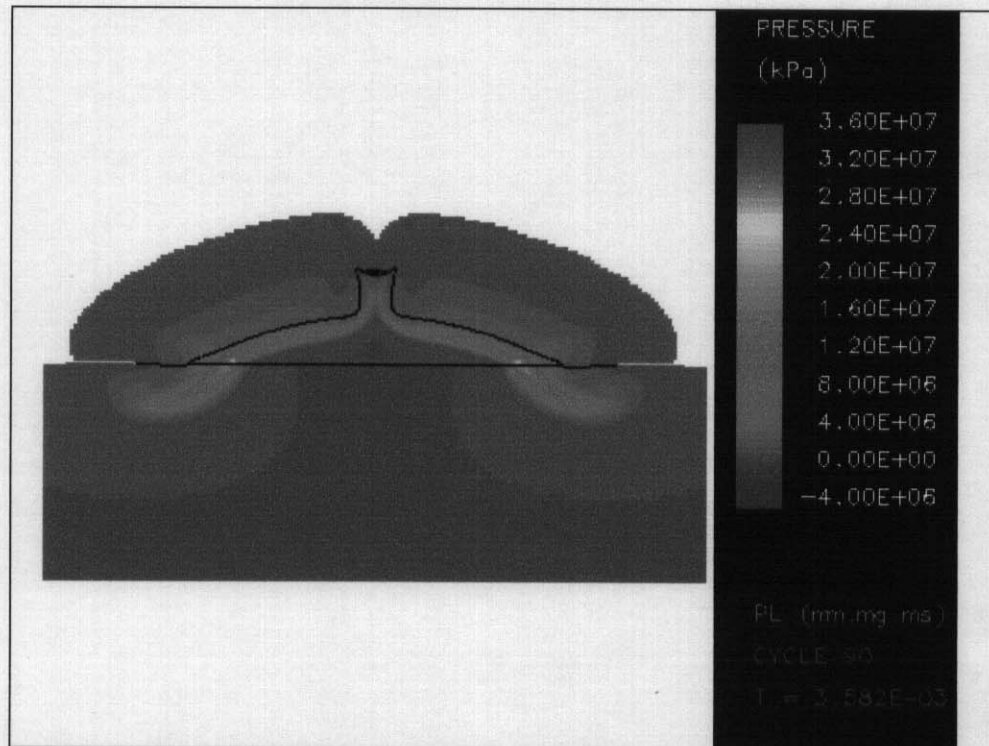


**Figure 3.16:** Detail from sequence shown in **Figure 3.15** for waveguide Type 2 using CS = 10 % of waveguide width.

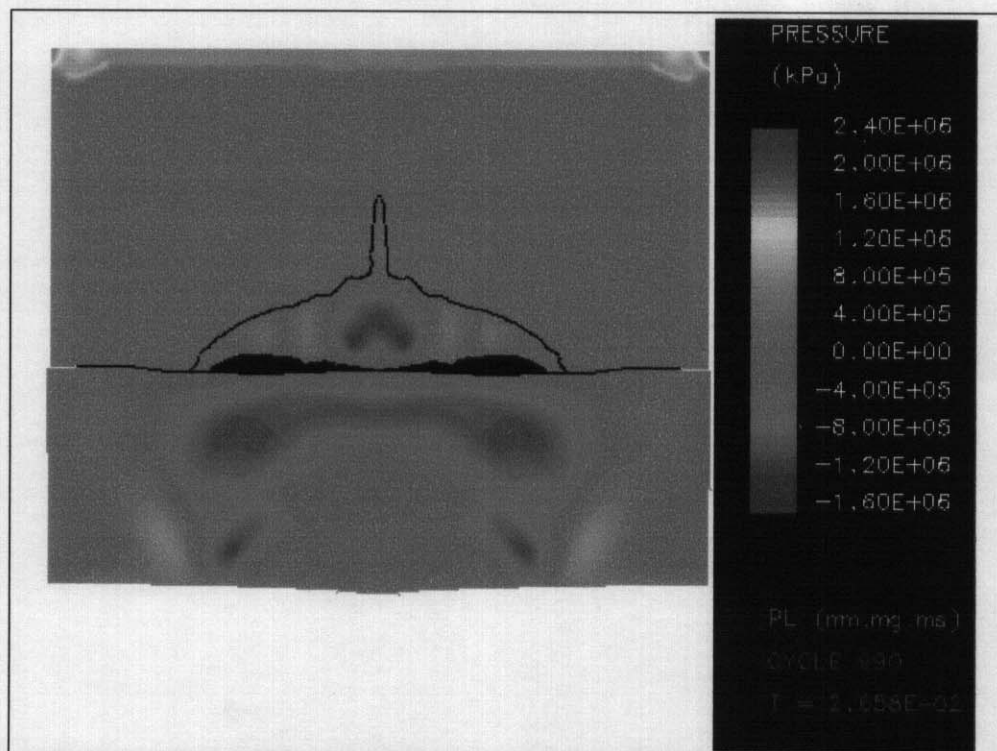


**Figure 3.17:** Additional slide for sequence shown in **Figure 3.15** for  $T = 26.5 \mu\text{s}$  waveguide (Type 2 using CS = 10 % of waveguide width).

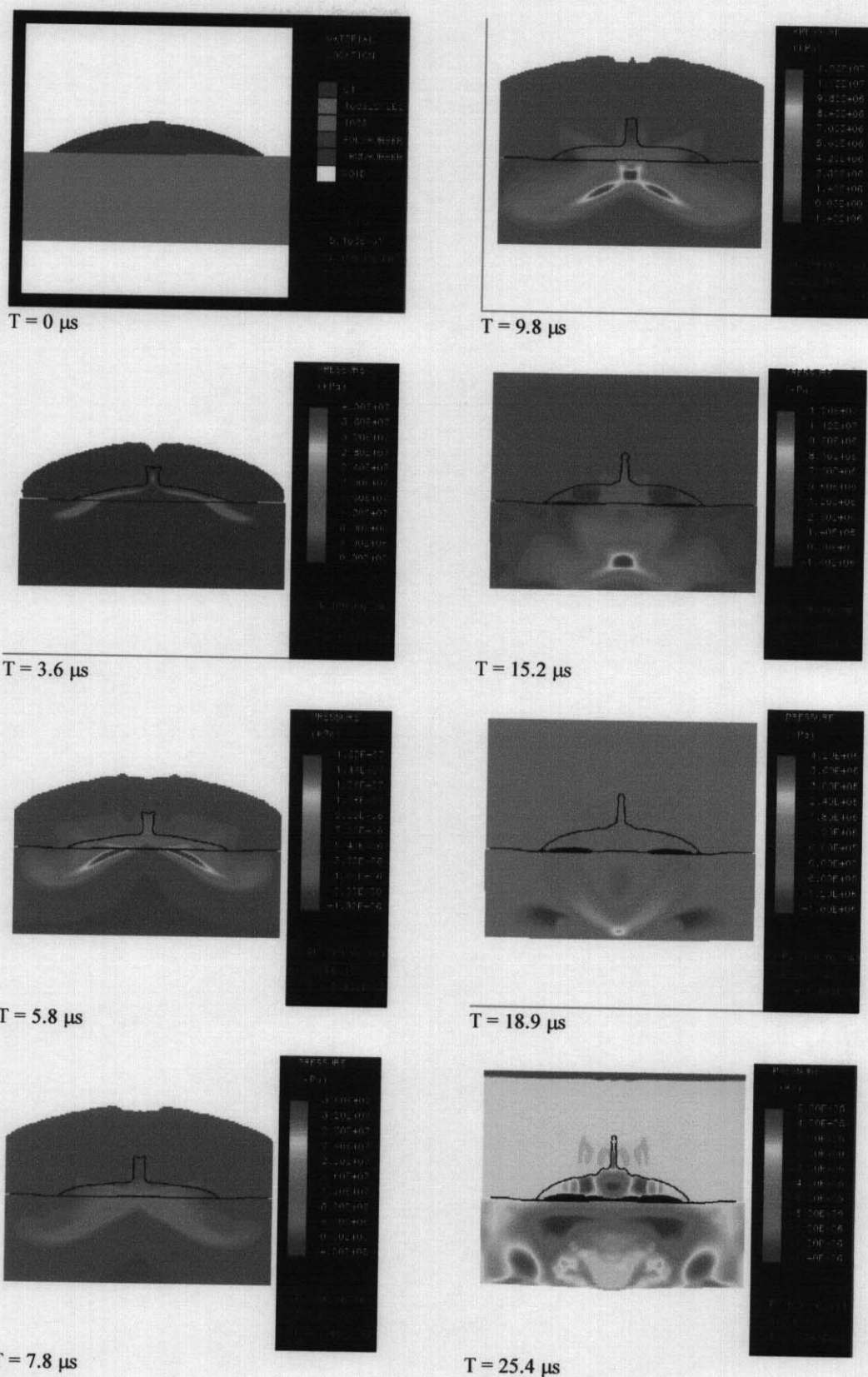


**Figure 3.18:** Sequence showing the development and interference of shockwaves using polymeric waveguide Type 3 with 9 mm RDX based explosive.



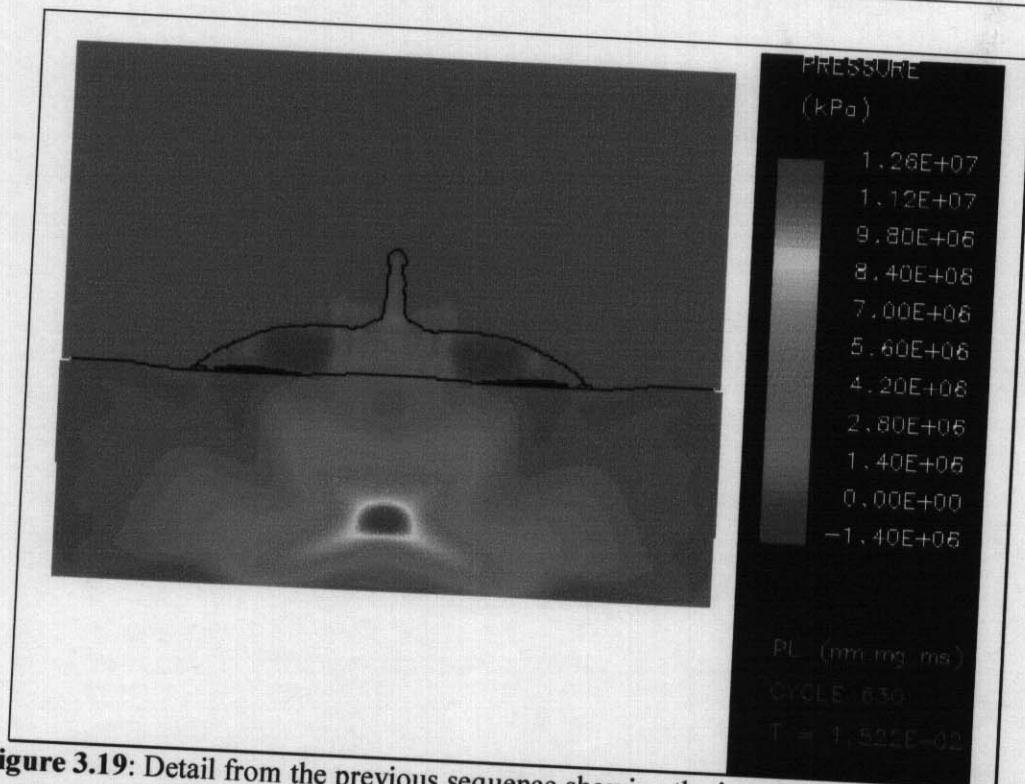


**Figure 3.19:** Detail from the previous sequence showing the interference of incident shock waves at  $T = 15.2 \mu\text{s}$

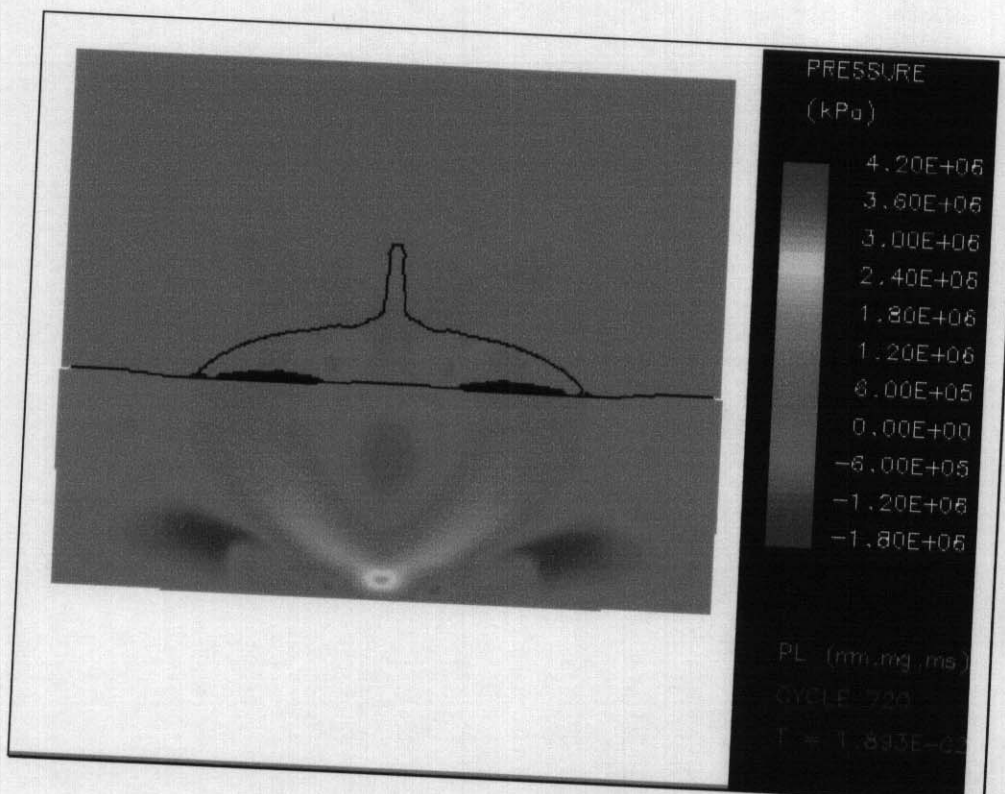


**Figure 3.20:** Detail from previous sequence showing that the initial stages of reflection, and a tensile tail behind the remaining incident shockwave. Note the tensile values of 1.8 GPa.

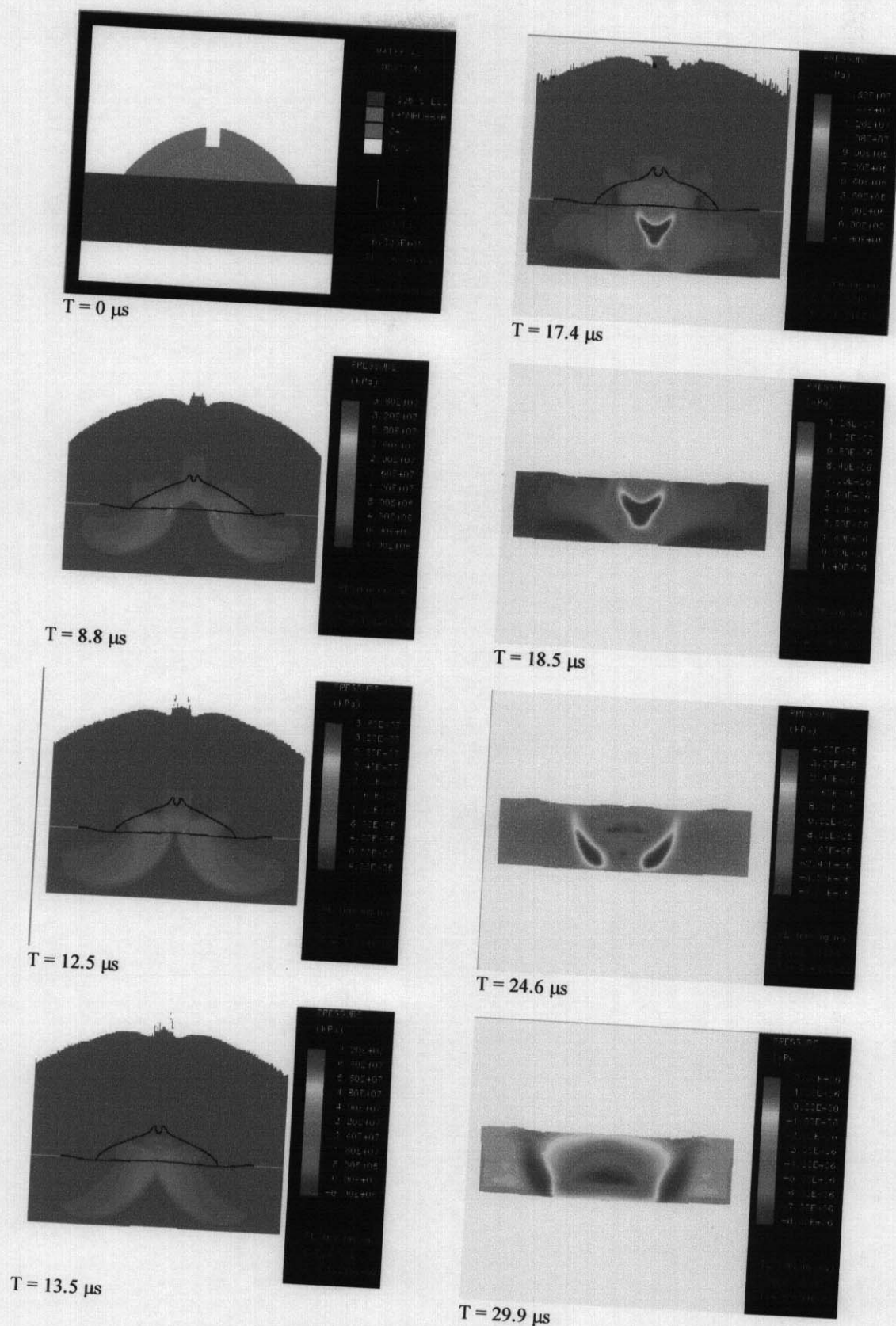


**Figure 3.21:** Sequence showing the development and interference of shockwaves using polymeric waveguide Type 4 with 18 mm RDX based explosive.



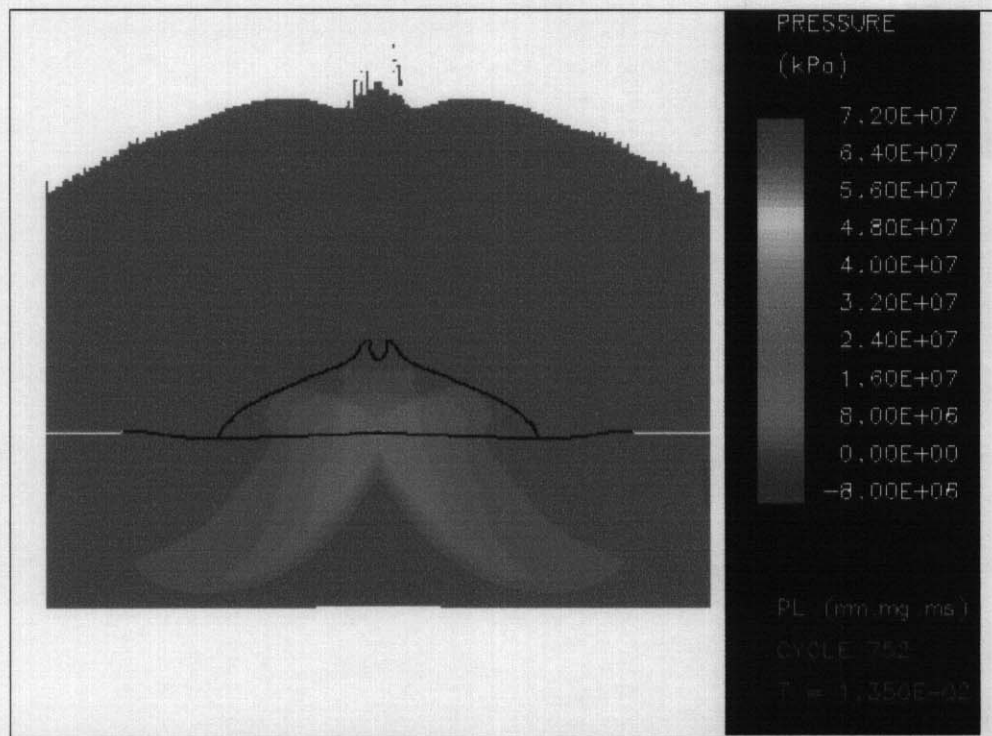


**Figure 3.22:** Detail from the previous sequence showing the interference of incident shock waves at  $T = 13.5 \mu\text{s}$ , Note the value of 72 GPa at the meeting point.

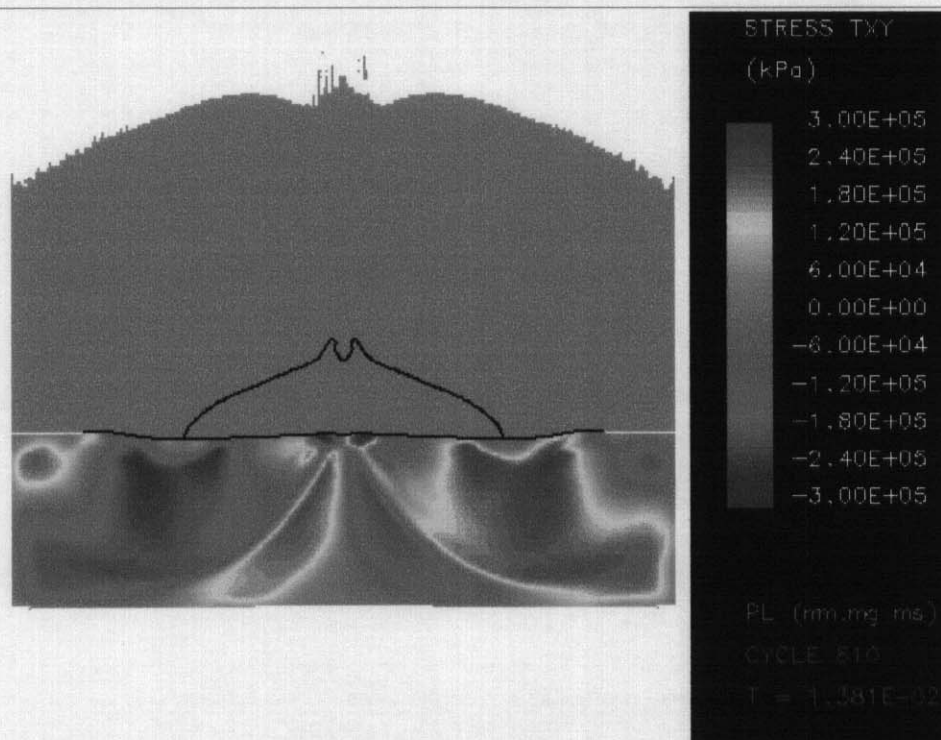


**Figure 3.23:** Associated shear stress immediately after the region of interference shown in the previous picture is transmitted to the target.

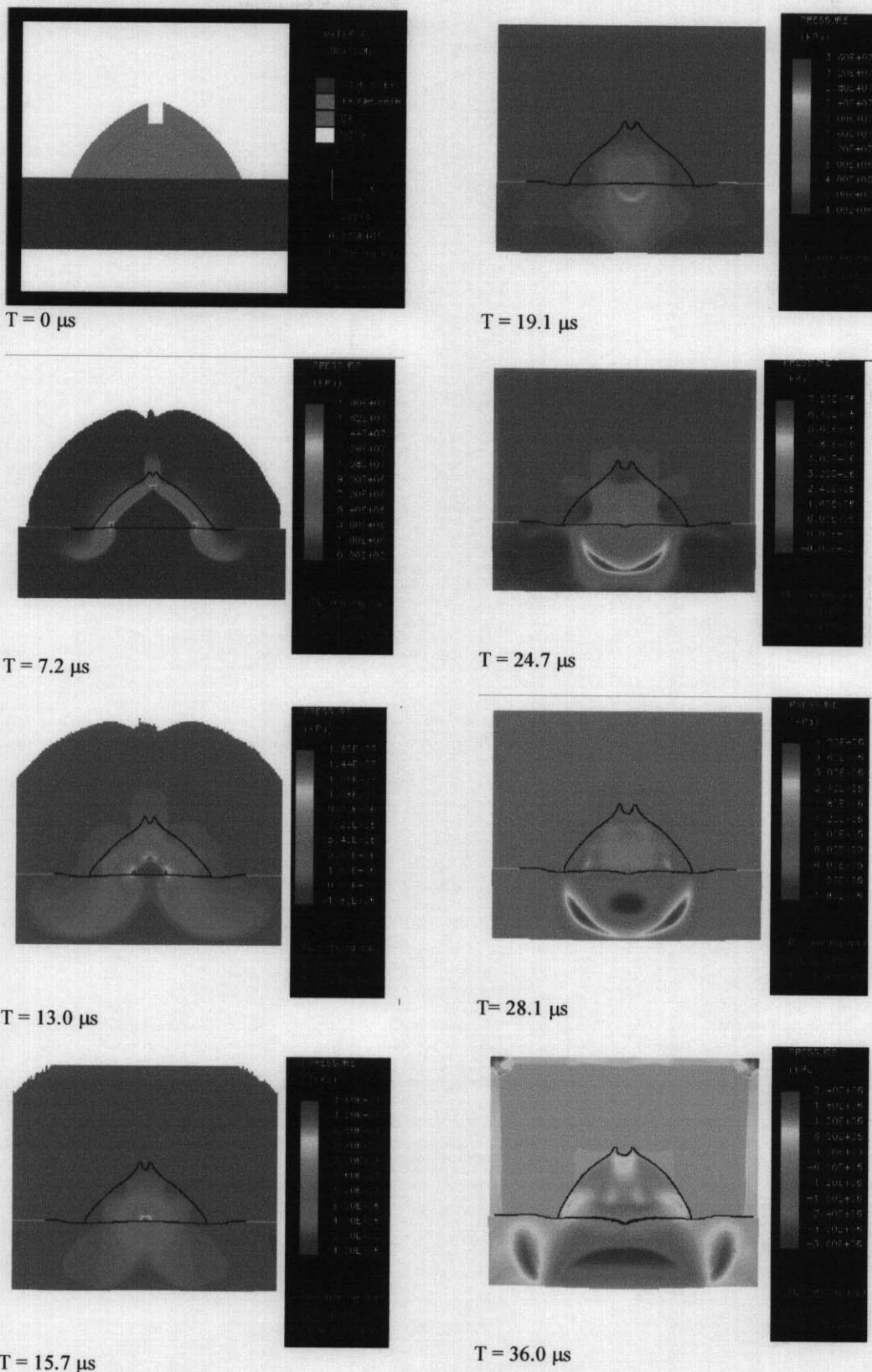


**Figure 3.24:** Sequence showing the development and interference of shockwaves using polymeric waveguide Type 5 with 18 mm RDX based explosive.



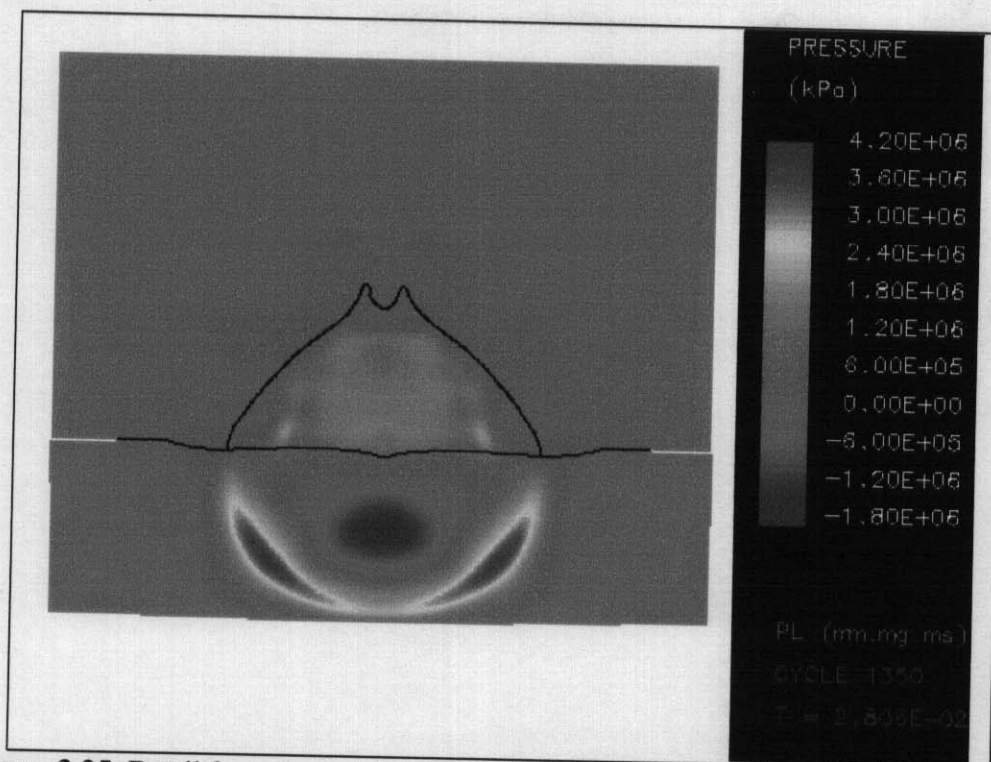


**Figure 3.25:** Detail from the previous sequence showing the interference of incident shock waves at  $T = 28.1 \mu\text{s}$ , Note that the incident shock waves pass each other before reflection.

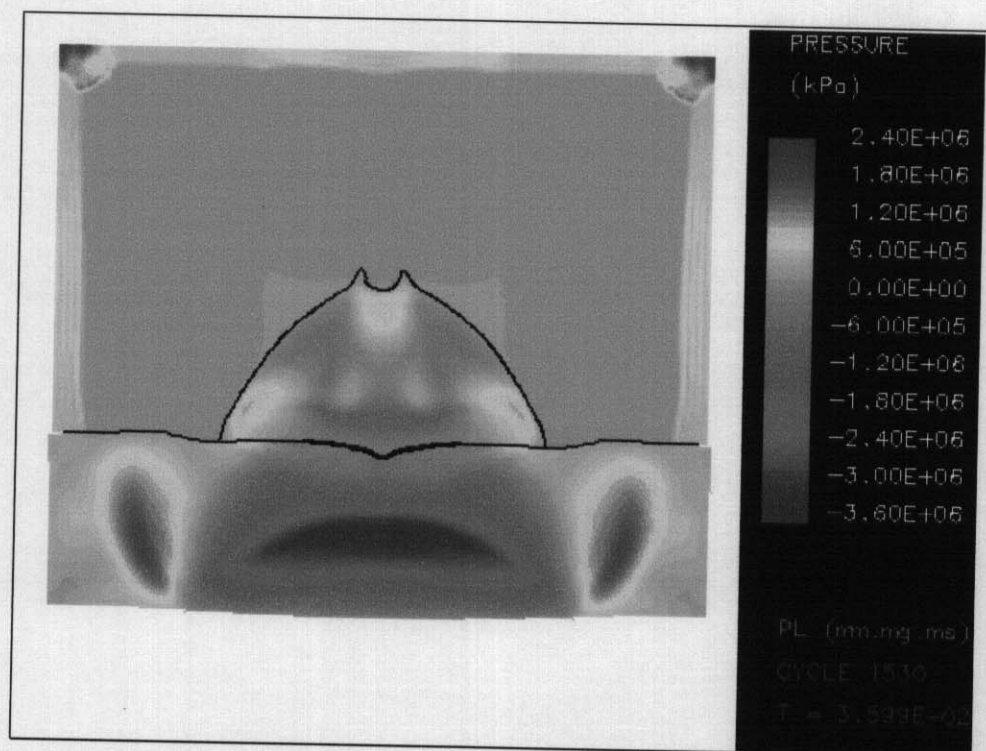


**Figure 3.26:** Detail from previous sequence showing that the initial stages of reflection, and a tensile tail behind the remaining incident shockwave. Note the tensile values of 3.6 GPa.

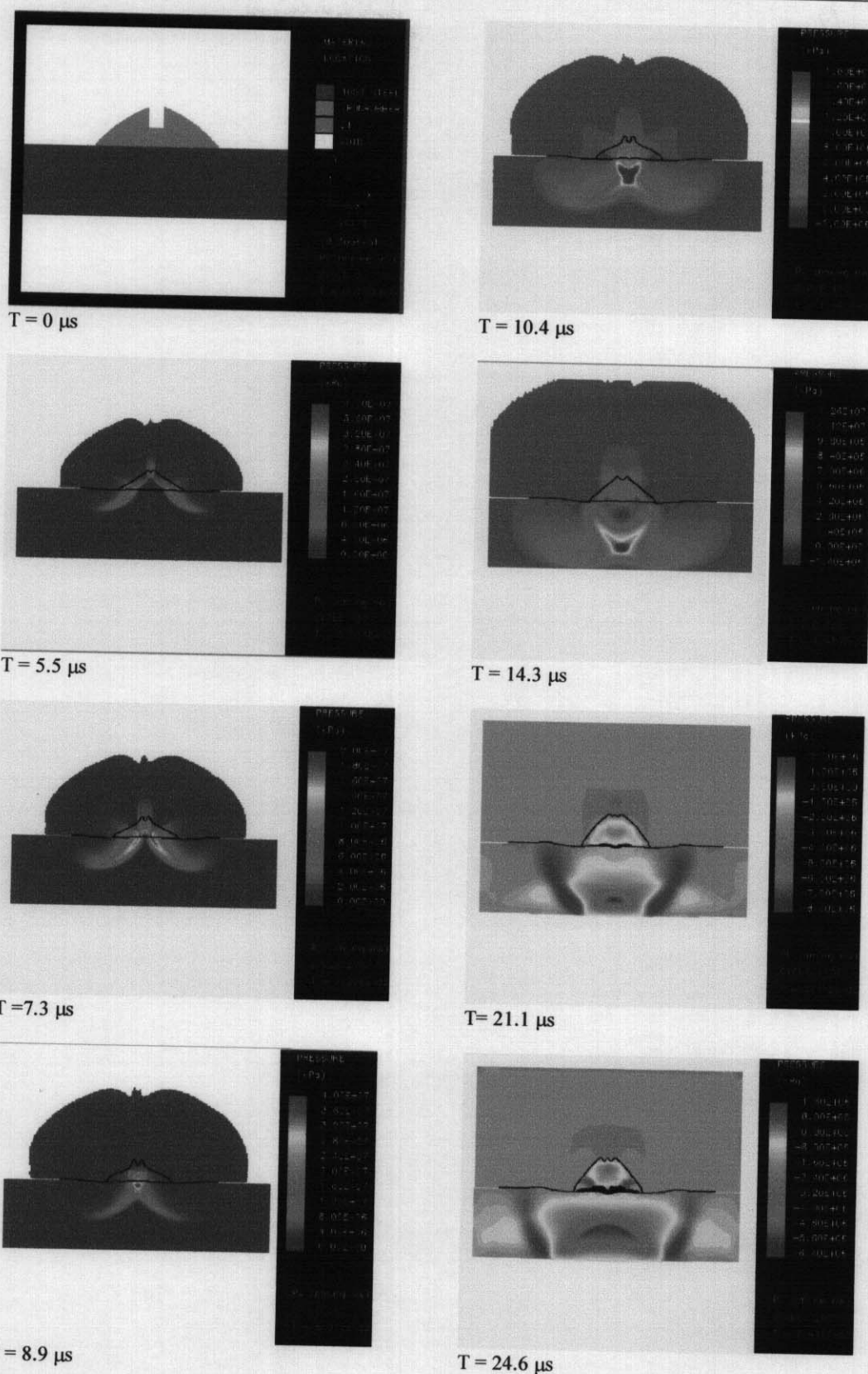


**Figure 3.27:** Sequence showing the development and interference of shockwaves using polymeric waveguide Type 6 with 18 mm RDX based explosive.



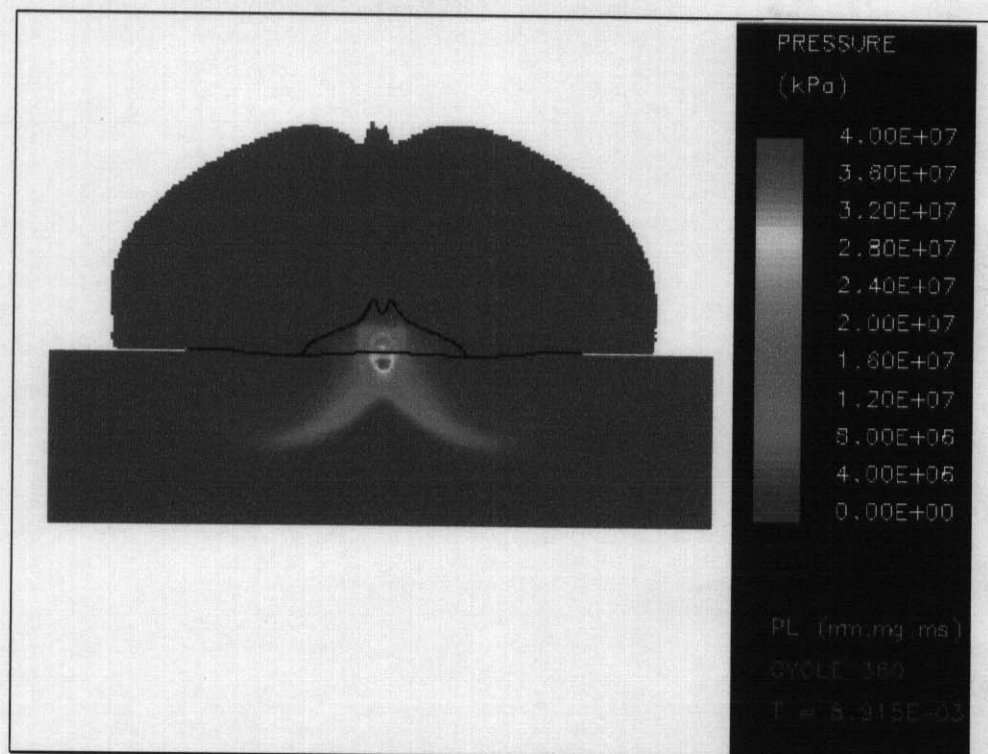


**Figure 3.28:** Detail from the previous sequence for  $T = 8.9 \mu\text{s}$ , showing a values of 40 GPa at the target top interference zone.

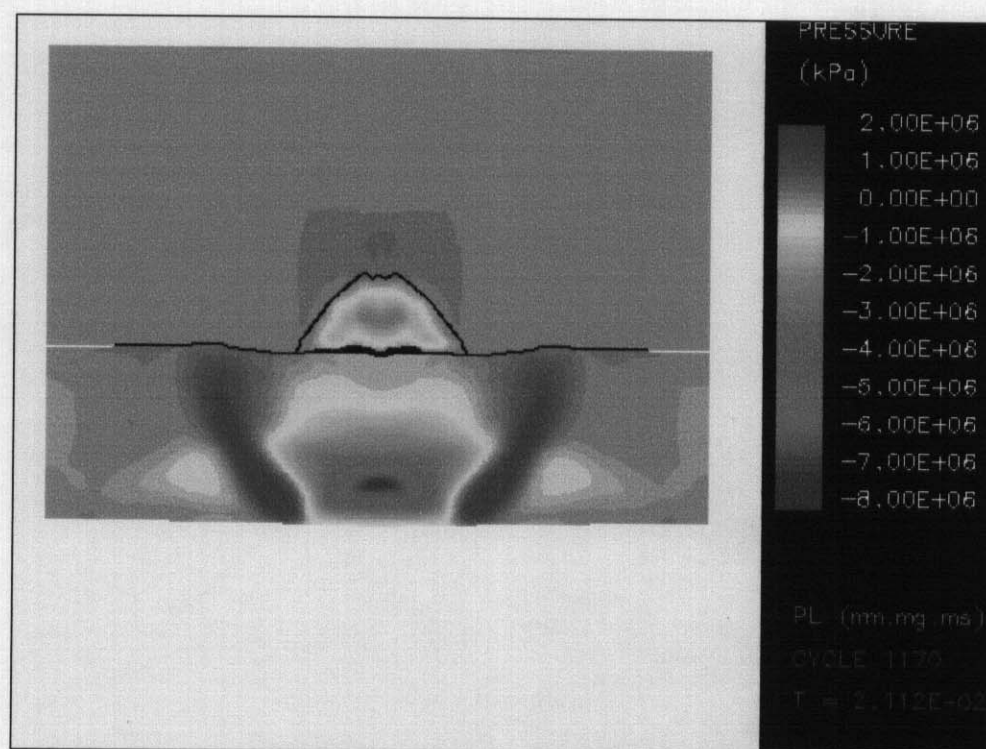


**Figure 3.29:** Detail from the previous sequence for  $T = 21.1 \mu\text{s}$ , showing a values of -8 GPa at the target back-face.

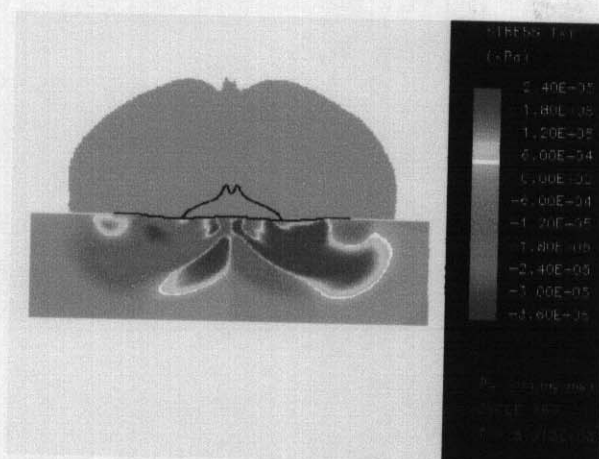


Figure 3.30: Shear stress profile for waveguide Type 6 at  $T = 8.9 \mu\text{s}$

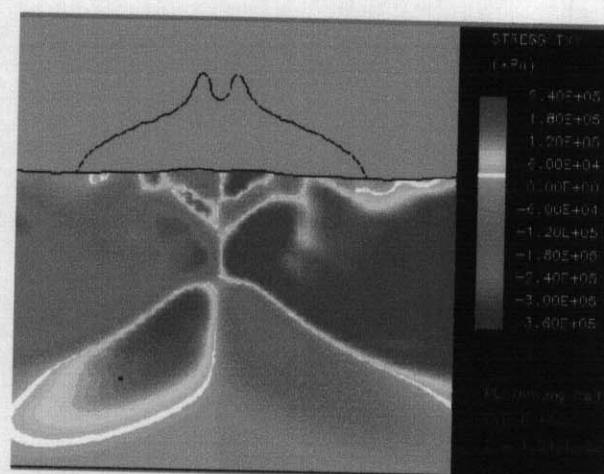


Figure 3.31: Shear stress profile for waveguide Type 6 at  $T = 10.4 \mu\text{s}$

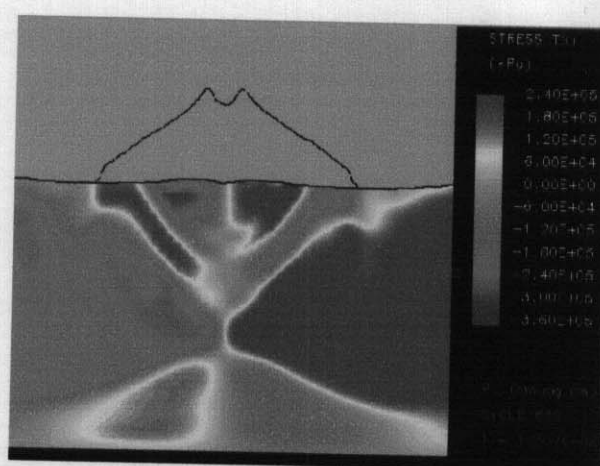
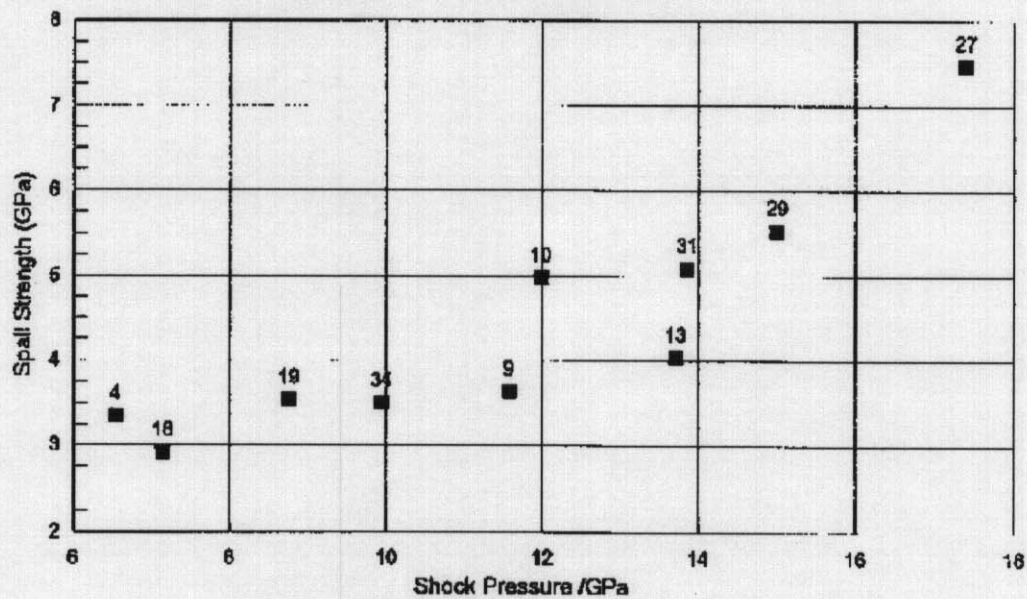
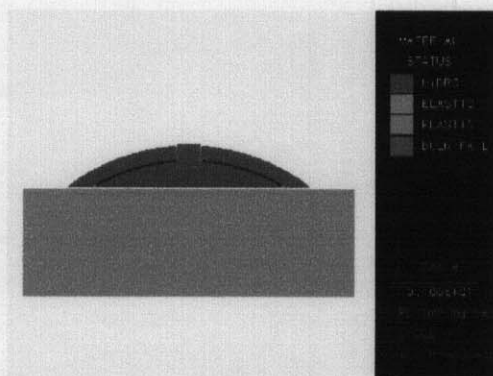


Figure 3.32: Shear stress profile for waveguide Type 6 at  $T = 13.0 \mu\text{s}$





**Figure 3.33:** Spall strength x Shock pressure for BS 4360 – 50D steel. Numbers above each experimental point refer to trial reference number.



**Figure 3.34:** Waveguide type 2, with a 9 mm explosive layer.

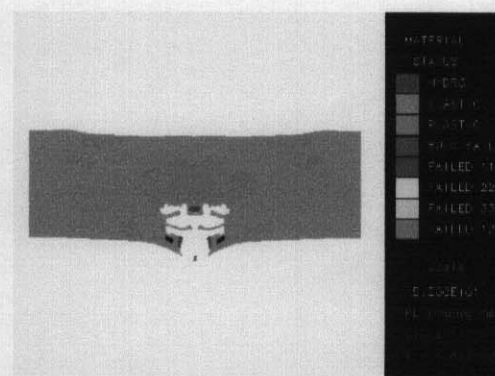


**Figure 3.35:** 68.3  $\mu$ sec, final cycle for the set up showed in Figure 3.34.

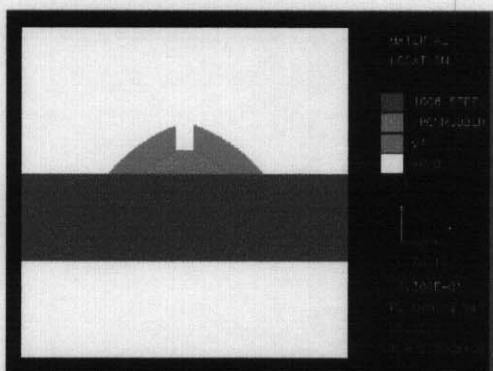


**Figure 3.36:** Waveguide Type 6 with an 18 mm of explosive layer.

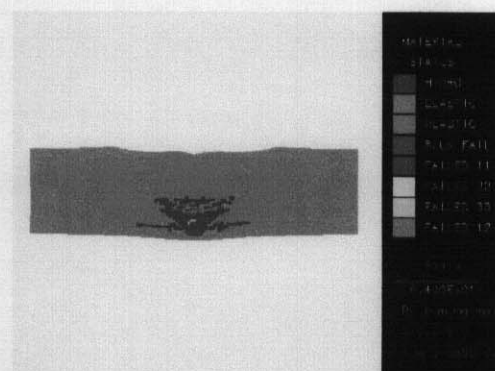


**Figure 3.37:** 30.8  $\mu$ sec, final cycle for the set up showed in Figure 3.36 using shear strength = 1.65 GPa.

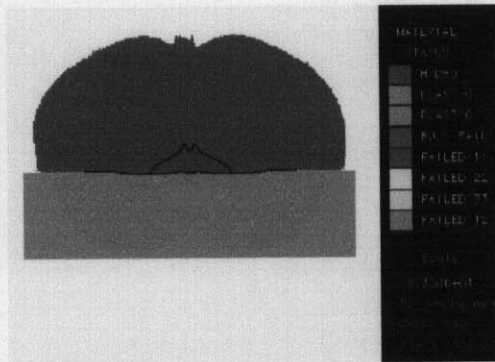


**Figure 3.38:** 11.7  $\mu\text{sec}$ , for the set up showed in **Figure 3.36** using shear strength = 330 MPa.

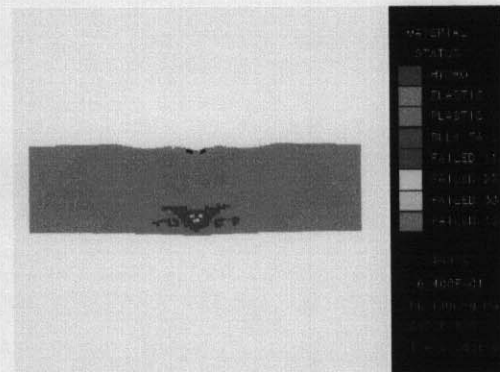


**Figure 3.39:** 23.8 msec, for the set up showed in **Figure 3.36** using shear strength = 330 MPa.

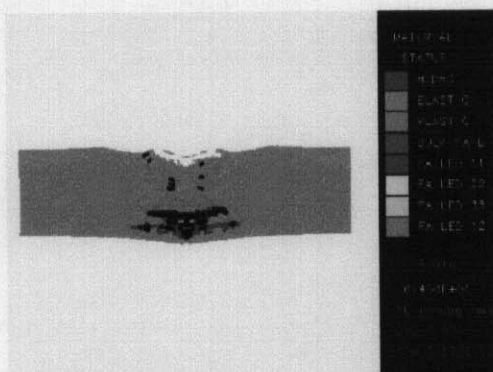


**Figure 3.40:** 35.7  $\mu\text{sec}$ , for the set up showed in Figure 5.37 using shear strength = 330 MPa.

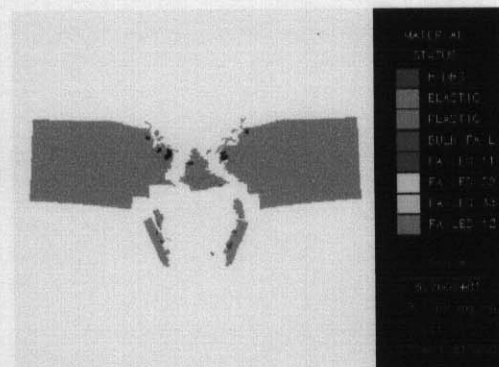


**Figure 3.41:** 181  $\mu\text{sec}$ , for the set up showed in Figure 5.37 using shear strength = 330 MPa.

## 4 Experimental Programme

### 4.1 Introduction

This section describes the analyses of specimens from tests performed for the development of the SWF technique as part of the THERMIE - EXCUT Project [14], and analyses the work of Al-Hassani and Burley [4][19]. The experimental work is described in this report for completeness and to assist in the understanding of the proposed “cutting window” where the SWF charge reliability is comparable with more established explosive cutting techniques.

### 4.2 Charge Design

By examining the work of Al-Hassani and Burley [4][19], it was possible to identify waveguides of similar geometry that cut and fail to cut, and also identify waveguides of quite different geometries that successfully cut 43A or similar steels. Considering these findings, it was decided to pay particular attention to the peripheral variables capable of jeopardising the waveguide performance and to reduce the overall number of variables.

To reduce the number of variables the explosive type was kept constant in the majority of the tests. The Royal Ordnance SX2 explosive was selected for most of the tests due to its excellent formability and previous good results. SX2 is an RDX based explosive (88% RDX and 12% plasticiser); it has a density of  $1.63 \text{ g cm}^{-3}$  and it is supplied in 3 mm thick flexible sheets.

Eight different waveguide geometries were designed and tested using different explosive loads according to the target material. Different combinations of waveguide geometry, anvils, and target materials have resulted in 24 tests on plates and 10 tests on curved plates and full tubulars.

The variables that were identified as being able to affect the waveguide performance (on plates) in the beginning of the work are:

- Waveguide geometry
- Waveguide width / Target thickness ratio
- Waveguide material properties
- Waveguide density
- Target material
- Target dimensions
- Target geometry
- Explosive thickness
- Explosive load

- Booster
- Initiation device for plates
- Synchronisation between the two sides of the explosive charge
- Adhesive used between explosive layers
- Anvil material
- Anvil offset
- Target Surface condition
- Confinement condition
- Relative position of the waveguide to the rolling direction

Two additional variables were identified during the testing programme:

- Size of the waveguide explosive free area
- Confinement by the explosive on the edges of the waveguide.

#### 4.2.1 Waveguide Geometry Design

The present work bases its design on a waveguide designed by Al-Hassani and Burley [4] that had partially cut a 65 mm plate made from 43A steel. This waveguide design is referred to as waveguide Type 1.

The geometric variables of the waveguide meant that often one parameter could not be changed without affecting another. This resulted in a difficult evaluation of the relative significance of a specific parameter, especially in the absence of a clear definition of how the fracturing phenomenon was operating. Eight different designs were initially considered. Due to the failure of Type 3, the Design type 7 was not tested and is not discussed in this work.

The initial design guidelines were provided by analysing the dimensionless plots from the results of [4][19] shown in **Figure 2.31** and **Figure 2.32**. The guidelines were also based on the possibility of applying the principles of stress wave focusing investigated by Al-Hassani and Silva Gomes [58], to fracturing belts and flat waveguides. This led to the design of waveguide Types 2 and 3 where the main design variables are:

- Radius of the waveguide
- Width of the waveguide
- Offset position of centre of curvature
- Explosive thickness

With the possibility of modelling the propagation and interference of stress waves using the AUTODYN code and in possession of new experimental results, the guidelines were continuously refined during the experimental work to take into account the new information generated. The numerical modelling and the proposed phenomenological description of the fracturing process are given in Section 5.

The design motivations are discussed in the test descriptions and a further discussion is given in Sections 5 and 6. All seven waveguide types were tested in air on plates. Curved plates were tested in air with two waveguide types (Type 4 and 6). Full tubulars were tested in air and under water using waveguide Type 6.

### **4.3 Experimental Design**

#### **4.3.1 Introduction**

The explosive type, waveguide material and initial design were selected from Al-Hassani and Burley [4][19]. The manufacturing procedures were improved and standardised for the production of the waveguides. This improved and standardised procedure was denominated “standard procedure”. The waveguide material selected consisted of a random composite of iron powder (120-mesh size) and polyurethane elastomer. This procedure produced dimensional accuracy, homogeneity, and reproducibility of properties, minimising the influence of peripheral variables like bubbles and segregation of the iron powder.

Different techniques used to produce the moulds are described below. These techniques proved to influence the dimensional accuracy of the final waveguide. Later this dimensional accuracy seemed to be over-designed and it was relaxed by the use of plaster moulds. A technique to produce curved waveguides using flat moulds is also described. This technique avoids the use of different moulds for different target diameters.

#### **4.3.2 Charge Manufacture**

##### **4.3.2.1 Mould manufacture**

###### **4.3.2.1.1 Laminated Moulds**

The first moulds were constructed from glass fibre reinforced polyester resin (GRP) laid up over a suitable pattern. In the early stages this was simply a length of standard metal or plastic piping around which the mould was shaped. All joints were then filled and sealed and the working faces were given several layers of mould release wax, each layer was polished and allowed to harden before the application of the next layer.

The GRP was then laid onto the pattern without a gel coat using standard techniques. The mould was then released from the pattern, it was allowed to stay at room temperature for 24 hours and subsequently it was post-cured in an oven at 60° for 16 hours. This allowed the mould to achieve full strength, thereby reducing the risk of damage when de-moulding. It also removed any residual styrene, which might have been contained in the waveguide.

The main body of the mould was completed with the addition of end closures and a perforated lid was made from Perspex. The end closures were fixed in place using nuts and

bolts and a clamping mechanism was made to hold the lid in place. This type of mould allowed for alteration of the waveguide geometry by altering the width of the lid. The polyurethane/iron powder mixture was poured into the mould using the mould in the horizontal position, so as the excess mixture could escape by the perforated lid.

As more precision was required to eliminate a possible variable, it was necessary to manufacture a pattern to serve as a model for the mould. For this purpose several layers of medium density fibreboard (MDF) were cut approximately to the desired shape and fixed with a threaded steel bar running through the centre. This assembly was put into a lathe and turned to the required diameter. The surface was then sealed with polyester resin and when this hardened the assembly was again turned to size to give a well-consolidated surface. The assembly was then transferred to a miller and diametrically opposed and parallel flats were machined.

Side shutters were then added and fixed and the whole assembly was sawn in half to provide two identical patterns. The addition of the removable end plates and surface waxing made the pattern ready for lamination. Once the body of the mould was ready, one end plate was added and a fixed lid was bolted in place thus allowing the resins to be poured in from one end.

#### 4.3.2.1.2 PVC Moulds

As the cutting charge performance proved to be less sensitive to small variation of dimensions than to other factors, it was decided to simplify the mould construction by fabricating it from sections of PVC pipe. The pipe sections were machined to size and welded together. Stiffeners were used to avoid distortions during handling and to resist the thermal cycle imposed by the waveguide curing. A lid and one end closure were added in the same manner as in the laminated moulds. Although conceptually simple, the moulds proved to be difficult and time consuming to make. Also their durability was reduced.

#### 4.3.2.1.3 Machined Plaster Moulds

Machined plaster moulds proved to be the easiest way to achieve dimensional accuracy in a relatively economical and fast way. Plaster was chosen because it is cheap, and during curing it has a period when it is easily machinable. A large block of plaster was cast (typically 700x150x200 mm) and as soon as this had sufficient strength to be handled, it was transferred to a milling machine and made flat, square and parallel. The plaster was left to continue curing. Whilst the plaster was still soft the bulk of waveguide shape was machined using a slow cutting speed. After the plaster had been fully cured a final machining was carried out using a template of the desired waveguide as a cutting tool.



#### 4.3.2.1.4 Cast Plaster Moulds

The necessity of repeating experiments with the same waveguide shape and the success of plaster as a mould material led to the simple solution of making a mould from an existing waveguide that was left to be used as template.

#### 4.3.2.2 Waveguide Manufacture

Most waveguides were cast in polyurethane elastomer/iron powder composite. Baxenden Chemicals resin polyurethane ES742 was chosen based on the experience of Al-Hassani and Burley [4]. The elastomer is a three parts mixture designated Resin 1, Resin 2 and Isocyanate component.

It is possible to vary the hardness of the final mixture by varying the ratio of Resin 1 and Resin 2. However, based on successful results and to reduce the amount of variables a mixture with hardness of 80 Shore was selected. The iron powder content was standardised as twice the weight of elastomer.

During the first 9 tests the previous waveguide manufacture procedure was constantly reviewed as the results suggested that one peripheral variable was preventing the results from the previous work [4] to be repeated. After some time a procedure capable of producing consistent results was developed as far as the waveguide material was concerned. The main variables controlled by the procedure were:

- Temperature of the constituents
- Duration and type of mixing
- Duration and pressure of degassing
- Percentage of constituents
- Thermal cycle applied for curing
- Moisture content of the metal powder
- Mesh size of metal powder
- Orientation of the mould during pouring and gelling time
- Order in which the components are added

The Standard Procedure developed can be described as follows:

##### 4.3.2.2.1 Mould Preparation

1. Clean internal surface
2. Polish with wax
3. Spray mould with silicone release agent
4. Spray lid with silicone release agent
5. Place a polyester release film on the lid surface

## 6. Assemble lid and body

### 4.3.2.2.2 Waveguide Casting and Curing

1. Pre-heat the resin component drums to about 50°C (It may take 24h to heat a 50 litres drum).
2. Warm up vacuum pump.
3. Put Resin 1 and 2 into a mixing bowl and mix mechanically for 5 minutes (slow speed).
4. Add iron powder, mix for 5 minutes.
5. Put into a vacuum chamber and take the pressure down up to 10 Bar, hold for 5 minutes.
6. Add the Isocyanate component and mix for 5 minutes.
7. Put mixture in the vacuum chamber and evacuated the chamber for 15 minutes, (the mixture will boil during the process, expanding and then collapsing abruptly).
8. Remove the bowl from the vacuum chamber.
9. Mix carefully by hand only in one direction to avoid air trapping (this is necessary due to the precipitation of the iron powder).
10. Pour slowly into moulds allowing air contained in the mould to escape.
11. Allow the mixture 2-3 hours to gel.
12. Remove semi-cured casting.
13. Leave 24 hours to cure in room temperature, about 20°C.
14. Post cure in an oven at 80°C for 16 hours
15. Cut to length.

Due to the expansion of the mixture in the vacuum chamber it is necessary that the chamber is several times bigger than the volume of the mixture needed. It is also necessary to have a transparent lid on the vacuum chamber to ensure that the mixture has boiled, and not overspilled from the mixer bowl (this could contaminate the vacuum pump).

It was found during gelling time that a layer of up to 4 mm with no iron powder in it appeared on the top of the mould. This segregation presented a major problem when using a horizontal mould, as the layer without iron powder introduced a potential reflective interface within the waveguide. Initially it was believed that using the mould in the horizontal position would avoid segregation. To reduce the segregation due to a taller mould the mixture was poured already gelling into the mould. No segregation of the bulk of the iron powder was noted, only the formation of a 4 mm layer without iron powder occurred at the top of the mould.

To avoid this 4 mm layer, a different mould was built to be used in the vertical position, which allowed the layer without iron powder to be discarded. The use of a vertical mould had the inconvenience of introducing air bubbles in the waveguide. It was found that



the mould should be kept only slightly inclined during the initial stages of pouring and the inclination should be increased as the mould fills up to avoid air trapping in the waveguide material.

The tests, using curved plates and tubulars, had to be performed using a curved waveguide. This was required because the explosive layers reduced the flexibility of the charge. Therefore, it was necessary to produce a curved charge assembled on a waveguide which fit the curved target. To produce curved waveguides presented a potential problem if different moulds were required for different diameters. This was considered to be unacceptable and an alternative to producing curve waveguides using flat moulds was found. This was achieved by introducing one more stage to the Casting and Curing procedure above. The new procedure enabled the production of curved waveguides of different diameters using the same mould. This procedure is referred as "Forming" and it is described below:

#### 4.3.2.2.3 Forming Procedure

1. Once the resin in the mould has started to gel and, most important of all, a skin has formed where the resin contacts the mould surface the waveguide should be ready to be taken from the mould. (to test whether a skin has formed, one can use a finger and apply light pressure on the exposed end of the waveguide at 45° into the resin and away from the mould surface. If the resin has reached the optimum state for the next stage, then a finger should sink easily into the resin and a small gap should open up between the resin and mould)

2. Remove the lid, leaving the polyester release film in place. The mould should then be inverted and raised on 50 mm blocks in such a way that the casting can fall clear of the mould.

3. If the casting does not start to fall under its own weight, then it can be helped by pushing with light finger pressure. Once the first 100 mm are free, its own weight will slowly draw the whole length of the lens from the mould. This can take up to 40 minutes. Beware that any forcing will inevitably cause distortion and may even tear the lens. It should be not attempted to draw the lens from the mould by pulling at the polyester release film, as this might detach the film from the lens. The lens should be attached to the film in order to prevent distortion of the flat face.

4. Once the lens is released from the mould, it should be ready to be laid onto a curved base of the same diameter of the target to be cut. It is important to ensure that the end of the lens runs parallel to the edge of the curved base. When handling, one should hold the release film and not the waveguide.

5. The waveguide should then be left to stand on the curved base for 24 hours and then post cured at 80° C for 16 hours resting on the curved base.

6. Once the lens is fully cured and cold, the release film can be removed. At this point the surfaces should be degreased to remove all traces of release agent prior to the assembling of the explosive.

The curved base was manufactured using plywood and a thin aluminium plate. The base also proved to be necessary as base to rest the waveguide during assembling of the explosive.

#### **4.3.2.3 Assembling of Explosive**

The SX2 explosive can be cut to the required width with a sharp blade commonly known as “Stanley Knife”. The explosive is flexible enough to be shaped against the waveguide by using a roller. The thickness of the explosive can be increased by adding 3 mm layers of SX2 as required. It proved to be necessary to shape each individual layer and to glue it to previous one instead of making a thicker sheet and shape it afterwards. Some sheets of SX2 presented blisters (air pockets) and were not used. It was also observed that (mainly during the winter) the explosive mouldability was severely restricted by low temperatures and in this case the explosive was removed from the magazine in the morning and left in a warm preparation room to be used in the afternoon.

Prior to assembling, the waveguides needed to be prepared. They were cut to length, trimmed and de-greased. When necessary, the top ridge was removed from the region where it would interfere with the positioning of the initiation system.

##### **4.3.2.3.1 Initiation System**

The main objective of the initiation system is to guarantee the synchronisation between the detonation fronts in both sides of the charge. This is normally achieved by initiating the detonation at points positioned at equal distances from both sides of the charge. The simplest way to achieve that is known as tail initiation where the length of the explosive from both sides of the charge is extended and joined at one point. More accurate systems were used to guarantee the equal distances eliminating the lack of synchronisation as a potential source of uncertainty. The systems used were the plane wave generator and a simplified version that is referred to as the “equilateral triangle”.

It was also important to ensure that the detonation was effectively transmitted from the initiation system to both sides of the charge. With the plane wave generator a simple butt joint was used and with the simplified device a staggered lap joint was used.

#### 4.3.2.3.2 The plane wave generator

The aim of this device was to generate two synchronised flat detonation fronts in the strips of explosive on each side of the waveguide. This was done by making a grid of rubber into which 6 mm thick layer of SX2 was laid in such a way that the detonation path had the same length through any of the possible paths.

The dimensions of the paths were not critical, provided that the proportions were maintained and the minimum of 3 mm (reaction zone for RDX) was respected (a minimum width and thickness of 6 mm was used). The two layers of explosive were attached, all butt joints overlapped, and joints on the two sides were arranged so as to be symmetrical. **Figure 4.1** shows an example of the plane wave generator.

#### 4.3.2.3.3 Equilateral triangle

Tests showed that the plane wave generator created a flat detonation front in the main charge. However it was suspected that this relatively complex system of initiation was not necessary. A much simpler configuration excluding the rubber obstacles was tested and proved equally effective. This simplified configuration is nothing more than an equilateral triangle where the dimensions of the sides are defined by the charge width as in **Figure 4.2**. The production of this initiation system proved to be much simpler than the plane wave generator. In practice the plane wave generator required more time to be assembled than the charge itself. The equilateral triangle also provided far fewer joints between the initiation device and the main charge. The explosive layers were overlapped to avoid butt joints.

#### 4.3.2.3.4 The Main Charge

The procedures for the assembly of the main explosive charge to the waveguide had to take into account the modifications in the charge design, in particular the necessity of covering most of the waveguide with explosive and attaching the explosive to the target.

The standardised procedure included a 3-5 mm allowance given on the width of the explosive strips. This ensured that the explosive was in good contact with the target. To achieve that one edge of the explosive strip was laid up against the dividing ridge of the waveguide, allowing the other edge to overlap outside the waveguide base. This excess was then trimmed flush with a sharp knife to allow a perfect contact of the explosive and the target.

As the lengths needed were longer than that of the sheet SX2, several joints within the main charge were necessary. The two halves of the charge were kept symmetrical, and the joints planned in such a way that they were staggered along the length of the waveguide.

In some cases the initiator was constructed separately and it was fixed in place on the site. In this case the joint was arranged as a stepped series of lap joints. This allowed the initiator to be built up on a separate plaster section, which minimised the effect that this part of the charge would have had upon the target. A much simpler, and possibly more effective method of achieving the same effect was to build the initiation on the waveguide and to fix the charge onto the target with the initiation outside the target area.

### **4.3.3 Experimental Set-up**

#### **4.3.3.1 Confinement**

Throughout the SWF trials it was necessary to control noise and air blast due to the test site proximity to inhabited areas. To standardise confinement conditions, an air chamber was used between the explosive charge and the sand or wet sand used to damp the noise from the blast. Care was taken to remove stones from the sand as they could turn into projectiles.

In some trials, a mixture of iron powder and oil was used to increase the confinement conditions near the initiation. Also the same polyurethane/iron powder material used in the waveguide was used as confinement around the initiation region.

Two trials were carried out underwater where water provided the confinement. In one underwater trial an additional confinement was provided with lead and stone aggregate.

#### **4.3.3.2 Target Preparation**

In the first 10 tests the surface of the target plates was prepared in such a way so as to improve the adhesion between the charge and the target and to standardise experimental conditions. The procedure used included complete cleaning of all corrosion, pitting, and oxidation due to hot rolling and heat treatment. The initial cleaning procedures proved to be unnecessary and for the rest of the trials only removal of excess corrosion was done to ensure a good adhesion of the waveguide.

#### **4.3.3.3 Anvil Preparation**

In most cases air was used as the anvil back-face condition. This was achieved either by using spacers between the target and the ground or by digging a channel under the charge to provide an air gap under the plate. There was some concern about the possibility of the trench dug in the ground could be providing assistance to the cutting process due to bending. To place the plate in air seemed not to be feasible at the test site used. Trials on curved plates and tubulars showed there was no assistance to produce the crack as such. Unfortunately direct comparison of the results was not possible due to different target thickness used.

In one case a solid rock anvil was used and the charge failed to cut. The detrimental effect of solid anvils was later clearly demonstrated by using steel plates as anvils with spacers to control the separation between the target and the anvil. The steel plate acted as a momentum trap while the crack was developing.

Water as an anvil condition was not intended as an air bag set-up was considered for the final underwater trials. The detrimental effect of water in the target back face became clear in two trials, where despite the cut areas the spall remained attached to the target.

#### 4.3.3.4 Fixing Charge to Target

A procedure to standardise the conditions in which the charge was fixed to the target was deemed necessary based on comments of Denis [5], Davis [7] and Al-Hassani and Burley [19], and furthermore in the lack of success in repeating Al-Hassani and Burley [4] results in the initial trials. This procedure helped to avoid the introduction of a possible uncontrolled variable, however it was not investigated whether it was necessary or not. The procedure can be described as:

1. Clear any soil or sand from the prepared area
2. Degrease the area with Acetone
3. Degrease the charge with genklene, and apply Explosive Approved Cyanoacrylate adhesive to the back of the charge and spread evenly.
4. Place the waveguide onto the target and slide into position, thus ensuring a layer of glue is applied to the target.
5. Apply pressure evenly over the entire charge, paying special attention to the ends. Hold the pressure until the glue is set (this could vary from 1 to 10 minutes depending of ambient temperature and moisture).

#### 4.3.4 **Test Sites**

All SWF tests in air were carried out at the Birch Vale Quarry in New Mills. One would expect that the small explosive charges would not represent a problem for a site used to large detonations associated with quarrying, but due to the location of the quarry near to residential houses even charges of less than 1 kg had to be covered with sand to reduce noise. The necessity of covering the charges with sand in addition to the work involved in recovering the targets (some times 2 metres underground) reduced the maximum number of trials per day to two or three. It also introduced another variable, i.e. the degree of confinement of the detonation.

For the underwater tests, a near-shore site in Vlissing - Holland was used providing a water depth of approximately 10 m. The transportation of explosive charges overseas was carried out using UN (United Nations) approved boxes and specialised transportation company.

#### 4.4 Instrumentation

The unsatisfactory results of the first 8 tests led to the speculation that the synchronisation between the two sides of the explosive charge was incorrect. The possibility of monitoring the detonation front on both sides of the waveguide was investigated and several options were considered, including D'autriche method, ionisation probes and optical devices. Ionisation probes seemed to be a proven technology but the field conditions experienced on the explosive site carried the risk of damage of the oscilloscope necessary to capture the events.

Later on, the experimental testing showed more positive results, but it was decided to monitor any alterations on the detonation front, that were introduced by a simplified initiation system. An Optical Velocity of Detonation Meter (VOD meter) was made available and it was used with success. The equipment manufactured by Kontinitro (Switzerland) is robust, compact and suitable for use in field conditions. The specification of the equipment can be summarised as:

Trade mark: Explomet-fo Multimode  
Accuracy : +/- 0.1 microsecond

Special care was taken in order to ensure that the procedures for the preparation of the connections were followed. Depending on the weather conditions even this apparently simple operation could be difficult to implement.

The VOD meter can be set to register the time difference between 5 probes in relation to a trigger point or the time difference between the probes. The setting for the trigger point was chosen for most of the tests.

Also the fact that the explosive is to a certain extent translucent had to be taken into account, as the instrument can register the presence of light from a region away from the detonation front. This concern was minimised by positioning of the fibre optic probes perpendicularly to the propagation of the detonation front, or by covering the ends with a thin aluminium foil.

#### 4.5 Target Material

To reduce the influence of variations in the material properties, target plates of the same material were cut from the same plate. Curved plates and tubular targets were cut from 2 different tubulars due to availability.

**Test with Grade 43A flat plates**

Tests: 1 to 5, 6A, 6B, 7 to 11, 14, 17 and 23

Chemical Composition:

C = 0.160, Si = 0.210, Mn = 0.780, P = 0.012, S = 0.160, Cr = 0.013, Mo = 0.003, Ni = 0.012, Al = 0.0670, B = 0.0001, Ca = 0.0000, Cu = 0.017, Nb = 0.003, Sn = 0.010, Ti = 0.002, V = 0.001,

Yield Stress: 350 N/mm<sup>2</sup>

Tensile Strength: 490 N/mm<sup>2</sup>

Elongation : 30%

Charpy (V notch) at -20°C: 26 J (Average of 30 / 28 / 20)

**Test with Grade 50D flat plates**

Tests No: 12, 13, 15, 16, 18 to 22

Chemical Composition:

C = 0.120, Si = 0.401, Mn = 1.510, P = 0.002, Nb = 0.32

Yield Stress: 440 N/mm<sup>2</sup>

Tensile Strength: 541 N/mm<sup>2</sup>

Elongation: 32%

Charpy Impact at -20°C: 99 J (Average of 96 / 90 / 112), Grade 50D requires minimum 27J at - 20 °C.

**Tests with curved plates and tubulars using steel grade similar to 50 EE**

Thickness: 50 mm

Tests No: C1 to C6

50 mm Curved Plates and tubular

Chemical Composition:

C = 0.107, Si = 0.415, Mn = 1.500, P: 0.014, S = 0.003, Cr = 0.19, Mo = 0.003, Ni = 0.265, Al = 0.031, B = 0.001, Cu = 0.010, Nb = 0.030, V = 0.002, N = 0.0045, Ti = 0.004

Yield Stress: 395 N/mm<sup>2</sup>

Tensile Strength: 500 N/mm<sup>2</sup>

Elongation: 35%

Charpy Energy (V notch) at -40°C: 240 J (Average of 225 / 255 / 250), Grade 50EE requires 27J at -50°C.

**Tests with curved plates and tubulars using steel grade similar to 50 E**

Thickness: 45 mm

Tests No: C7 to C10

Chemical Composition:

C = 0.118, Si = 0.415, Mn = 1.510, P: 0.015, S = 0.004, Cr = 0.30, Mo = 0.006, Ni = 0.230, Al = 0.036, B = 0.001, Cu = 0.010, Nb = 0.037, V = 0.001, N = 0.0061, Ti = 0.003

Yield Stress: 418 N/mm<sup>2</sup>

Tensile Strength: 551 N/mm<sup>2</sup>

Elongation : 36%

Charpy (V notch) at -40°C: 167 J (Average of 154 / 162 / 186), Grade 50E requires minimum 27J at - 30°C

## 4.6 Experimental Results

**Table 4.1** summarises the results of tests using plates, curved plates and full tubulars. **Table 4.2** summarises the dimensionless design parameters from the same tests. The design variables from **Tables 4.1** and **4.2** are presented in the same way as Burley and Hassani [4] for easier comparison.

Further comparison of the charges' variables is presented in Section 6. The results are described in terms of fracture geometry for each test in conjunction with the drawing of the respective explosive charge and other information about the test. The SWF tests were divided in two set numbering:

- Tests 1 to 27: Flat plates including 43A and 50D steels
- Tests C1 to C10: Tests on curved plates and full tubulars including only 50 D steel.



Table 4.1 Summary of Waveguides design parameters and explosive dimensions

Tests on flat plates

No	Plate		Rad.		Off-set		Waveguide		Rubber Type	Type	Explosive		Comments
	Mat.	Thick mm	mm	mm	mm	mm	Separation mm	mm			Thickness mm	Load $\text{Kg}\cdot\text{m}^{-1}$	
1	43A	65	104	10	10	0	0	0	ES 74280A non standard	SX2	6	1.17	No cracks, no indentation
2	43A	65	104	10	10	0	0	0	ES 74280A non standard	SX2	6	1.17	No cracks, no indentation
3	43A	65	104	10	10	0	0	0	ES 74280A non standard	SX2	6	1.17	No cracks, no indentation
4	43A	65	104	10	10	0	0	0	Mild steel	SX2	6	1.2	Cracks parallel to the rolling plane, left indentation
5	43A	65	104	10	10	0	0	0	ES 74280A non standard	SX2	6	1.2	No cracks, left indentation
6A	43A	65	NA	NA	NA	NA	NA	NA	NA	SX2	6	1.2	Cracks parallel to the rolling plane
6B	43A	65	112.5	27	27	0	0	0	Devcon Rubber non standard	SX2	6 and 9	6 = 1.39 9 = 2.16	Slight bend on the target
7	43A	65	104	10	10	0	0	0	ES 74280A non standard	SX2	9		Left indentation, virtually no bend.
8	43A	65	104	10	10	0	0	0	ES 74280A standard procedure	SX2	9		Left indentation, vertical crack 2/3 of the thickness
9	43A	65	112.5	10	10	0	0	0	ES 74280A standard procedure	SX2	6 and 9	6 = 1.39 9 = 2.16	Cut, spall + vertical crack

Table 4.1 (cont.) Summary of Waveguides design parameters and explosive dimensions

Tests on flat plates

No	Plate		Radius mm	Waveguide		Rubber Type	Type	Explosive		Comments
	Mat.	Thick mm		Off-set mm	Separati on mm			Thickness mm	Load Kg.m <sup>-1</sup>	
10	43A	65	112.5	10	0	ES 74280A standard procedure	SX2	6 and 9	6 = 1.39 9 = 2.16	Cut, spall + vertical crack
11	43A	65	112.5	10	0	ES 74280A standard procedure	SX2	6 and 9	6 = 1.39 9 = 2.16	Cut, spall + vertical crack
12	50D	65	112.5	10	0	ES 74280A standard procedure	SX2	6 and 9	6 = 1.39 9 = 2.16	No vertical crack, spall under 9 mm
13	50D	65	112.5	10	0	ES 74280A standard procedure	SX2	6 and 9	6 = 1.39 9 = 2.16	No vertical crack, spall under 9 mm
14	43A	65	150.0	72	0	ES 74280A Standard procedure	SX2	6 and 9	6 = 1.88 9 = 2.56	No vertical crack, spall under 9 mm
15	50D	65	114	13	- 40	ES 74280A standard procedure	SX2	6 and 9	6 = 1.45 9 = 2.20	Slight bend, cracks parallel to the rolling direction
16	50D	65	150	72	0	ES 74280A standard procedure	SX2	6 and 9	6 = 1.88 9 = 2.56	Spall under 9 mm
17	43A	65	114	13	- 40	ES 74280A standard procedure	SX2	6 and 9	6 = 1.90 9 = 2.20	Cut, no spall, small surface crack
18	50D	65	114	13	- 40	ES 74280A standard procedure	SX2	18	4.59	Cut, central spall, internal and surface cracks
19	50D	65	113	20	- 78	ES 74280A standard procedure	SX2	18	2.80	Cut, central spall, internal and surface cracks

Table 4.1 (cont.) Summary of Waveguides design parameters and explosive dimensions

Tests on flat plates

Plate		Waveguide			Explosive		Comments			
No	Mat.	Thick mm	Radius mm	Off-set mm	Separation mm	Rubber Type		Type	Thickness mm	Load g.m <sup>-1</sup>
20	50D	65	113	-15	-78	ES 74280A standard procedure	SX2	18	5.20	60° bending, indentation, vertical crack 4/5 of the thickness
21	50D	65	113	32	-78	ES 74280A standard procedure	SX2	18	1.80	Internal vertical and horizontal cracks, surface cracks
22	50D	65	113	20	-78	ES 74280A standard procedure	SX2	18	2.85	Internal vertical and horizontal cracks, surface cracks
23	43A	65	114	13	-40	ES 74280A standard procedure	SX2	9	2.20	300 mm charge cut a 600 mm 43A steel plate. Brittle fracture propagated 150 mm backwards and forwards.

Table 4.1 (Cont.) Summary of Waveguides design parameters and explosive dimensions

Tests on curved plates and tubulars

Plate			Waveguide			Explosive		Comments		
No	Mat.	Thick mm	Rad. mm	Off-set mm	Separation mm	Rubber Type	Type		Thickness mm	Load g.m <sup>-1</sup>
C1	50EE	50	113	20	- 78	ES 74280A standard procedure	SX2	18	3.20	Cut with internal vertical and horizontal cracks, surface crack and spalling.
C2	50EE	50	114	13	- 40	ES 74280A standard procedure	SX2	18	5.30	Cut with internal vertical and horizontal cracks, surface crack and spalling
C3	50EE	50	113	20	- 78	ES 74280A standard procedure	SX2	18	3.15	Cut with internal vertical and horizontal cracks, surface crack and spalling
C4	50EE	50	114	13	- 40	ES 74280A standard procedure	SX2	18	5.30	Cut with internal vertical and horizontal cracks, surface crack and spalling
C5	50EE	50	113	20	- 78	ES 74280A standard procedure	SX2	18	3.20	Cut with internal vertical and horizontal cracks, surface crack, failed under initiation
C6	50EE	50	113	20	- 78	ES 74280A standard procedure	SX2	18	3.20	Cut with internal vertical and horizontal cracks, surface crack, reduced vertical crack under initiation
C7	50E	45	113	20	- 78	ES 74280A standard procedure	SX2	18	3.20	Cut with internal vertical and horizontal cracks, surface crack, reduced vertical crack under initiation
C8	50E	45	113	20	- 78	ES 74280A standard procedure	SX2	18	3.20	Cut with internal vertical and horizontal cracks, surface crack, reduced vertical crack under initiation
C9	50E	45	113	20	- 78	ES 74280A standard procedure	SX2	18	3.20	Cut with internal vertical and horizontal cracks, surface crack, failed under initiation, spall remained attached

C10	50E	45	113	20	- 78	ES 74280A standard procedure	SX2	18	3.20	Cut with internal vertical and horizontal cracks, surface crack, failed under initiation, spall remained attached
-----	-----	----	-----	----	------	------------------------------------	-----	----	------	---

Table 4.2: Dimensionless parameters for flat plate tests

Plate	Waveguide Type	Off-set / Thickness	Waveguide Width / Thickness	Loading ( $\text{g/m}^{-1}$ )	Comments
1	1	0.15	2.20	1.17	No cracks, no indentation
2	1	0.15	2.20	1.17	No cracks, no indentation
3	1	0.15	2.20	1.17	No cracks, no indentation
4	1	0.15	2.20	1.2	Cracks parallel to the rolling plane, left indentation
5	1	0.15	2.20	1.2	No cracks, left indentation
6A	NA	NA	NA	1.2	Cracks parallel to the rolling plane
6B	2	0.42	1.92	6 = 1.39 9 = 2.16	Slight bend on the target
7	1	0.15	2.20		Left indentation, virtually no bend.
8	1	0.15	2.20		Left indentation, vertical crack 2/3 of the thickness
9	2	0.42	1.92	6 = 1.39 9 = 2.16	Cut, spall + vertical crack
10	2	0.42	1.92	6 = 1.39 9 = 2.16	Cut, spall + vertical crack
11	2	0.42	1.92	6 = 1.39 9 = 2.16	Cut, spall + vertical crack
12	2	0.42	1.92	6 = 1.39 9 = 2.16	No vertical crack, spall under 9 mm
13	2	0.42	1.92	6 = 1.39 9 = 2.16	No vertical crack, spall under 9 mm
14	3	1.10	1.92	6 = 1.88 9 = 2.56	No vertical crack, spall under 9 mm

Shock Wave Focusing Technical Report

15	4	0.20	1.92	6 = 1.45 9 = 2.20	Slight bend, cracks parallel to the rolling direction
16	3	1.10	1.92	6 = 1.88 9 = 2.56	Spall under 9 mm

Table 4.2 (cont.): Dimensionless parameters for flat plate tests

Plate	Waveguide Type	Off-set / Thickness	Waveguide Width / Thickness	Loading (g/m <sup>-1</sup> )	Comments
17	4	0.20	1.92	6 = 1.90 9 = 2.20	Cut, small surface crack
18	4	0.20	1.92	4.59	Cut, central spall, internal and surface cracks
19	6	0.31	1.92	2.80	Cut, central spall, internal and surface cracks
20	5	-0.23	1.92	5.20	60° bending, indentation, vertical crack 4/5 of the thickness
21	8	0.49	0.61	1.80	Internal vertical and horizontal cracks, surface cracks
22	6	0.31	1.15	2.85	Internal vertical and horizontal cracks, surface cracks
23	4	0.20	1.92	2.20	

Table 4.2 (cont.): Dimensionless parameters for curved plate and tubular tests

Plate	Waveguide Type	Off-set / Thickness	Waveguide Width / Thickness	Loading ( $\text{g/m}^{-1}$ )	Comments
C1	6	0.70 (35/50)	1.50	3.20	Cut with internal vertical and horizontal cracks, surface crack and spalling.
C2	4	0.56 (28/50)	2.50	5.30	Cut with internal vertical and horizontal cracks, surface crack and spalling
C3	6	0.70 (35/50)	1.50	3.15	Cut with internal vertical and horizontal cracks, surface crack and spalling
C4	4	0.56 (28/50)	2.50	5.30	Cut with internal vertical and horizontal cracks, surface crack and spalling
C5	6	0.70 (35/50)	1.50	3.20	Cut with internal vertical and horizontal cracks, surface crack, failed under initiation
C6	6	0.93 (41/44)	1.67	3.20	Cut with internal vertical and horizontal cracks, surface crack, reduced vertical crack under initiation
C7	6	0.93 (41/44)	1.67	3.20	Cut with internal vertical and horizontal cracks, surface crack, reduced vertical crack under initiation
C8	6	0.93 (41/44)	1.67	3.20	Cut with internal vertical and horizontal cracks, surface crack, reduced vertical crack under initiation
C9	6	0.93 (41/44)	1.67	3.20	Cut with internal vertical and horizontal cracks, surface crack, failed under initiation, spall remained attached
C10	6	0.93 (41/44)	1.67	3.20	Cut with internal vertical and horizontal cracks, surface crack, failed under initiation, spall remained attached





#### 4.6.1 Tests on Plates

To avoid considerations about edge effects and based on previous experience the target dimensions used were 600x600x65 mm. At 180 kg represented the upper limit of manual handling. Only BS 4360 43A and 50 D plates were used.

##### TEST 1

Test 1 was performed to repeat an experiment conducted by Burley and Al-Hassani [4] where a fracture almost through the whole thickness was achieved. Burley and Al-Hassani's experiment also left an indentation on the plate surface under the waveguide.

The result from Test 1 showed a dramatic discrepancy between the previous work. The plate appeared to be untouched by the detonation showing no indentation or internal cracks of any sort. Many possibilities were raised including the waveguide material, the lack of attachment between the explosive and the target, the back face in close contact with the ground and the lack of synchronisation between the two detonation fronts. The original aim of test 1 was to verify if experimental conditions were similar to Burley and Hassani's work. Following the result of Test it became apparent that the role of peripheral variables were extremely important. Test 1 used identical geometry, explosive type, target material used in Burley and Al-Hassani's tests.

**Table 4.3** describes the results and gives details of the experimental conditions. **Figure 4.3** shows the charge dimensions. **Figure 4.4** shows the assembled charge on the plate. In Test 1 the initiation was done by joining an extension of the explosive from both sides of the charge.

**Table 4.3 Test 1 Results and Experimental Conditions**

Waveguide type	1
Waveguide material	Standard composite, cast horizontally ( Non standard procedure)
Target material	43 A, 65 mm thick
Explosive	SX2, 3 mm sheets, 2 layers, 60 mm wide (not attached to the target)
Central space	40 mm, air
Initiation	Tail initiation
Adhesive	Impact adhesive only
Anvil	Compacted sand
Surface condition	Black condition with a thin layer of rust
Confinement condition	Sand over air chamber
<b>Results</b>	Little or no indentation was left by the waveguide, little or no bend, no internal or surface cracks

##### TEST 2

Test 2 was designed to prevent the influence of the contact between the target and the ground in Test 1. To assess the synchronisation between the two detonation fronts, a D'autriche method witness plate was used connecting the two sides of the waveguide. An explanation of the D'autriche method can be found in the work of Crossland [74]. Experimental conditions like the initiation or the adhesive type used were kept constant, but the results showed no significant difference from the results obtained in Test 1. **Table 4.4** describes the results and gives details of the experimental conditions.

**Table 4.4 - Test 2 Results and Experimental Conditions**

Waveguide Type	1
Waveguide material	Standard composite, cast horizontally ( Non standard procedure)
Target material	43 A, 65 mm thick
Explosive	SX2, 3 mm sheets, 2 layers, 60 mm wide (not attached to the target)
Central space	40 mm, air
Initiation	Tail initiation
Adhesive	Impact adhesive between WG/explosive, explosive/explosive and Araldite between WG/target
Anvil	Air , Stones separating the plate from the ground
Surface condition	Black condition with a thin layer of rust
Confinement condition	Sand over air chamber
Results	Little or no indentation was left by the waveguide, little or no bend, no internal or surface cracks. The D'autriche witness showed good synchronisation between the two detonation fronts.

### TEST 3

In Test 3 the amount of explosive was increased from 2 to 3 layers of SX2 in an attempt to overcome the influence of some unknown variable that could have prevented the energy to be transmitted efficiently from the waveguide to the target. The Araldite adhesive between waveguide and target was substituted by the same impact adhesive used in the previous work [4]. A plane wave generator was introduced to increase reliability of the initiation and to ensure synchronisation of the two detonation fronts. Despite this measures no significant difference between the result of Test 3 and the two previous tests was achieved. **Table 4.5** describes the results and gives details of the experimental conditions. **Figure 4.5** shows the charge assembled onto the target where the plane wave generator can be observed.

**Table 4.5 - Test 3 Results and Experimental Conditions**

Waveguide Type	1
Waveguide material	Standard composite, cast horizontally ( Non standard procedure)
Target material	43 A, 65 mm thick
Explosive	SX2, 3 mm sheets, 2 layers, 60 mm wide (not attached to the target)
Central space	40 mm, air

Initiation	Plane wave generator
Adhesive	Impact adhesive between WG/explosive, explosive/explosive and Araldite between WG/target
Anvil	Air (plate was supported by wood on the edges)
Surface condition	Black condition with a thin layer of rust
Confinement condition	Sand over air chamber
Results	Little or no indentation was left by the waveguide, little or no bend, no internal or surface cracks.

#### TEST 4

The lack of indentation on the targets of Tests 1, 2, and 3 represented a fundamental difference between these tests and the partial successful trial from the work of Burley and Al-Hassani [4] on 65 mm plates. This fact suggested that very little energy was being transmitted to the target and therefore conditions of Tests 1, 2 and 3 were carefully compared with the mentioned trial. By examining photographs, it was found that previously the explosive was cut levelled with the waveguide bottom face being in direct contact with the target (see **Figure 4.6**). In Test 4 the explosive was then cut levelled, the contact between the explosive and the target was improved. The target surface was polished to eliminate this variable.

Another important source of uncertainties was the waveguide material itself and for Test 4 it was decided to use a steel waveguide to discard the influence of the waveguide material on the test. The results of Test 4 showed some cracks parallel to the rolling plane and a strong indentation left on the plate surface. **Table 4.6** describes the results and gives details of the experimental conditions. **Figure 4.6** shows the alterations made on the explosive trimming and typical position and sizes of the induced cracks. Actual dimensions and positions varied considerably throughout the length of the target. **Figure 4.7** and **Figure 4.8** show photographs of the charge assembled onto the target and after the detonation.

**Table 4.6 - Test 4 Results and Experimental Conditions**

Waveguide Type	1
Waveguide material	Machined mild steel
Target material	43 A, 65 mm thick
Explosive	SX2, 3 mm sheets, 2 layers, ( attached to the target)
Central space	40 mm, air
Initiation	Plane wave generator
Adhesive	Cyanoacrylate between explosive/explosive and explosive /WG, no adhesive between WG/target
Anvil	Air under the waveguide region
Surface condition	Polished
Confinement	Sand over air chamber

<b>Results</b>	Strong indentation was left by the waveguide, little bend, internal cracks parallel to the rolling plane.
----------------	---

### TEST 5

Test 5 was designed to evaluate improvements in the waveguide manufacturing procedure, and to evaluate the effect of using the explosive attached to the target in conjunction with the polymeric waveguide.

**Table 4.7** describes the results and give details of the experimental conditions. The results showed an indentation on the target but not as pronounced as Test 4 and also no internal cracks. A D'autriche method was used to assess the synchronisation between the two detonation fronts but the witness could not be found. **Figure 4.9** shows the test set up before detonation.

**Table 4.7 - Test 5 Results and Experimental Conditions**

Waveguide Type	1
Waveguide material	Standard composite, cast vertically improved procedure
Target material	43 A, 65 mm thick
Explosive	SX2, 3 mm sheets, 2 layers, ( attached to the target)
Central space	40 mm, air
Initiation	Plane wave generator
Adhesive	Cyanoacrylate only
Anvil	Air under the waveguide region
Surface condition	Black condition with a thin layer of rust
Confinement condition	Sand over air chamber
<b>Results</b>	Indentation, little bend

### Test 6A

Test 6 did not include any waveguide. This test was carried out to assess the explosive load used in Tests 1 and 2. A simple test was carried out in order to establish the amount of damage left on a plate due to the detonation of the same amount of explosive without a waveguide. Four strips of explosive were cut to 60 mm wide and were glued on a steel plate as shown in **Figure 4.10**. The strips were detonated using a tail initiation.

The position and size of the induced cracks were determined using dye penetrant liquid and are showed in **Figure 4.10**. For completeness **Table 4.8** describes the results and gives details of the experimental conditions.

**Table 4.8 - Test 6.A Results and Experimental Conditions**

Waveguide Type	NONE
Waveguide material	NONE
Target material	43 A, 65 mm thick

Explosive	SX2, 3 mm sheets, 2 layers, ( attached to the target)
Central space	22 mm, air
Initiation	Tail initiation
Adhesive	Cyanoacrylate only
Anvil	Air under the waveguide region
Surface condition	Black condition with a thin layer of rust
Confinement condition	Sand over air chamber
Results	Indentation, crack parallel to the rolling plane

### TEST 6 B

Test 6B assesses waveguide type 2 and should be analysed in conjunction with Tests 9,10 and 11. In these 3 cases the same new design was successfully tested with the standard elastomer using the standard procedure described in item 4.3.2.2. In Test 6B a DEVECON elastomer was used which require a complete different procedure to be manufacture. The cast was considered to be of poor quality, with an excessive amount of air bubbles.

It was decided to test the DEVECON waveguide anyway for comparison with the standard elastomer later on. Due to the results in Test 6A, it was opted to test the waveguide with 3 layers of SX2. One modification introduced was to fill the central space without explosive with a 5 mm strip of rubber to facilitate on the assembling of explosives. **Table 4.9** describe the results and give details of the experimental conditions. **Figure 4.11** shows Waveguide type 2 dimensions with 3 layers of SX2.

**Table 4.9 - Test 6.B Results and Experimental Conditions**

Waveguide Type	2
Waveguide material	DEVECON polymer (Polyurethane) and iron powder. Excessive amount of trapped air bubbles
Target material	43 A, 65 mm thick
Explosive	SX2, 3 mm sheets, 3 layers, ( attached to the target)
Central space	14 mm, rubber
Initiation	Plane wave generator
Adhesive	Cyanoacrylate only
Anvil	Air under the waveguide region
Surface condition	Polished
Confinement condition	Sand over air chamber
Results	Indentation, little bend, no internal or surface cracks

In **Figure 4.11** (1) is waveguide polymer + iron powder, (2) plastic explosive SX2, (3) is the steel target, (4) central spacer consisting of ordinary rubber.

### TEST 7

Test 7 was carried out based on the assumption that the energy from the top part of a curved waveguide would contribute mainly to fractures parallel to the rolling plane, where planes rich in inclusions tend to exist in plates of mild steel of that thickness. Test 7 used waveguide Type 1 with the standard manufacture procedure and the explosive layer was rearranged leaving a bigger central space without explosive as depicted in **Figure 4.12**. **Table 4.10** describe the results and give details of the experimental conditions. **Figure 4.13** shows the charge being assembled on the target.

**Table 4.10 - Test 7 Results and Experimental Conditions**

Waveguide Type	1
Waveguide material	Standard composition and manufacture procedure
Target material	43 A, 65 mm thick
Explosive	SX2, 3 mm sheets, 3 layers, ( attached to the target)
Central space	71 mm, air
Initiation	Plane wave generator
Adhesive	Cyanoacrylate only
Anvil	Air under the waveguide region
Surface condition	Polished
Confinement condition	Sand over air chamber
<b>Results</b>	Indentation was left by the waveguide, virtually no bend, no internal or surface cracks. The central part of the waveguide was found.

## TEST 8

Test 8 was carried out using the waveguide Type 1 and the standard manufacture procedure using 3 layers of SX2 with the central space without explosive of 40 mm as in Tests 1 to 5. The results showed the presence of a single vertical crack in the centre line of the waveguide, this was determined using dye penetrant liquid and are shown in **Figure 4.14**. **Table 4.11** describes the results and gives details of the experimental conditions. **Figure 4.15** shows the charge assembled on to the target.

**Table 4.11 - Test 8 Results and Experimental Conditions**

Waveguide Type	1
Waveguide material	Standard composition and manufacture procedure
Target material	43 A, 65 mm thick
Explosive	SX2, 3 mm sheets, 3 layers, ( attached to the target)
Central space	40 mm, rubber
Initiation	Plane wave generator
Adhesive	Cyanoacrylate only
Anvil	Air under the waveguide region
Surface condition	Polished
Confinement condition	Sand over air chamber

<b>Results</b>	Indentation was left by the waveguide, little bend, crack covering 2/3 of the thickness of the target, no cracks parallel to the rolling plane.
----------------	---

**TEST 9**

Test 9 was design to test the waveguide Type 2 design with a less controversial waveguide material than the one used in Test 6B. It was decided to vary the explosive load from 2 to 3 layers of SX2 after the first 100 mm of the waveguide in order to test the two explosive loads in one trial. **Table 4.12** describe the results and give details of the experimental conditions. **Figure 4.16** shows the charge assembled on the target, **Figure 4.17** shows the target as found after the detonation.

**Table 4.12 - Test 9 Results and Experimental Conditions**

Waveguide Type	2
Waveguide material	Standard composition and manufacture procedure
Target material	43 A, 65 mm thick
Explosive	SX2, 3 mm sheets, 2 complete layers plus a third layer after 100 mm (attached to the target)
Central space	13 mm, rubber
Initiation	Plane wave generator
Adhesive	Cyanoacrylate only
Anvil	Air under the waveguide region
Surface condition	Polished
Confinement condition	Sand over air chamber
<b>Results</b>	The target was cut in two halves with a spall 15 mm thick and 30 mm wide was found detached from the region under 3 layers of SX2 and attached to the region under 2 layers. The fracture pattern under the initiation system suggested that the fracture propagated backwards from the region with explosive load.

**TEST 10**

Test 10 was carried out to repeat Test 9, The explosive charge was placed parallel to the rolling direction. **Table 4.13** describes the results and gives details of the experimental conditions.

**Table 4.13 - Test 10 Results and Experimental Conditions**

Waveguide Type	2
Waveguide material	Standard composition and manufacture procedure
Target material	43 A, 65 mm thick
Explosive	SX2, 3 mm sheets, 2 complete layers plus a third layer after 100 mm ( attached to the target)
Central space	13 mm, rubber
Initiation	Plane wave generator
Adhesive	Cyanoacrylate only
Anvil	Air under the waveguide region
Surface condition	Polished
Confinement condition	Sand over air chamber



Rolling direction	Parallel
Results	Identical to Test 9

### TEST 11

Test 11 was carried out to repeat Tests 9 and 10 without the use of a plane wave generator. This reduced substantially the amount of time to produce a waveguide and proved to be harmless. The explosive charge was placed perpendicular to the rolling direction. This test was also used to assess how the confinement provided by the sand would affect the cut if the air chamber was removed. **Table 4.14** describes the results and gives details of the experimental conditions.

**Table 4.14 - Test 11 Results and Experimental Conditions**

Waveguide Types	2
Waveguide material	Standard composition and manufacture procedure
Target material	43 A, 65 mm thick
Explosive	SX2, 3 mm sheets, 2 complete layers plus a third layer after 100 mm ( attached to the target)
Central space	13 mm, rubber
Initiation	Equilateral Triangle
Adhesive	Cyanoacrylate only
Anvil	Air under the waveguide region
Surface condition	Polished
Confinement condition	Sand
Rolling Direction	Perpendicular
Results	Identical to Tests 9 and 10. The spall thickness increased to an average of 20 mm, width 30 mm.

### TEST 12

Test 12 was carried out using a 50D target and using exactly the same conditions as in Test 10. The results showed a lack of vertical crack despite the presence of spall. It clearly demonstrated the difference in behaviour between the 50D and 43A steels. **Table 4.15** describes the results and gives details of the experimental conditions.

**Table 4.15 - Test 12 Results and Experimental Conditions**

Waveguide Type	2
Waveguide material	Standard composition and manufacture procedure
Target material	50 D, 65 mm thick
Explosive	SX2, 3 mm sheets, 2 complete layers plus a third layer after 100 mm ( attached to the target)
Central space	13 mm, rubber
Initiation	Plane wave generator
Adhesive	Cyanoacrylate only
Anvil	Air under the waveguide region

Surface condition	Polished
Confinement condition	Sand over air chamber
Results	Spall under the 3 layer region (in average 15 mm thick), internal crack parallel to the rolling plane at mid thickness, no vertical crack.

**TEST 13**

Test 13 was carried out using a 50D target and the same conditions of Test 11, with reference in particular to triangle initiation and the lack of air chamber. **Table 4.16** describes the results and gives details of the experimental conditions. The results showed confirmed the increase in spall size due the extra confinement provided by the sand. The difference in behaviour between the 50D and 43A steels was also observed.

**Table 4.16 - Test 13 Results and Experimental Conditions**

Waveguide Type	2
Waveguide material	Standard composition and manufacture procedure
Target material	50 D, 65 mm thick
Explosive	SX2, 3 mm sheets, 2 complete layers plus a third layer after 100 mm (attached to the target)
Central space	13 mm, rubber
Initiation	Plane wave generator
Adhesive	Cyanoacrylate only
Anvil	Air under the waveguide region
Surface condition	Polished
Confinement condition	Sand
Results	Spall under the 3 layer region in average 20 mm thick, 30 mm width, no vertical crack

**TEST 14**

Test 14 was carried out using a Type 3 design with a 43 A target. **Table 4.17** describes the results and gives details of the experimental conditions. The dimensions of the fracture pattern were measured by sectioning the target under the region with 3 layers of SX2. **Figure 4.18** shows the charge configuration and the induced crack pattern.

**Table 4.17 - Test 14 Results and Experimental Conditions**

Waveguide Type	3
Waveguide material	Standard composition and manufacture procedure
Target material	43 A, 65 mm thick
Explosive	SX2, 3 mm sheets, 2 complete layers plus a third layer after 100 mm (attached to the target)
Central space	13 mm, rubber
Initiation	Equilateral triangle
Adhesive	Cyanoacrylate only
Anvil	Air under the waveguide region
Rolling direction	Parallel
Surface condition	Polished

Confinement condition	Sand over air chamber
Results	Spall under the 3 layer region, no vertical crack

### TEST 15

Test 15 was carried out using a Type 4 design with a 50D target. **Table 4.18** describes the results and gives details of the experimental conditions. The dimensions of the fracture pattern were measured by sectioning the target under the region with 3 layers of SX2. **Figure 4.19** shows the charge configuration.

**Table 4.18 - Test 15 Results and Experimental Conditions**

Waveguide Type	4
Waveguide material	Standard composition and manufacture procedure
Target material	50D, 65 mm thick
Explosive	SX2, 3 mm sheets, 2 complete layers plus a third layer after 100 mm (attached to the target)
Central space	13 mm, rubber
Initiation	Equilateral triangle
Adhesive	Cyanoacrylate only
Anvil	Air under the waveguide region
Rolling direction	Parallel
Surface condition	Polished
Confinement condition	Sand over air chamber
Results	Little bend, no internal cracks

### TEST 16

Test 16 repeats the Test 14 with a 50D target. **Table 4.19** describes the results and gives details of the experimental conditions. The dimensions of the fracture pattern were measured by sectioning the target under the region with 3 layers of SX2. **Figure 4.21** and **Figure 4.22** show the charge assembled onto the target and the target back-face after detonation.

**Table 4.19 - Test 16 Results and Experimental Conditions**

Waveguide Type	3
Waveguide material	Standard composition and manufacture procedure
Target material	50D, 65 mm thick
Explosive	SX2, 3 mm sheets, 2 complete layers plus a third layer after 100 mm (attached to the target)
Central space	13 mm, rubber
Initiation	Equilateral triangle
Adhesive	Cyanoacrylate only

Anvil	Air under the waveguide region
Rolling direction	Parallel
Surface condition	Polished
Confinement condition	Sand over air chamber
Results	Attached spall under the 3 layers region, 15 mm thick in average and approximately the charge width. No vertical crack

## TEST 17

Test 17 uses a waveguide Type 4 and repeats Test 15 with a 43A target. **Table 4.20** describes the results and gives details of the experimental conditions. **Figure 4.23** show the charge configuration and position of the induced crack pattern. **Figure 4.24** shows the charge assembled on the target, **Figure 4.25** shows the target as found after the detonation.

**Table 4.20 - Test 17 Results and Experimental Conditions**

Waveguide Type	4
Waveguide material	Standard composition and manufacture procedure
Target material	43 A, 65 mm thick
Explosive	SX2, 3 mm sheets, 2 complete layers plus a third layer after 100 mm ( attached to the target)
Central space	13 mm, air
Initiation	Equilateral triangle
Adhesive	Cyanoacrylate only
Anvil	Air under the waveguide region
Rolling Direction	Parallel
Surface condition	Polished
Confinement condition	Sand over air chamber
Results	No spall, separation of the plate in two halves. Fractures surfaces under 2 and 3 layers of explosive were similar. Fracture surface under the initiation system suggested that the fracture propagated backwards from the explosively loaded area.

## TEST 18

Test 18 uses a waveguide Type 4 with 6 layers of SX2 on a 50D target. **Table 4.21** describes the results and gives details of the experimental conditions. **Figure 4.26** show the charge configuration and the sizes and position of the induced crack. The top part of the cracks, inclined 45°, showed evidence of being produced by adiabatic shear. **Figure 4.27** shows the charge assembled on the target, **Figure 4.28** shows the target being recovered after the detonation.

**Table 4.21 - Test 18 Results and Experimental Conditions**

Waveguide Type	4 (with acrylic insert in the centre)
Waveguide material	Standard composition and manufacture procedure
Target material	50 D, 65 mm thick
Explosive	SX2, 3 mm sheets, 6 layers

Central space	13 mm, air
Initiation	Equilateral triangle
Adhesive	Cyanoacrylate only
Anvil	Air under the waveguide region
Rolling Direction	Parallel
Surface condition	Polished
Confinement condition	Sand
Results	Plate cut in two halves. Detached spall 15 to 20 mm thick in average. Initial portion of the spall attached under the region of initiation. Separation of the plate in two halves.

## TEST 19

Test 19 uses a waveguide Type 6 with 6 layers of SX2 on a 50D target. **Table 4.22** describes the results and gives details of the experimental conditions. **Figure 4.29** show the charge configuration. **Figure 4.30** shows the sizes and position of the induced cracks. The top part of the cracks, inclined  $45^\circ$ , showed evidence of being produced by adiabatic shear. **Figure 4.31** shows the charge assembled on the target, **Figure 4.32** shows the cut target back in UMIST

**Table 4.22 - Test 19 Results and Experimental Conditions**

Waveguide Type	6
Waveguide material	Standard composition and manufacture procedure
Target material	50 D, 65 mm thick
Explosive	SX2, 3 mm sheets, 6 layers
Central space	13 mm, air
Initiation	Equilateral triangle
Adhesive	Cyanoacrylate only
Anvil	Air under the waveguide region
Rolling Direction	Parallel
Surface condition	Polished
Confinement condition	Sand
Results	Detached central spall varying from 13 to 20 mm thick and 40 to 60 mm wide. Separation of the plate in two halves

## TEST 20

Test 20 used a waveguide Type 5 with 6 layers of SX2 on a 50D target. **Table 4.23** describes the results and gives details of the experimental conditions. **Figure 4.33** shows the charge dimensions. **Figure 4.34** shows the charge assembled on the target, **Figure 4.35** shows the bending left on the plate after detonation.

**Table 4.23 - Test 20 Results and Experimental Conditions**

Waveguide Type	5
Waveguide material	Standard composition and manufacture procedure
Target material	50 D, 65 mm thick
Explosive	SX2, 3 mm sheets, 6 layers
Central space	13 mm, rubber

Initiation	Equilateral triangle
Adhesive	Cyanoacrylate only
Anvil	Air under the waveguide region
Rolling Direction	Parallel
Surface condition	Polished
Confinement condition	Sand
Results	Bending of the plate of about 60°, indentation, vertical crack of about 90% of the thickness. Attached spall of 20 mm thick and 60 mm wide in average. Absence of the V shaped crack near the surface as produced by waveguides types 4 and 6 in Tests 18 and 19.

## TEST 21

Test 21 was carried out with a Type 8 (no charge Type 7 was tested) waveguide on 50D steel plate. Due to lack of space on the firing pit the testing was accidentally carried out on a solid rock anvil. This compromised any comparison of the results, but stressed the necessity of testing the successful designs on a solid anvil. **Figure 4.36** and **Figure 4.37** show the charge configuration and the induced crack pattern respectively. **Figure 4.38** shows the charge assembled onto the target. **Figure 4.39** shows the bending of the target. **Figure 4.40** shows the cracks on the target backface. **Table 4.24** describes the results and gives details of the experimental conditions.

**Table 4.24 - Test 21 Results and Experimental Conditions**

Waveguide Type	8
Waveguide material	Standard composition and manufacture procedure
Target material	50D, 65 mm thick
Explosive	SX2, 3 mm sheets, 6 layers
Central space	13 mm, waveguide material
Initiation	Equilateral triangle
Adhesive	Cyanoacrylate only
Anvil	Solid Rock
Rolling direction	Parallel
Surface condition	Polished
Confinement condition	Sand
Results	Internal cracks parallel and perpendicular to the rolling plane, bending varying from 15° to 18°.

## TEST 22

The test was designed, in function of the Test 21 results, to assess the effect of a solid rock anvil on the waveguide Type 6 performance. Test 22 repeats Test 19 using a solid rock base as anvil condition. The results showed an evolution of the crack patterns starting from the stage depicted in **Figure 4.41** near to the initiation, up to the complete cut stages showed in **Figure 4.42** mid length and **Figure 4.43** near the edge opposite to the initiation. The results

confirmed the detrimental effect of a solid anvil. **Table 4.25** describes the results and gives details of the experimental conditions.

**Table 4.25 - Test 22 Results and Experimental Conditions**

Waveguide Type	6
Waveguide material	Standard composition and manufacture procedure
Target material	50D, 65 mm thick
Explosive	SX2, 3 mm sheets, 6 layers
Central space	13 mm, waveguide material
Initiation	Equilateral triangle
Adhesive	Cyanoacrylate only
Anvil	Solid Rock
Rolling direction	Perpendicular
Surface condition	Polished
Confinement condition	Sand
Results	Crack pattern evolution from Internal cracks parallel and perpendicular to the rolling plane to complete cut. Bending varying from 15° to 18°.

It is possible to note that the top part of both specimens failed in shear. It is also possible to observe 2 different sizes of spall, in **Figure 4.42** the fracture plane above the spall shows the same dimension of the spall shown in **Figure 4.43** which also had multiple fracture planes.

### TEST 23

Following the results of Test 22 it was decided to investigate the possibility of obtaining the same kind of information with 43A steel targets. Test 23 was carried out with a Type 4 waveguide on a 43A steel. A 25 mm spacer between the solid anvil and the target was designed to assist the fracturing process. The waveguide length was 300 mm and it was positioned on the centre of the plate to investigate how much the crack would propagate.

The resulted fracture underneath the explosive charge was very similar to Test 17, however with a presence of small spall attached to one side of the plate. The crack propagated to both sides of the plate cutting the target in two halves. **Figure 4.44** shows the anvil and spacers used to separate the target from the anvil. **Figure 4.45** and **Figure 4.46** show the Test 23 before and after the detonation. **Table 4.26** describes the results and gives details of the experimental conditions.

**Table 4.26 - Test 23 Results and Experimental Conditions**

Waveguide Type	4
Waveguide material	Standard composition and manufacture procedure
Target material	43A, 65 mm thick
Explosive	SX2, 3 mm sheets, 3 layers

Central space	13 mm, waveguide material
Initiation	Equilateral triangle on a plaster support
Adhesive	Cyanoacrylate only
Anvil	43A steel plate with 25 mm spacers between the target and the anvil
Rolling direction	Parallel
Surface condition	Polished but with corrosion spots
Confinement condition	Sand over air chamber
Results	Separation of the plate in two halves with a central spall attached to one side (15 to 20 mm thick, 30 to 40 mm wide). The explosive induced crack propagated 150 mm on the front and back of the waveguide.

#### 4.6.2 Testing on Curved Plate and Tubulars

The development of the SWF technique was motivated by the necessity of cutting tubulars, with radius varying typically from 1 metre to 3 metres and thickness from 25 to 65 mm. Curved plates cut from 0.9 and 1 metre diameter tubulars of about 50 mm thick were made available to perform the trials. It was decided not to scale down the charge dimensions before trying the same waveguide on the new smaller thickness as it would show the ability of the waveguide design to cope with variations on target thickness. The successful results showed that the same charge configuration can be used in targets of different dimensions.

Two designs were selected from the tests on flat plates (Types 4 and 6) to be tested further using curved plates and tubular targets. Despite concerns of anvil conditions it was decided to proceed with the testing on curved plates and tubulars, as it would be possible in many situations to ensure an air environment on the internal parts of the tubular. All trials on curved plates and tubulars were originally intended to be performed using air as back-face condition. Tests C9 and C10 were performed under water with water as back-face condition the results confirmed the sensitivity of this method to back-face condition. The effect of confinement was investigated by performing trials where the charge was covered directly with sand and comparing with identical trials where an air chamber was used.

##### 4.6.2.1 Design Modifications

Curved plates were tested in much the same way as plates. Tests on full tubulars proved to require modification on the initiation system as the initiation used on flat and curved plates failed to cut under the initiation region. On flat and curved plates, it was possible to observe a fracture pattern suggesting that the fracture had propagated backwards towards the initiation. Initial trials on full tubulars showed that the fracture did not propagate backwards failing to cut under the initiation. An alternative was successfully tested in air but proved to be inadequate for underwater applications.



#### 4.6.2.2 Tests on Curved Plates and Tubulars

##### Test C1

Test C1 used a waveguide Type 6 on 50D curved plate. The plate was cut from a tubular 900 mm diameter, 50 mm thick. The waveguide successfully cut the target in two halves. By the lack of distortion on the original target curvature suggested that the fracturing was not assisted by bending.

The trial was monitored using the optical VOD meter to assess the synchronisation between the two detonation fronts. The results showed a  $0.7 \pm 0.1$  Microsecond between symmetric points at the end of the charge. **Figure 4.47** and **Figure 4.48** show the charge assemble on the target and the VOD meter optical probes inserted in the explosive. **Figure 4.49** and **Figure 4.50** show the cut target after the detonation. . **Table 4.27** describes the results and gives details of the experimental conditions

**Table 4.27 - Test C1 Results and Experimental Conditions**

Waveguide Type	6 (curved)
Waveguide material	Standard composition and manufacture procedure
Target material	50D, 50 mm thick, curved 900 mm diameter
Explosive	SX2, 3 mm sheets, 6 layers
Central space	13 mm, waveguide material
Initiation	Equilateral triangle
Adhesive	Cyanoacrylate only
Anvil	Air
Rolling direction	Unknown
Surface condition	Polished
Confinement condition	Sand
Results	Separation of the plate in two halves with a central spall (20 mm thick in average) attached to one side under the initiation region. Fracture surface under the initiation region suggested that the fracture propagated backwards from the main charge.

##### Test C2

Test C2 used a waveguide Type 4 on 50 D curved plate. The plate was cut from a tubular 900 mm diameter, 50 mm thick which contained a weld. The weld was ground flush and charge was place perpendicular to the weld as shown in **Figure 4.51**. The trial was monitored using the optical VOD meter Kontinitro to assess the synchronisation between the two detonation fronts, see **Figure 4.52**. The results showed a  $0.0 \pm 0.1$  Microsecond between

symmetric points at the end of the charge. **Figure 4.53** shows the cut target. **Table 4.28** describes the results and gives details of the experimental conditions.

**Table 4.28 - Test C2 Results and Experimental Conditions**

Waveguide Type	4 (curved)
Waveguide material	Standard composition and manufacture procedure
Target material	50D , 50 mm thick, curved 900 mm diameter
Explosive	SX2, 3 mm sheets, 6 layers
Central space	13 mm, waveguide material
Initiation	Equilateral triangle
Adhesive	Cyanoacrylate only
Anvil	Air
Rolling direction	Unknown
Surface condition	Polished
Confinement condition	Sand
<b>Results</b>	Separation of the plate in two halves with a central spall detached from the target (20 mm thick in average). Fracture surface under the initiation region suggested that the fracture propagated backwards from the main charge.

### Test C3

Test C3 used a waveguide Type 6 on 50 D curved plate. The plate was cut from a tubular 900 mm diameter, 50 mm thick. This test was carried out to repeat the results from Test C1 with air chamber between the sand cover and the charge. Very little difference was noticed between Tests C1 and C3, Test C3 result showed smaller indentation marks and slightly thinner spall than Test C1. **Table 4.29** describes the results and gives details of the experimental conditions. **Figure 4.54** shows Test C3 set-up, **Figure 4.55** shows the air chamber being covered with sand and **Figure 4.56** shows cut target as found after detonation.

**Table 4.29 - Test C3 Results and Experimental Conditions**

Waveguide Type	6 (curved)
Waveguide material	Standard composition and manufacture procedure
Target material	50D , 50 mm thick, curved 900 mm diameter
Explosive	SX2, 3 mm sheets, 6 layers
Central space	13 mm, waveguide material
Initiation	Equilateral triangle
Adhesive	Cyanoacrylate only
Anvil	Air
Rolling direction	Unknown
Surface condition	Polished
Confinement condition	Sand over air chamber
<b>Results</b>	Separation of the plate in two halves with a central spall attached to one side under the initiation region (15 mm thick in average). Fracture surface under the initiation region suggested that the fracture propagated backwards from the main charge

### Test C4

Test C4 used a waveguide Type 4 on 50 D curved plate. The plate was cut from a tubular 900 mm diameter, 50 mm thick. Test C4 was carried out to repeat the results from Test C2 with air chamber between the sand cover and the charge. The spall remained attached to the initiation region, this might have happened due to the difference in the confinement condition. **Table 4.30** describes the results and gives details of the experimental conditions.

**Table 4.30 - Test C4 Results and Experimental Conditions**

Waveguide Type	4 (curved)
Waveguide material	Standard composition and manufacture procedure
Target material	50D , 50 mm thick, curved 900 mm diameter
Explosive	SX2, 3 mm sheets, 6 layers
Central space	13 mm, waveguide material
Initiation	Equilateral triangle
Adhesive	Cyanoacrylate only
Anvil	Air
Rolling direction	Unknown
Surface condition	Polished
Confinement condition	Sand over air chamber
Results	Separation of the plate in two halves with a central spall attached to one side under the initiation region. Fracture surface under the initiation region suggested that the fracture propagated backwards from the main charge.

**Figure 4.57** shows that the target was placed on stones to raise it from the ground. The results demonstrated that this procedure when used on curved plates avoid the target being driven into the ground. **Figure 4.58** shows the initiation portion of the charge assembled onto the target where a lack of contact between the waveguide and the target can be observed. **Figure 4.59** shows the target as found after the detonation. **Figure 4.60** shows the back-face of the target where the spall attached to the initiation region can be observed.

### Test C5

Test C5 used a waveguide Type 6 on 50 D full tubular. The tubular was the same as the one used on tests C1 to C4. This test was carried out to with 4 waveguides, 3 using SX2 explosive and one using an experimental batch of an SX2 equivalent (RDX based) from another supplier. The test failed to separate the tubular in two halves. The regions under the initiation system did not fracture. The regions under the SX2 charge cut through the thickness of the target. The experimental explosive cut only on half the length in which was applied. The manufacture would not give any information about VOD or composition and was not interested in pursuing the matter further, therefore no attention was given to this result. **Table 4.31** describes the results and gives details of the experimental conditions. **Figure 4.61** to **Figure 4.64** show some photographs of the test before and after the detonation.

**Table 4.31 - Test C5 Results and Experimental Conditions**

Waveguide Type	6 ( in 4 segments, curved waveguides)
Waveguide material	Standard composition and manufacture procedure
Target material	50D , 50 mm thick, Tubular 900 mm diameter
Explosive	3 Waveguides SX2, 3 mm sheets, 6 layers, 1 Waveguide with experimental batch of PW2 (Paine & Wessex – UK)
Central space	13 mm, waveguide material
Initiation	Equilateral triangle
Adhesive	Cyanoacrylate only
Anvil	Air
Rolling direction	Unknown
Surface condition	Polished
Confinement condition	Sand over air chamber
<b>Results</b>	Cut regions restricted to regions underneath 6 layers of SX2. PW2 experimental batch waveguide cut only 50% of waveguide length Cracks failed to propagate towards the initiation regions and unloaded regions

**Test C6**

Test C6 was designed to test a new initiation system using a waveguide Type 6 on 50D curved plate. The new system intended to reduce the length of explosively unloaded regions around the initiation. The new initiation system was called vertical triangle and is shown in **Figure 4.65 to Figure 4.68**. The initiation system consisted of a vertical triangle made from 6 layers of SX2 and some confinement material (in this case some iron powder mixed with grease). **Table 4.32** describes the results and gives details of the experimental conditions. **Figure 4.65 and Figure 4.66** show the details of the Vertical Triangle initiation system. **Figure 4.67 and Figure 4.68** show the charge positioned on a target and confinement material placed around the initiation. **Figure 4.70 and Figure 4.71** show the fracture surfaces. **Figure 4.72** shows a section of the cut target under the main charge region.

**Table 4.32 - Test C6 Results and Experimental Conditions**

Waveguide Type	6
Waveguide material	Standard composition and manufacture procedure
Target material	50D , 45 mm thick, curved 1000 mm diameter
Explosive	SX2, 3 mm sheets, 6 layers
Central space	13 mm, waveguide material
Initiation	Vertical triangle
Adhesive	Cyanoacrylate only
Anvil	Air
Rolling direction	Unknown
Surface condition	Polished
Confinement condition	Iron power, around the initiation.
<b>Results</b>	Separation of the plate in two halves with a central spall detached from the plate in the regions away from the initiation system. The fracture surface indicate that the fracture occurred due to explosive loading and not

	propagating backwards as previously. It was clearly however that the pattern was more chaotic and showing multiple spalling being quite distinct from the region under the waveguide. The length affected by the initiation system was approximately 70 mm on each side of the Vertical Triangle.
--	---

### Test C7

Test C7 used a waveguide Type 6 on a 45 mm thick, 50D steel tubular. This test was designed to test a new initiation system on a full tubular. One Vertical Triangle was confined with a pre-cast confinement sleeve as shown in **Figure 4.73** (initiation point 1) and a second used the iron powder with grease (initiation point 2) as shown in **Figure 4.74** and **Figure 4.75**. **Figure 4.76** shows a 7 mm space between waveguides. **Figure 4.77** shows detonation cord lines (PETN based – ICI – Cordtex) of same length used to ensure synchronisation between the two initiation regions. **Figure 4.78** shows the cut target. **Table 4.33** describes the results and gives details of the experimental conditions.

**Table 4.33 - Test C7 Results and Experimental Conditions**

Waveguide Type	6
Waveguide material	Standard composition and manufacture procedure
Target material	50D , 45 mm thick, curved 1000 mm diameter, 750 mm long
Explosive	SX2, 3 mm sheets, 6 layers
Central space	13 mm, waveguide material
Initiation	Vertical triangle
Adhesive	Cyanoacrylate only
Anvil	Air
Rolling direction	Unknown
Surface condition	Polished
Confinement condition	Pre-cast Waveguide material around initiation (1) Iron power + grease around initiation (2)
Results	Separation of the tubular in two halves with a central spall detached from the tubular. The fracture pattern was similar of Test C6. The length affected by the initiation system was approximately 150 mm on each side of the Vertical Triangle (probably due to the extra confinement length).

### Test C8

Test C8 used a waveguide Type 6 on a 45 mm thick, 50D steel tubular. This test was carried out to repeat Test C7. The target used was 1 metre long as the C7 target had shown severe distortion, specially under the initiation region. **Figure 4.79** shows the iron and grease confinement being placed on the initiation (2). **Figure 4.80** shows the chamber dug on the ground for the detonation. The chamber was covered with a lid and some 4 cubic metres of sand was used to cover the lid in order to reduce noise. **Figure 4.81** shows the cut target. **Table 4.34** describes the results and gives details of the experimental conditions.

**Table 4.34 - Test C8 Results and Experimental Conditions**

Waveguide Type	6
Waveguide material	Standard composition and manufacture procedure
Target material	50D , 45 mm thick, curved 1000 mm diameter, 1000 mm long
Explosive	SX2, 3 mm sheets, 6 layers
Central space	13 mm, waveguide material
Initiation	Vertical triangle
Adhesive	Cyanoacrylate only
Anvil	Air
Rolling direction	Unknown
Surface condition	Polished
Confinement condition	Waveguide material around initiation (1) Iron power + grease around initiation (2)
Results	Separation of the tubular in two halves with a central spall detached from the tubular. The fracture pattern was similar of Test C6 and C7. The length affected by the initiation system was approximately 150 mm on each side of the Vertical. The tubular showed much less ovalisation than in C7.

### Test C9

Test C9 used a waveguide Type 6 on a 45 mm thick, 50D steel tubular. This test was carried out to test the charge performance underwater. The test was carried out in 10 metre deep water in a near shore site in Holland. The target used was 1 metre long and was originally designed to be cut using an air chamber inside the tubular. Unfortunately, as a condition for the trial to be performed, the back-face condition used was seawater. Therefore Tests C9 represents a deviation of the controlled conditions of previous tests and introduced a new variable.

One planned alteration for this test in relation to Test C8, was the exclusion of the confinement in the initiation region. This was decided as the water would have significant effect on the confinement, and the confinement sleeve could represent an unnecessary weight for the charge, taking into account that air was the intended back face condition.

The Vertical Triangle was reinforced with rubber stiffeners to resist the deployment operations. The stiffeners were glued in the central space of the waveguide, as shown in **Figure 4.82**. **Figure 4.83** and **Figure 4.84** show the protective cage used to place the target and the cage being lowered to the water. The effect on the protective cage can be seen in **Figure 4.85**, which shows the target being retrieved after the detonation. **Figure 4.86** and **Figure 4.87** show the inner surface of the tubular where the spall on the waveguide and initiation regions can be observed. **Table 4.35** describes the results and gives details of the experimental conditions.

**Table 4.35 - Test C9 Results and Experimental Conditions**

Waveguide Type	6
Waveguide material	Standard composition and manufacture procedure
Target material	50D , 45 mm thick, curved 1000 mm diameter, 1,000 mm long
Explosive	SX2, 3 mm sheets, 6 layers
Central space	13 mm, waveguide material
Initiation	Vertical triangle, with rubber stiffeners, No iron powder confinement
Adhesive	Cyanoacrylate only
Anvil	Sea Water
Rolling direction	Unknown
Surface condition	Polished
Confinement condition	Sea water
<b>Results</b>	On approximately 65% of the circumference of the tubular, the charge cut the target as Tests C7 and 8 but with the spall still attached at intervals. Two remaining areas under the two initiations (of about 300 mm long each) fail to cut through the thickness.

**Figure 4.88** shows the section from the target approximately 400 mm away from the initiation. This section shows a detached spall plus the top shear fracture characteristic of trials with waveguide 6 on 50D targets. **Figure 4.89** shows a section from the target under the initiation region. The section shows a spall (in fact attached) but no top fracture as found in tests C6, C7 and C8.

### Test C10

Test C10 used a waveguide Type 6 on a 45 mm thick, 50D steel tubular. This test was initially designed to repeat test C9, or as originally intended, to be carried out using an air bag on the back face of the target. Again the set-up using water on the back face was imposed as a condition to carried out the test. The results of C9 Test were analysed and it was believed that the initiation system would benefit from extra confinement. It was also thought that an extra confinement would increase the chances of the spall along the length of the waveguide to detach from the target. An improvised solution using lead and fine stones aggregate was used to achieve the confinement intended.

A 2.5 to 3 mm thick lead cover was applied all over the circumference, gluing it to the explosive. The lead layer was then covered with a layer of 20 to 30 mm made from an aggregate of plastic binder and stones (2 to 5 mm). The test was then carried out in the same way as in Test C9, by lowering down the target to the sea bottom, moving the support boat away to a distance of about 1000 metres and detonating the charge in a previously agreed time. **Figure 4.90** shows the charge assembled onto the target. **Figure 4.91** shows the target covered with the fine stone aggregate. **Figure 4.92 and Figure 4.93** shows the target being

lowered into the water. **Figure 4.94** show the target being retrieved. **Figure 4.95** and **Figure 4.96** show sections of the target under the main charge region and initiation region respectively. **Table 4.36** describes the results and gives details of the experimental conditions.

**Table 4.36 - Test C10 Results and Experimental Conditions**

Waveguide Type	6
Waveguide material	Standard composition and manufacture procedure
Target material	50D , 45 mm thick, curved 1,000 mm diameter, 1,000 mm long
Explosive	SX2, 3 mm sheets, 6 layers
Central space	13 mm, waveguide material
Initiation	Vertical triangle
Adhesive	Cyanoacrylate only
Anvil	Sea Water
Rolling direction	Unknown
Surface condition	Polished
Confinement condition	2.5 mm to 3 mm of led covered with 20 mm to 30 mm of fine stone aggregate
Results	The main characteristic observed was the absence of shear fractures at top surface. Being this way the charge failed to produce a crack that completely cut through the thickness of the target. A spall was produced in a similar fashion as in Test C9, but again remained attached to the target. The results, despite of a negative nature, revelled an extremely relevant aspect of the charge behaviour.

It can be observed from **Figure 4.95** that the top crack failed to propagate to the surface. This was effect noticed all around the tubular which had (as in all tubular tests) four waveguides initiated in pairs. It can be observed in **Figure 4.96** that the deformation under the initiation was bigger than in Test C9 suggesting a longer duration for the pressure pulse.

#### 4.7 Metallographies and Hardness Profiles of Selected Samples.

The hardness profiles of some selected samples are presented in this section, also some of features present on the fracture patterns are described using optical microscopy. The use of electron microscopy was not made available to this work.

The micrographs were scanned into this document using their original size to maintain the enlargement accuracy and to allow easier visualisation of the features presented.

##### 4.7.1 Metallographic Examination

###### Test 22

**Figure 4.97** shows the locations where optical microscopy was used to analyse samples taken from Test 22 . The results are shown in **Figure 4.98** to **Figure 4.107** The adiabatic shear



failure at the top of the specimen can be observed in **Figure 4.103**. The spall formation due to coalescence of voids and micro-cracks can be observed in **Figure 4.104** to **Figure 4.107**.

#### Test C9

**Figure 4.108** shows the locations where optical microscopy was used to analyse samples taken from Test 22. The specimen was taken 300 mm away from the initiation and is representative of the fracture patterns under the main charge. The spall formation due to the coalescence of micro-cracks can be observed in **Figure 4.109** to **Figure 4.112**.

#### Test C10

**Figure 4.113** shows the location of samples. The specimen was taken from a region under the initiation system. **Figure 4.114** to **Figure 4.129** show the different stages of crack formation.

### 4.7.2 Hardness profiles

Hardness examination was performed in some selected specimens. Hardness profiles of tests using 9 mm of SX2 did not provide significant variation in hardness, this is in agreement with results from [7], where hardness profiles proved inconclusive.

Some of the results using 18 mm explosive thickness (Test 22, C9 and C10), showed significant variation of hardness and its profiles are presented in **Figure 4.130** to **Figure 4.134**.

**Figure 4.130** shows Vickers' hardness profiles for Test 22. Significantly higher values (258/238 Hv) can be observed at the central region failed in shear and at the point where the explosive was in contact with the target (at the edge of the waveguide). **Figure 4.131** shows the profile for Test C9, 400 mm away from the initiation region. Higher values are also found near the central shear crack and the position where the explosive was in direct contact with the surface. **Figure 4.132** shows the profile for Test C9 under the initiation region. The values do not show the clear increase near the surface or at the cut centre line. This result could suggest that the interference of incident shockwaves at the centre line did not occur. **Figure 4.133** shows the profile for Test C10, 400 mm away from the initiation. The values at the region where explosives were in contact with the metal did not show the same increase observed in Test C9. The values at the centre line are higher near the two shear cracks surfaces. **Figure 4.134** shows the profile for Test C10 under the initiation region. Cluster of high hardness

values seems randomly positioned in the specimen. It can also be observed that the degree of plastic deformation is much higher than on the other specimens.

## **4.8 Discussion and conclusions of SWF Technique experimental results**

### **4.8.1 Overview**

The present work gives continuation to the work of Al-Hassani and Burley [4][19] on the development of Shock Wave Focusing. By re-examining experimental results from references [4] and [19] it was noticed that different waveguide geometries were capable of cutting 1 inch mild steel targets while on the other hand, charges using waveguide geometries similar to successful ones were not able to cut. It became apparent that the performance of a particular waveguide geometry was strongly affected by one or more additional variables. As described in section 4.2, seventeen variables in addition to the waveguide geometry were identified as capable of influencing test results. Several steps were taken to minimise this influence and allow meaningful comparisons to be made.

After initial trials, the waveguide **Central Space Without Explosive (CS)** was identified as the main peripheral variable capable of jeopardising the charge performance. CS is defined as the space between the explosive strips on top of the waveguide. The results from references [4],[19] when analysed in conjunction with the results in the present work show strong evidence to support this claim. As shown in Section 5, the immediate consequence of covering the waveguide with explosive is the interference of incident shock waves within the waveguide while probably increasing the waveguide density during shock transmission. A description of the CS analysis of [4][19] is given in this Section. The trials carried out in the present work kept CS to a minimum and a better evaluation of the effect of other variables was possible.

The design of improved waveguide geometries proved to be a complex matter as main waveguide properties are unknown at the pressures and strain rates considered. The main unknown material characteristics are the material shock properties (Hugoniot), especially when it is taken into account the relative thickness of explosive and waveguide material used. Seven waveguide geometries were proposed, some intended to rely mainly on the interference of reflected stress waves and some taking into account the interference of incident shock waves. Design Types 1, 2 and 3 were aimed to fracture the material using reflected stress waves while Types 4 and 6 also relied on the interference of incident shock waves. Types 5 and 8 were not intended to cut but aimed to provide limits to the reviewed design parameters.

Waveguide Types 2 and 4 successfully cut 43A steels and waveguide Types 4 and 6

cut 50 D steel plates and tubulars. Waveguide Type 2 failed to cut 50D steel with the same explosive load used with 43A and Waveguide Type 6 was not tested on 43A steels. Metallographic examination of 50D specimens in conjunction with numerical analyses suggest that the cutting process using waveguide Types 4 and 6 rely greatly on the interference of incident stress waves and spall formation to achieve the cut in the 50D targets. Tests using waveguide Type 2 on 50D steel failed to produce any cracks with the explosive load used. Tests using waveguide Type 3 failed to cut 43A and 50D steels.

Tests on tubulars required the development of an annular initiation system which was successfully tested in air but failed to cut underwater. The results in air suggested that the Type 6 charge would have cut the tubular if the trial was conducted with air on the back face as originally intended.

A detailed discussion of the issues raised above is presented bellow. It has to be pointed out that the experimental and numerical limitations greatly reduced the ability to provide a comprehensive understanding of all the issues raised and that the discussion and results are limited to the waveguide material used.

#### **4.8.2 Discussion of SWF experimental results**

##### **4.8.2.1 Explosive Distribution**

Within the experiments performed during the present work, Test 7 highlighted the notion that the explosive distribution on top of the waveguide could affect the charge cutting performance. Test 7 used a waveguide Type 1 and the same explosive load of Test 8. Test 7 concentrated the explosive distribution on the edges of the waveguide aiming to decrease the amount of energy used to create spall and increase the amount of energy used to create a vertical crack. When compared results of Tests 7 and 8 it became clear that the explosive distribution in Test 7 actually reduced the amount of energy available to create a vertical crack. Test 7 had a much larger central area without explosive - CS when compared with Test 8, the results of Test 7 showed complete absence of cracks and the central part of the waveguide was found after the detonation. The difference in performance suggested that a larger central part of the waveguide without explosive had reduced the efficiency of the waveguide in transmitting the pressure pulse from the explosive to the target.

Based on the results of Tests 7 and 8, the results from [4][19] using polymeric waveguides were analysed, and showed that 93 % of the failed geometries had (CS) values larger than 20% of the total waveguide width. When results that used cold rolled steel targets are excluded from the analyses it can be seen that all tests failed with (CS) bigger than 25%.

Also only 2 tests failed with (CS) smaller than 20%. In all successful experiments carried out during the current work, (CS) was reduced to 13 mm giving values of CS/charge width from 10% to 17%. To compare (CS) from flat waveguides, segmental waveguides and circular waveguides the results from the latter two were plotted in terms of average angle (A), defined as the angle described by the arc determined by the explosive on the waveguide. To analyse the results of [4][19], it was necessary to draw all the explosive charges and measure (CS) and Average Angle (A). **Figure 4.135** shows results of 25.4 mm thick plates from [4][19] plotted in terms of (CS) as a percentage of the total waveguide width against Average Angle (A) in degrees, the circle diameters represent explosive load in Kg per meter. It can be seen from **Figure 4.135** that trials using cold rolled steel seem insensitive to variations in (CS) values with success achieved from 0 to 55%. The only unsuccessful result in using cold rolled steel with CS below 20% had  $(A) = 10^\circ$  and could have been beyond a lower boundary for values of (A). Unsuccessful results using 50D steel could have been explained by insufficient explosive load but as shown by the circle diameters this does not seem to be a correct assumption in all cases. When comparing results using 070M20 steels the pattern is quite clear showing successful results for values of (CS) lower than 20%. Only one test using 070M20 steel failed using  $(CS) = 0\%$  and can not be explained in terms of the variables analysed, however this seems remarkable taking into account the number of experiments considered.

**Figure 4.136** shows a similar analysis for the results described in Section 4. The data include all Tests with the exception of Tests 6B and C10. Test 6B was excluded due to the fact that it was performed with a waveguide of known poor quality material where excessive amounts of air bubbles were present throughout the waveguide. Test C10 was excluded as it was performed underwater with additional lead and concrete confinement. On **Figure 4.136** it can be observed that successful trials using 50D steel had (CS) values smaller than 17% and average angle (A) varying between  $20^\circ$  to  $35^\circ$ . Tests from Al-Hassani & Burley [4] using 65 mm 43A steel are included for completeness. Tests performed during the present work had not intended to assess (CS) limits, some of the initial Tests had higher CS values but most tests were performed with CS values within the perceived limit of 20%.

#### 4.8.2.2 Waveguide geometry

The sound speed in the waveguide could be considered as the main parameter necessary for the design of a waveguide geometry, as it will affect the refraction angle between the waveguide material and the steel target. Also waveguide density together with its

sound speed will control the amount of energy transmitted to the steel target. Both parameters will vary within the pressure range considered and the Hugoniot properties becoming more important for higher values of pressure. Initial waveguide material density of approximately 2.5 g/mm<sup>2</sup> and a sound speed of approximately 1.000 m/sec provided the lower limit for the waveguide material used. Considering the case where the stress waves would be predominantly elastic, both sound speed and density of the waveguide were initially considered to be significantly smaller than steel. Being this the case, a graphic solution for the 2 dimensional - elastic case was proposed and is presented below for the case where the velocity of propagation of the stress wave within the waveguide is assumed to be half of the steel target.

The direction of the reflected and transmitted elastic waves is determined by Snell's law which was initially developed for optics but is widely applied in acoustics and is as follows [75]:

$$\frac{\sin \alpha_i}{\sin \alpha_t} = \frac{C_i}{C_t} \quad (4.1)$$

where  $\alpha_i$  is the incident angle and  $\alpha_t$  is the transmitted angle,  $C_i$  is the wave speed in the incident medium and  $C_t$  is the wave speed in the transmitted medium. From the above relation it can be seen that the angle of the transmitted stress wave will depend on the incident angle and the ratio between the wave speeds of incident and transmitted mediums. In the case of an interface between a curved waveguide and a flat plate,  $\alpha_i$  varies resulting in different  $\alpha_t$  for a particular ratio  $C_i/C_t$ .

From the dimensionless design parameters from references [4][19] shown in **Figure 2.31** it can be observed that for the same waveguide width/plate thickness success was achieved with higher values of offset/plate thickness (in other words with larger diameters). This suggested at the time of the trials with waveguide 1, that the success with large diameters could have provided a correction to compensate a possible lower wave speed within the waveguide. Waveguide Types 2 and 3 were designed to provide larger diameters when compared with results using 65 mm 43A targets from [4] shown in **Figure 2.32**. This comparison is shown in **Figure 4.137**, however the results using offset values around 0.15 / 0.20 had values of CS higher than 20% and includes results from Test 8, which used a waveguide Type 1, CS of 22% and achieve a vertical crack through 2/3 of the thickness.

Despite the fact that a successful cut was obtained when the offset value was increased

from 0.15 to 0.42 (Tests 9,10 and 11 - Waveguide Type 2) it can be observed that the results using offset value of 1.1 (Test 14 - Waveguide Type 3) failed to cut and showed a large spall (same width as the explosive charge) with no vertical crack. The large spall in Test 14 suggested that the particle velocities were predominantly perpendicular to the surface indicating a small variation in the original incident angle  $\alpha_i$ . This suggests that the wave speed within the waveguide material was possibly closer to the wave speed in the steel target than originally expected for elastic waves. To analyse this apparent conflicting results, the data from **Figure 2.31** were revisited and when results with  $CS > 20\%$  are excluded, **Figure 2.31** become as shown in **Figure 4.138**.

It can be seen from **Figure 4.138** that no relation can be drawn once the results with  $CS > 20\%$  are excluded. Up to the point where waveguide Types 1 to 3 were tested, waveguide Types 2 ( $CS < 20\%$ ) successfully cut 43 A targets but failed to cut a 50D target with the same amount of explosive. Waveguide Type 3 ( $CS < 20\%$ ), which had a larger diameter than Type 2, failed to cut 43A target (despite using more explosive than Type 2), and also failed to cut 50D target and also produced a spall. At this stage it became apparent that the failure using waveguide Type 1 could have been more related to  $CS$  than to its geometry. By observing the geometry of waveguide Type 3 in **Figure 4.18**, it can be noticed that it consists of a very flat curve with low Average Angle, and looking back to **Figure 4.135** it can be observed a failed trial using cold rolled steel with  $CS = 0\%$ , Average Angle =  $10^\circ$ . This occurred despite the relative large amount of explosive used. The data was then reanalysed in terms of Average Angle. It can be observed from **Figure 4.135** that successful results were achieved using average angles from  $20^\circ$  to  $40^\circ$ . Based on that, the search of a focus point using elastic theory was abandoned in favour of a set of trials assuming that shock waves would require waveguides that provide higher Average Angles. Waveguide Types 4, 5 and 6 were designed and tested with this philosophy while maintaining similar Charge-Width/Target Thickness ratio. Waveguide Type 8 was intended to use approximately  $30^\circ$  with a different Charge-Width/Target-Thickness ratio.

The results are presented in **Figure 4.139** plotting values of Average Angles against Charge-Width/Target-Thickness ratio. **Figure 4.139** include results from all waveguide types, failed results using waveguide Type 1 are included for completeness but they were tested with  $CS > 20\%$ . Results from tests 6B and C10 were omitted, as 6B-waveguide material contained excessive amounts of air bubbles and C10 was fired underwater with additional lead confinement. It can be observed from **Figure 4.139** that it seems to appear an upper and lower boundary for values of Average Angle with the same Charge-Width/Target-Thickness

ratio beyond which cutting is not achieved. It is not clear if there is an upper boundary for values of same Charge-Width/Target-Thickness ratio, but to maintain  $CS < 20\%$ , larger Charge-Width/Target-Thickness ratio would result in excessive explosive loading. A lower boundary for values of Charge-Width/Target-Thickness ratio was not precisely determined as Test 21 result was affected by back-face condition and its narrow geometry resulted in lower explosive load. Nevertheless the Charge-Width/Target-Thickness ratio of 1.15 (Waveguide Type 6) successfully cut 50D steel which is substantially lower than the value of 1.5 determined by Denis [5] using demolition charges for mild steel.

#### **4.8.2.3 Back Face Condition**

The detrimental effect of hard anvil and water as back face condition was clearly demonstrated in the case of 50D steels. The evidence for a hard anvil like solid rock base is found in Tests 21 and 22 while the results from Tests C9 and C10 show evidence of the detrimental effect of water as anvil condition. It is particularly interesting the effect of water had in Test C9 suppressing the detachment of the spall and the fracturing under the initiation region. The effect of anvil condition under the initiation region is discussed in the following subsection "cutting phenomenology". The result from Test C9 showed a smaller, but significant, local deformation in the tubular when compared with Test C8 carried out in air.

The effect of anvil condition on 43A steel seemed less acute as Test 23 suggested. Test 23 was intended to assess if the cutting process was assisted by bending, and to achieve that a 300 mm long cutting charge was used on a 600 mm long 43A target with a 25 mm gap between the target and a steel anvil. The result showed a complete cut with very little deformation of the target, only a localised depression under the charge. As it will be discussed later the possible main effect of a solid anvil on 50D targets could be the suppression of localised deformation required to complete the cutting process. Nevertheless the work described in Section 4 aimed to cut tubulars used as offshore platform legs and in many cases there are no anvil other than water. Access to the internal parts of the tubular is often feasible enabling the deployment of an air environment by introducing specialised but commercially available air bags.

#### **4.8.2.4 Initiation**

The successful tests on 50D plates and curved plates showed that charges were able to cut the target in two halves despite the reduced explosive load under the initiation region, in all cases it was possible to observe that the fracture had propagated backwards towards the

initiation. Test C5 showed however that when cutting a tubular the cracks failed to propagate towards the unloaded regions. An initiation system was proposed, aiming to reduce the unloaded regions to a minimum and it successfully cut a curved plate in Test C6 and Tubulars in Tests C7 and C8. The fracture pattern as shown in **Figure 4.69** and **Figure 4.70** showed clearly that a different cutting mechanism was responsible for the cutting under the initiation region. The region affected by the initiation system (about 140 mm) was much greater than the 18 mm of the vertical triangle used as initiation system. In any case the target cut under the initiation and no further improvement was planned for the underwater trials to avoid the introduction of uncertainties. The results of the underwater trials introduced an unplanned variable which was the water in the back face, and the results showed that the fracture under the initiation systems failed to propagate to the top surface of the target as shown in **Figure 4.89** and **Figure 4.96**. Comparison between the hardness profiles of regions under the vertical triangle initiation with regions away from the initiation showed that the specimens under the initiation system lack high values of hardness in the centre of the of the specimen as observed in samples away from the initiation region.

#### 4.8.2.5 Target material

It was not the objective of this work to analyse the influence of the material properties on the cutting process, nevertheless the following observations can be made:

- Identical charges successfully cut 43A targets and fail to cut 50D grade targets of the same thickness. Taking into consideration the similar range of Tensile Strength and Yield strength between 43A and 50D grade it is possible to suggest that the dramatic difference in results are related to the difference in fracture toughness. This effect is discussed in reference [31] where the effect fracture toughness on the time required to initiate the crack is pointed out. In the case analysed in this work, by increasing the explosive load, not only the duration of the pulse was increased but also the maximum peak pressure, therefore a direct comparison for the effect of the duration of the pulse is not possible. However it was observed that charges detonated with sand as confinement produced slightly more damaged and deformation than charges detonated with air chambers.
- Identical charges successfully cut 50D, 50E and 50EE grades. Despite the variation in thickness, it is possible to suggest that the explosive load used was



above a threshold valid for the 50EE grade and therefore it was not possible to observe any difference in behaviour between the 3 grades.

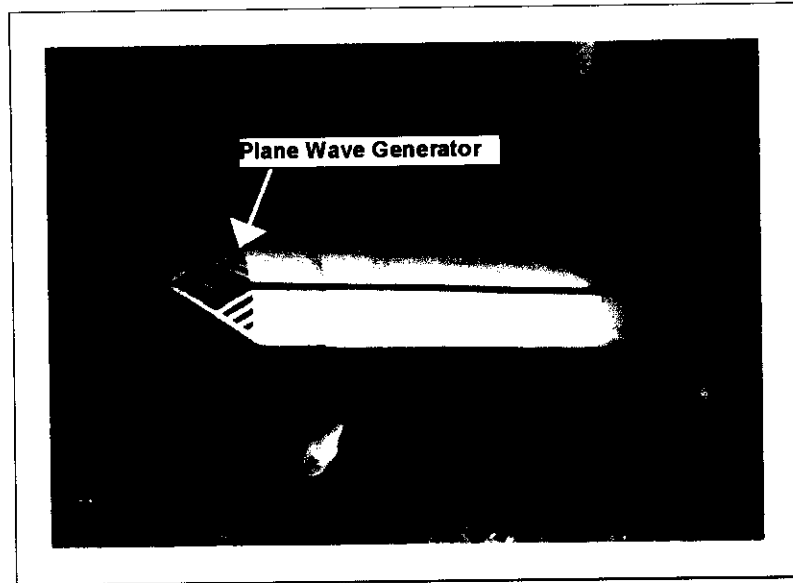


**Figure 4.1:** A waveguide being assembled with a plane wave generator.

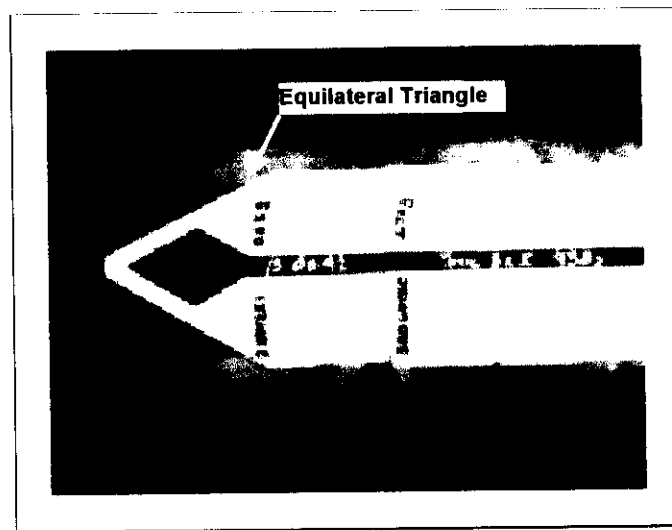


**Figure 4.2** An equilateral triangle mounted on a waveguide

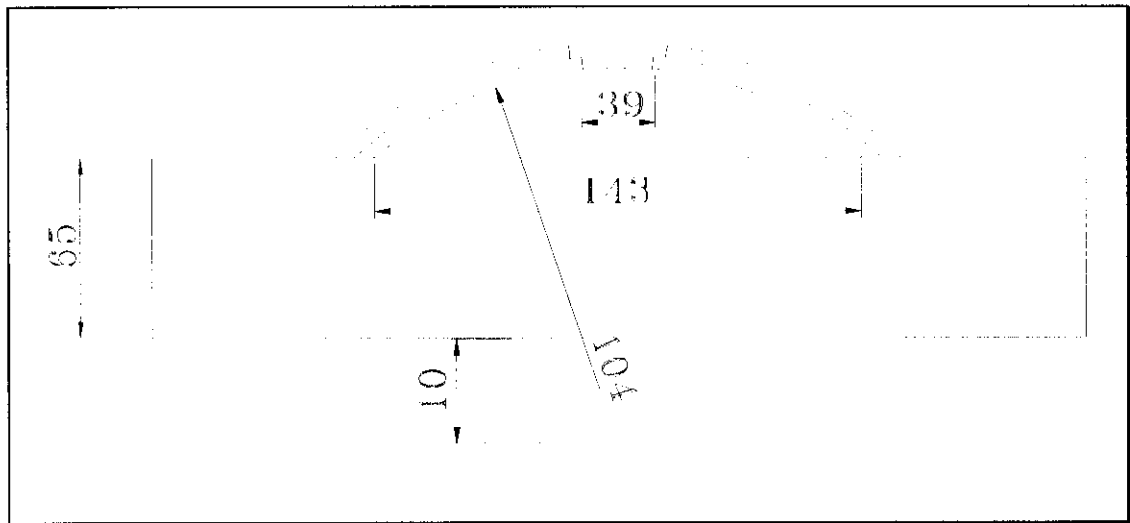


**Figure 4.3:** Test 1 configuration, note that the explosive nearly does not touch the target

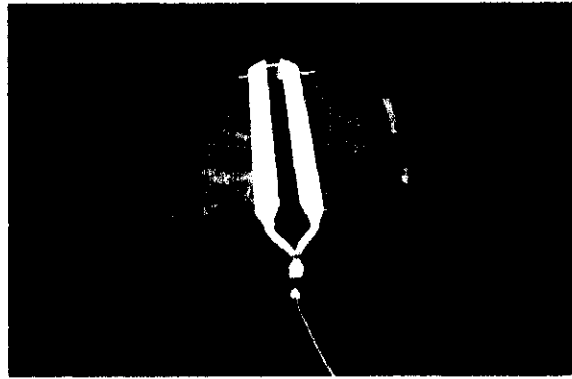


**Figure 4.4:** Charge assembled on the target where the tail initiation can be observed.

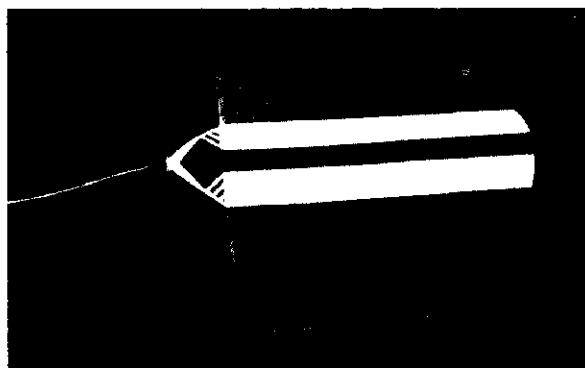


**Figure 4.5:** Charge assembled on the target. The plane wave generator assembled outside the target can be seen.

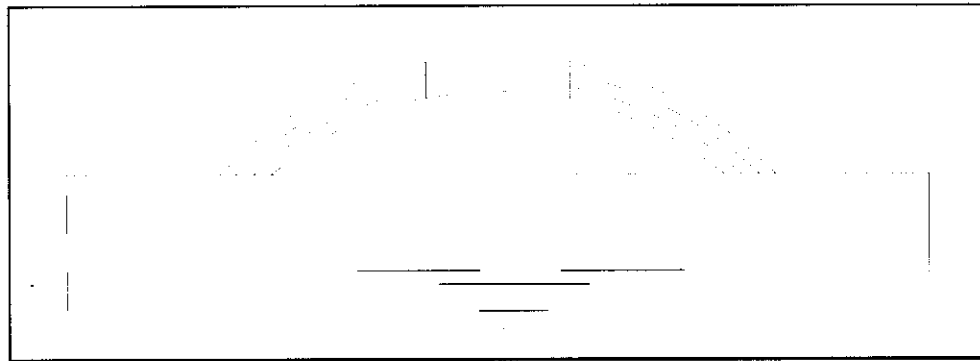


**Figure 4.6:** Test 4 configuration, explosive is in contact with the target. Note the position of induced cracks.

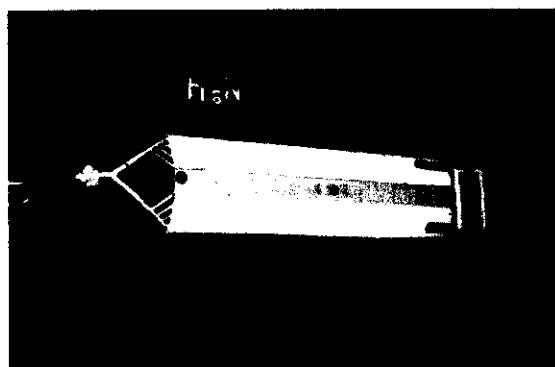


**Figure 4.7:** Steel waveguide assembled on the target.



**Figure 4.8:** Test 4 as found after the detonation. Indentation marks on the target can be observed.

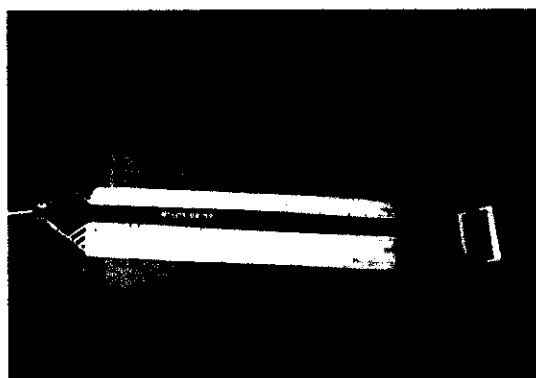


**Figure 4.9** Test 5 before detonation. The D'autriche witness lead plate can be seen protected by a steel tubular.

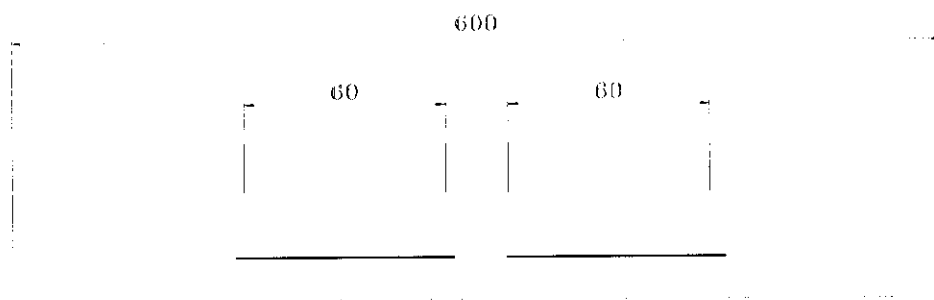


**Figure 4.10: Test 6A configuration and crack positions.**

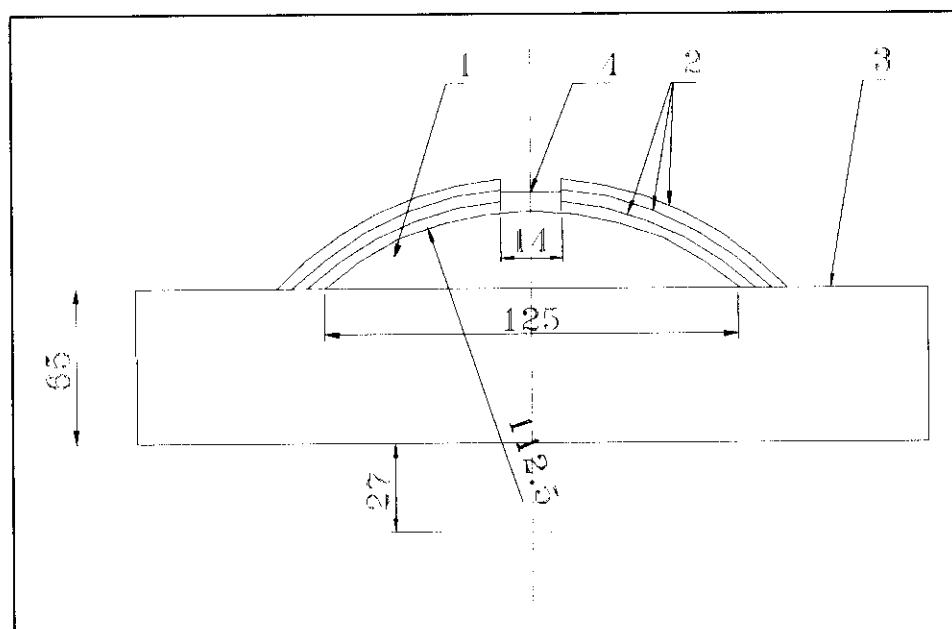


**Figure 4.11: Waveguide Type 2 with 3 layers of SX2.**

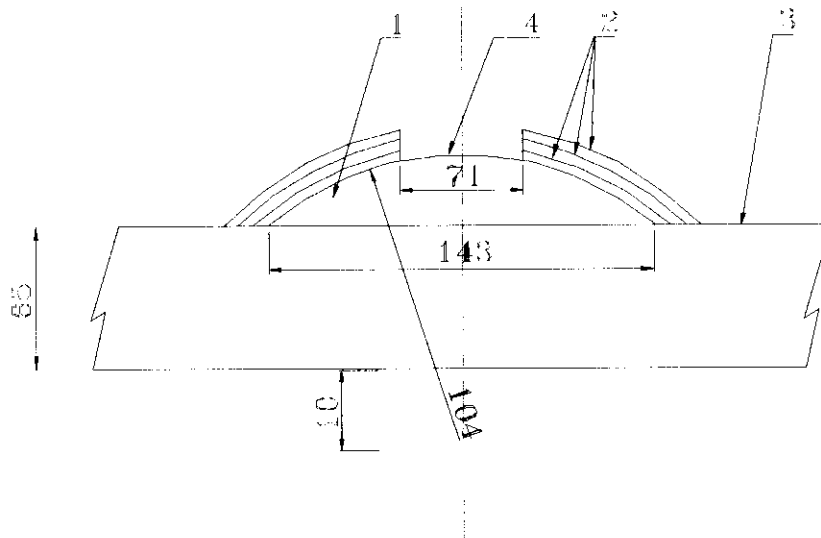


**Figure 4.12:** Test 7 configuration, explosive is concentrated on the edges of the waveguide. Note the size of the space on the waveguide without explosive.

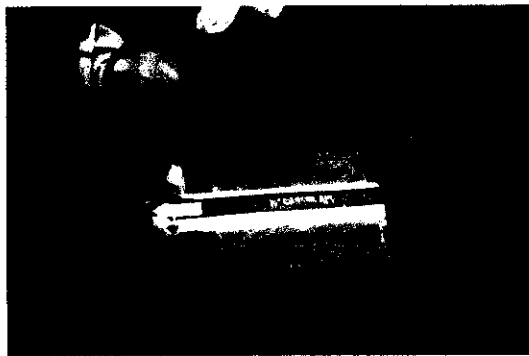


**Figure 4.13:** Test 7 before detonation. The initiation system on a plaster base outside the target plate can be observed.

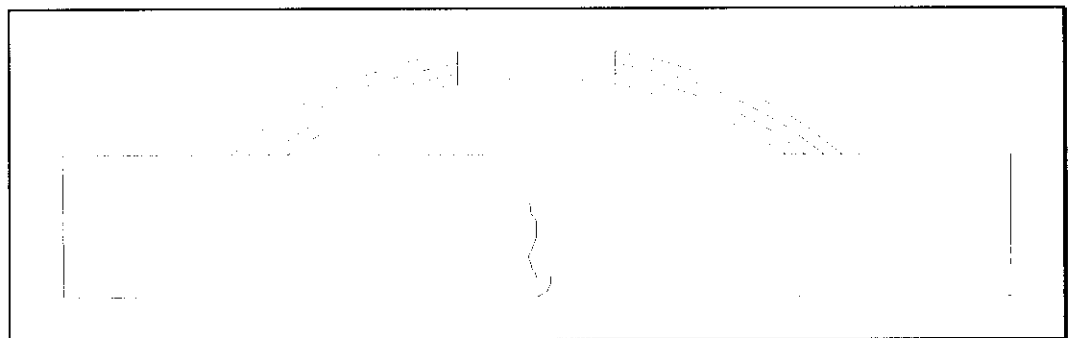


**Figure 4.14:** Test 8 charge configuration and induced crack pattern.



**Figure 4.15:** Test 8 before detonation.

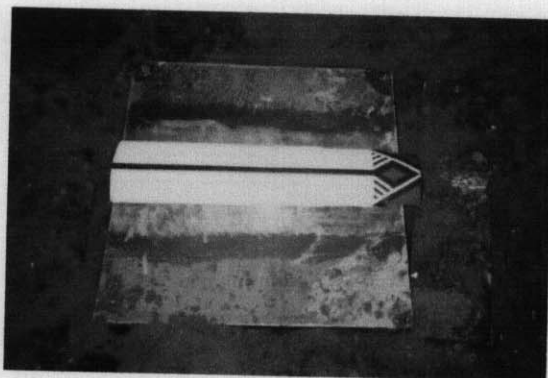


**Figure 4.16:** Test 9, charge assembled on the target.



**Figure 4.17:** Cut target as found after the detonation.

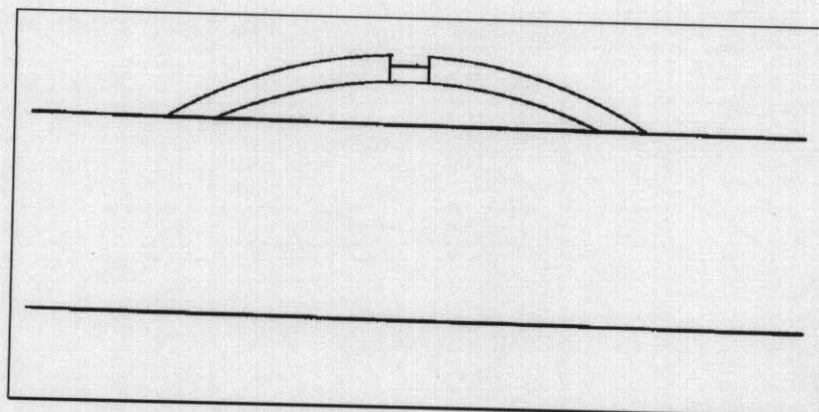


**Figure 4.18:** Test 14 charge configuration and the induced crack pattern.

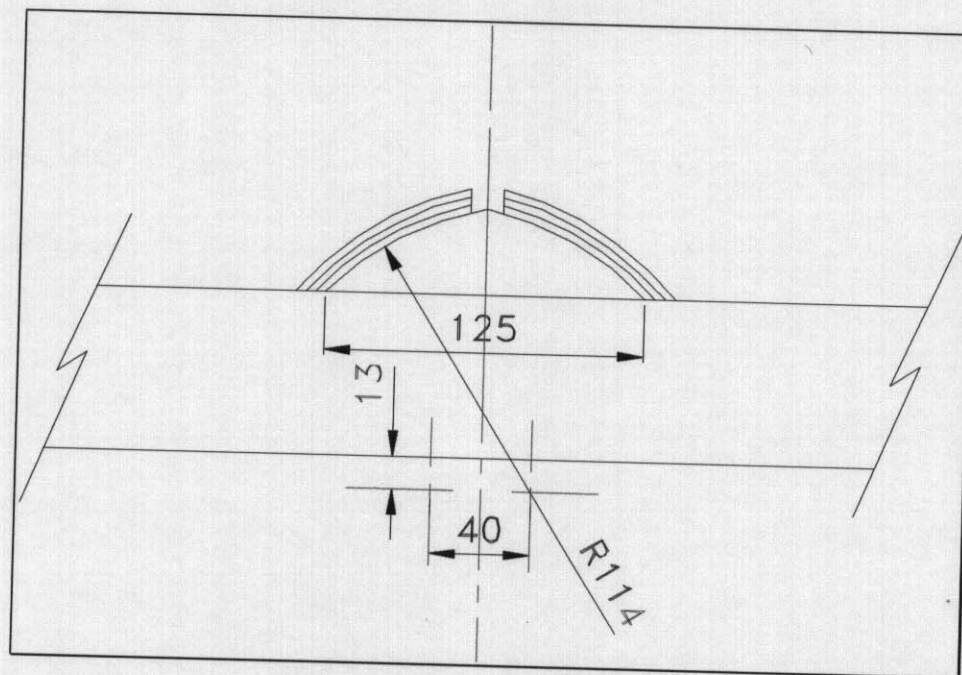


**Figure 4.19:** Waveguide type 4 charge configuration.



**Figure 4.20:** Test 15, charge assembled onto the target.



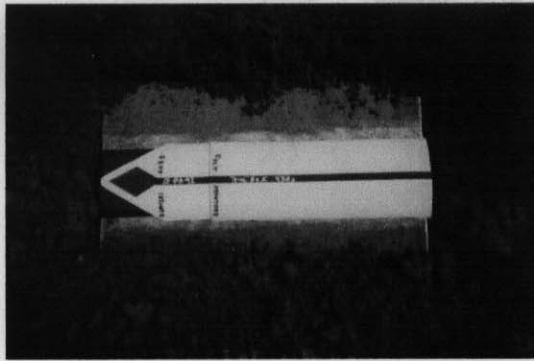


**Figure 4.21:** Test 16 charge assembled on the target.

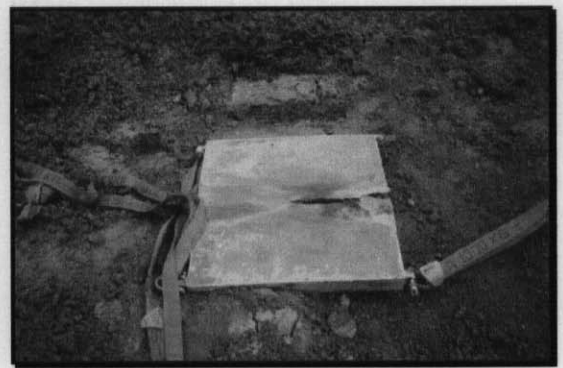


**Figure 4.22:** Test 16, target back face after recovery.

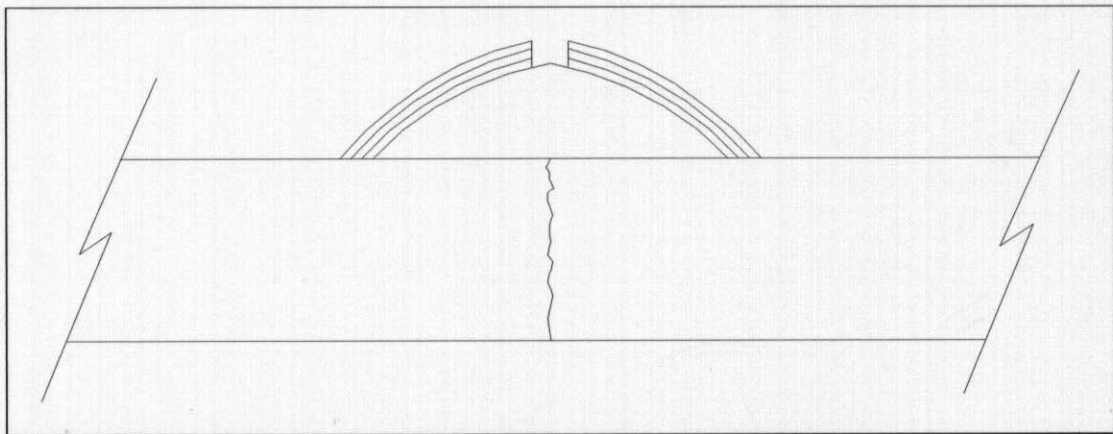


**Figure 4.23:** Test 17 charge configuration and the induced crack pattern.

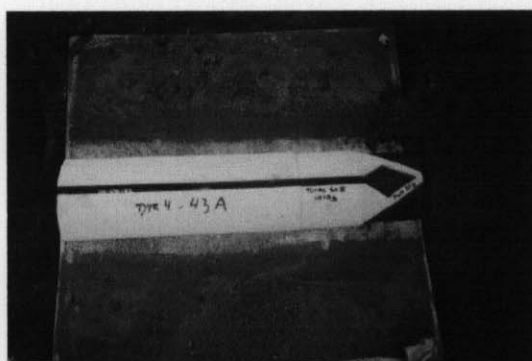


**Figure 4.24:** Test 17, charge assembled on the target.



**Figure 4.25:** Test 17, cut target as found after the detonation.

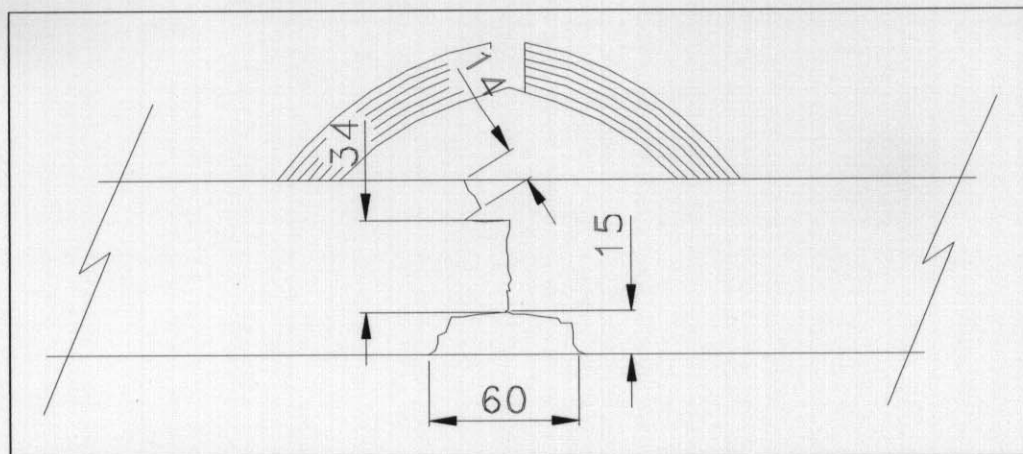


**Figure 4.26:** Test 18, charge configuration and the induced crack pattern.

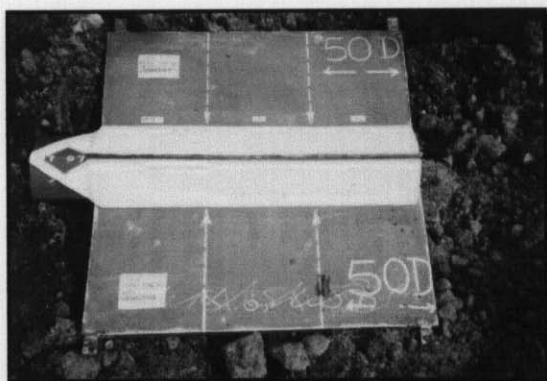


**Figure 4.27:** Test 18, charge assembled on the target.



**Figure 4.28:** Test 18, target being removed from soft ground.

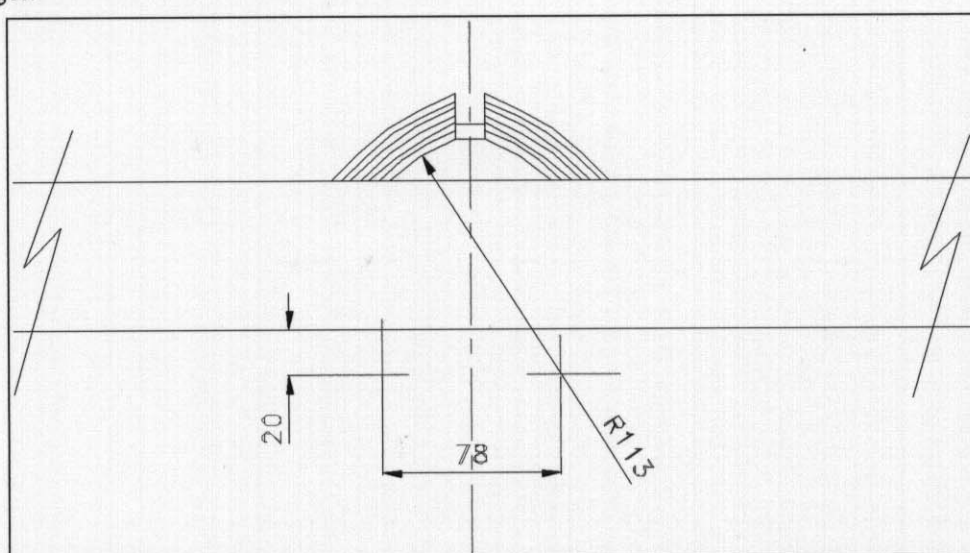


**Figure 4.29:** Test 19, charge Type 6 dimensions.

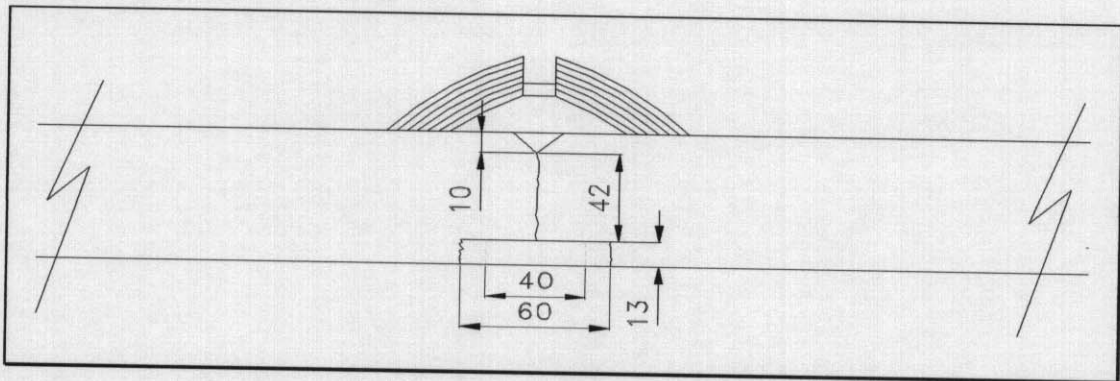


**Figure 4.30:** Test 19, charge configuration and the induced crack pattern.



**Figure 4.31:** Test 19, charge assembled on the target.

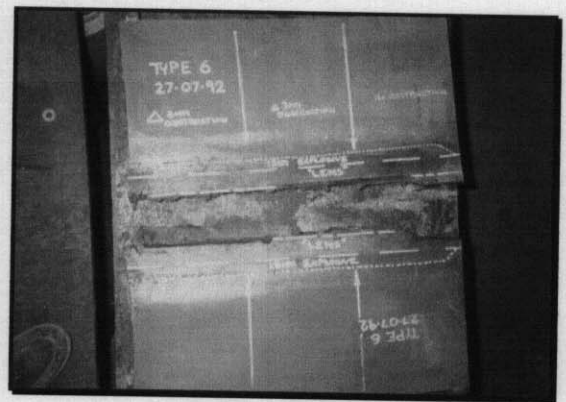


**Figure 4.32:** Test 19, cut target.

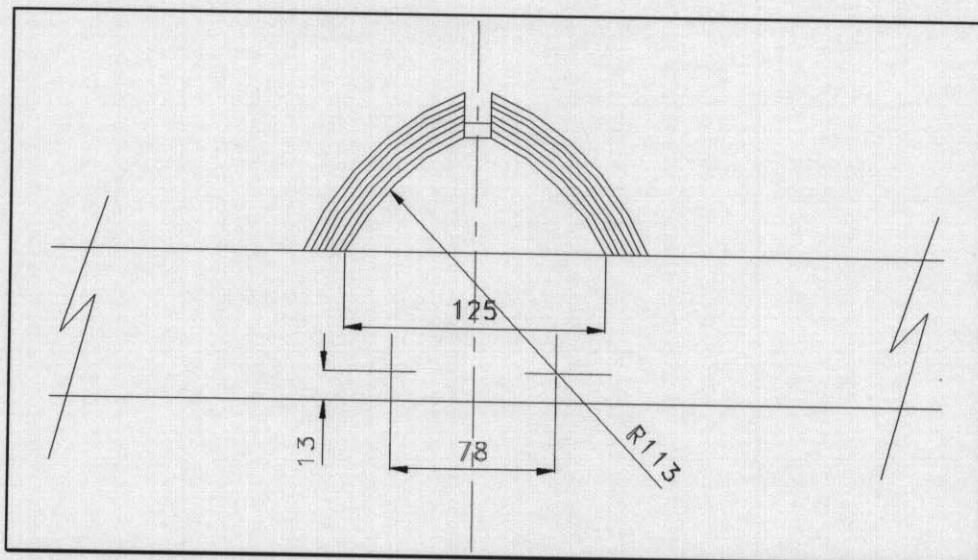


**Figure 4.33:** Test 20, charge type 5 with 6 layers of SX2.



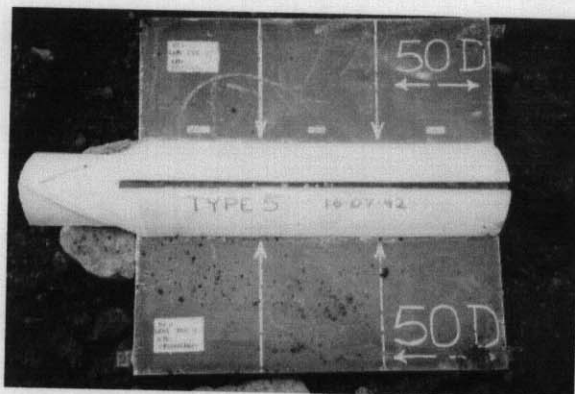


**Figure 4.34:** Test 20, charge Type 5 assembled on the target.

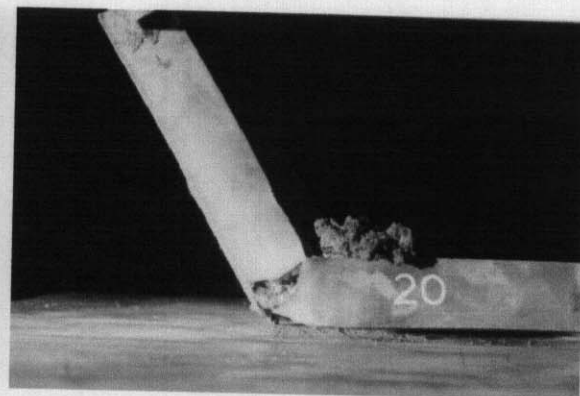


**Figure 4.35:** Test 20, view showing the bend target.

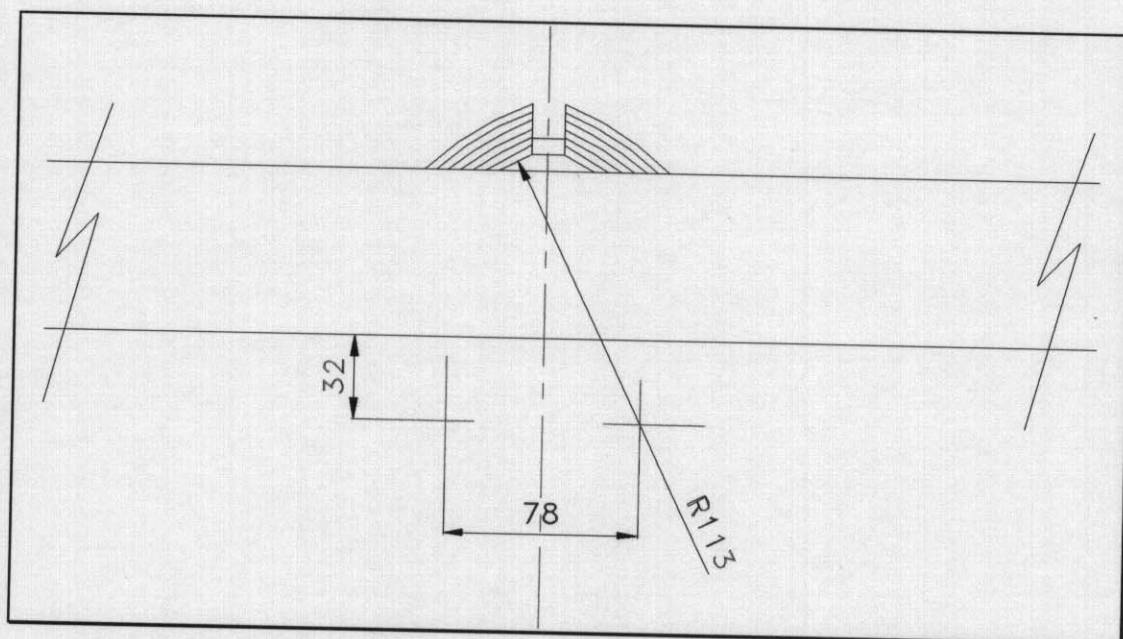


**Figure 4.36:** Charge Type 8 dimensions.

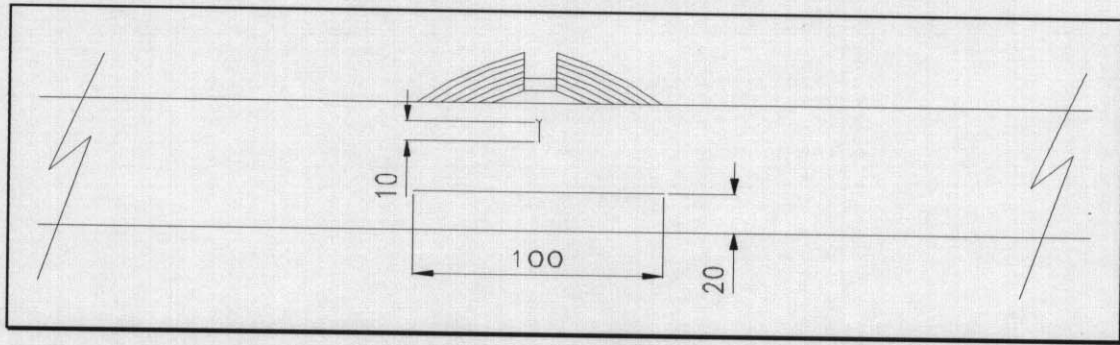


**Figure 4.37:** Test 21 charge configuration and the induced crack pattern.



**Figure 4.38:** Test 21, charge assembled on target.



**Figure 4.39:** Test 21, showing the bend left on the target.



**Figure 4.40:** Test 21, target back face.



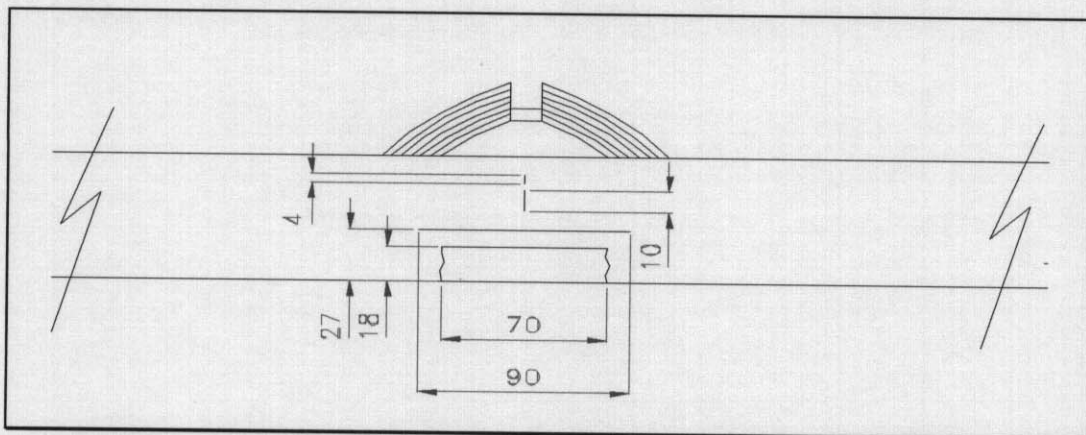


**Figure 4.41:** Test 22 charge configuration and the induced crack pattern 200 mm from the initiation.

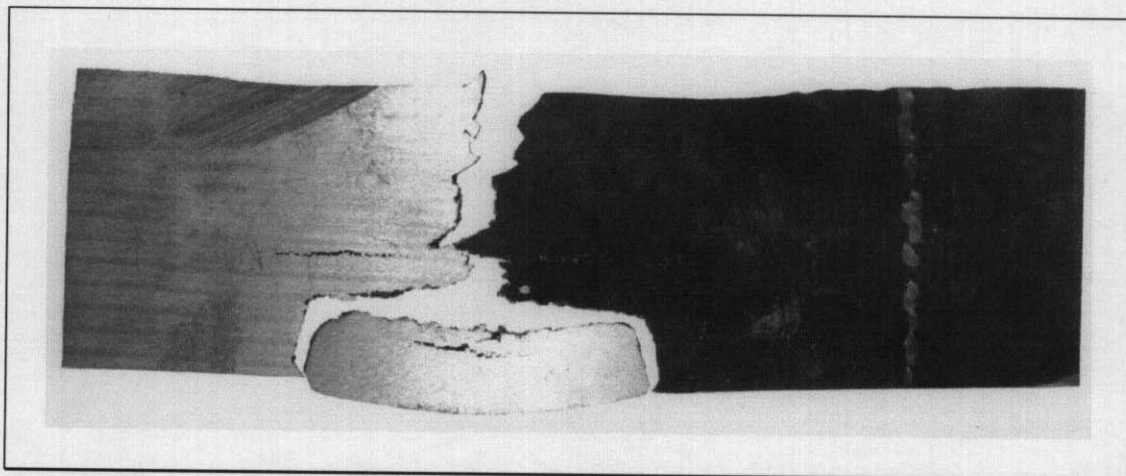


**Figure 4.42:** Test 22, section of target 300 mm from initiation.

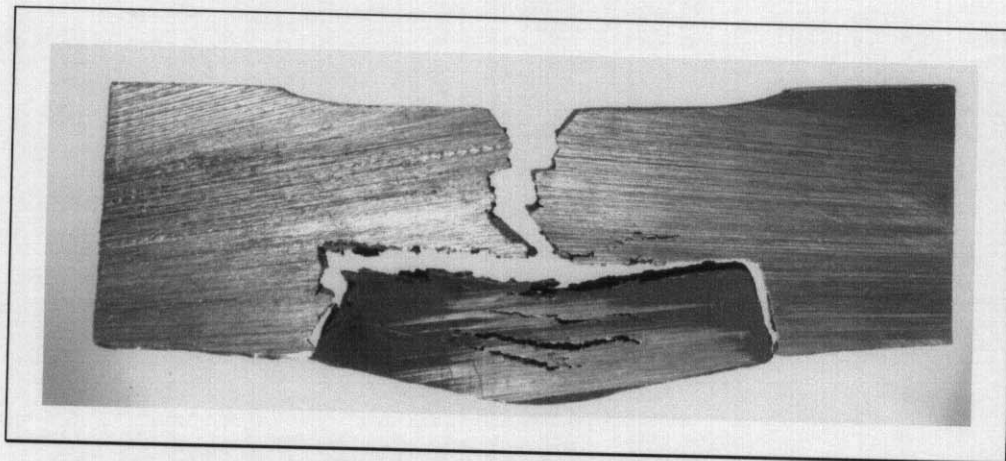


**Figure 4.43:** Test 22, section of target 500 mm from initiation.

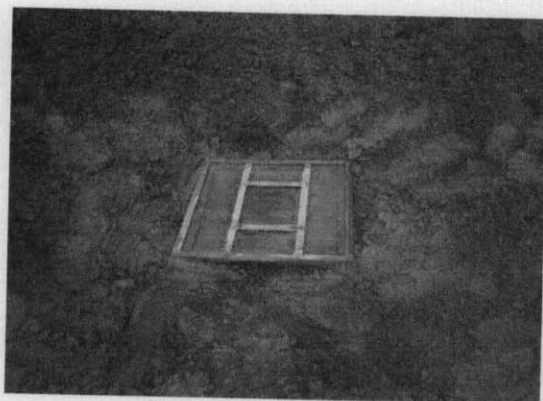


**Figure 4.44:** Test 23 anvil.

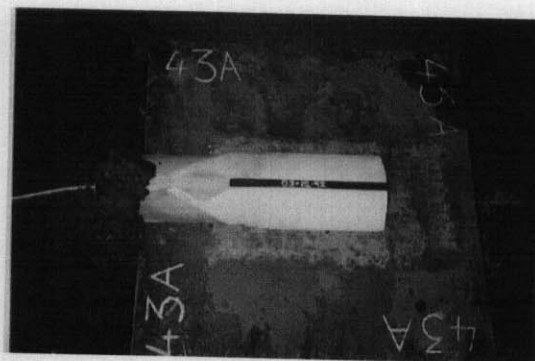


**Figure 4.45 :** Test 23, view showing the charge and initiation system mounted on a plaster base.

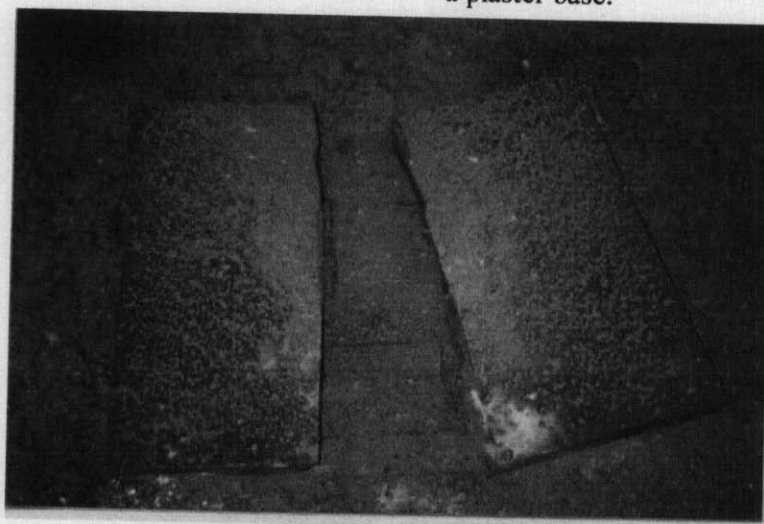


**Figure 4.46:** Test 23, view showing the cut target.



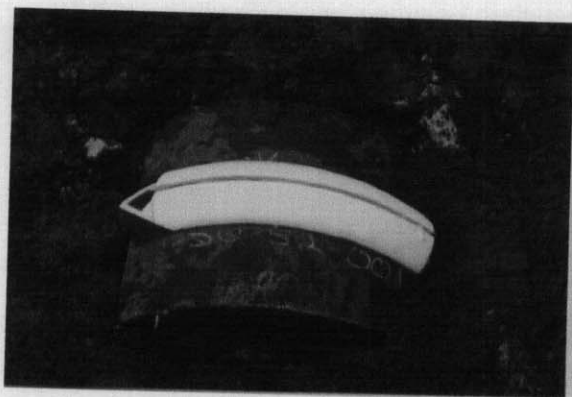


**Figure 4.47:** Test C1, charge assembled on the target.

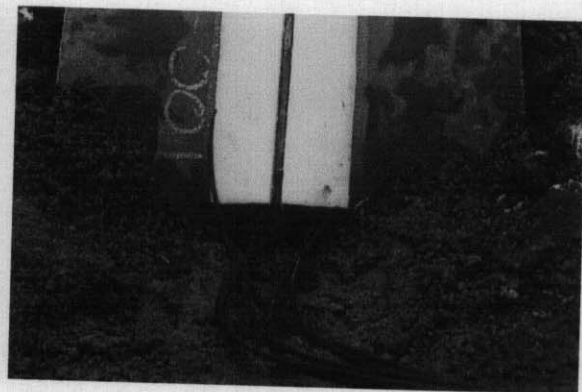


**Figure 4.48:** Test C1, optical fibre probes assembled on the charge.



**Figure 4.49:** Test C1, view showing the cut target as found after the detonation.

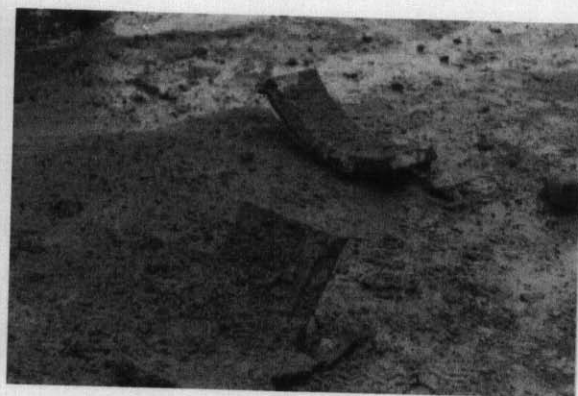


**Figure 4.50:** Test C1, view showing the cut target.



**Figure 4.51:** Test C2 showing that the weld was ground to improve contact.

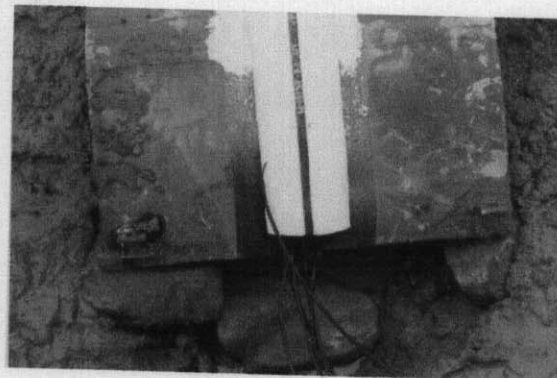


**Figure 4.52:** Test C2, Detail showing VOD probes at the end of the charge.



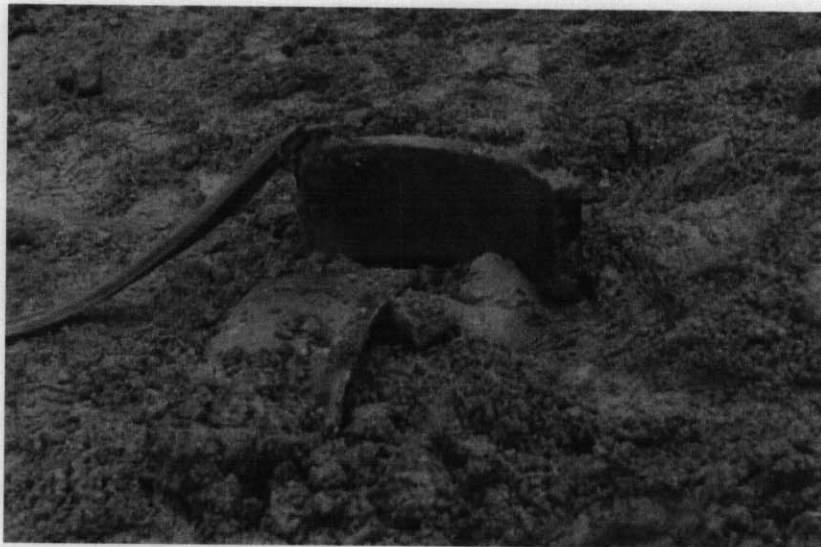


**Figure 4.53:** Test C2, cut target.

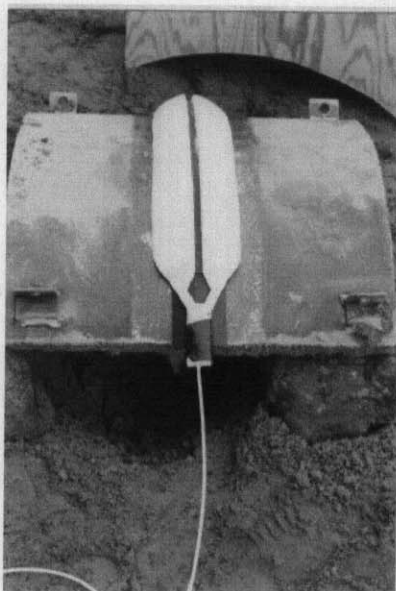


**Figure 4.54:** Charge Assembled on the target.



**Figure 4.55:** Test C3 Air chamber before covering with sand. .



**Figure 4.56:** Test C3, target as found after detonation.

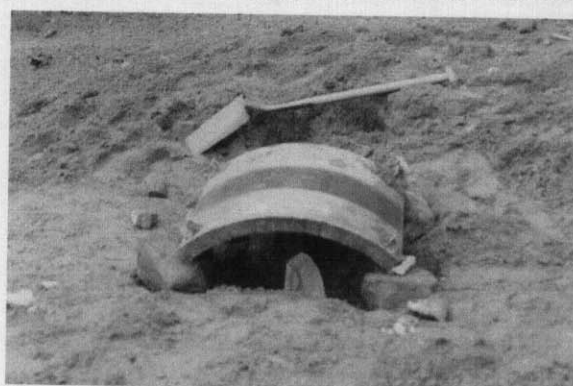


**Figure 4.57:** Test C4 target raised from the ground.



**Figure 4.58:** Test C4, detail of initiation region the charge.



**Figure 4.59:** Test C4 target as found after detonation.



**Figure 4.60:** Test C4, back face of the cut target showing the spall attached at the initiation region



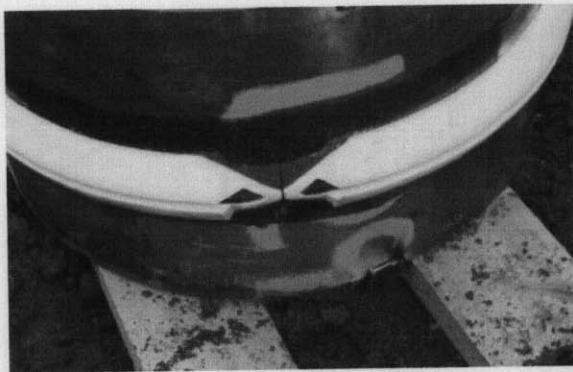


**Figure 4.61:** Charge at the initiation region.



**Figure 4.62:** Gap left at the end region to assess propagation of the cut



**Figure 4.63:** Note some detached spall pieces inside the tubular and the attached spall under the initiation region.



**Figure 4.64:** The sharp cut line can be observed on the target surface (end region with no gap).

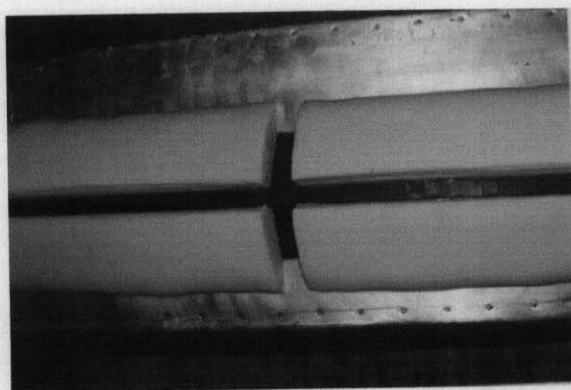


**Figure 4.65:** Charge type 6 with the groove for inserting the vertical triangle.

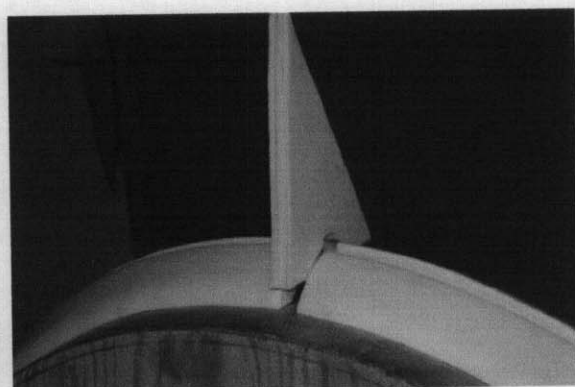


**Figure 4.66:** The vertical triangle being positioned on the charge.

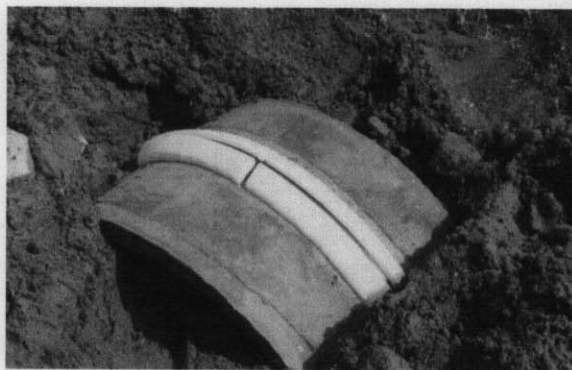


**Figure 4.67:** Charge assembled on the target.

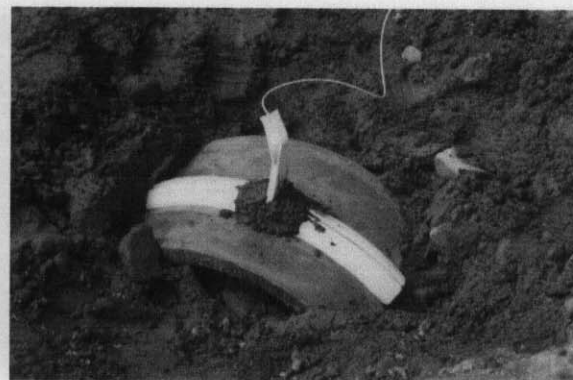


**Figure 4.68:** Vertical triangle assembled on the charge with the confinement material to assist the initiation.

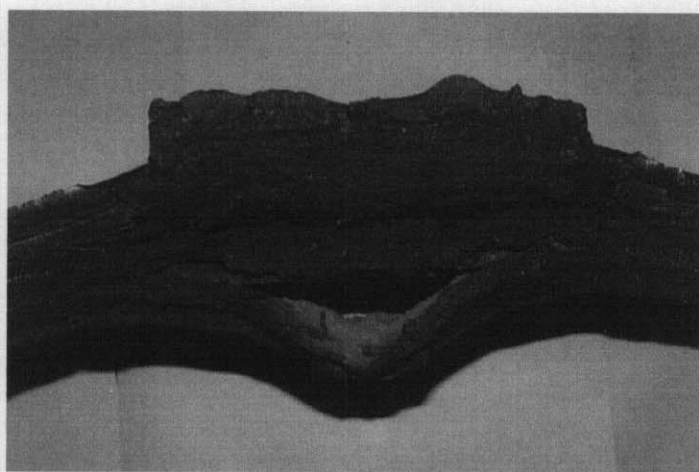


**Figure 4.69:** Fracture target under the initiation region.

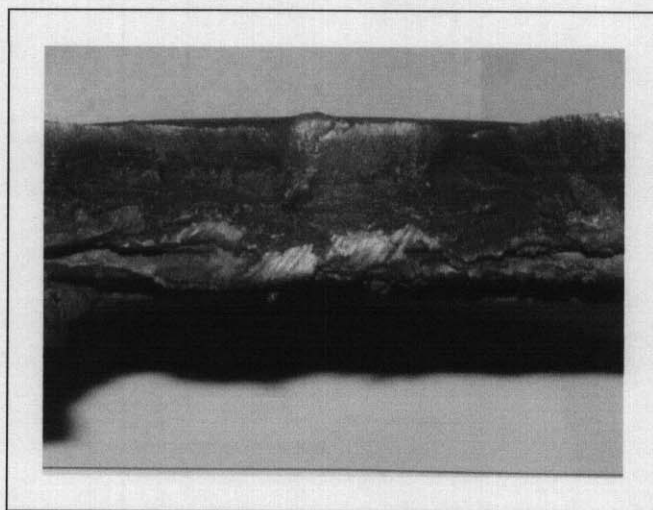


**Figure 4.70:** Fracture target under the initiation region, opposite side.





**Figure 4.71:** Fracture target under the main charge region.

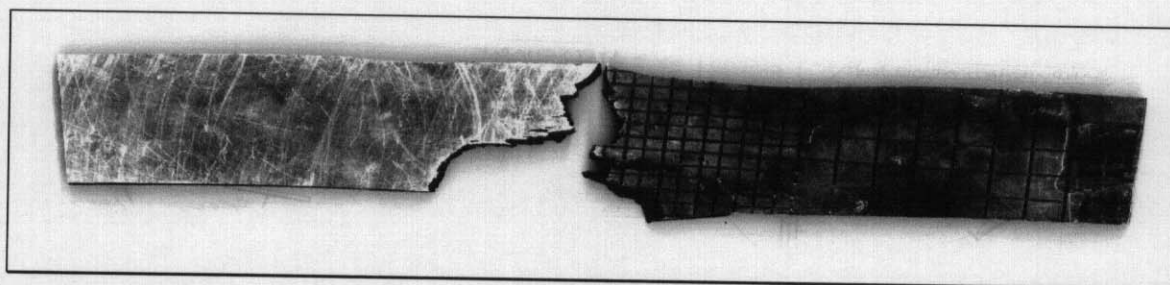


**Figure 4.72:** Section under the main charge region ( Two pieces from the same side).



**Figure 4.73:** Test C7, showing initiation region (1) with confinement sleeve made from waveguide material.



**Figure 4.74:** Test C7, showing the initiation region (2), before placing iron powder paste.

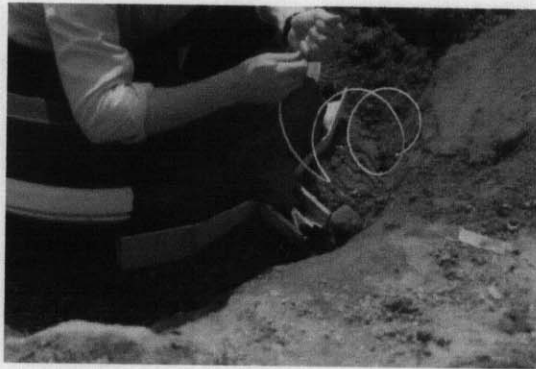


**Figure 4.75:** Test C7, showing the initiation region (2) with iron powder paste.



**Figure 4.76:** Test C7, showing the meeting point of two waveguides and a 7 mm gap.



**Figure 4.77:** Test C7, showing the Cordtex detonation lines used for synchronised initiation

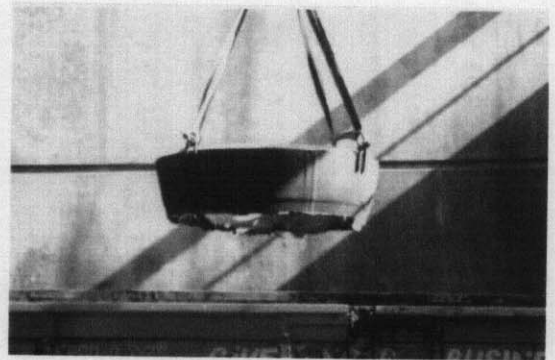


**Figure 4.78:** Test C7, cut half.



**Figure 4.79:** Test C8, charge assembled on the target.



**Figure 4.80:** Test C8, the target placed inside a hole on the ground.





**Figure 4.81:** Test C8, cut target as found after detonation.

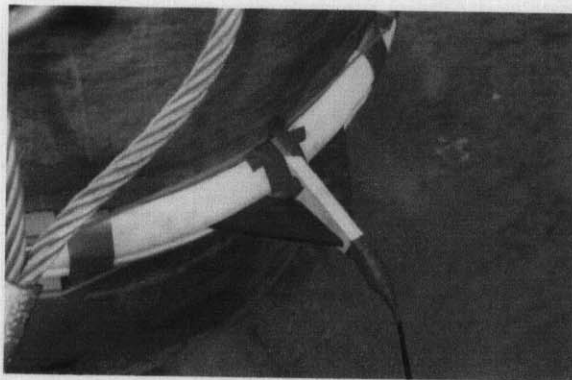


**Figure 4.82:** Rubber stiffeners used to support the vertical triangle in position.

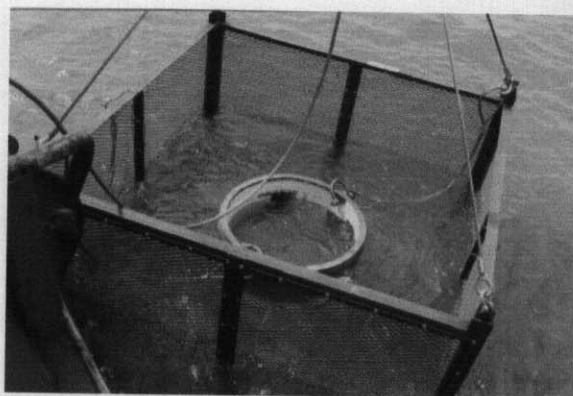


**Figure 4.83:** Test C9, target being lowered into the water.



**Figure 4.84:** Test C9, target protective cage.



**Figure 4.81:** Test C8, cut target as found after detonation.

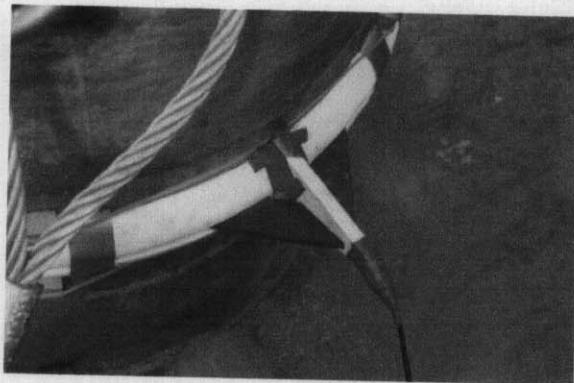


**Figure 4.82:** Rubber stiffeners used to support the vertical triangle in position.



**Figure 4.83:** Test C9, target being lowered into the water.



**Figure 4.84:** Test C9, target protective cage.



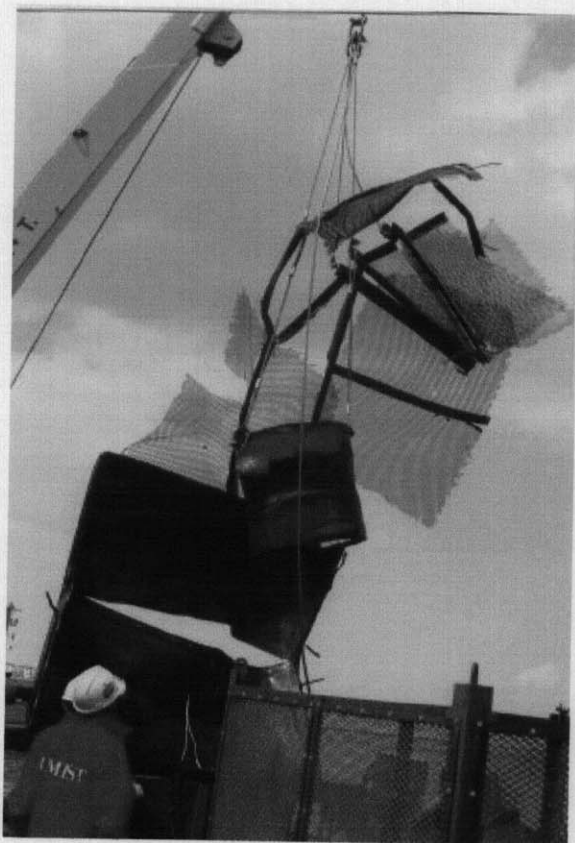


**Figure 4.85:** Test C9, target being retrieved.

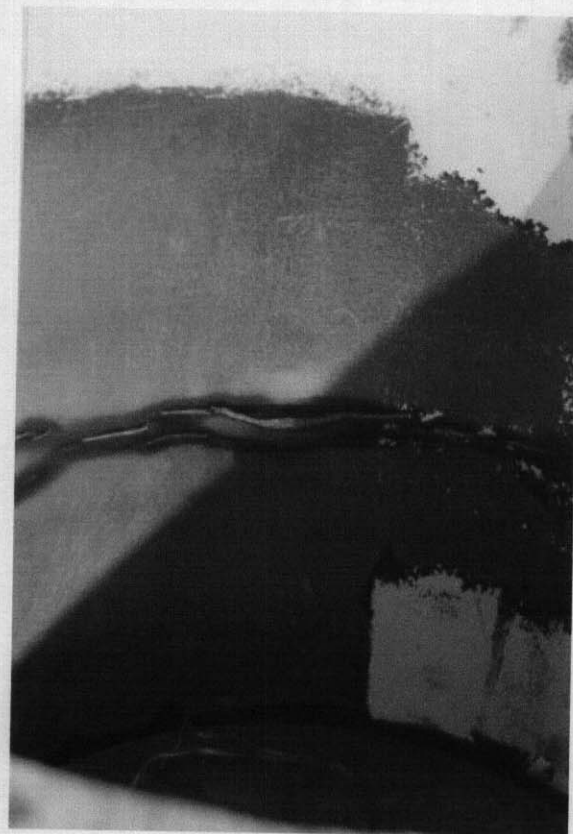


**Figure 4.86:** Test C9 internal surface near initiation region (1), showing the spall formed but still attached in some points.



**Figure 4.87:** Test C9 inner surface of the tubular near initiation region (2), showing the spall formed but still attached in some points.

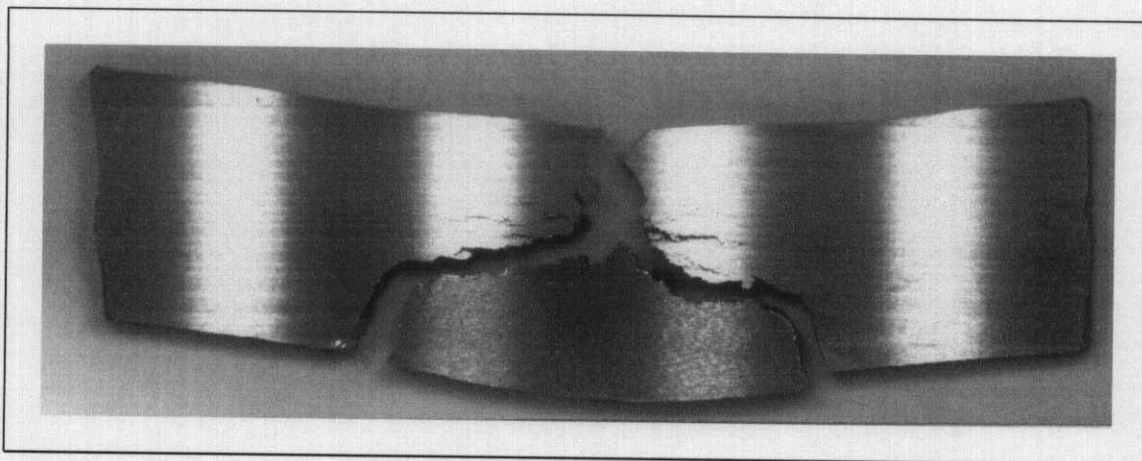


**Figure 4.88:** Test C9 section of the tubular 400 mm away from the initiation.

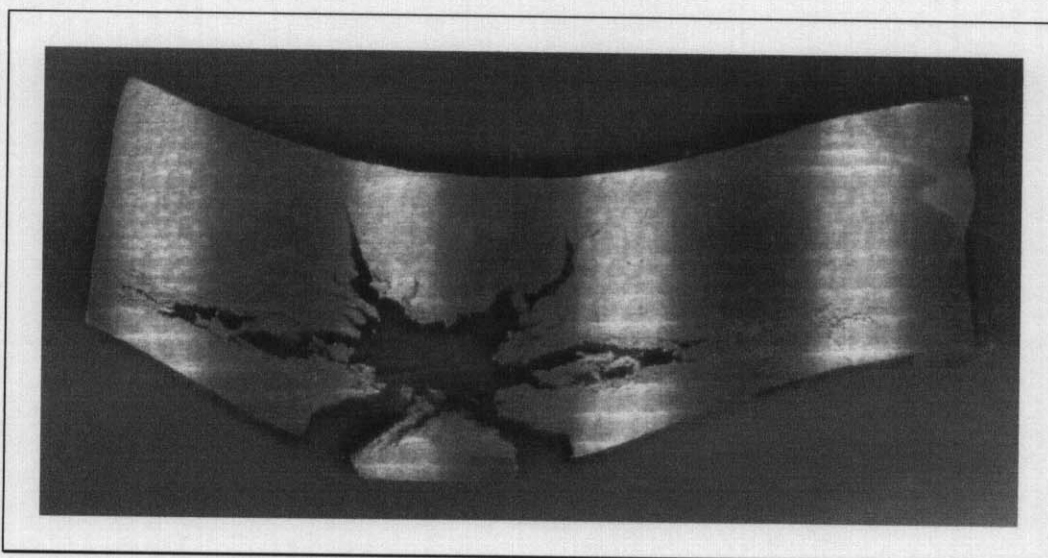


**Figure 4.89:** Test C9 section of the tubular under the initiation region.



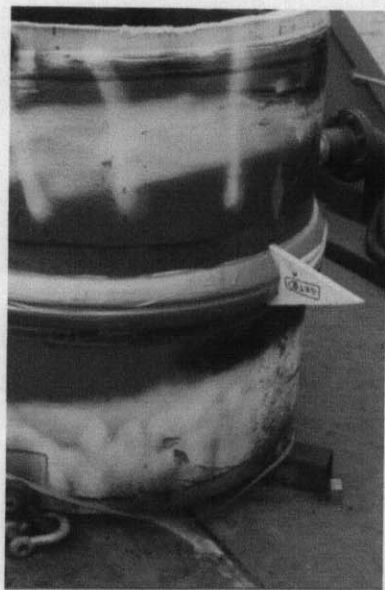


**Figure 4.90:** Test C10, charge assembled onto the target.



**Figure 4.91:** Test C10, target covered with a layer of fine stone aggregate.

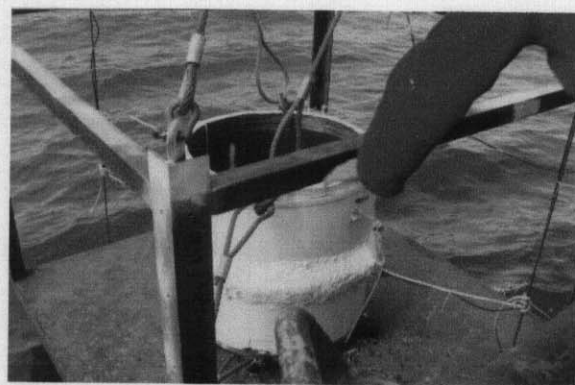


**Figure 4.92:** Test C10, target being lowered into the water.



**Figure 4.93:** Detail showing the way the target had both ends attached to a steel rope for recovery of both halves in case of a successful cut.



**Figure 4.94:** Test C10, target being retrieved after detonation.



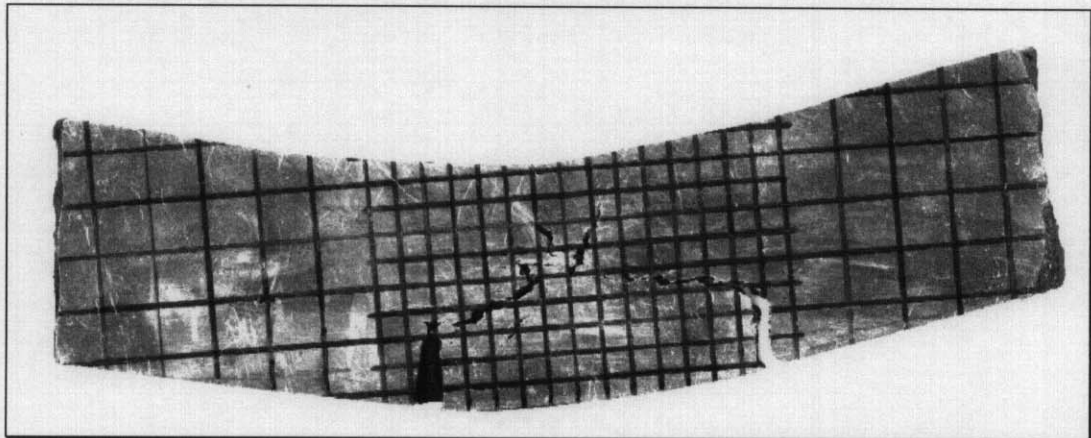


**Figure 4.95:** Test C10 section of the tubular 300 mm away from the initiation

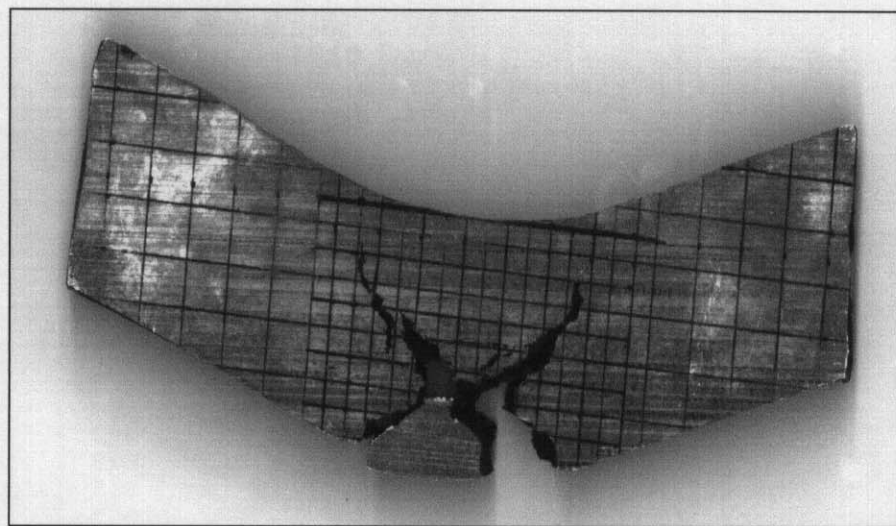


**Figure 4.96:** Test C10 section of the tubular under the initiation region.

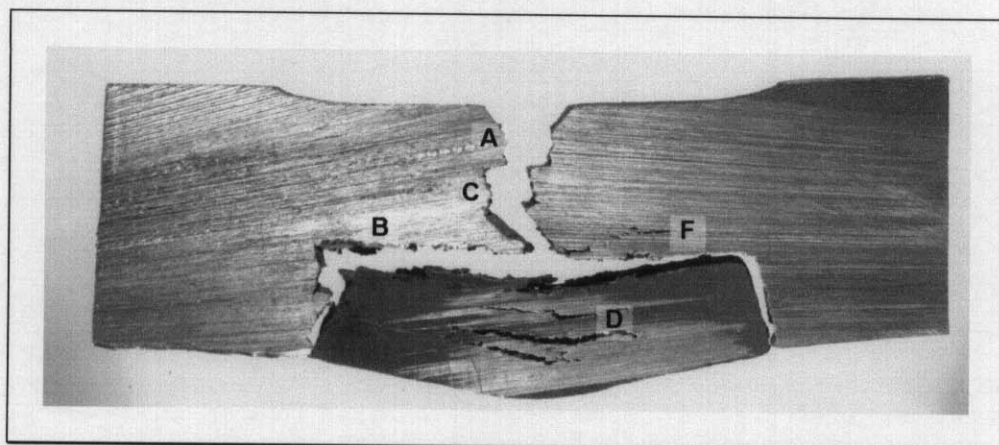


**Figure 4.97:** Section from Test 22, samples locations.

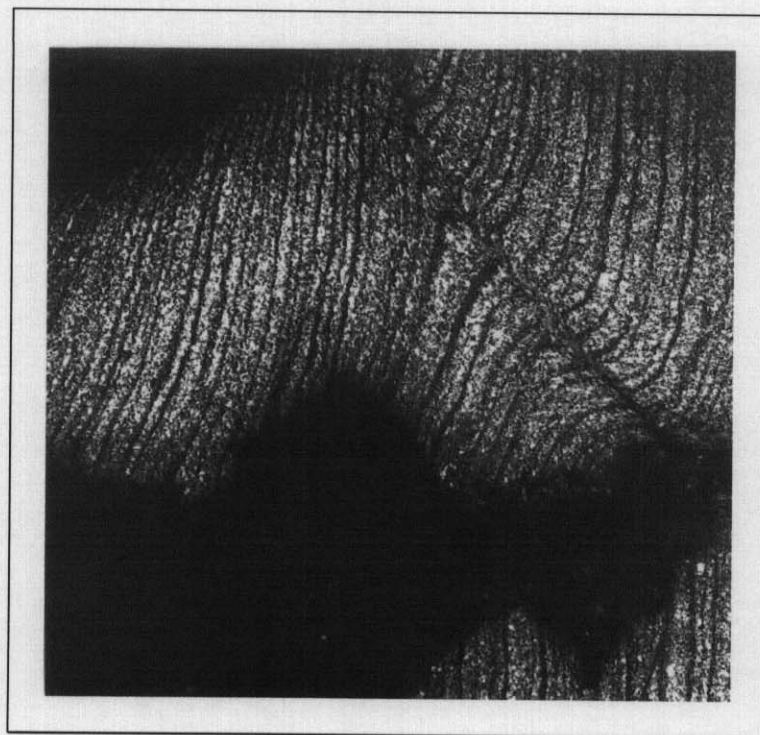


**Figure 4.98:** Detail from region A showing outer surface of the main fracture where a shear line can be observed interrupting the pearlite bands (40X).

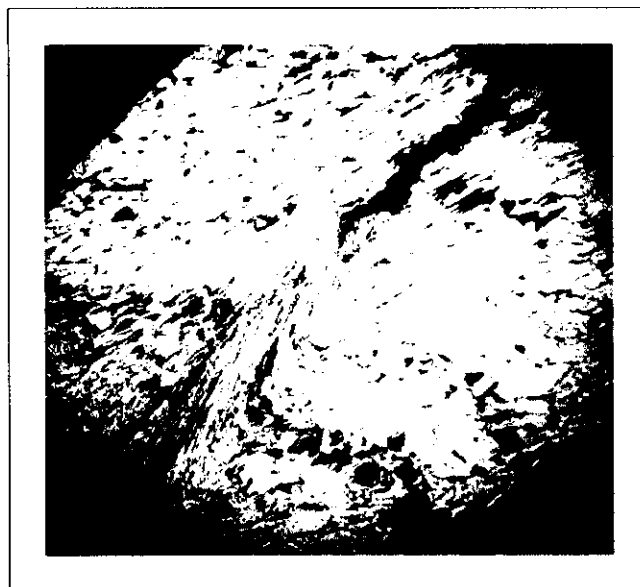


**Figure 4.99:** Detail of position A showing highly concentrated plastic deformation being followed by a row of voids (400x).

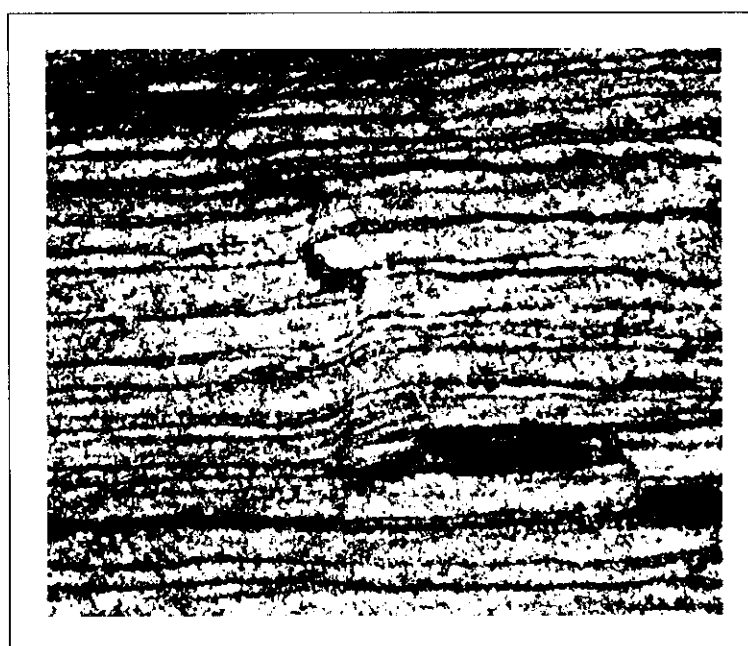


**Figure 4.100:** Detail of region B showing localised shear across pearlite bands (40X).





**Figure 4.101:** Detail of region B showing a row of voids along a pearlite band (40X).

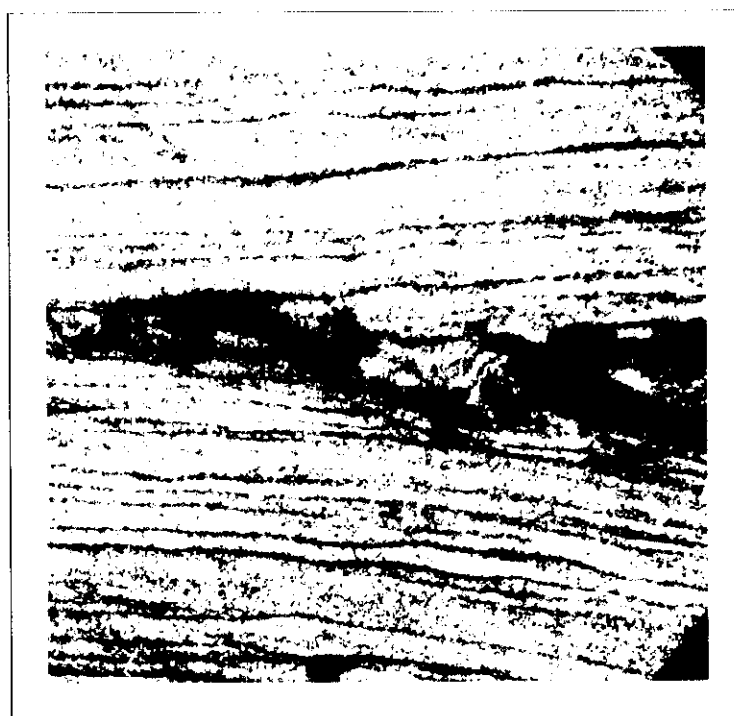


**Figure 4.102:** Detail of region B showing the coalescence of voids along the pearlite and (40X).

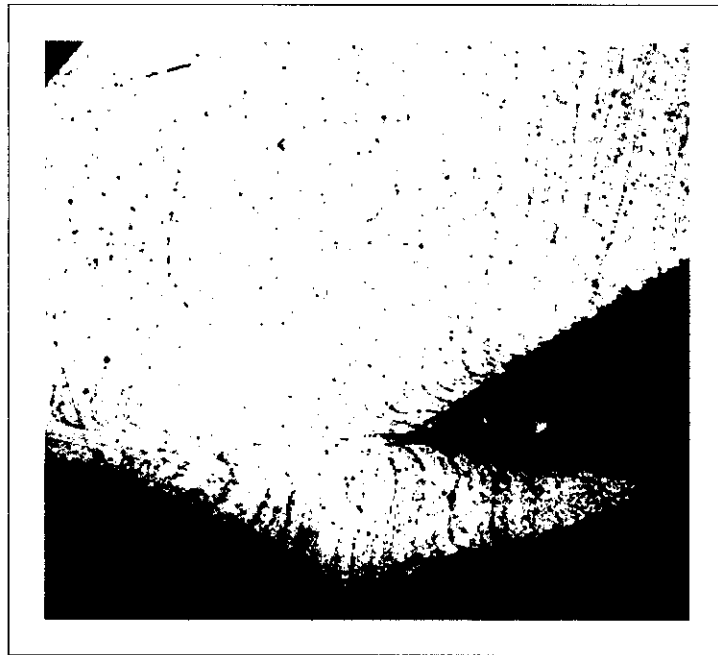


**Figure 4.103:** Detail of region C showing what appears to be an adiabatic shear band as the pearlite/ferrite bands are displaced into a "Z" shape undulation. The outer surface of the fracture also shows similar undulations near the edge (40X).



**Figure 4.104:** Detail of region D without etching, showing a great amount of voids and in some places voids coalescence at different stages (35X).

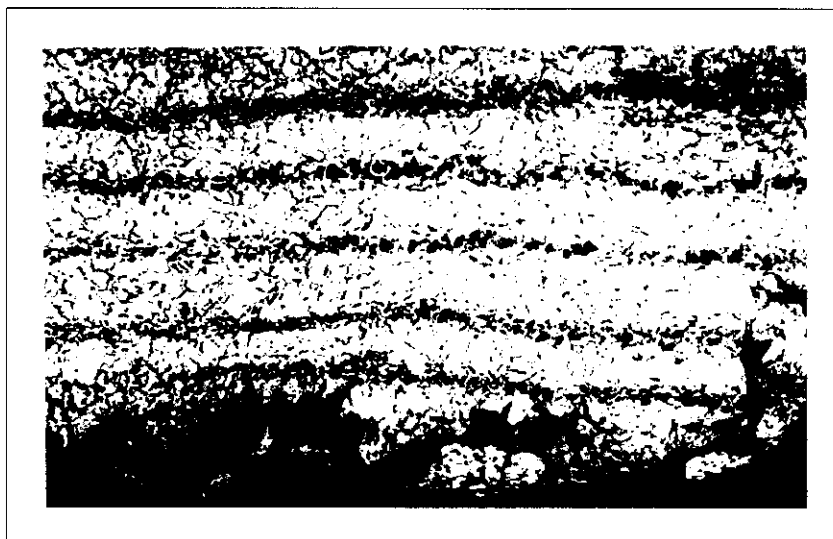


**Figure 4.105:** Detail of region D showing the line of fracture (bottom) parallel to the pearlite/ferrite bands (100X).



**Figure 4.106:** Detail of region D showing cracks across pearlite/ferrite bands (100X).

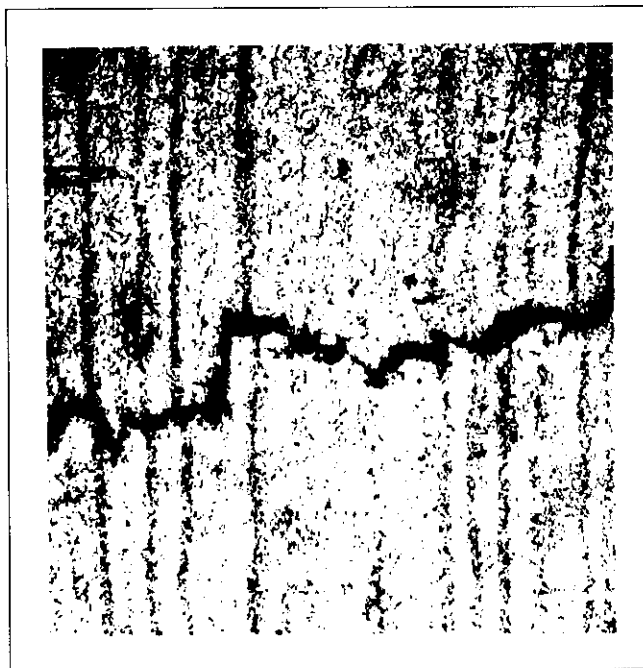


**Figure 4.107:** Detail of region F showing a crack crossing several pearlite/ferrite bands (75X).

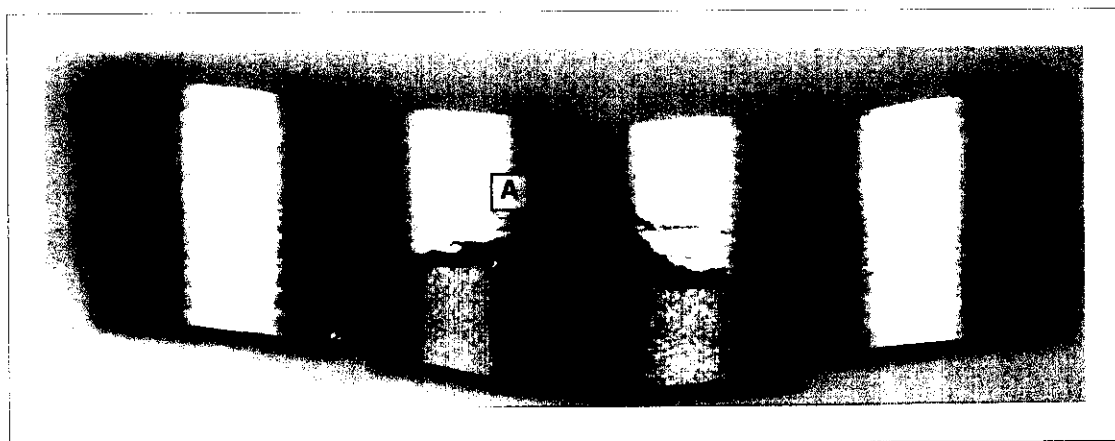


**Figure 4.108:** Test C9, Section of target 300 mm away from initiation.

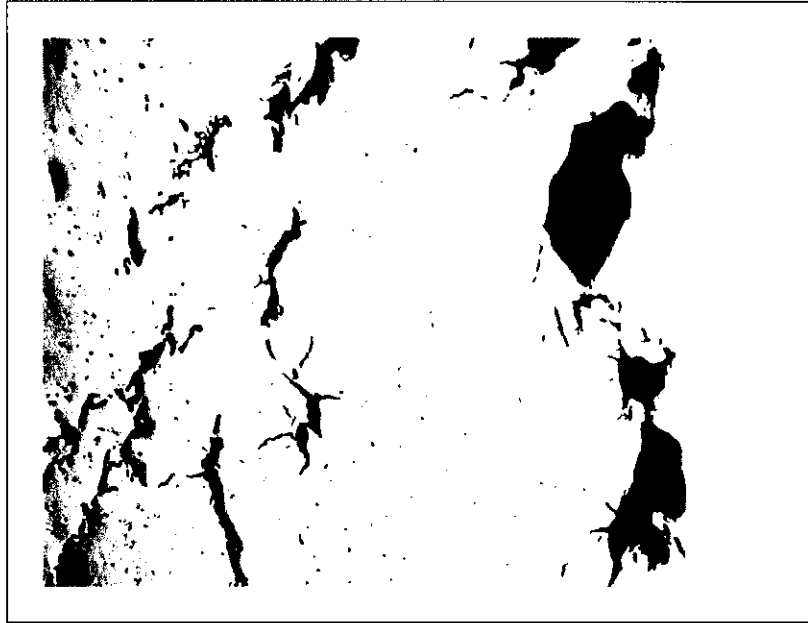


**Figure 4.109:** Test C9, Detail of region A showing a great amount of voids, coalescence of voids into micro-cracks and coalescence of micro-cracks into cracks (35X).

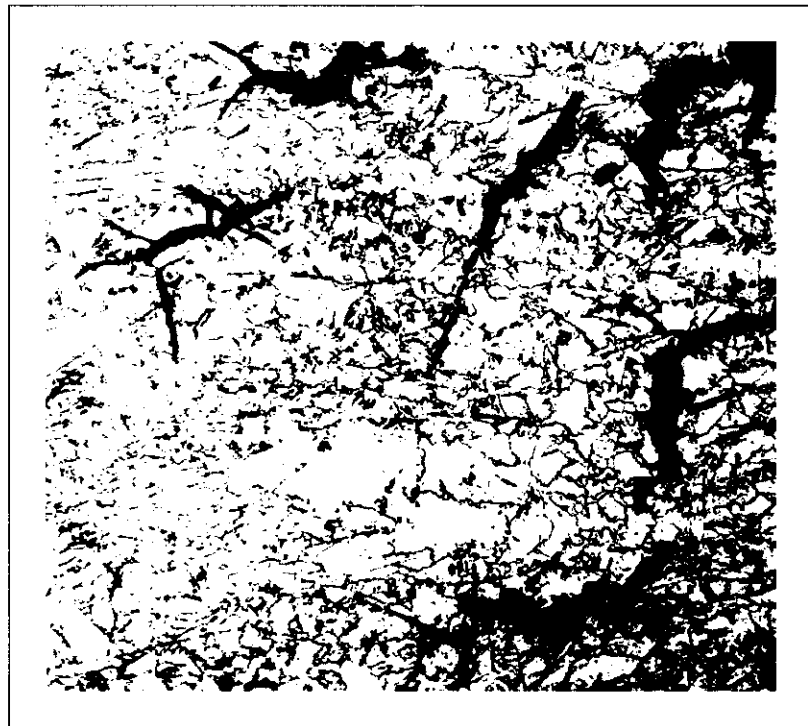


**Figure 4.110:** Detail of region A showing some evidence of inter-granular nucleation of voids (100X).

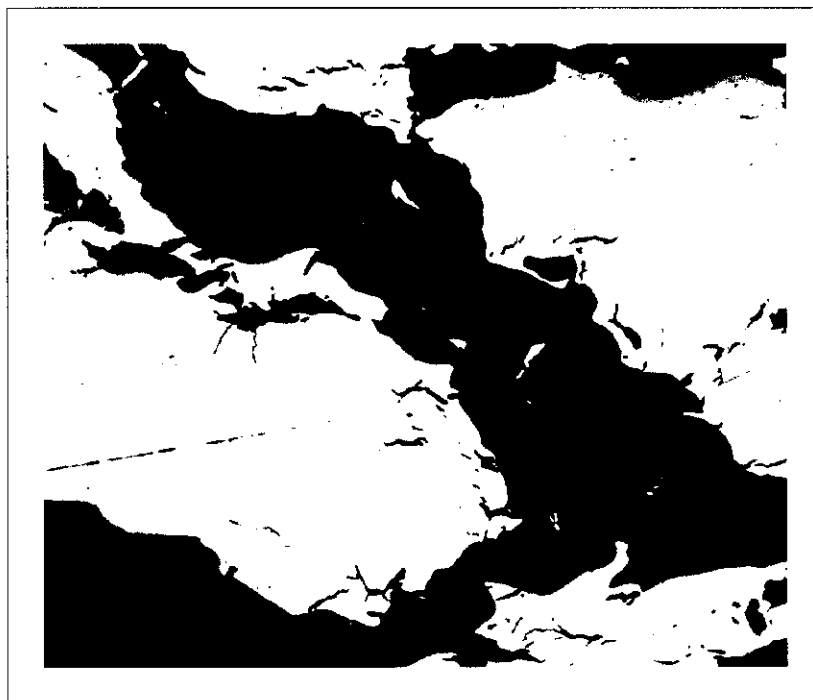


**Figure 4.111:** Test C9, Detail of region **B** without etching showing a crack surrounded by an area of generalised damaged with voids micro-cracks and lines of micro-cracks (35X).



**Figure 4.112:** Test C9, Detail of region **B** showing small localised distortion of the ferrite/pearlite bands (35X).

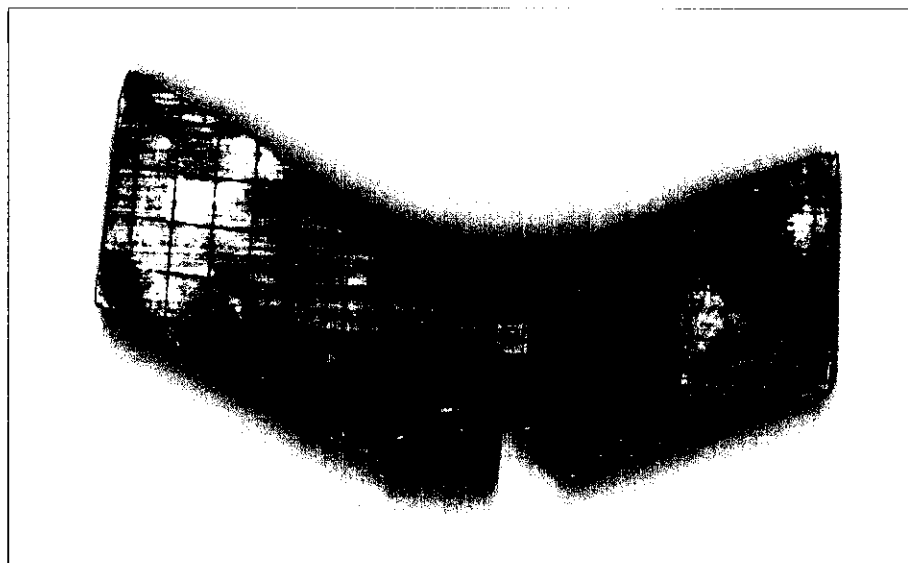


**Figure 4.113:** Test C10, Section of target under the initiation region.

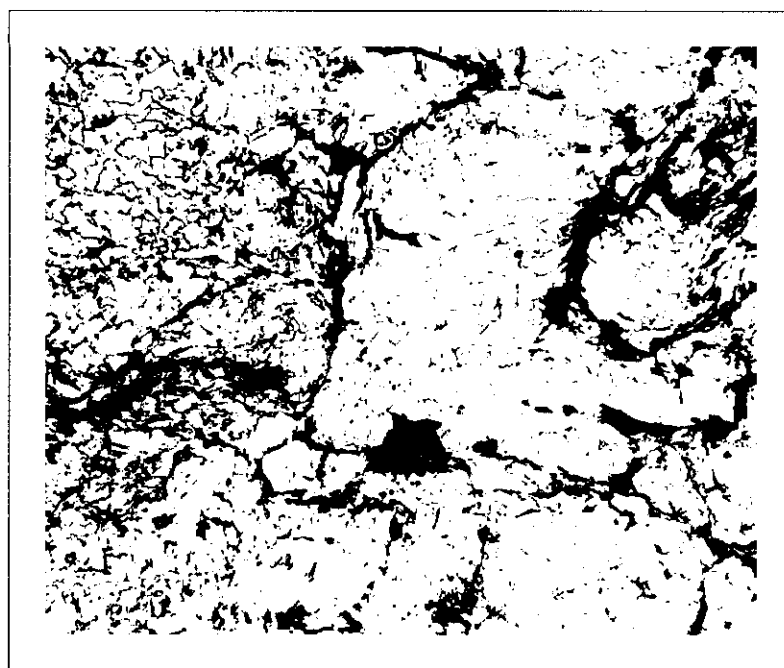


**Figure 4.114:** Test C10, Detail of region A deformed ferrite (100X).



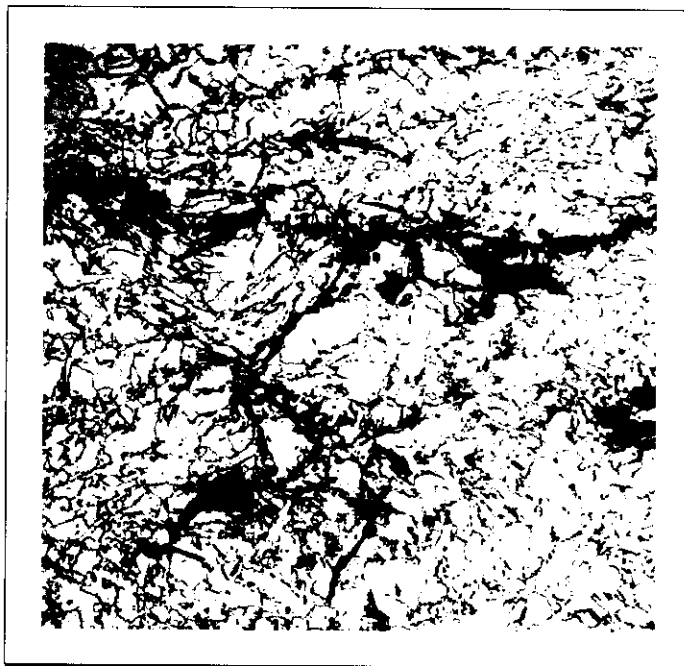


**Figure 4.115:** Test C10, Detail of region A showing showing evidence of void nucleation at grain boundaries (100X).

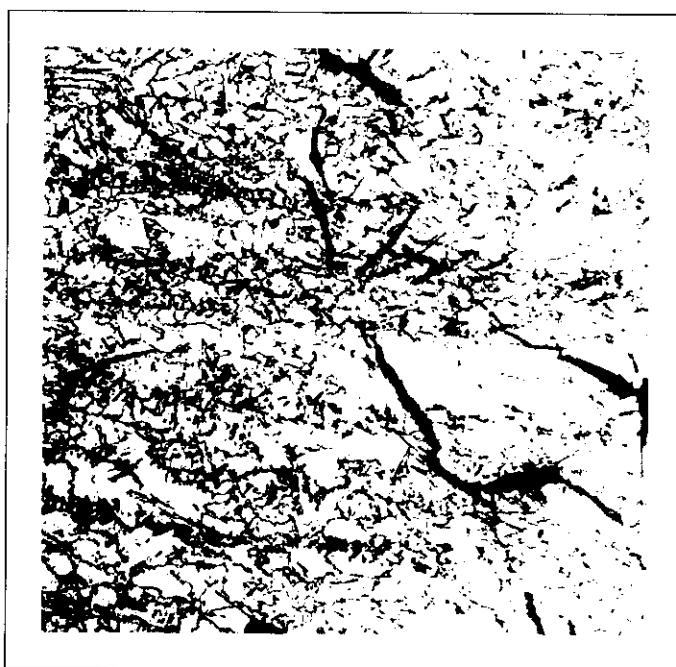


**Figure 4.116:** Test C10, Detail of region A showing micro-cracks (100X).

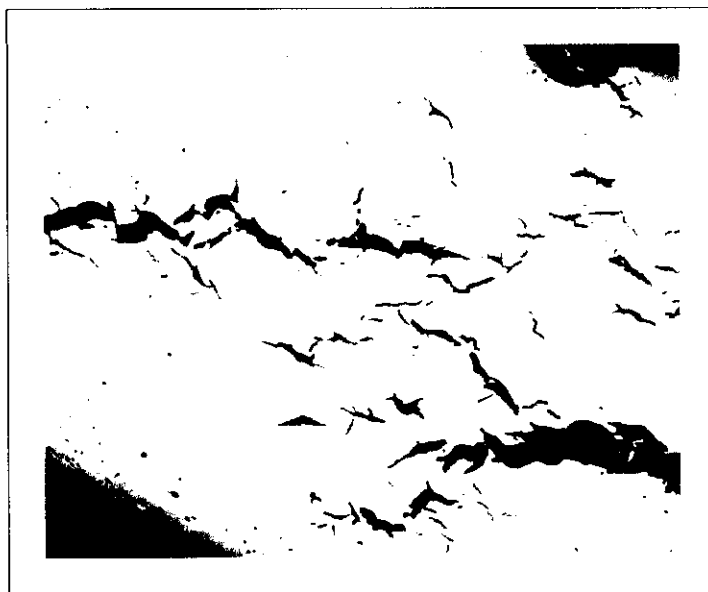


**Figure 4.117:** Test C10, Detail of region A showing micro-cracks coalescence (35X).

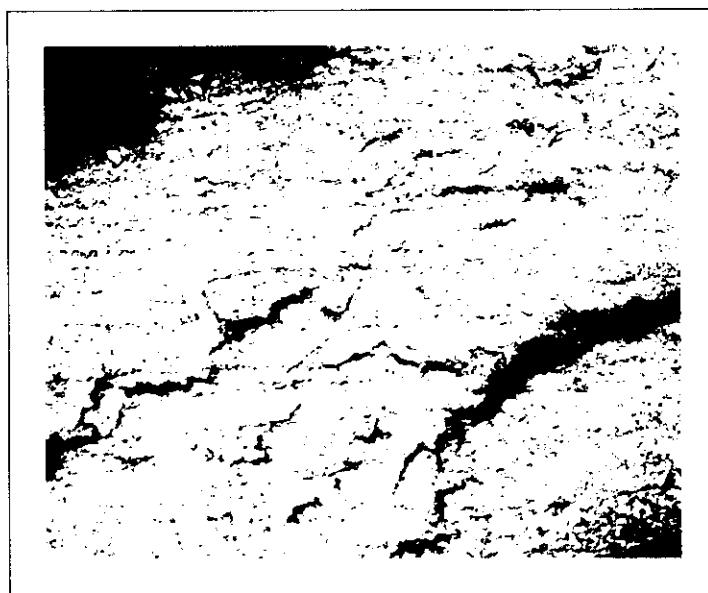


**Figure 4.118:** Test C10, Detail of region A showing same location as **Figure 4.117** (35X).

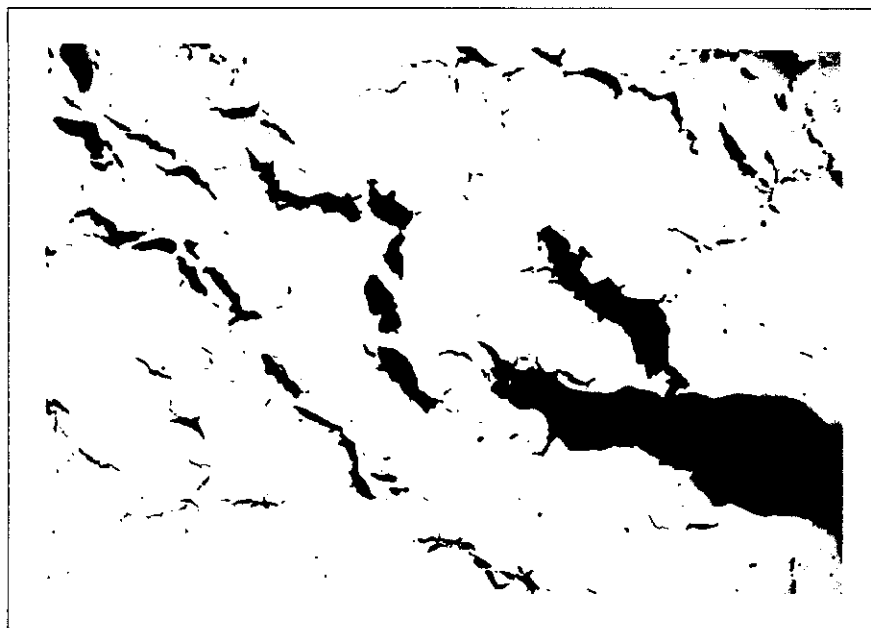


**Figure 4.119:** Test C10, Detail of region A showing micro-crack coalescence at different stages (100X).

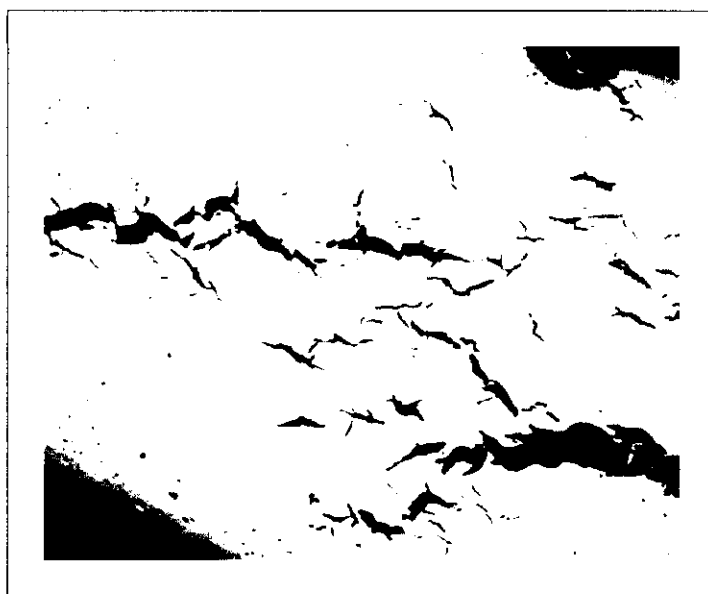


**Figure 4.120:** Test C10, Detail of region B showing A showing micro-crack coalescence at different stages (100X).

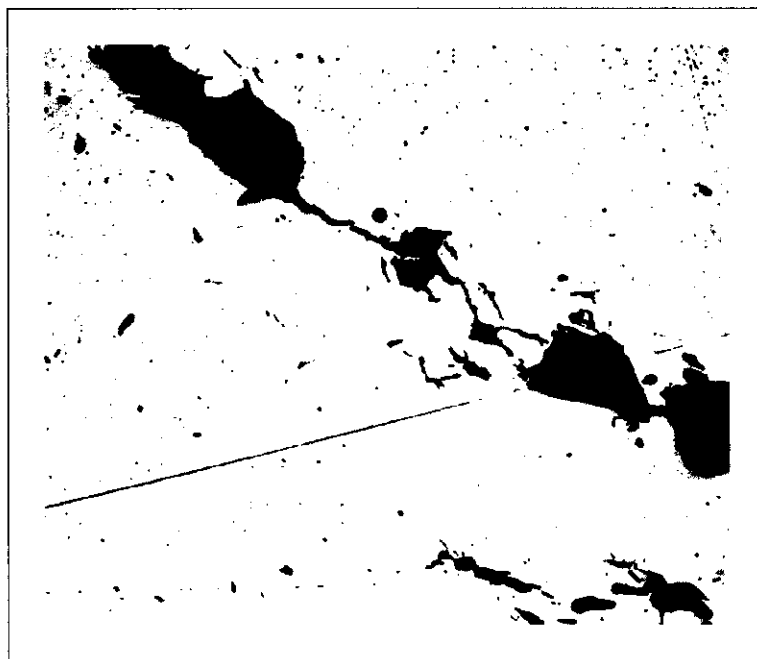


**Figure 4.121:** Test C10, Detail of region B showing presence of great amount of voids around a main crack (100X).

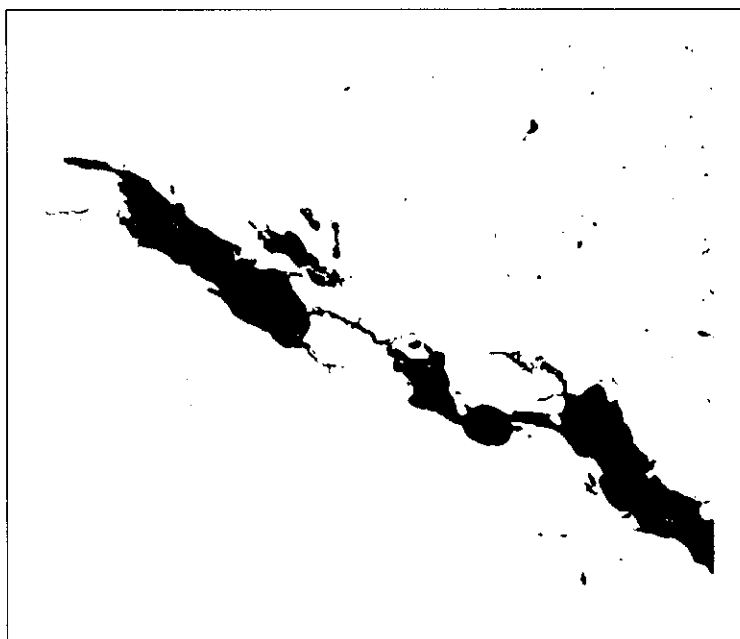


**Figure 4.122:** Test C10, Detail of region B showing presence of great amount of voids around a main crack (100X).

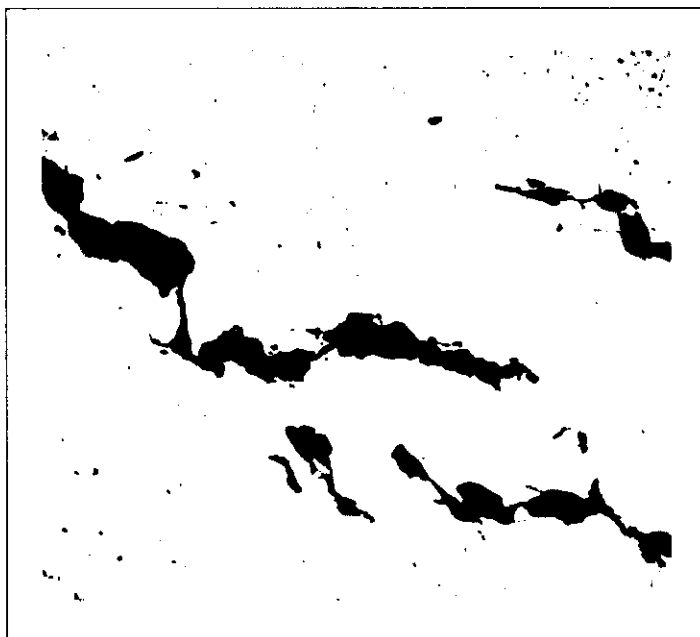


**Figure 4.123:** Test C10, Detail of region **B** showing presence of great amount of voids around a main crack (100X).



**Figure 4.124:** Test C10, Detail of region **B** showing coalescence of micro-cracks and voids (35X).

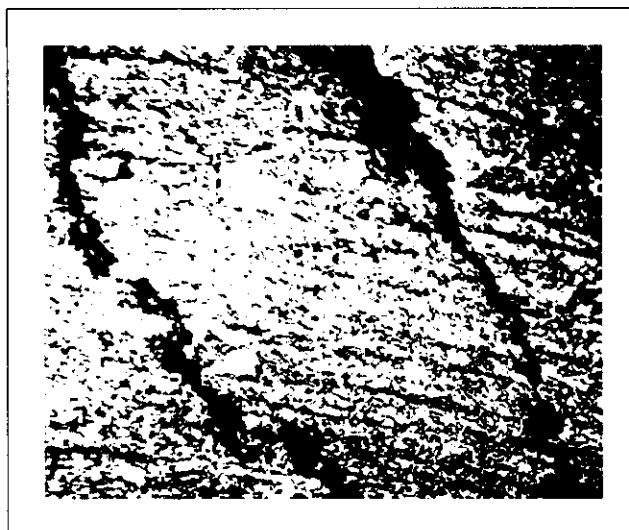


**Figure 4.125:** Test C10, Detail of region **B** showing two cracks appearing to be originated by the coalescence of voids and micro-cracks (35X).

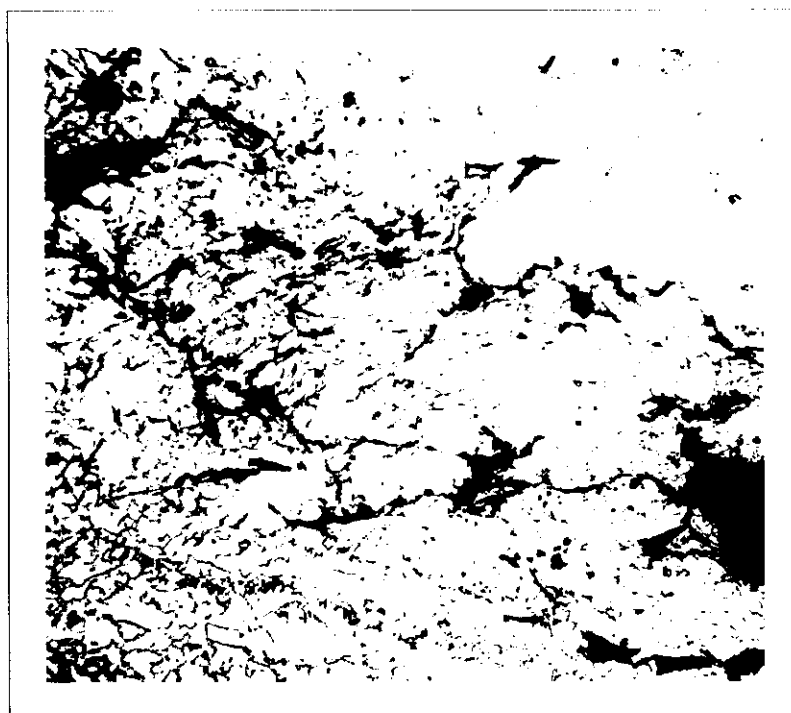


**Figure 4.126:** Test C10, Detail of region **B** showing distortion and generalised damaged with voids, micro-cracks and cracks (35X).

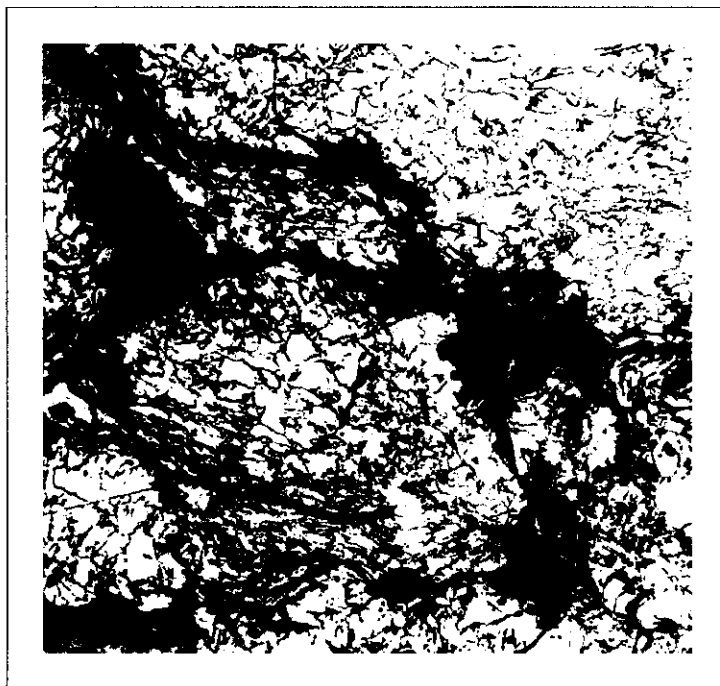


**Figure 4.127:** Test C10, Detail of region B showing a region of generalised damaged and distortion (100X).



**Figure 4.128:** Test C10, Detail of region B showing coalescence of voids into a crack line (100X).



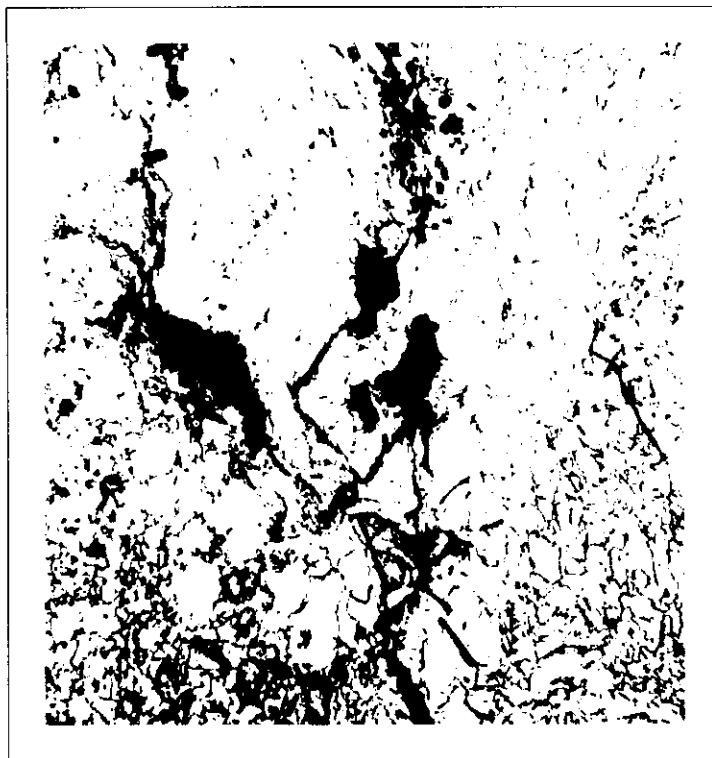


**Figure 4.129:** Test C10, Detail of region **B** showing areas of concentration of voids linked by micro-cracks (100X).















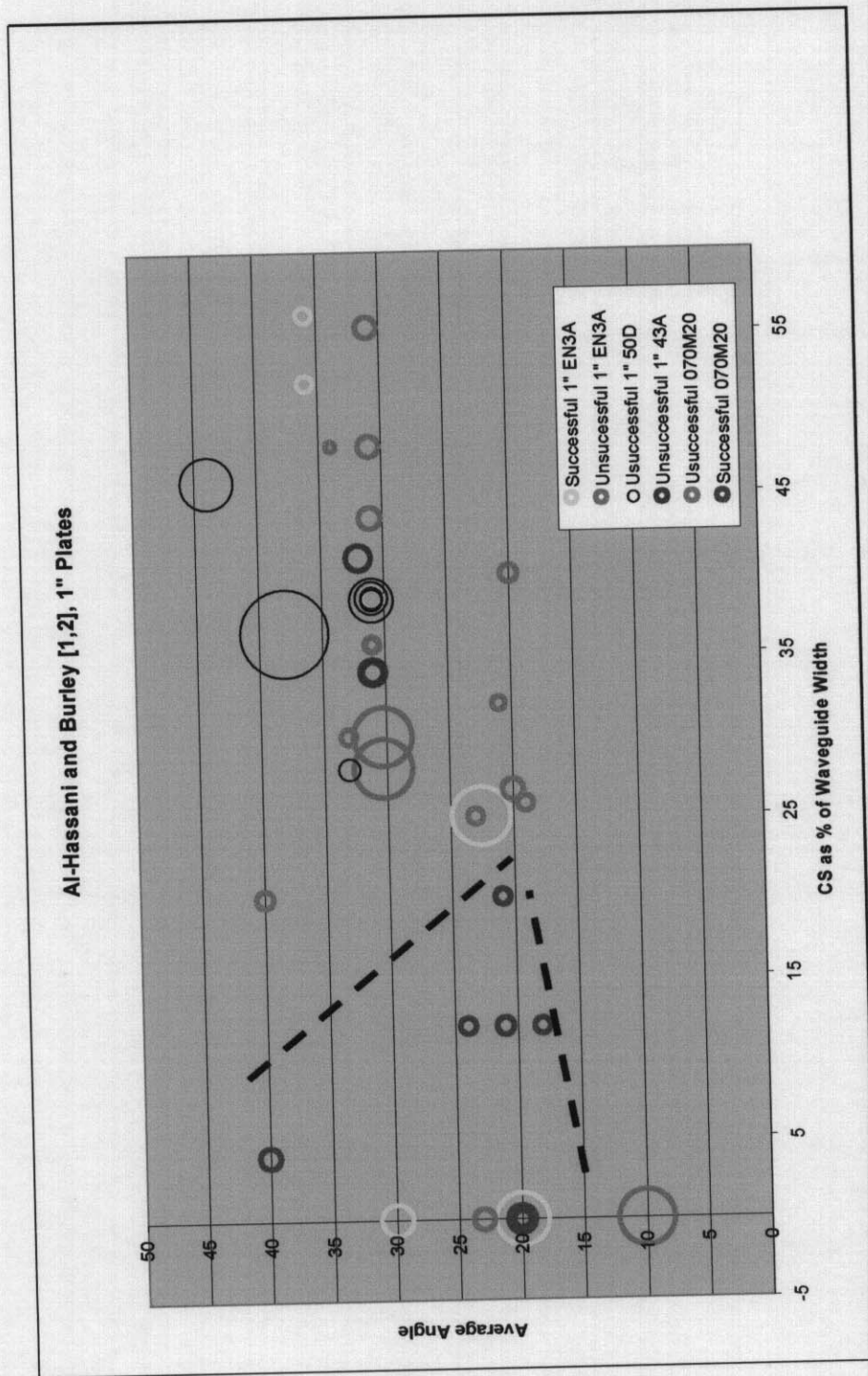


**Figure 4.135:** Evaluation of the effect of CS. Data extracted from Al-Hassani and Burley [1,2] tests using polymeric waveguides. Circle diameters represent relative explosive loads



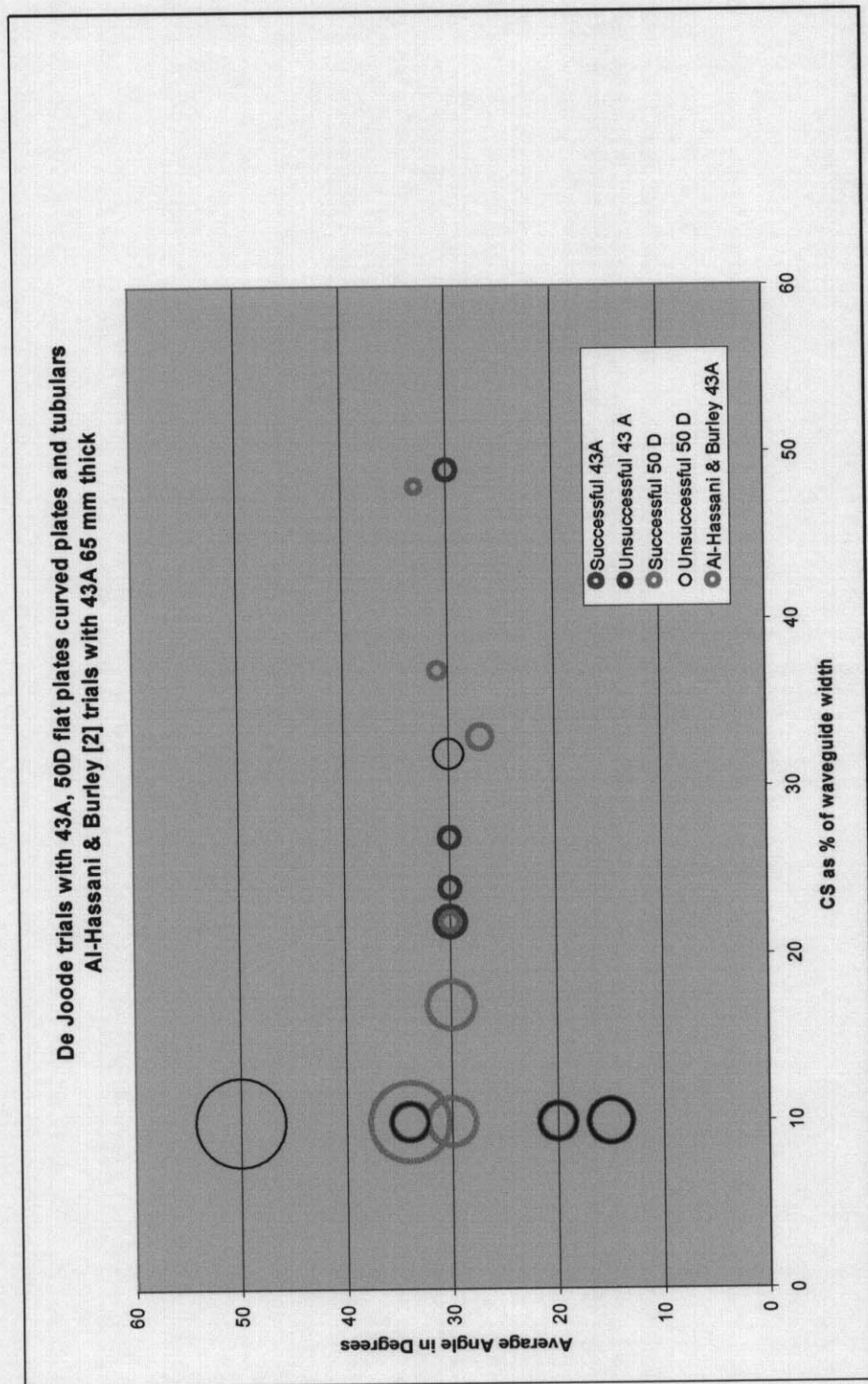


**Figure 4.136:** Evaluation of the effect of CS. Data extracted from all Tests described in Chapter 4 with exception of Tests 6B and C10. Circle diameters represent relative explosive loads.

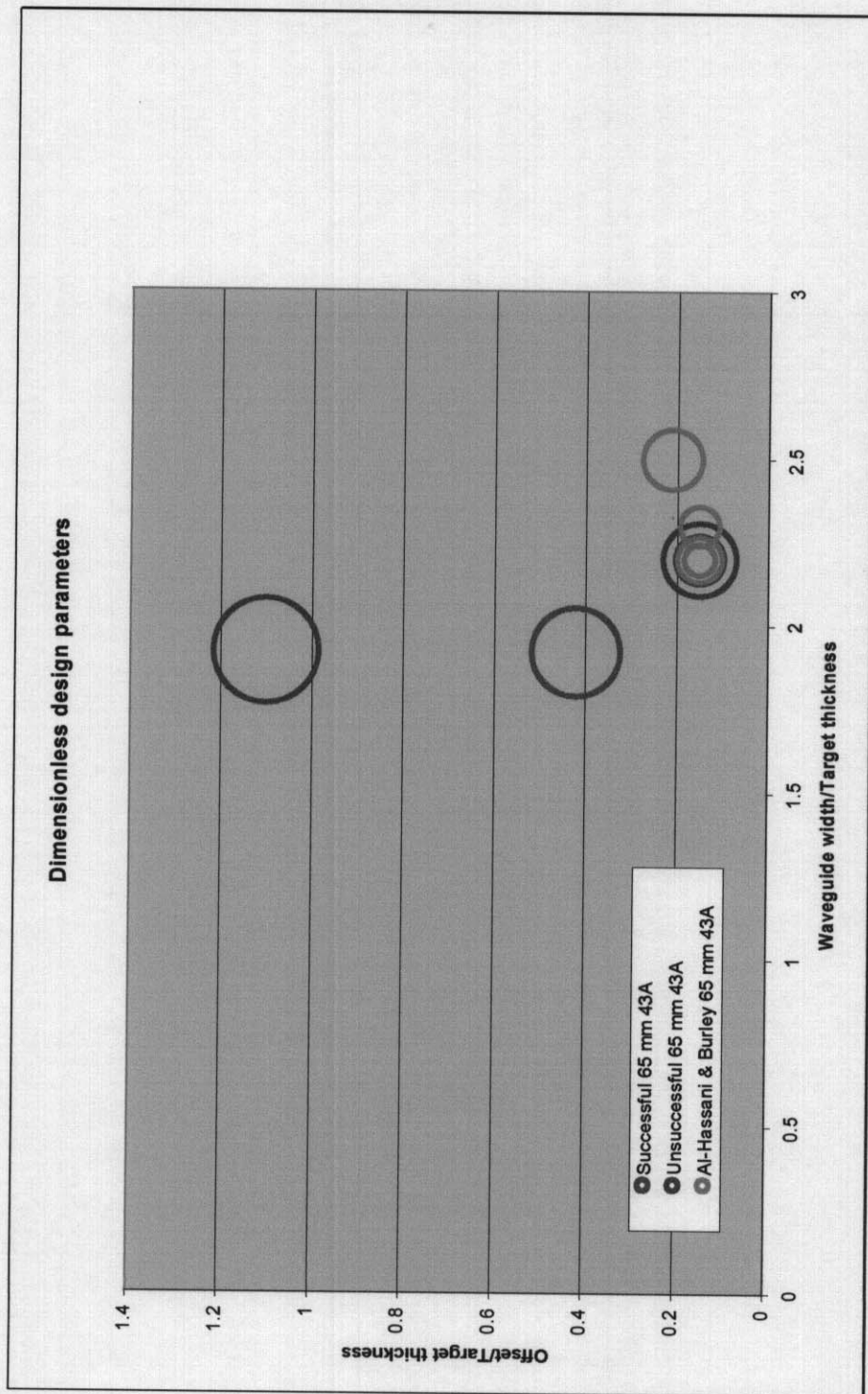


**Figure 4.137:** Results using waveguides Types 1, 2 and 3 on 43A steel target. Results from Al-Hassani & Burley [2] included for completeness. Circle diameters represent relative explosive loads.

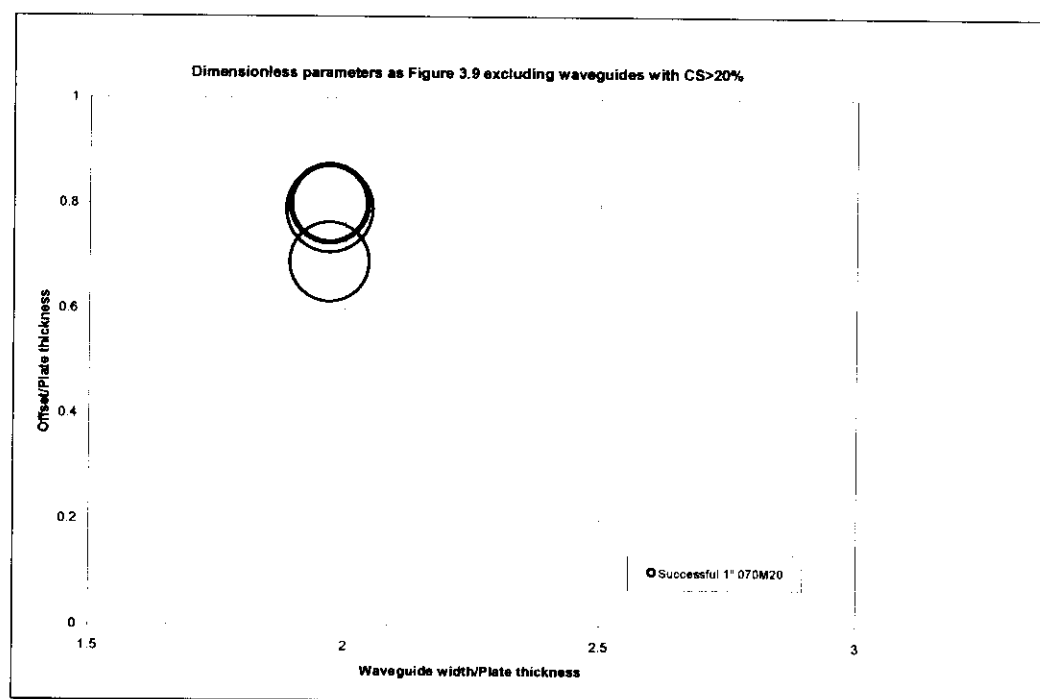


**Figure 4.138:** Data from Figure 3.20 [6.2], excluding waveguides with CS >20%.

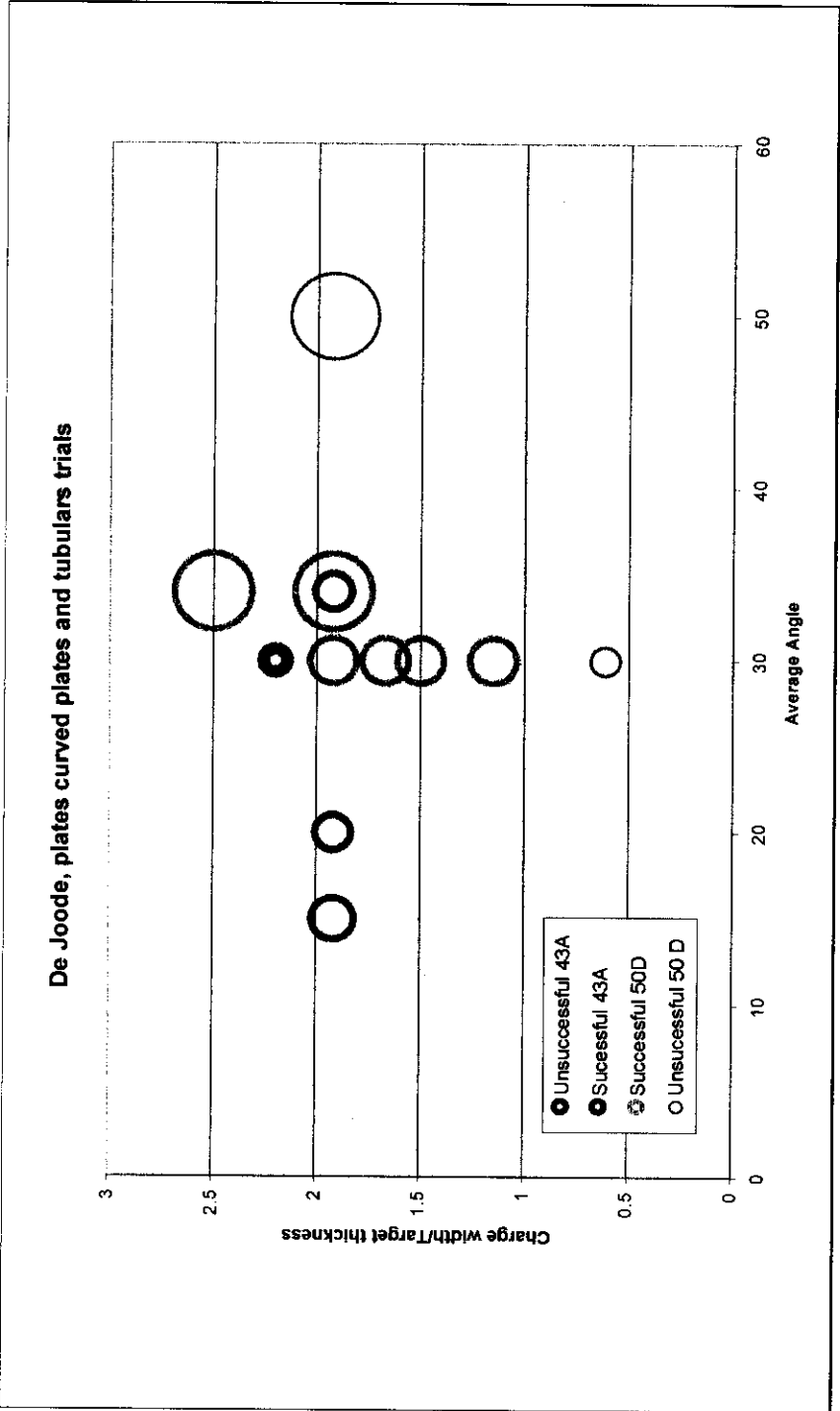


Figure 4.139: Results from Chapter 4 plotted in terms of Average Angle and the ratio Charge-Width/Target Thickness.

## 5 Comparison between numerical and experimental results

### 5.1 Comparison between numerical and experimental results

#### 5.1.1 Curved Waveguides (Types 1,2 and 3)

Unfortunately most tests using Waveguide Types 1 were carried out while the waveguide material was being developed, however it was also tested with a steel waveguide (Test 4). Unfortunately no test was carried out using waveguide Type 1 and  $CS < 20\%$ , it is not possible to say if waveguide Type 1 would have cut the 43A target if a smaller value of CS

appeared to interfere with each other. This analysis has to take into account that in a 3D situation the interaction between incident and reflected stress pulses would have been less intense as incidence and reflection would occur in different planes.

The results of testing a polymeric Type 1 waveguide in Test 8 showed a vertical crack without spall on a 43A target. The numerical simulation of Test 8 used a rubber polymer from the AUTODYN material library, which had the initial density adjusted to reflect the Iron powder content used in the trials. From **Figure 3.12** a shift can be observed from a converging concave wave front observed in **Figure 3.6** to a pattern which is clearly divided in two. The first within the waveguide, is convergent and concave reflecting the waveguide geometry. The second starts after the incident shock reaches the interface and is flatter more similar to the patterns obtained for flat steel waveguides. This reflects the difference in wave speed of rubber waveguide and the steel target. The general trend shown by the isopressure profiles sequence of **Figure 3.12** is that of region of positive interference which gradually moves from top to the back-face followed by a region of interference of reflected tensile stress waves which move gradually upwards to the top face. This is in agreement with theory and the vertical crack found.

Waveguide Type 2 (Tests 9, 10 and 11) cuts the 43A target. The numerical analyses shown in **Figure 3.15 to Figure 3.17** describe a similar pattern to Waveguide Type 1, with values of the region of the reflected tensile waves marginally superior to Test 8. It can be seen that the value of  $-2\text{GPa}$  is maintained up to half of the thickness of the target, while in Test 8 (**Figure 3.12**,  $T=24.2\text{ }\mu\text{s}$ ) the value dropped to  $-1.4\text{GPa}$ .

Waveguide Type 3 fails to cut 43A target despite having  $CS<20\%$  and an explosive load higher than Waveguide Type 2. This suggested that Waveguide Type 3 is outside a “Cutting Window” and could define a lower boundary for average angles. Waveguide Type 3 numerical analysis (**Figure 3.18 to Figure 3.20**) showed a large region of interference between the incident shockwave and the reflected tensile stress wave reducing the regions for interference between reflected stress waves.

#### 5.1.2 Segmental Waveguides (Types 4, 5, 6 & 8)

Waveguide Types 4 was tested on 43A targets in Tests 17 & 23 cutting the target in both cases. It was also tested in 50D steels, using the same explosive load and failed to cut or produce cracks (Test 15), however when the explosive thickness was doubled produced a cut in 50 D targets (Tests 18, C2 & C4). Fracture patterns obtained with 43A targets are similar to those obtained with waveguide Type 2, and significantly different to those obtained with 50D targets. A direct comparison between the behaviour of 43A and 50 targets is not possible as they were not cut with the same explosive thickness, and therefore did not experienced the same pressure time histories.

The fracture patterns obtained using waveguide Types 4 and 6 on 50D steels were achieved with the same explosive thickness of 18 mm and are remarkably similar. They showed consistently in Tests 18, 19, 22, C1 to C9 evidence of a top V shaped shear fracture which is followed underneath by wedged shaped shear fractures. Metallographic examination of cut samples showed the characteristics of adiabatic shear as shown in **Figure 4.103**.

The numerical modelling of waveguides Types 4 and 6 (see **Figure 3.21 to Figure 3.23 and Figure 3.27 to Figure 3.32**) showed that the segmental waveguides with negative separation allow a positive interference of the incident shockwave within the waveguide. This interference generates a region of high pressure that travel down the centre of the waveguide

until it reaches the target surface. The resultant particle velocity is vertical and downwards which hits the target in the centre of the waveguide as projectile. A parallel can be made to the V shaped fracturing showed in **Figure 2.10**, which occurred under the effect of a high-velocity impacting rod. From **Figure 2.8** it can also be observed that the maximum shear trajectories of a flat surface under contact pressure provide a similar fracture pattern as seen on the top part of 50D targets cut using waveguides Types 4 and 6.

Type 6 numerical and experimental result show good agreement between the general crack pattern produced by the model and the experiment as well as failure modes observed (see **Figure 3.41** and **Figure 4.42**). The lack of an appropriate failure model to describe adiabatic shear can be described as the main limitation of the model. In addition to this limitation, it has to be considered that if an appropriate adiabatic shear failure model was available, a mesh size ten times smaller should be used to accurately capture the event.

Test C10 provided an accidental but interesting contribution for this discussion. The first contribution is that it provided an experiment that can be directly compared with Test C9 where the results showed a crack pattern similar to C9 with exception of the top shear fractures. The results from Test C10 also shows a similar local deformation. Test C10 consisted of a set-up identical to Test C9 which was covered with a 2 to 3 mm lead sheet and a further 25 to 30 mm stone and plastic binder aggregate. The results suggest that the compressive shockwave in the lead reflected at the stone aggregate interface as a strong tensile pulse and interfered with the incident pressure pulse within the waveguide, reducing its pressure near the interface.

Results with waveguide Type 5 (Test 20) showed vertical cracks, large attached spall and produced a 60° bending on the target as shown in **Figure 4.35**. Waveguide Type 5 as shown in **Figure 4.33** is larger segmental waveguide, using nearly twice as much explosive as Waveguide Type 6. This result suggested that waveguide Type 5 is outside the “Cutting window” and could define a upper value for averages angles. The numerical analysis (see **Figure 3.24** to **Figure 3.26**) shows that the despite forming a region of positive interference within the waveguide, the transmitted shockwaves are weaker and pass each other before reaching the back interface.

Waveguide type 8 was originally intended to provide a lower boundary for values of



Waveguide-width/Target-thickness but results with waveguide Type 8 were partially affected by a solid rock used as anvil. Waveguide Type 8 had also a large CS = 30% and 35% less explosive than waveguide Type 6 not enabling a meaningful comparison. However it has to be noticed the remarkable amount of damage waveguide Type 8 left on a 50D target when compared with the initial trials using waveguide Type 1 and 2. Test 8 for instance had the same amount of explosive and a similar CS ratio.

## **5.2 Discussion of experimental and numerical results and proposed cutting mechanism for SWF technique**

The experimental results showed two distinct types of cutting processes: The first is characterised by the importance adiabatic shear bands play in the cutting process of 50D steels near the surface in contact with the waveguide. The second is similar to the process already described by Davis [7] and Al-Hassani & Burley [4][19] where the presence of adiabatic shear bands was noticed but its importance in the cutting process was negligible.

The role of interference between incident shock waves and local deformation is proposed as a key factor in the formation of the adiabatic shear bands and for the success of waveguide Types 6 and 4 when cutting the BS4360-50D steel target. The participation of the incident shock waves interference and local deformation when cutting BS 4360-43A steels targets were inconclusive as lower explosive loads were used to cut 43A.

# **6 General Discussion and Conclusions**

## **6.1 Discussion**

### **6.1.1 Proven Capabilities**

The present work contributed to expand the proven capabilities of the SWF technique by developing the technique further, testing it in air and to a limited extend underwater. In the present context, the technique proven “capability” is defined by the experimental track record

available to prove its maximum cutting thickness, taking into account the target environment (air or underwater) and the target geometry (plate, curved plate, tubular).

### **In Air**

Experiments in air prove the charge capabilities using BS 4360 43A, 50 D, 50E and 50EE grade steels, using the same charge design but target thickness varying from 65 mm for 43A and 50D, 50 mm for 50 EE and 44 mm of 50E. Plates, curved plates and full tubulars were cut. Two types of initiation systems were used to cut tubulars, the first system used the same design used successfully to cut plates and curved plates but this design was not able to cut the tubular in two halves in air. The initiation system was modified and two tubulars were successfully cut in air. The tested capabilities of the SWF by the present work can be summarised as follows:

In Air environment, with air on the target back face:

#### **Plates:**

65 mm thick made of 43A (5 tests)

65 mm thick made of 50D (2 tests)

#### **Curved Plates (0.5 meter radius):**

50 mm thick made of 50EE (5 tests)

45 mm thick made of 50E (1 test)

#### **Tubulars (1 meter diameter):**

50 mm thick made of 50 EE (1 test)

44 mm thick made of 50 E (1 test)

### **Underwater**

Most SWF trials were performed in air, with only two trials performed underwater. Only one partially successful experiment was achieved using a 45 mm thick, 1 m diameter

tubular made of BS 4360 50E. The target did not separated in two halves after detonation with the uncut areas restricted to the areas under the two initiation regions. The effect of water is believed to be confined to the presence of water on the target back face.

The results suggest that the SWF technique work better with air (or low density materials) in the target back face. The results also suggest that the annular initiation system used, the so called “vertical triangle”, despite being successful in air is not suitable for underwater applications. The design of a suitable initiation systems should take into account the numerical analyses presented in this report, where the explosive charge is initiated simultaneously on the tow sides of the waveguide at the outer surface of the explosive.

### 6.1.2 Reliability

SWF is a recent technology and is still under development, therefore it is not expected to have the same level of reliability as shaped charges enjoy at the moment. The present work have contributed to enhance the SWF reliability by identifying the cutting mechanisms and the effect of the explosive distribution on the waveguide. By analysing this important parameter it was possible to identify a “Cutting Window” where the reliability of the SWF charges seems comparable to shaped charges provided that:

- Underwater data considered only cutting regions outside the influence of the charge initiation region
- The charge is in good contact with the target
- Target back face material is water or air, preferably air.

These three points characterise the main limitations of the SWF technique. The first limitation is temporary, as the development of a annular initiation system for waveguide charges represents a feasible task. The second limitation was not studied in the present work as all SWF charges were in good contact with their targets. Reference to the detrimental effect of the lack of contact between fracturing charges and their targets suggest that the same would occur with SWF charges. The third limitation is related to the basic principles of the method, where variations on the back face material can have a detrimental effect on the intensity of the

reflected tensile stress waves at the target back face. The presence of back face materials like rock and steel proved to be detrimental to a point where the cut was inhibited.

Once a suitable annular initiation system is developed, it is possible to anticipate situations where the other limitations can be eliminated by ensuring that the back face condition is water or preferably air and ensuring that a good contact between charge and target is achieved. In this situations the SWF technique is expected to be reliable if the charge design is within the cutting window previously identified.

### 6.1.3 Relative Environmental Impact

The scenario presented by small and medium platforms in the GOM include a large number of small platforms and widespread presence of sensitive marine life, therefore reduction of explosive weight could have a significant reduction in the environmental impact of overall decommissioning effort. Within the context of the present work, the relative environmental impact of the SWF explosive cutting techniques is measured in terms of explosive load used to cut one meter of target length or circumference. This is a qualitative analyses and no attempt is made to quantify the relative environmental impact.

The main motivations for the development of the SWF technology was its potential to reduce the explosive load necessary to produce a reliable cutting tool. The SWF technique cut successfully 65 mm thick plates made of 50D steel in air and 44 mm of 50E underwater using approximately 3 kg of explosive load per linear meter of charge. This compares very favourably with other explosive cutting techniques, specially when considering that the typical grades of steel used in small jackets in the GOM.

Measures to reduce the underwater environmental impact include the reduction of the explosive load of individual charges and the use time delays between firing of multiple charges. Some efforts have been made in UMIST to investigate the effectiveness of shock mitigation devices based on low density materials. For the use of such devices to be considered as a feasible alternative, it is necessary to take into account the impact of the dimensions of an effective mitigation device on the deployment operations. If the size of an effective mitigation device is unmanageable it is likely that the device would not be used at all.

The potential reduction of explosive load provided by the SWF technique may enable future efforts of constructing a effective mitigation device of realistic dimensions.

## 6.2 General Conclusions

The SWF portion of the work was concentrated in develop the technique and prove its capability in the cutting of plates, curved plates and tubulars made of BS 4360 grade 50D steel underwater. This was in great part achieved, the cutting phenomenology was investigated and contribution to its understanding include:

- The identification of the importance of explosive distribution in addition to the waveguide geometry.
- The description of the fracturing process in 50D steels including the important participation of the interference of compressive shockwaves on top surface of the target, making the material in a first stage followed by spalling of the back surface due to the interference of the reflected tensile stress waves, followed by further fracturing between these two regions due to further interference of reflected tensile stress waves. This phenomena was not observed in the 43A steel targets fractured using lower explosive loads.
- The identification of a “cutting window” for 50D, 50E and 50EE steel grades where the reliability of the SWF technique was comparable to shaped charges when water or air was used in the back face.
- A numerical simulation of the cutting process was performed using AUTODYN 2D, finite difference method package. The numerical results were in good agreement with the experimental results, but further work is still necessary to accurately capture the complexity of the cutting process.

## Bibliographic References

- [1] Twomey, BG "Literature review of circular shaped charges" Department of Mechanical Engineering, University of Manchester Institute of Science and Technology and Reverse Engineering Limited as part of the EROS project prepared for Amoco (UK), October 1994.
- [2] Shaw, D; "Deconstruction and disposal of offshore platform topsides" Eng.D. (Engineering Doctorate) Thesis, University of Manchester Institute of Science and Technology, August 1999.
- [3] Commission of European Community, OSPAR resolution, Official Journal of the European Union, European Commission, 1999/C 158/03, 4<sup>th</sup> June 1999.
- [4] Al-Hassani, STS and Burley, SJ; "Fracturing of 50D steel and concrete by stress wave focusing technique", Department of Mechanical Engineering, University of Manchester Institute of Science and Technology, Final Report for Marinotech North West, 1991.
- [5] Denis, JA; "Steel cutting with high-explosive charges", U.S. Army Engineer Research and Development Laboratories Fort Belvoir, Virginia, December 1965.
- [6] Poulter, TC; "Controlled fracturing of solids by explosives", US patent No3076408, 1963
- [7] Davis, L; "Explosive cutting of plates by stress wave interaction", MSc. Thesis, Department of Mechanical Engineering, University of Manchester Institute of Science and Technology, March 1984.
- [8] Millar, RP; "An investigation into the cutting of steel plate with a curvilinear shaped charge" M.Sc. Thesis, Department of Mechanical Engineering, University of Manchester Institute of Science and Technology, May 1993.
- [9] Twomey, BG; "Circular shaped charges for underwater applications" Ph.D. Thesis, Department of Mechanical Engineering, University of Manchester Institute of Science and Technology, 1994.
- [10] Goulding, L; "The abandonment of offshore platforms with steel jacket structures" Eng.D. (Engineering Doctorate), University of Manchester Institute of Science and Technology, 1999.
- [11] Abd, IJ; "Structural response to through-water explosive loading" Ph.D. Thesis, Department of Mechanical Engineering, University of Manchester Institute of Science and Technology, 1997.
- [12] Vartal, B, Ph.D. Thesis, Department of Mechanical Engineering, University of Manchester Institute of Science and Technology, 1999.
- [13] Al-Hassani, STS, Twomey BG, De Joode A, Sarumi, M, Abd, I and Gregory, A; "EROS - Explosive Response of Offshore Structure", Department of Mechanical Engineering, University of Manchester Institute of Science and Technology and Reverse Engineering Limited, prepared for Amoco, 1996.
- [14] Al-Hassani, STS, Twomey BG., De Joode, A, and Millar, RP; "Engineered explosives for underwater cutting using minimum explosive for safe reliable platform removal (EXCUT)". Prepared for the Commission of European Communities, Directorate General for Energy, Thermie programme, Project No OG\042\90\UK, 1994.
- [15] Al-Hassani, STS, Twomey BG and De Joode, AS; "Engineered explosives for underwater cutting using minimum explosive for safe reliable platform removal – Phase II (EXCUT II). Prepared for the Commission of European Communities, Directorate General for Energy, Thermie programme, Project No OG\420\90\UK, 1996.

- [16] Al-Hassani, STS, Twomey BG and De Joode, AS; "Deepcut project – Documentation Suite". Department of Mechanical Engineering, University of Manchester Institute of Science and Technology, and Reverse Engineering Limited Prepared for the Commission of European Communities, Directorate General for Energy, Thermie programme, Project No OG\00\00147\94\UK, 1996.
- [17] Vartal, B, Burley, SJ, Goulding, L, Gjelsuik, K; "Hinge Study", Department of Mechanical Engineering, University of Manchester Institute of Science and Technology and Reverse Engineering Limited, prepared for Amoco (UK) and Phillips Petroleum Company Norway, May 1998.
- [18] Al-Hassani, STS. and Burley SJ; UK Patent application No 88 007044
- [19] Al-Hassani, STS and Burley SJ; "Fracturing of 50D steel and concrete by stress wave focusing", Department of Mechanical Engineering UMIST, prepared for Marinetechn 1987.
- [20] Davis, TL; "The chemistry of powder explosives", John Wiley & Sons, New York, 1943
- [21] Fordham, S; "High explosives and propellants", Pergamon Press, 1980
- [22] US Army and US Airforce. "Military explosives" Technical Manual No 9-1300-214, November 1967.
- [23] Rinehart, JS and Pearson, J. "Explosive working of metals" Pergamon Press New York 1963.
- [24] ABD, I and Sarumi, M; "Modules 2 and 3" in "EROS - Explosive Response of Offshore Structure", Department of Mechanical Engineering, University of Manchester Institute of Science and Technology and Reverse Engineering Limited, prepared for Amoco, 1996.
- [25] Silva Gomes, J.F.; "Elastic and plastic response of a chain of circular rings to impact loading and stress wave focusing in axisymmetric solids", Ph.D. Thesis UMIST, October 1977.
- [26] Rinehart, J.S.; "Stress transients in solids" Hyperdynamics, Santa Fe, New Mexico 230pp, 1975
- [27] Rinehart J.S. and Pearson J. , "Behaviour of metals under impulsive loads", Dover Publications, 256 pp, 1965
- [28] Meyers, MA and Murr, LE, "Propagation of Stress Waves in Metals" in Explosive Welding, Forming and Compaction, Ed TZ Blazynski, Applied Sciences Publishers, pp 17-82, 1983
- [29] Nicholas,T. and Recht R.; "Introduction to impact phenomena" Section 1 in High Velocity Impacts Dynamics, Ed. Zukas J.A., John Wiley & Sons, Inc., 63 pp, 1990
- [30] Nicholas, T and Rajendran A.M.; " Material characterisation at high strain rates" Chapter 3 in High Velocity Impacts Dynamics, Ed. Zukas J.A., John Wiley & Sons, Inc., 127-295pp, 1990
- [31] Tuler, F.R. and Butcher, B.M., "A Criterion for the Time Dependence of Dynamic Fracture", Int., J. Fract. Mech., vol. 4, pp 431-437, 1968
- [32] Johnson, G.R. and Cook W.H., "Fracture Characteristics of Three Metals Subjected to Various Strains, Strains Rates, Temperatures and Pressures" Engng, Fract. Mech., vol 21, pp 31, 1985
- [33] Asay, J.R. and Kerley G.I., "The response of materials to dynamic loading", Int. J Impact Engng., Vol 5, pp 69-99, 1987
- [34] Curran, D.R., Seaman L. and Shockey, D.A., "Dynamic failure of solids", Physics Reports 147, N 5 & 6, pp 253-388, Elsevier Science Publishers BV( North -Holland Physics Publishing Division), 1987



- [35] British Standard Institute, "Methods for Crack Opening Displacement (COD) Testing", BS 5762, 1979
- [36] British Standard Institute, "Methods of Test for Plane Strain Fracture Toughness ( $K_{Ic}$ ) of Metallic Materials", BS 5447, 1977.
- [37] British Standard Institute, "Guidance on Some Methods for the Derivation of Acceptance Levels for fusion Welded Joints", BSI document PD 6493, 1980.
- [38] Shockey D.A. and Erlich, D.C. "Metallurgical Influences on Shear Band Activity", in Shock Waves and High-Strain-Rate Phenomena in Metals, Ed. Meyers and Murr, Plenum Press, pp249-261, 1981
- [39] Argon, A.S. and Safogler, R.; Metallurgical Transactions, A 6, pp 825, 1975.
- [40] Kalthoff, JF and Shockey, DA; "Instability of cracks under impulsive load", J. of Applied Physics, Vol. 48, No 3, pp 986-993, March 1977.
- [41] Mackenzie, A.C., Hancock J.W. and Brown D.K. ; "On the influence of state of stress on ductile failure initiation in high strength steels" Eng Fract.Mech., Vol 9 pp 167, 1977.
- [42] Seaman, L., Shockey D.A. and Curran D.R., "Dynamic Crack Propagation", Ed G C Sih ( Noordhoff), Leyden, pp 629, 1973
- [43] Zenner C. and Hollomon J. H., "Effect of Strain Rate upon Plastic Flow of Steel", J Appl. Physics, vol 15 pp22-32, 1944.
- [44] Shockey D.A., "Materials aspects of the adiabatic shear phenomenon", in Metallurgical Applications of Shock-Wave and High-Strain-Rate Phenomena, Ed. L Murr et all , Marcel Dekker Inc, pp 663-656, 1986
- [45] Woodward R.L., "Material Failure at High Strain Rates", in High Velocity Impact Dynamics, Ed J.A. Zukas , Jonh Wiley & Sons Inc. , pp 65-125, 1990.
- [46] Stelly, M. and Dornmeval, R., "Adiabatic Shearing", in Metallurgical Applications of Shock-Wave and High-Strain-Rate Phenomena, Ed. L Murr et all , Marcel Dekker Inc, pp 607-632, 1986
- [47] Walker, T.J. and Shaw M. C., "On Deformation at Large Strains" in Advances of Machine Tool Design and Research, Ed Tobias and Koenigsberger, Pergamon Press, NY, PP241, 1969.
- [48] Olson, G.B., Mescall, J.F. and Azrin M., "Adiabatic Deformation and Strain Localisation", in Shock Waves and High-Strain-Rate Phenomena in Metals, Ed. Meyers and Murr, Plenum Press, pp221-247, 1981
- [49] Mescall, J.F "On the Relative Roles of Strain -Hardening and Thermal-Softening in Adiabatic Shear Bands" in Metallurgical Applications of Shock-Wave and High-Strain-Rate Phenomena, Ed. L Murr et all , Marcel Dekker Inc, pp 689-704, 1986
- [50] Swegle, J.W. and Grady, D.E., "Calculation of Thermal Trapping in Shear Bands", in Metallurgical Applications of Shock-Wave and High-Strain-Rate Phenomena, Ed. L Murr et all , Marcel Dekker Inc, pp 705-722, 1986
- [51] Rogers, H.C. and Shastry, C.V., "Material Factors in Adiabatic Shearing in Steels", in Shock Waves and High-Strain-Rate Phenomena in Metals, Ed. Meyers and Murr, Plenum Press 1981, pp285-298.
- [52] Moss, G.L., "Shear Strains, Strain Rates and Temperature Changes in Adiabatic Shear Bands", in Shock Waves and High-Strain-Rate Phenomena in Metals, Ed. Meyers and Murr, Plenum Press, pp299-312, 1981
- [53] Meyer, L.W. and Manwaring, S; "Critical Adiabatic Shear Stregth of Low Alloyed Steels Under Compressive Loading", in Metallurgical Applications of Shock-Wave and High-Strain-Rate Phenomena, Ed. L Murr et all , Marcel Dekker Inc, pp 657-674, 1986